The Dissertation Committee for Heath Heinrich Reising Certifies that this is the approved version of the following dissertation:

Application of Spontaneous Raman Scattering for Measurements of Thermal Non-Equilibrium in High-Speed Mixing and Combustion

Committee:

Noel Clemens, Supervisor

Philip Varghese, Co-Supervisor

Fabrizio Bisetti

Matthew Hall

Laxminarayan Raja

Application of Spontaneous Raman Scattering for Measurements of Thermal Non-Equilibrium in High-Speed Mixing and Combustion

by

Heath Heinrich Reising

Dissertation

Presented to the Faculty of the Graduate School of
The University of Texas at Austin
in Partial Fulfillment
of the Requirements
for the Degree of

Doctor of Philosophy

The University of Texas at Austin
December 2017

Acknowledgements

There are so many to thank for helping me through my time at the University of Texas, as one does not complete this process without a multitude of support from others. I would first like to thank my advisors, Prof. Noel Clemens and Prof. Philip Varghese. Their guidance, both technical and editorial, made me a better researcher. Their patience with me as I learned throughout my Ph.D. work is greatly appreciated. I also would like to thank Prof. Fabrizio Bisetti, Prof. Matthew Hall, and Prof. Laxminarayan Raja for their time and effort spent serving on my dissertation committee.

I would like to thank the graduate students and post-docs who I have had the privilege of working and teaching alongside: Dr. Chris Combs, Dr. Dominik Ebi, Benton Greene, Mohammed Saleem, Rakesh Ranjan, Serdar Seckin, Sina Rafati. Dr. Oli Buxton, Dr. Okjoo Park, and Dr. Leon Vanstone. Each of them in some way has helped me complete this work, whether through lending an extra hand or for light-hearted discussion which made a dark laboratory seem a little brighter. I would like to extend special thanks to Dr. Ross Burns who guided me through my first few years in graduate school when I felt lost at times and countless times provided assistance at the expense of his own productivity. I am also appreciative of Dr. Utsav KC for his tutelage in the fine details of setting up a spontaneous Raman scattering experiment. Last, but not least, I would like to thank Tim Haller for his assistance is operating these experiments, sometimes late into the night.

I owe debt of gratitude to many on the staff of the Department of Aerospace Engineering and Engineering Mechanics. In particular, Dr. Jeremy Jagodzinski, our lab technician, was an invaluable resource through the process of setting up and running my experiments. His effort in maintaining a clean and organized lab through the onslaught of

messes created by myself and my fellow graduate students was much appreciated. I also have to thank Geetha Rajagopal for her assistance in making the countless purchases required to set up and operate these experiments. I would like to thank Joe Pokluda for his guidance in fabricating many of the parts used within this experiment. For those parts which required special skill, I would like to thank the machinists in the ASE Machine Shop: David Gray, Travis Crooks, and Ricardo Palacios.

Recognition should also be given to the Air Force Office of Scientific Research for funding this work under BRI grant FA9550-12-0460. I would also like to thank the Cockrell School of Engineering and Crain family for their financial support through the Cullen M. Crain Endowed Scholarship in Engineering.

Finally, I would like to thank my family for their reassurance and love throughout this process. To my parents, who instilled in me at a young age an appetite for learning, this dissertation would not have been possible without your guidance. The level of rigor has increased from my third grade science fair experiments, but your support has never wavered. Last, but certainly not least, I could not possibly have made it through this process without the constant support from my wife, Emily. Thank you for always cheering me up when things didn’t go my way and listening to me try to explain the minutiae of my day-to-day struggles.

Application of Spontaneous Raman Scattering for Measurements of Thermal Non-Equilibrium in High-Speed Mixing and Combustion

Heath Heinrich Reising, Ph.D.
The University of Texas at Austin, 2017

Supervisors: Noel T. Clemens and Philip L. Varghese

Mixing-induced vibrational non-equilibrium is studied in the turbulent shear layer between a high-speed jet and a surrounding hot-air coflow. The vibrational and rotational temperatures of N_2 and O_2 are determined by fitting measured spontaneous Raman scattering spectra to a model that allows for different equilibrium distributions of the vibrational and rotational states. The mixing of the jet fluid with the coflow gases occurs over microsecond time scales, which is sufficiently fast to induce vibrational non-equilibrium in the mixture of hot and cold gases. I measured the non-equilibrium on the hot side of the shear layer, but not on the cold side where the vibrational population in the first hot band is negligible. The effect of fluctuating temperatures on the time-averaged Raman measurement was quantified using single-shot Rayleigh thermometry. The Raman scattering results were found to be insensitive to fluctuations except where the flame is present intermittently. It was also found that the measured non-equilibrium increases in the shear layer when N_2 is removed from the jet fluid, indicating that the measurements average two competing processes that occur simultaneously at a molecular scale: vibrationally hot N_2 cooled by the fast jet fluid and vibrationally cold jet fluid heated by a hot coflow. An interesting inference is that the averaging effect is always present, regardless of the measurement resolution. No measurable vibrational non-equilibrium is found in the O_2 molecules in the same non-reacting regions. This difference between species temperatures violates the two-temperature assumption often used in the modeling of high-temperature non-equilibrium flow.

A new technique was developed to obtain spontaneous Raman scattering temperature measurements from a single laser pulse. This technique required the construction of a multiple-pass cell to obtain adequate scattered signal. Additionally, the pulse was stretched temporally with a system of partial reflectors and time-flight-delay ring cavities in order to reduce the peak power of the 1 J laser pulses. These measurements were found to be in agreement with the previous time-average results and allowed for measurement to be made near the fluctuating base of a lifted flame – a region where time-averaged measurements do not give meaningful results.

Table of Contents

List of Tables

List of Figures

Chapter 1: Introduction

Thermal non-equilibrium is inherent to hypersonic flight owing to the presence of aerothermal heating, chemical reactions and rapid changes in flow conditions. In particular, shocks, isentropic compressions and expansions, and viscous dissipation can lead to rapidly changing kinetic temperatures, which result in the transfer of energy into or out of vibrational states to maintain thermal equilibrium. If the rate of change of kinetic temperature outpaces the rate at which molecular collisions can exchange energy between modes, a local non-equilibrium state will be produced. While rotational-to-translational (R-T) energy transfer may take only a few nanoseconds, vibrational-to-translational (V-T) energy transfer timescales are on the order of microseconds to milliseconds [1]. Thermal non-equilibrium may play a particularly important role in hypersonic engines since the residence times of the gas inside the engine are particularly short. For example, it has been shown that vibrational non-equilibrium can have a significant impact on the overall performance of the combustor through alteration of the chemical reaction rates or the transport properties [2]. Thus, knowledge of the production and transport of vibrational non-equilibrium upstream and at the ignition site is of utmost importance to accurately determine the impact on combustor performance.

1.1 – LITERATURE SURVEY

The research described in this dissertation aims to provide insight into the complex interaction between turbulent mixing and finite-rate vibrational relaxation processes. Section 1.1.1.1 will focus on describing the physics that govern the relaxation of vibrational non-equilibrium. First, analytical models of the relaxation process are introduced, which indicate the overall trend in relaxation rate with temperature. Then, current state-of-the-art computational models are summarized, which move beyond the simple geometry of the analytical models. Finally, non-equilibrium relaxation times from experiments and calculations are summarized for a variety of molecules relevant to the current study. Section 1.1.1.2 summarizes previous literature on experimental studies of vibrational non-equilibrium in various flows.

Section 1.1.2 will provide background on the two scattering techniques used in this study. Spontaneous Raman scattering is utilized in order to record simultaneously the vibrational and rotational temperatures of the gas. This provides species-specific temperatures for diatomic species present in the oxidizer and fuel streams of the jet flame. Section 1.1.2.1 outlines the specifics of this technique, focusing on its use for thermometry. The use of Rayleigh scattering as a thermometric technique is also reviewed in Section 1.1.2.2.

1.1.1 – Thermal Non-equilibrium

This study focuses on non-equilibrium between vibrational and translational energy states that occurs without electronic excitation or molecular dissociation. This type of non-equilibrium is typical of moderate temperature (<2000 K) high-speed flows. While there are a large number of studies on non-equilibrium in atmospheric re-entry flows, these will not be considered for this study due to the difficulty in isolating the effects vibrational non-equilibrium processes from the dissociation and charged particle chemistry.

1.1.1.1 – Non-equilibrium Relaxation Rates

A system in thermal equilibrium is defined by having all its “parts” at the same temperature. For the moderate temperature flows of interest in this study, these “parts” are the translation, rotational, and vibrational modes of gaseous molecules. Any perturbation of a state from equilibrium will eventually be driven back to equilibrium by molecular collisions. The rate at which this relaxation will occur is dependent on the dynamics of the collisions, which is discussed below.

In the commonly used Born-Oppenheimer approximation of molecular collisions, electronic motions are assumed to be very rapid when compared with the nuclear motion. As a consequence, the electrons readjust with such speed to the alterations in the intermolecular field due to the collision that they do not experience any energy change. This process is then considered to be adiabatic in terms of electronic energy, as the collision does not transfer significant energy from the nuclear motions. This principle, known as Ehrenfest's Adiabatic Principle, can be applied similarly to rotational and vibrational energy transfer. Following the procedure in Clarke & McChesney [3], one can show that vibrational-translational interactions of typical diatomic molecules are expected to be nearly adiabatic at low temperatures with a trend to more energy transfer at higher temperatures and lower collision reduced mass. This is due to quasi-equilibrium being maintained between the collision partners due to the relatively long interaction time relative to the vibrational period of the oscillator. Conversely, rotation-translation energy transfer is expected to be a very efficient process for all diatomic molecules except cryogenic hydrogen due to the much smaller energy spacing of rotational levels (and therefore short rotational period when compared with the collision interaction time). Therefore, it takes only a few collisions for the energy transfer between modes for rotational-translational equilibration. Vibrational-translational equilibration, on the other hand, occurs on timescales many orders of magnitude longer. For all of the following analysis, rotational temperature will be assumed to be identical to the translational temperature.

For diatomic molecules, the simplest model for vibrational motion is that of a "simile harmonic oscillator," where each atom is attracted toward the equilibrium position by a restoring force which is proportional to the displacement from equilibrium. In fact, diatomic molecules do behave much like harmonic oscillators for the lowest energy vibrational states [4]. The relaxation process of a system of harmonic oscillators can be described by a single characteristic time, defined in terms of the vibrational energy as

$$\frac{d}{dt}\varepsilon_v = \frac{\varepsilon_{v,eq} - \varepsilon_v}{\tau}, \tag{0.1}$$

where ε_v is the total vibrational energy, $\varepsilon_{v,eq}$ is the equilibrium value of ε_v, and τ is the relaxation time. This result does not imply that all transitions relax at the same rate, but that they may be grouped together by a macroscopic relaxation time for the entire vibrational energy mode. For anharmonic oscillators, master equation modeling, which solves the relaxation problem through a system of differential equations modeling each state-to-state transition, provides the most detailed results. In a series of papers, Montroll and Shuler showed that a system of anharmonic oscillators in an initial Boltzmann distribution can be represented accurately by a system of harmonic oscillators if the anharmonicity constants are small, as they are for most diatomic molecules [5]–[7]. It is important to note that this relaxation time is defined for vibrational energy, and not vibrational temperature. Temperature relaxation does not follow a simple exponential decay law, and therefore cannot be characterized by a simple relaxation time, except in the “acoustical” approximation where non-equilibrium is very weak so that the non-linear relation between vibrational energy and vibrational temperature can be linearized [8]. The relaxation time of a harmonic oscillator is given as

$$\frac{1}{\tau} = P_{1,0} Z' n \left(1 - e^{\theta_v / T}\right), \tag{0.2}$$

where the transition probability, $P_{1,0}$, must be determined based on knowledge of the vibration-translation interaction, while the collision rate, Z', and number density, n, can be determined from kinetic theory [3].

The well-known Landau-Teller theory assumes a collinear interaction of molecules with an exponential repulsive interaction potential such that the probability of de-excitation is

$$P_{1,0} = P^* A\ exp\left(-\frac{fs}{\vartheta}\right), \tag{0.3}$$

where P^* is a steric factor that adjusts for the inherent error of the one-dimensional analysis, A and s are constants of the interaction potential, f is the vibrational frequency, and ϑ is the collision velocity. When Eqn. 1.3 is integrated over a Maxwellian velocity distribution at a particular temperature, the result is shown in [8] to be

$$\tau = Z_0' \sqrt{\frac{3}{2\pi}\left(\frac{\varepsilon'}{kT}\right)^{-1/6}} exp\left[\frac{3}{2}\left(\frac{\varepsilon'}{kT}\right)^{-1/3}\right]\left[1 - exp\left(-\frac{\theta_v}{T}\right)\right]^{-1}, \tag{0.4}$$

where $Z_0{}'$ incorporates the steric factor, which is determined to be approximately 3 from comparison with experimental results, θ_v is the characteristic temperature of the vibration, and T is the local kinetic temperature. The ε' factor is a simplified representation of an energy-like term which depends on the "hardness" of the repulsive potential as well as the vibrational frequency. The parameter $\frac{\varepsilon\prime}{kT}$ is essentially a measure of the efficiency of the energy transfer due to the collision, as it is a ratio of the collision duration to the vibrational period of the oscillator. This result illustrates the characteristic Landau-Teller temperature dependence of

$$\tau \propto T^{1/6}\ exp\left(T^{-1/3}\right), \tag{0.5}$$

(for $T \ll \theta_v$) which is commonly used to scale vibrational relaxation time data. This interaction acts at large molecular separations and therefore is weak, causing Landau-

Teller results to have low transition probabilities due to the lack of an attractive component in the potential.

Schwartz, Slawsky, and Herzfeld considered the same configuration as Landau and Teller, but used an interaction potential which was fitted from a Lennard-Jones potential instead of the purely exponential interaction [9],[10]. This analysis yields

$$\tau = \mathrm{Z}\left(\frac{kT}{\varepsilon'}\right)^{1/6} exp\left[\frac{3}{2}\left(\frac{\varepsilon'}{kT}\right)^{-1/3} - \frac{\theta_v}{2T}\right]\frac{exp\left(-\frac{\varepsilon_{LJ}}{kT}\right)}{1 - exp\left(-\frac{\theta_v}{T}\right)}, \tag{0.6}$$

which shows a similar form as the Landau-Teller result, but with additional correction terms in the exponent. The attractive Lennard-Jones constant is represented by ε_{LJ} and Z contains a steric factor as well as other temperature-independent terms. The relaxation times of pure N_2 and O_2 are shown below in Figure 2.1. The relaxation time of N_2 is longer than that of O_2 due to larger vibrational energy level spacing. Both SSH and Landau-Teller methods show the same $\exp\left(T^{-1/3}\right)$ dependence at high temperatures.

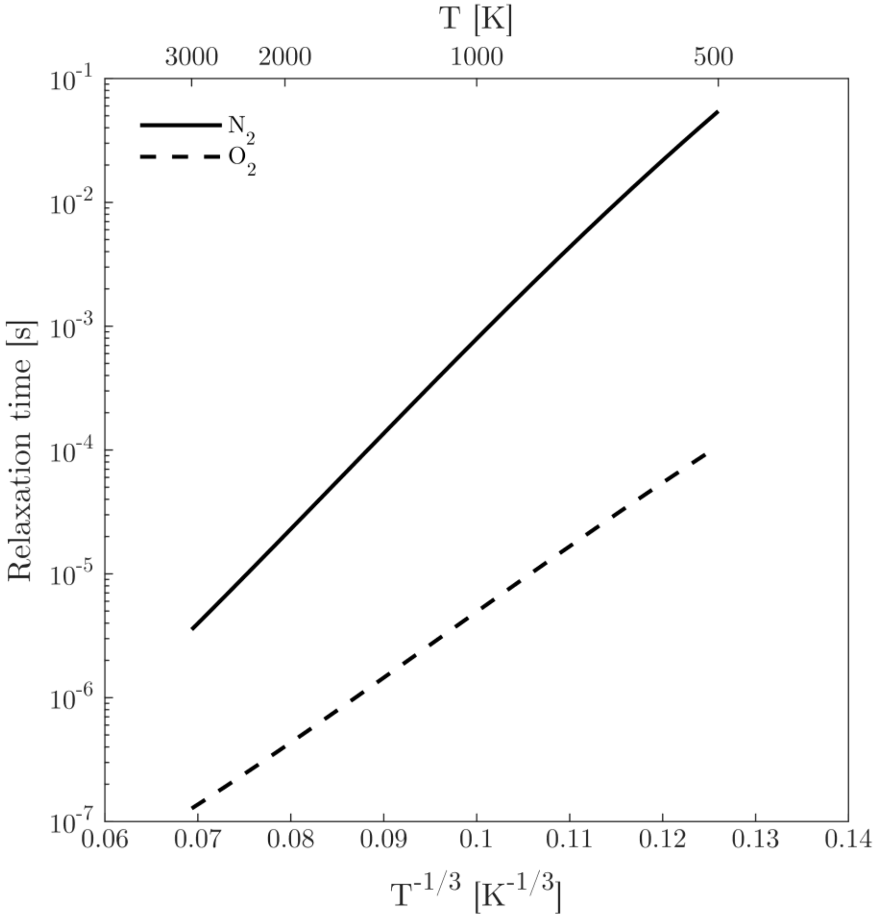

Figure 1.1: Calculated relaxation times for pure gases using SSH method

These analytical results, while useful in showing general trends for relaxation time, are valid only for harmonic oscillators undergoing single-quantum transitions. They also require a steric factor to account for the error in the assumption of collinear collisions. More recent work by Adamovich and coworkers has applied a Forced Harmonic Oscillator (FHO) model to analyze vibrational energy transfer in molecular collisions [11]. This model does not require the assumption of Landau-Teller and SSH models and also shows good agreement with numerical results. This model, while too complex to be explained in detail here, is the state-of-the-art in analytical modeling of vibrational relaxation.

Modern computational power has opened up many new avenues for calculation of relaxation rates. Numerical quantum mechanical calculations of colliding harmonic oscillators have been performed using simple collinear collision geometries [12],[13]. These calculations provide a test case for more approximate methods, but do not provide useful values for 3D behavior without the addition of a steric factor, much like the analytic collinear models. More recent calculations have been performed for 3D geometries, but have focused on high energy collisions in re-entry flows, which are not relevant to this study [14]. Billing and coworkers developed a "semi-classical" calculation method by treating just the vibrational degree of freedom quantum mechanically and using a classical approach for the rotational and translational motion [15]. A Monte Carlo average is taken over a large set of randomly chosen trajectories to compute an average transition probability for a given initial energy state. These calculations require detailed knowledge of the potential energy surface for the colliding pair and have been carried out for a variety of molecules, but of most interest to this study are the results for N_2-N_2 collisions [16], O_2-O_2 collisions [17], and N_2-O_2 collisions [18].

Many experiments have been carried out to quantify the relaxation time of different gas combinations. Most often, a shock tube is used to measure post-shock temperature decay, but little data is available at the relatively low temperatures relevant to the current study. A summary of relaxation rate values is provided in Table 1.1 for selected temperatures near 1000 K. It is obvious that the most abundant air constituent, N_2, is very slow to relax, while O_2 has much shorter relaxation times. The addition of water vapor to the flow is seen to significantly accelerate the relaxation of both N_2 and O_2. This is not predicted by SSH theory for V-T relaxation, indicating that interspecies V-V energy transfer may be playing a role. Because V-T relaxation is very slow at these temperatures, the fastest path for the vibrational energy to relax may be through a V-V exchange and V-T relaxation of the collision partner. H_2O itself relaxes at a very short time on the order of tens of nanoseconds [19]; therefore, if the effective rate of N_2-H_2O V-V exchange is higher than that of N_2 V-T relaxation, the vibrational energy will relax through the V-V-T process. In practice, the relaxation times reported in Table 1.1 are a combination of simple V-T relaxation and the V-V-T process. It is evident from Table 1.1 that the V-V transfer between N_2 and O_2 is not as efficient as the N_2-H_2O and O_2-H_2O processes, due to the relatively similar relaxation times of rows 1 and 3. This inefficient coupling between N_2 and O_2 is in agreement with direct measures of V-V exchange probability [20].

	Experimental relaxation time [sec]	Temperature [K]	Experimental data source(s)
$N_2(v) + N_2 \leftrightarrow N_2(v-1) + N_2$	1.4×10^{-3}, 59.7×10^{-3}	1020, 1000	[21], [22]
$O_2(v) + O_2 \leftrightarrow O_2(v-1) + O_2$	100×10^{-6}, 126×10^{-6}	1000	[23]
$N_2(v) + O_2 \leftrightarrow N_2(v-1) + O_2$	1×10^{-3}	1000	[24]
$N_2(v) + H_2O \leftrightarrow N_2(v-1) + H_2O$	5.6×10^{-6}, 8.5×10^{-6}	1000, 993	[25],[26]
$O_2(v) + H_2O \leftrightarrow O_2(v-1) + H_2O$	9×10^{-6}	1000	[27]

Table 1.1: Summary of experimental data for vibrational relaxation times of several important species at 1 atm.

This V-V-T process is especially important between N_2 and CO_2 due to a highly efficient resonant energy transfer. The asymmetric stretch vibrational mode of CO_2 and N_2 differ in energy by only 18 cm^{-1}. This small energy difference causes a strong coupling between the two modes and leads to a rapid V-V exchange[28],[29]. Figure 1.2 illustrates these energy levels along with the stretching and bending modes of CO_2. Owing to the more closely spaced energy levels available in its stretch-bend manifold, CO_2 is able to transfer the excess vibrational energy more easily to the translational modes than N_2. The *V-V* energy transfer between these intermediate modes and the subsequent *V-T* relaxation from the (01^10) mode occur much more readily than the large energy jump required to relax the $v = 1$ state of N_2 [29]. This increase in relaxation rate is utilized in our experiments to perturb the relaxation process. If the non-equilibrium we measure is genuine, the addition of CO_2 should manifest in our measurements as a reduction in the difference between vibrational and rotational temperature.

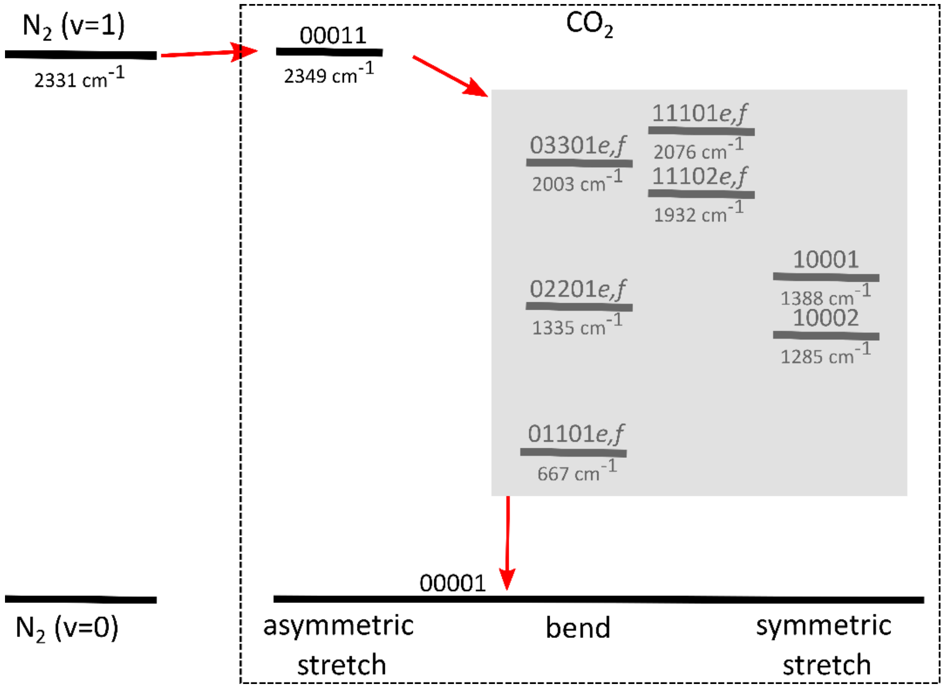

Figure 1.2: Energy level diagram for the resonant vibrational energy transfer between N_2 and CO_2 [30].

1.1.1.2 – Experimental Studies of Vibration Non-equilibrium

Vibrational non-equilibrium has been studied in a vast array of flows. For example, the effect of shock-generated non-equilibrium on hypersonic boundary layer transition to turbulence has been studied extensively in reflected shock tunnels [28]–[30]. In this series of studies, it was found that vibrational relaxation of CO_2 attenuated the acoustic disturbances at frequencies that typically drive the transition process. Non-equilibrium effects in shock tubes has been studied using planar laser-induced fluorescence (PLIF) [31] and coherent anti-Stokes Raman spectroscopy (CARS) [32] for comparison with theoretical relaxation models. Furthermore, the extent of freestream non-equilibrium in shock tunnels has been studied using CARS [33],[34] and PLIF [35],[36]. In all four studies, non-equilibrium was found to be present in the tunnel freestream. Using CARS measurements the magnitude of non-equilibrium in a Mach 2 heated blowdown tunnel was shown to vary strongly with the presence of water vapor, demonstrating the inherent difference between electrically-heated and vitiated supersonic facilities [37].

Non-equilibrium has also been quantified using spontaneous Raman scattering in an arc jet, where vibrational temperature measurements were made axially along the nozzle axis and compared with analytical predictions [38]. The authors proposed a correction factor of 1.5 to the Landau-Teller relaxation time for flows where the vibrational temperature is higher than the translational temperature. This accelerated relaxation is consistent with the behavior found through analytical calculations, where it was determined that vibrational anharmonicity drives the accelerated relaxation [39]–[41].

Plasma-generated non-equilibrium has been studied extensively due to its applications in combustion enhancement and flow control [42]. For example, the deposition of energy into vibrational modes and the subsequent relaxation process has been studied using spontaneous Raman scattering [43] and CARS [44]. The effect of non-equilibrium plasmas on shock strength were studied for both wedge [45] and cone geometries [46]. Control of cylinder bow shock standoff distance [47] and airfoil separation point [48] has been demonstrated using plasma actuators. Furthermore, a study of plasma-driven non-equilibrium in a channel flow showed vibrational excitation of N_2 in room temperature air reduced the peak axial turbulence intensities, diminished large-scale structures, and accelerated turbulent kinetic energy decay rates with a trend toward stronger relaminarization at higher levels of non-equilibrium [49].

The goal of the current work is to understand the interaction between a vibrationally-relaxing gas and turbulence in a shear layer. The only other study on vibrational non-equilibrium in two-stream mixing is reported by Frederickson et al. [50]. In this paper, the influence of CO_2 injection on a non-equilibrium supersonic flow was characterized by observing the expansion wave angle behind a rearward step and making CARS measurements for vibrational temperature and species concentrations in the downstream shear layer. The expansion angle was shown to decrease with injection of CO_2 and transverse traces across the downstream shear layer showed the local concentration of CO_2 to be inversely correlated with vibrational temperature, implying a reduction in non-equilibrium due to the presence of CO_2.

1.1.2 – Laser Scattering Techniques

The interaction between electromagnetic radiation and dielectric media is usually categorized into 3 types: absorption, emission, and scattering. Absorption is defined as the interaction of a photon with an atom or molecule that leaves it in a state of higher energy. Emission is the reverse process, where a photon is generated as the atom or molecule undergoes a transition from an excited state to a lower energy state. In the case of scattering, the atom/molecule is excited to a short-lived virtual state, which leaves the incident radiation as mostly transmitted through the medium without change. The small fraction of incident photons that are not transmitted are considered to be “scattered” by the medium. Both the polarization and intensity of the scattered light will depend on the direction of observation. Of the scattered photons, most will contain the same energy as the incident light, E_I, with a small fraction having energies $E_I \pm E_m$. This energy shift E_m

is determined by the rotational, vibrational, and electronic properties of the scattering medium. This type of interaction is the focus of both of the laser-based techniques which are used in this dissertation.

The radiant intensity generated by an oscillating dipole in a particular direction over a finite collection angle is given in [31] as

$$I = \frac{\pi^2 c\omega^4}{2\epsilon_0} \int_{\varphi-\Delta\varphi}^{\varphi+\Delta\varphi} \int_{\theta-\Delta\theta}^{\theta+\Delta\theta} \vec{P}^2 \sin^3\theta' \, d\theta' d\varphi', \tag{0.7}$$

where θ' is the angle between the incident and scattered photons and φ' is the angle between the polarization of the incident photon and the scattering direction. The induced dipole moment, $\vec{P}$, in the medium is related to the incident electric field, $\vec{E}$, by the polarizability, α, via the relation

$$\vec{P} = \epsilon_0 \langle \psi_f | \alpha | \psi_i \rangle \vec{E}, \tag{0.8}$$

where $\psi_f$and ψ_f are the wave functions of the final and initial energy states of the molecule. In the case of a particular internal molecular mode, this polarizability can be expanded in a truncated Taylor series as a function of the molecular motion as

$$\alpha = \alpha_0 + \left(\frac{\partial\alpha}{\partial Q}\right)_0 Q, \tag{0.9}$$

where Q is the coordinate of motion, which can be characterized by harmonic motion at a natural frequency, ω_v, which is a property of the molecule. If the incident radiation has a frequency of ω_0, the previous equations can be combined to form

$$\begin{aligned} \vec{P} &= \alpha_0 \epsilon_0 \vec{E}_0 \cos\omega_0 t \\ &+ \left(\frac{\partial\alpha}{\partial Q}\right)_0 \epsilon_0 \frac{Q_0 \vec{E}_0}{2} \left[\cos(\omega_0 - \omega_v)\, t + \cos(\omega_0 + \omega_v)\, t\right] \end{aligned} \tag{0.10}$$

The first term represents scattered light at the incident frequency ω_0 , while the second represents scattered light at frequencies shifted from ω_0 by the characteristic frequency ω_v of the molecule.

The light which is scattered without frequency (i.e. photon energy) change is said to be scattered “elastically”. This process is termed Rayleigh scattering. The inelastically scattered light is called spontaneous Raman scattering after C.V. Raman who first observed the process in 1928. Long [31] provides a deep background on the history of this technique and its early applications. Both scattering processes have wide applications as diagnostic techniques. The following sections will provide an overview of these two techniques as they relate to their use in the current study.

1.1.2.1 – Spontaneous Raman Scattering

Raman scattering from rotational and vibrational transitions are termed lines and bands, respectively. The lines or bands with energy less than the incident radiation are termed Stokes shifted and those with increased energy are termed anti-Stokes shifted. For rotational-vibrational spectra as will be used in this study, the vibrational state is denoted by the vibrational quantum number, v, and the rotational state by the nuclear angular momentum quantum number. This quantum number is identified by the letter N, although the letter J is used throughout the literature. This is because most molecules exist in a singlet ground electronic state, and thus they have a net electronic spin of 0. This makes the total angular momentum (J) equal to the nuclear angular momentum (N) and the distinction between these two numbers is ignored. This leads to the unfortunate convention of using J instead of N in the literature to denote rotational state in singlet electronic states. A notable exception to this is O_2, which exists in a triplet ground electronic state. Thus, $N \neq J$ and the typical notation is not applicable. A summary of transition labels for a singlet state molecule is given below in Table 1.2.

	Stokes, $\Delta v = +1, +2, +3, etc.$					**Anti-Stokes, $\Delta v = -1, -2, -3, etc.$**				
Branch	O	P	Q	R	S	O	P	Q	R	S
ΔJ	-2	-1	0	$+1$	$+2$	-2	-1	0	$+1$	$+2$

Table 1.2: Summary of spectroscopic line notation.

The P and R branches are forbidden for spontaneous Raman scattering. For a harmonic oscillator, only $\Delta v = \pm 1$ is allowed, but anharmonicity effects allow for the possibility of Raman scattering involving other transitions. Lines where the vibrational energy changes by more than a single quantum are referred to as overtone bands and are usually very faint relative to the fundamental transitions $(\Delta v = \pm 1)$ due to the nearly linear behavior of the polarizability near the equilibrium position [31].

In practice, the polarizability, α, is a tensor and is usually represented by a "polarizability ellipsoid", which is a three-dimensional representation of the polarizability matrix. This ellipsoid can be defined by a maximum of 3 components: one along the bond axis and two at right angles to the bond direction. In the case of diatomic molecules, this is reduced to just two components due to the rotational symmetry about the bond axis. These are defined as $\alpha_{||}$ for the polarizability component along the bond axis, and $\alpha_{\perp}$ for the polarizability component orthogonal to it.

Owing to the symmetry of the polarizability tensor $(\alpha_{ij} = \alpha_{ji})$, it may be represented by a pair of invariant quantities: the mean polarizability, a, and the anisotropy, γ. These can be written in terms of the polarizability components as

$$a \equiv \frac{1}{3}\left(\alpha_{xx} + \alpha_{yy} + \alpha_{zz}\right) \tag{0.11}$$

$$\gamma^2 \equiv \frac{1}{2}\Big[\left(\alpha_{xx} - \alpha_{yy}\right)^2 + \left(\alpha_{yy} - \alpha_{zz}\right)^2 + (\alpha_{zz} - \alpha_{xx})^2 \\ + 6\left(\alpha_{xy}{}^2 + \alpha_{yz}{}^2 + \alpha_{zx}{}^2\right)\Big] \tag{0.12}$$

Each of these invariants can be expanded in a Taylor series with respect to a normal mode of molecular motion about an equilibrium value in the same fashion that the polarizability was expanded previously. This leads to equilibrium invariant values, a_0 and γ_0, and invariant derivatives, a' and γ'. The equilibrium quantities are associated with Rayleigh scattering and rotational Raman scattering and the derivatives are used in vibrational and vibrational-rotational Raman scattering. In order to determine how these terms vary with vibrational motion (and thus the Raman activity of the vibration), one can look at quantum mechanical calculations for H_2 which show that both $\left(\frac{\partial \alpha_{||}}{\partial Q}\right)_0$ and $\left(\frac{\partial \alpha_{\perp}}{\partial Q}\right)_0$ are positive [32]. This result can be generalized to all homonuclear diatomics [31].

In order to account for molecules that are freely translating and rotating, the polarizabilities must be averaged over all orientations. As shown in Eqn. (0.7), the scattered intensity depends on the square of the polarizability, therefore the space-averaged polarizability components are calculated as averages of the square of the polarizabilities. The expressions for the space-averaged quantities are given for each transition in Table 1.3. The $b_{J',J''}$ terms are the Placzek-Teller coefficients, which are purely a function of rotational level and are written in algebraic form in [31].

Transition	Lower state, v'',J''	Upper state, v',J'	$\langle(\alpha'_{xx})^2{}_{v',J':v'',J''}\rangle$	$\langle(\alpha'_{xy})^2{}_{v',J':v'',J''}\rangle$
O branch	v,J	$v+1,J-2$	$\frac{4}{45}b_{J-2,J}{\gamma'}^2$	$\frac{1}{15}b_{J-2,J}{\gamma'}^2$
Q branch	v,J	$v+1,J$	${a'}^2+\frac{4}{45}b_{J,J}{\gamma'}^2$	$\frac{1}{15}b_{J,J}{\gamma'}^2$
S branch	v,J	$v+1,J+2$	$\frac{4}{45}b_{J+2,J}{\gamma'}^2$	$\frac{1}{15}b_{J+2,J}{\gamma'}^2$

Table 1.3: Space-averaged polarizability components for diatomic molecules [31].

For a typical 90° scattering experiment, let us define a set of space-fixed axes where $\hat{e}_z$ is the direction of the incident laser, the laser beam is linearly polarized such that its electric field aligns with $\hat{e}_y$, and the collection optics are aligned along $\hat{e}_x$. The components of scattered signal polarized parallel and perpendicular to the scattering (*x-z*) plane will be determined by the induced dipole moment magnitudes which are given by [33] as

$$\overline{\left|\vec{P}_{||}\right|^2} = \left[\overline{(\alpha'_{xy})^2}\cos^2\varphi\cos^2\theta + \overline{(\alpha'_{yy})^2}\sin^2\varphi\cos^2\theta + \overline{(\alpha'_{zy})^2}\sin^2\theta\right]{E_y}^2; \tag{0.13}$$

$$\overline{\left|\vec{P}_{\perp}\right|^2} = \left[\overline{(\alpha'_{xy})^2}\sin^2\varphi + \overline{(\alpha'_{yy})^2}\cos^2\varphi\right]{E_y}^2. \tag{0.14}$$

Assuming that the vibrational and rotational state populations can be represented by Boltzmann distributions at characteristic temperatures T_V and T_R, the previous expressions can be combined into a general relation for the spontaneous Raman scattering signal for a particular Stokes line:

$$I(v,J,\Delta v,\Delta J) = \frac{G}{T_R}[\tilde{\nu}_0-\tilde{\nu}_k(\Delta v,\Delta J)]^4 g_s(J)\frac{(2J+1)e^{-\frac{hcE_V(v)}{kT_V}}e^{-\frac{hcE_R(v,J)}{kT_R}}}{Q(T_V,T_R)}\Phi(\Delta v,\Delta J), \tag{0.15}$$

where G is a scaling constant which is set by the incident laser energy, Q is the internal partition function, g_s is the weight accounting for the nuclear spin statistics, and Φ includes the square of the space-averaged polarizability tensor and the angular dependence [31],[34]. In practice, transition cross-sections and depolarization ratios are determined experimentally and the transition matrix elements are extracted from the data [35]. For N_2 and O_2, expressions for the polarizability tensor components given by Buldakov et al. [36].

The spectral location of each line can be determined from the difference in energies of the initial and final states of the molecule. For the diatomic species studied here, the anharmonic oscillator and nonrigid rotor model has an internal energy given by

$$\begin{aligned} E(v,J) = {} & \omega_e\left(v+{}^{1}\!/_{2}\right) - \omega_e x_e\left(v+{}^{1}\!/_{2}\right)^2 + \omega_e y_e\left(v+{}^{1}\!/_{2}\right)^3 \\ & + \left[B_e - \alpha_e\left(v+{}^{1}\!/_{2}\right) + \gamma_e\left(v+{}^{1}\!/_{2}\right)^2\right] J(J+1) \\ & - D_e J^2(J+1)^2 \end{aligned} \tag{0.16}$$

where the molecular constants used are summarized below in Table 1.4.

	ω_e	$\omega_e x_e$	$\omega_e y_e$	B_e	α_e	γ_e	D_e
N_2	2358.57	14.324	-2.26×10^{-3}	1.99824	0.07318	-3.3×10^{-3}	-5.71×10^{-6}
O_2	1580.39	12.112	0.0754	1.4451	0.01523	-8.25×10^{-3}	-4.835×10^{-6}

Table 1.4: Molecular constants for rotation and vibration in cm^{-1} [37],[38]

The triplet ground state of molecular oxygen has an electronic spin which leads to each transition splitting into 3 lines having total angular momentum $J = \{N-1, N, N+1\}$. These triplets have been observed as a central $J = N$ line with weaker side branches separated by approximately 2 cm^{-1} which were only detectable for $N < 11$ [39]. Other studies of O_2 Raman scattering have neglected this triplet contribution under specific conditions. At pressures greater than 500 Torr, the error induced by treating the O_2 ground state as a singlet state was found to show no appreciable difference in the analysis of Q-branch collisional broadening, [40]. Similarly, Millot *et al.* computed the maximum pressure limit at which triplet splitting needed to be modeled for their analysis of collisional broadening in O_2-N_2 mixtures to be around 300 Torr [41]. Thus, for simplicity O_2 is treated in this study in the same fashion as N_2: as a molecule with a singlet ground electronic state. The spectral separation is small relative to instrument broadening function (discussed in detail in Appendix B). Therefore, whatever small contribution the $J = N - 1$ and $J = N + 1$ lines may have is most likely not resolved from the stronger $J = N$ line.

There are many ways to determine temperature from Raman scattering data depending on the spectral coverage of the collection system. Extracting the intensity of transition peaks allows for the determination of gas temperature through the comparison of the vibrational fundamental and hot bands [42],[43] or by fitting a Boltzmann plot of the many rotational lines [42],[44]. The ratio of the Stokes to anti-Stokes Q-branch intensities can also be used to determine temperature [45],[46]. The “envelope” of the pure rotational bands has also been used with low resolution spectra to determine temperature in single-shot measurements [47]. Another method, which is used in conjunction with species detection, is to spectrally bin regions corresponding to vibrational bands of particular species. A library of expected signal in these Raman channels is predetermined for all possible conditions and experimental data are correlated with its nearest match [48].

There have been several recent studies that utilized a detailed fitting procedure on high resolution spectra. Sepman et al. performed detailed fits to Stokes vibrational spectra of N_2, O_2, CO_2, CO, and H_2O [49]. The spectra were collected from long integrations of 4.8-24 kJ of incident laser energy to achieve adequate signal. Over the range of 400 K to 2150 K, they deemed the temperatures measured from all species to be accurate to within

±100 K. Utsav and Varghese measured flame temperatures from detailed fits of Stokes vibration-rotational N_2 scattering [34]. A pair of concave mirrors was used to create a multi-pass cell that repeatedly passed the incident laser through the probe volume to increase laser energy by about 20 times. They were able to successfully measure flame temperatures to within ±9 K from 600 J of incident energy. The current work expands upon their detailed fitting procedure by fitting for rotational and vibrational temperatures independently from Stokes vibrational spectra of N_2 and O_2.

1.1.2.2 – Rayleigh Scattering

Predicting the elastically scattered signal is considerably simpler than in the Raman scattering case. By space averaging the polarizability components to account for all possible molecular orientations, one obtains an effective polarizability term

$$\alpha_{eff}{}^2 = a^2\left(\frac{2+\rho_n}{6-7\rho_n}\right), \tag{0.17}$$

$$\rho_n \equiv \frac{6\gamma^2}{45a^2+7\gamma^2}, \tag{0.18}$$

where a and γ are the mean polarizability and anisotropy defined previously and ρ_n is a "depolarization factor" [50]. This depolarization factor can be substituted into Eqn. (0.7) to obtain the differential scattering intensity

$$\frac{dI}{d\Omega} = \frac{\pi^2}{\epsilon_0{}^2}\tilde{\nu}_0{}^4\alpha_{eff}{}^2\sin^2\theta\, I. \tag{0.19}$$

Eqn. (1.19) can also be written in the more common form in terms of index of refraction as

$$\frac{dI}{d\Omega} = \frac{4\pi^2(n-1)^2}{N_0{}^2}\tilde{\nu}_0{}^4\sin^2\theta\, I, \tag{0.20}$$

where n is the index of refraction and N_0 is number density at STP [51]. The total scattered energy from a single laser pulse of energy E_i can be determined by integrating Eqn. 1.19 over the extent of the collection solid angle, Ω, and multiplying by the total number of molecules irradiated. For relatively small collection solid angle where the sine term can be considered constant, the result becomes

$$E_{scatt} = \hat{n}\left(\frac{d\sigma}{d\Omega}\right)\Omega\ell E_i, \tag{0.21}$$

where $\hat{n}$ is the number density of the scattering medium, ℓ is the sampling extent along the laser beam propagation direction, and $\left(\frac{d\sigma}{d\Omega}\right)$ is the differential cross section. This cross section is defined simply as

$$\left(\frac{d\sigma}{d\Omega}\right) = \frac{4\pi^2(n-1)^2}{{N_0}^2}{\tilde{\nu}_0}^4, \tag{0.22}$$

and can be computed directly for pure gases or as a mole fraction weighted sum of the individual species within a mixture.

Rayleigh scattering can be used to quantify mixing, measure number density, or measure temperature. Mixing is the simplest case. Since the last three terms in Eqn. 0.21 are constant for a given imaging/excitation system, only the number density and scattering cross-section of the medium affects the collected signal. When two streams of different cross-sections are mixed, the intensity of the scattered signal will correspond to the proportion of each stream present in the scattering volume. Making these measurements quantitative is difficult as number density variations will also affect the collected signal. For number density or temperature measurements, information about the scattering cross-section must be known. The simplest solution is to probe a flow that has constant scattering cross-section since the Rayleigh scattering signal is directly proportional to local number density, *n* in this case. If the scattering medium is also considered isobaric, the Rayleigh signal is inversely proportional to the local temperature. The signal collected in each pixel can then be related to the local temperature through the relation:

$$T = \frac{T_{ref}I_{ref}}{I}, \tag{0.23}$$

where the reference signal (I_{ref}) is taken for a region of the flow at known temperature (T_{ref}). Before this calculation can be made, careful correction must be done to the aforementioned signals, I and I_{ref}, to correct for background scattering, laser intensity variations, and detector response [52].

The differential scattering cross-sections for Rayleigh scattering are of order a thousand times greater than those for vibrational Raman scattering. The higher signals generated by Rayleigh scattering allow for measurements to be made from a single laser shot of relatively low energy (hundreds of millijoules for atmospheric pressure conditions). This freezes the flow motion and provides snapshots of flow conditions. For a rapid enough laser repetition rate, this can be extended to make time-resolved flow measurements. In addition, modern high-energy lasers provide adequate signal for two-dimensional measurements to be made by spreading the laser out into a sheet.

The earliest use of Rayleigh scattering as a thermometric measurement in flames was by Dibble and Hollenbach [53], who used a carefully chosen fuel mixture that had the property that the Rayleigh scattering cross-section was approximately constant for all mixture fractions. They used a CW laser to obtain time series point measurements of temperature in turbulent jet flames. Their fuel mixture consisted of 62% H_2 and 38% CH_4 (by mole). If the fuel is not designed such that the Rayleigh scattering cross section matches the oxidizer stream, simultaneous Raman scattering measurements can be used to determine gas composition and compute a Rayleigh cross-section [48],[54]–[57]. This technique is limited to line measurements since a spectrograph or polychromator is needed to collect the spectrally dispersed Raman signal. The constant cross-section technique and Raman scattering technique were compared in a turbulent flame study at DLR [58]. In this experiment, the fuel was chosen to be a mixture of 33.2% H_2, 22.1% CH_4, and 44.7% N_2 (by mole) in order to match the Rayleigh cross-section of air. Using the combined Raman/Rayleigh technique, it was shown that the error in assuming a constant cross-section for this fuel mixture introduces approximately 5% error.

Rayleigh thermometry was extended to two-dimensional measurements in flames using a multipass cell consisting of two cylindrical reflectors to form a sheet from the repeated retro-reflection of the laser beam at a slight angular offset [59]. A similar multipass technique was used in combination with large laser energy to image Rayleigh and specific Raman transition signals to compute mixture fraction fields [60]. This type of multi-scalar technique has been applied to look at many turbulent flames using Rayleigh/CO-LIF [61],[62] and Rayleigh/Raman/OH-LIF [63] as well. Instead of making multiple simultaneous measurements to obtain mixture fraction in order to compute scalar dissipation rate, the thermal dissipation rate is commonly used as a surrogate. Thermal dissipation rate has been studied extensively using 2D Rayleigh scattering measurements of turbulent flames using the Dibble fuel mixture [64] and the DLR fuel mixture [65]. Using Taylor's hypothesis to approximate spatial derivatives from time derivatives, high repetition rate time-series point measurements have also been used to estimate the thermal dissipation rate [66],[67]. Recently, Rayleigh thermometry measurements that are both high resolution and high repetition rate have been made with the use of a pulse-burst laser [68].

1.2 – CONTEXT OF THE PRESENT WORK

Although vibrational non-equilibrium in shock-heated flows and plasma discharges has been extensively studied, turbulent mixing-induced thermal non-equilibrium has received relatively little attention in the literature. In the current work, a new supersonic jet-in-coflow facility is used to study turbulence-induced vibrational non-equilibrium of N_2 and O_2 gas in the axisymmetric shear layer region of the jet. This study provides the first experimental observation of mixing producing vibrational non-equilibrium in a high-speed jet shear layer. Because this flow configuration is of the same general configuration as fuel injection in a scramjet combustor, the production of non-equilibrium in this flow implies that the same is true for the more extreme conditions in a scramjet. This could have a significant impact on engine efficiency and flame-holding. This work may also provide a useful data set for validation for CFD models which include vibrational non-equilibrium effects.

The primary objective of this work is to expand the knowledge base related to mixing-induced vibrational non-equilibrium. To do so, laser measurement techniques (Raman and Rayleigh scattering) were applied to make independent measurements of the vibrational, rotational, and translational temperatures of the gas. The use of Raman and Rayleigh scattering as thermometric measurement techniques is not unique to this study. The novelty of the current work lies in the application of these laser techniques to quantify the mixing-induced non-equilibrium in this flow. The Raman scattering technique was first applied as a time-averaged measurement in order to obtain high signal-to-noise spectra for detailed fitting of the O-, Q-, and S-branches. These high fidelity spectra allowed for accurate vibrational and rotational temperatures to be obtained independently from spectral fitting. With this technique, the production of thermal non-equilibrium within a turbulent mixing layer and the subsequent transport within the flow can be quantified.

Another objective of this work was to expand the current capability of the spontaneous Raman scattering technique. The fitting code was updated to add the capability to make O_2 temperature measurements in addition to N_2. This was invaluable as it provided the opportunity to study the interspecies coupling of vibrational energy.

There is relatively little information on this type of energy transfer in the temperature ranges explored in this work available in the literature.

Time-averaged Raman scattering measurements cannot be made in a region of large temperature fluctuations, owing to the non-linear weighting of the scattered intensity as a function of temperature. A method for measuring vibrational and rotational temperatures near the turbulent flame base was needed. A new single-shot measurement apparatus was conceived in order to expand the Raman measurement technique to measurements in this region. The use of single-shot spontaneous Raman spectra to obtain simultaneous measurements of vibrational and rotational temperatures is unique to this work. This new method also provided measurements which no longer required a secondary measurement for validation, as was needed with the time-averaged measurements, and, thus, simplified the process of interpreting results.

1.3 – ORGANIZATION OF THIS DISSERTATION

This document provides a somewhat chronological description of the complete body of work — from construction of a new flow facility, to the initial application of optical diagnostic measurements, and then improvements made upon those measurements. Chapter 2 begins by detailing the design and assembly of the jet facility which was constructed for these experiments. The next two chapters describe the implementation of Raman and Rayleigh scattering measurement techniques for the study of mixing-induced vibrational non-equilibrium. Time-average Raman measurements were implemented first and thus are presented in Chapter 3. These measurements provided a method for quantifying the vibrational non-equilibrium, but did require supplementary Rayleigh scattering measurements to quantify the bias induced in the Raman measurements by time-averaging over temperature fluctuations. A single-shot

Raman measurement technique was devised and implemented which circumvents several drawbacks of the time-averaged measurements. A description of this system and the conclusions gleaned from the single-shot measurements is given in Chapter 4. This chapter concludes with suggestions for future uses of this technique. Finally, supplementary information on the specifics of calibrating the Raman measurements, the Raman fitting code, and the design of the single-shot Raman measurement system is provided in the appendices that follow the main text, as well as a collection of photographs of the construction and operation of the experiments.

Chapter 2: Jet in Coflow Facility

This chapter presents the design process and evolution of the flow facility used for the experiments described in later chapters. The turbulent mixing process generated by this facility serves as a simplified representation for the more complex flow environment in a practical scramjet combustor. In this flow, turbulence-induced vibrational non-equilibrium can be produced in a jet shear layer without the use of vitiation. This method for generating non-equilibrium avoids the addition of vibrationally-participating species that can complicate the vibrational relaxation process. The systems that control the operation of the facility and ensure its safe operation are also described.

2.1 – FACILITY DESIGN AND CONTROL

The facility used for these experiments was designed to provide a small axisymmetric jet in a high temperature air coflow. The facility was mostly constructed of Type 304 and 316 stainless steel to prevent rust and allow for high temperature operation. The jet and coflow exit to the ambient room air. The coflow air supply was driven by a 250 W blower (Leister SILENCE) through a HEPA filter to remove the dust particles larger than 0.1 μm in order to facilitate the flow diagnostics. The resultant coflow exit velocity was less than 1 m/s. The jet gas was provided by compressed gas cylinders stored in standard K-size bottles. The center jet flow issues through a CNC-machined stainless nozzle, which can be replaced to provide different flow velocities. An overall schematic of the jet in coflow facility is shown below in Fig. 2.1. Translation of the entire assembly was provided by a NEMA 23 stepper motor and stepper motor driver (Intelligent Motion Systems MicroLYNX) driving a screw-driven linear slide (Lintech 172618-CP0) for simple and precise (75 μm accuracy) scanning of the flow. Two custom-built “outrigger” shaft and bearing assemblies helped support and balance the weight of the facility on the translation stage. The complete translation system is shown in detail in Fig. 2.2.

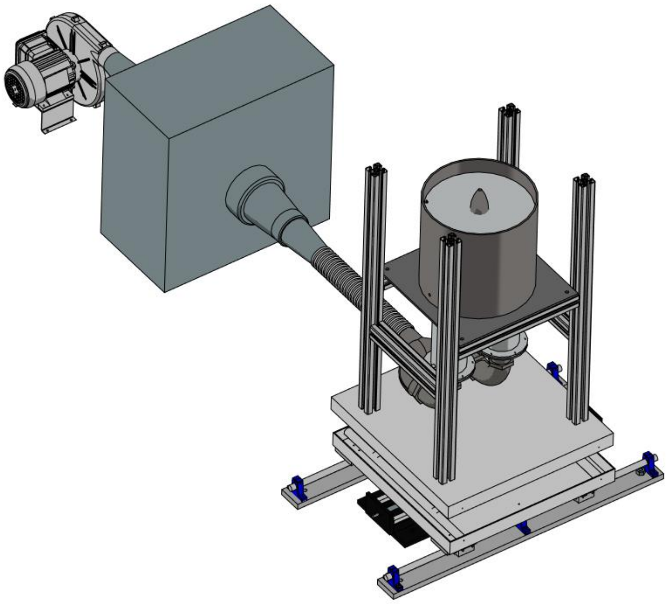

Figure 2.1: Jet in coflow facility with coflow blower and translation system.

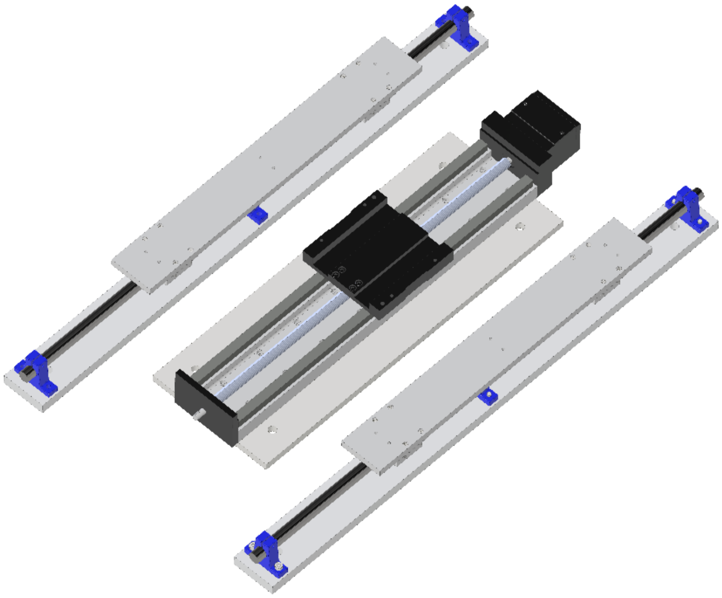

Figure 2.2: Translation system for jet facility with outer shaft slides.

This facility differs from those used in some other jet-in-coflow studies [69],[70] in that this case the coflow is electrically heated. The advantage of electrical heating is that it does not alter the chemical composition of the gases, while a vitiated coflow would include combustion products that could significantly affect the vibrational relaxation process. The coflow air was heated by a pair of 15 kW electric-resistance flow-through heaters (Leister LE 10000 DFHT). The maximum temperature of the heating element is rated at 1200 K. Two type K thermocouples were inserted radially through the pipe wall 75 mm above the heating elements to measure the temperature of the coflow in the settling chamber and allowed for feedback control of the heater power. The jet was similarly heated by a pair of 6 kW electric heaters (Sylvania F038825). The coflow section was also fitted with a series of perforated plates, honeycomb and screens to provide flow conditioning. The perforated plates (40% open area, 0.25” hole diameter) serve to provide a blockage at the heater outlets to evenly distribute the hot gas in the chamber. The 1" thick welded honeycomb (Benecor, 3/16" cell size) breaks up the large-scale eddies induced by the holes in the perforated plate. The final pair of screens (73% open area) reduce the scale of the turbulence further to

Figure 2.3 shows two facility configurations used for the experiments presented in later chapters. Figure 2.3a shows the flow facility configuration for the air mixing studies, which consisted of a Mach 1.5 round jet, with an 8 mm exit diameter, and centered in a 0.3 m diameter circular coflow chamber. For the reacting flow studies, a converging jet nozzle with an identical 8 mm exit diameter was installed. The contours of the two jet nozzle designs are illustrated below in Fig. 2.4. Additionally, for the reacting flow studies, a conical coflow shroud served as a nozzle, which reduced the coflow exit diameter to 100 mm. The reacting-flow configuration is illustrated below in Fig. 2.3b. The addition of the coflow shroud allowed for the placement of detector optics much closer to the measurement region without risk of overheating. Additionally, accelerating the coflow velocity reduces the computational cost of simulating this flow by reducing the disparity in between coflow and jet velocity. This increase in coflow velocity did not appreciably change the overall mixing layer behavior due to the coflow velocity being orders of magnitude slower than the jet.

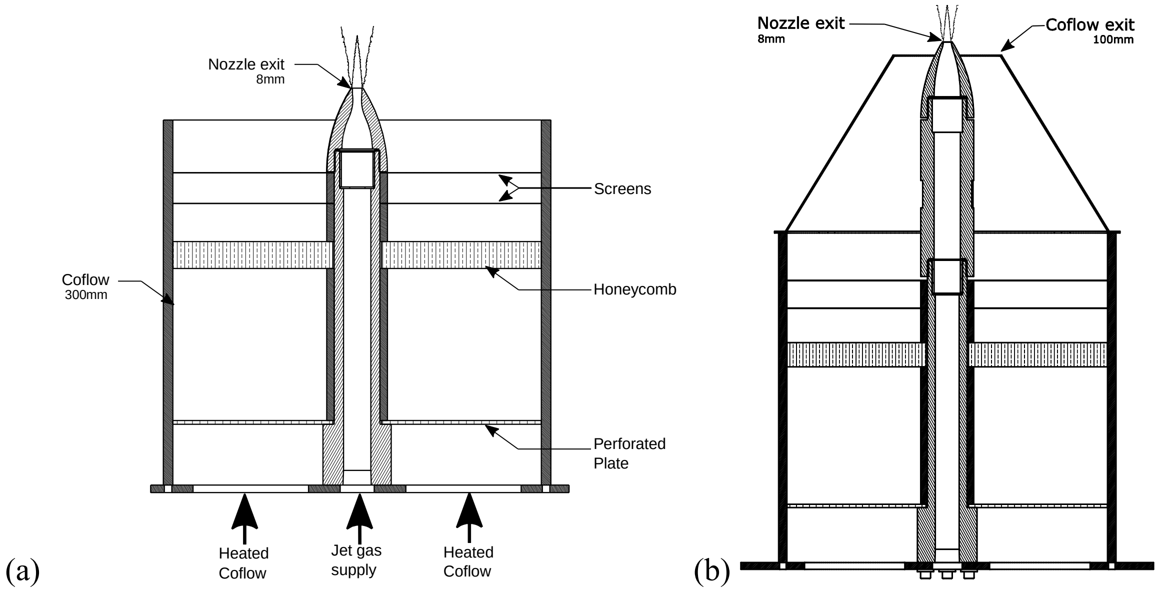

Figure 2.3: Cross-section view of the jet-in-coflow facility. (a) air-air mixing configuration with Mach 1.5 nozzle installed, and (b) reacting-flow configuration with converging nozzle and coflow shroud.

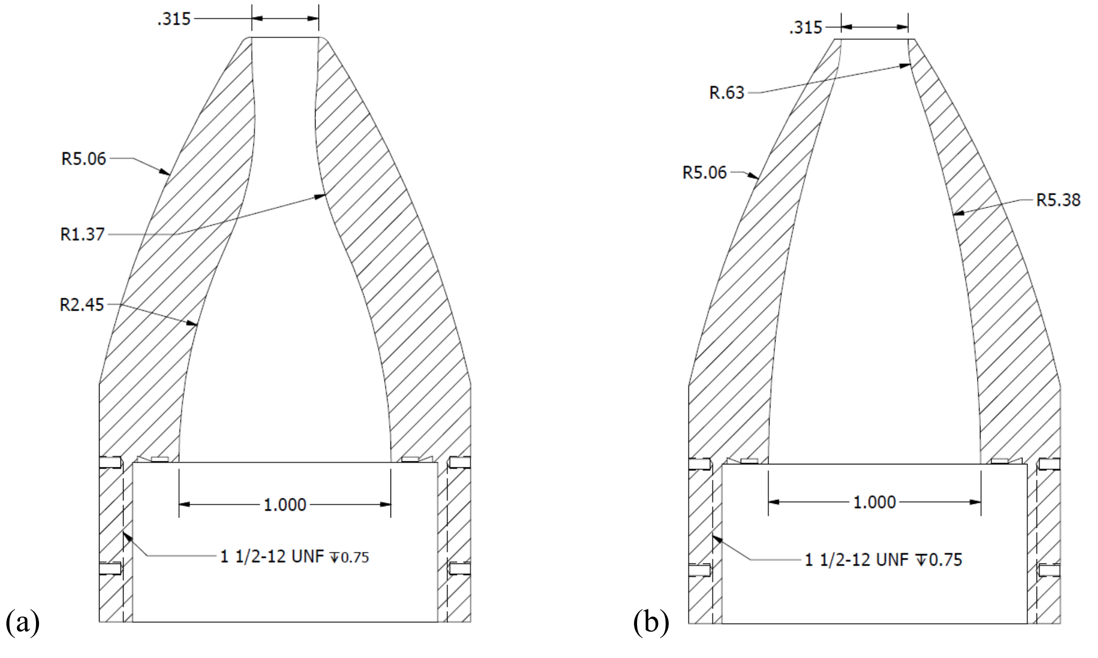

Figure 2.4: Nozzle section views for (a) Mach 1.5 converging-diverging contour and (b) subsonic converging contour.

Preheating the coflow air caused heating of the central jet components and thus ensuring a proper seal between components of the jet flow path was challenging. In the piping between the jet heaters and the portion of the facility shown in Fig. 2.3, all pipe threads were dressed with a high temperature liquid sealant (Copaltite) because Teflon tape was found to melt and burn due to the high temperatures involved. In the final portions of the flow path, a custom gasket design made of annealed oxygen-free copper was used to achieve a pressure seal which is insensitive to temperature and provides a flush inner surface to prevent disturbances to the boundary layer. Similarly to the coflow, flow conditioning elements were installed in the jet flow path. They consisted of a perforated plate (51% open area, 3/16" hole diameters), which broke up thermal boundary layers by inducing large-scale eddies, and a wire mesh screen (73% open area, 0.057" openings), which reduced the broke down the eddies to reduce the turbulent scale and produce a spatially-uniform outflow conditions. A section view of the central jet components is presented in Fig. 2.5 below.

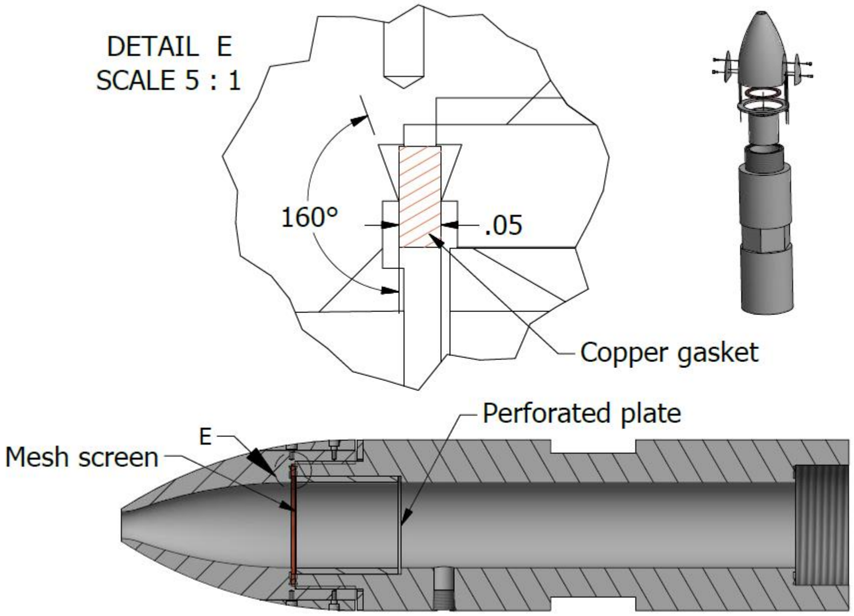

Figure 2.5: Section view of facility center body illustrating the jet flow conditioning location and copper gasket knife edge geometry.

To evacuate the hot gas and combustion products generated by the facility, an overhead exhaust system was designed and installed in the laboratory. The exhaust system was designed around the requirements that:

1. Sufficient room air be ingested with the facility gases such that the bulk gas temperature is reduced below the maximum temperature rating of the fan bearings.
2. Velocity at the hood inlet is kept to a minimum to avoid altering the behavior of the jet flame.

A conservative calculation of the maximum heat load generated by the facility was made based on complete combustion of the fuel contained in the jet. Figure 2.6 shows calculated exhaust gas bulk temperatures as a function of exhaust system flow rate for various levels of H_2 content in a Mach 1.5 jet. Ultimately, a system flow rate of 120

m^3/min was selected. The high-temperature blower model (Peerless BI-150) that was selected is rated for bulk gas temperatures up to 260 C. This allows for the jet to safely operate with H_2 concentrations up to 80% by mole for the supersonic case and 100% for the subsonic nozzle. The chosen blower design was sized to provide the required flow rate of air through the 500 Pa of pressure drop in the 46 cm diameter ducting system at standard conditions. The blower was constructed for high-temperature service. A belt drive reduces the fan speed to 2475 RPM from the 3500 RPM speed of the 5 HP drive motor. A variable frequency drive was also installed to allow for the modulation of fan speed for use with future experiments with varying flow rate requirements. The 1.37×1.68 m rectangular hood was sized to cover the entire range of the facility translation stage and keep the face velocity well below 1 m/s. An overall schematic of the laboratory is shown below in Fig. 2.7. Additional photographs of the actual exhaust system are presented in Appendix A.

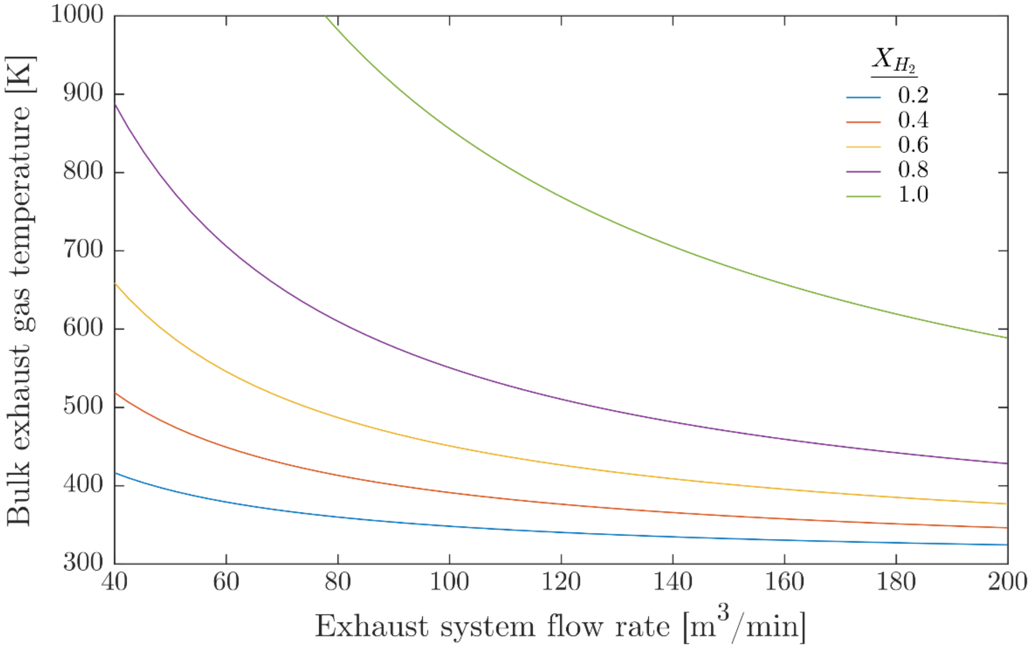

Figure 2.6: Exhaust system bulk gas temperature for different exhaust fan flow rates and jet H_2 concentrations in the Mach 1.5 nozzle.

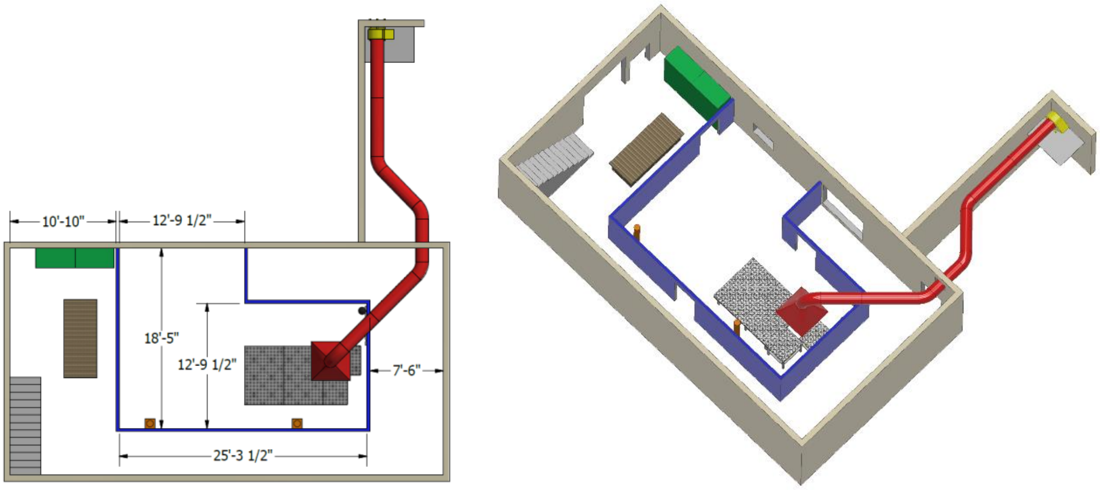

Figure 2.7: Isometric and side view of the building modification made to facilitate this experiment from top and isometric views. New ducting for this experiment is shown in red and new laser barrier walls are colored blue.

With the use of hydrogen as a fuel for this facility and the large flow capabilities of the supply system, care was taken to ensure that the exhaust system was working effectively. The concentration of combustible gases in the lab was monitored with a set of three gas sensors (Detcon FP424C). The signals from these sensors were tied into a central controller (Detcon 610A-FB), which provided a readout of the gas sensor readings and several relay outputs which switch state in the event that high combustible gas concentrations are detected. The system was set up to close a normally-closed valve in the combustible gas supply outside in the event that the sensors detected concentrations greater than 5% of the lower explosive limit.

To control the operation of the facility, a custom LabVIEW program was developed. This program provided live monitoring of the facility conditions during operation and also stored relevant data for later use. In addition to the thermocouples installed in the jet and coflow supply lines for feedback control of heater power, thermocouples were also used to monitor the coflow temperature at the exit plane and the jet temperature in the plenum upstream of the nozzle. These values, as well as the power levels being supplied to the heaters were read into the PC using a National Instruments multifunction data acquisition (DAQ) device (PCIe-6321) and recorded to a text file for each run of the facility. The stagnation pressure in the jet-nozzle plenum was also measured using a pressure transducer (Cooper Instruments DPG1000DR) which was read by an analog voltage channel on a second National Instruments DAQ board (PCI-6110). This board was used in addition to the previously-mentioned board to isolate the acquisition of low voltage (millivolts) signals (thermocouples, Hall effect current sensors) from the high voltages (0-10 V) involved with the pressure transducer and flow controllers.

In addition to recording information about the run conditions, the LabVIEW program set the flow rate of jet gases and measurement location through control of the translation stage. The desired flow rate of each constituent gas sent by analog voltage from the PCI-6110 board to a differential pressure mass flow controller (Omega FMA-2600A) where the flow rate was maintained by internal PID logic. The two modes of operation for this program are either in a feedback-control mode that maintains a constant jet-nozzle plenum pressure or a constant flow rate mode that sends a user-specified flow rate of each gas through the jet. Facility movement was controlled through RS-232 communication between the PC and stepper motor controller. In some cases, the program monitored the state of the detector and automatically scanned through a preset list of measurement locations after each data acquisition. For increased safety for those running the experiment, the entire facility is controlled remotely from a 3 personal computers located in an adjacent room and monitored using IP surveillance cameras (model). The rooms were separated by a solid masonry wall between the operator and the experiment and also provides the ability to simultaneously monitor the state of the experiment, dictate facility conditions, and control the various cameras used for data acquisition. The digital output channels of the PCI-6110 DAQ board commanded a set of relays which allowed for rapid shutdown of the facility in an emergency. These relays were wired to, on command, cut the power supply to the jet and coflow heaters and close solenoid valves at both the hydrogen fuel supply outside and just upstream of the facility. The remote control station is pictured in Appendix A.

2.2 – OPERATING CONDITIONS

The nozzle exit diameter of 8 mm was selected as a balance between flow rate and spatial resolution requirement. A smaller jet requires less flow to reach the same exit conditions and therefore allows for a longer experimental run time. However, the jet should be large enough that the flow is well-resolved by the measurement techniques used. Figure 2.8 below shows calculations made to size the supersonic nozzle used in the air mixing experiments. The air flow rate required for various nozzle exit Mach numbers and the resulting facility run time from a single standard gas cylinder is plotted. The jet was unheated in the air mixing studies to maximize the temperature difference between coflow and jet and thus drive the largest possible non-equilibrium. Including time to allow jet flow to ramp-up to the set point and for temperatures to stabilize, a jet exit diameter greater than 8 mm was determined to consume gas too rapidly. The converging nozzle used for the fuel jet cases was sized to match the exit diameter of the supersonic nozzle.

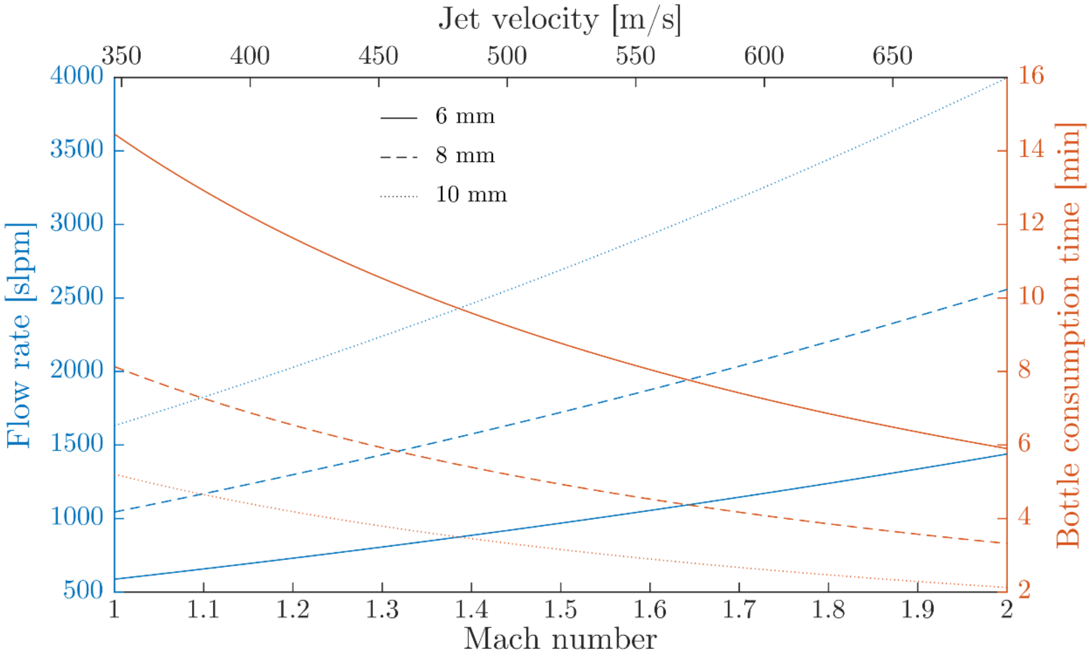

Figure 2.8: Jet flow rate for unheated air as a function of nozzle design Mach numbers for different exit diameters.

Two main fuel mixtures were used in the reacting flow studies presented in this dissertation: a H_2/N_2 mixture and a H_2/CH_4 mixture. The fuel jet conditions were selected such that the facility provided an autoigniting flame which reached a repeatable lift-off height. The lift-off height also was required to be short enough that the region downstream of the flame was within the scanning range of the laser measurements. This required the use of the jet heaters to raise the stagnation temperature of the jet. Owing to the much higher speed of sound of H_2, the jet Mach number in either of these cases did not need to be supersonic. As will be discussed in depth in Ch. 3, the H_2/CH_4 mixture proportion is fixed to match the Rayleigh cross-section to air, and thus the operating parameters were constrained by the flame lift-off height requirements. In the case of the H_2/N_2 fuel, however, the mixture proportions could be varied. The fuel composition was used as an additional parameter when selecting run conditions that allowed for the jet velocity to be specified while meeting the stable flame requirements. Figure 2.9 shows the required flow rates, exit Mach number, and heat addition to reach a jet velocity which matches that of the Mach 1.5 air mixing conditions. With the use of this subsonic nozzle, it was observed that the jet did not self-ignite consistently when the total temperature was below 350 K. Additionally, it was found that H_2 molar concentrations much below 60% did not readily ignite. This reduced the matrix of possible fuel jet conditions to the area outlined in red.

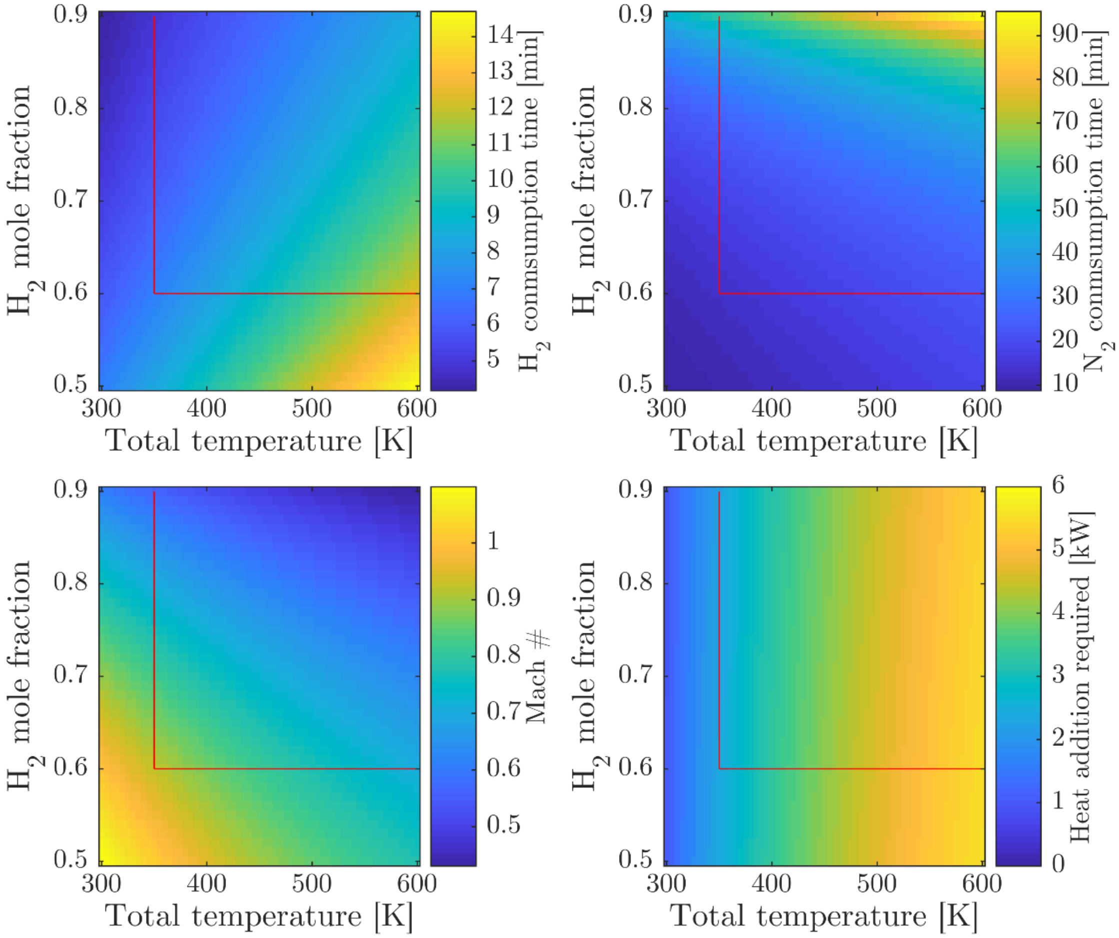

Figure 2.9: Facility requirements for an array of H_2/N_2 flow conditions which match air jet velocity: H_2 flow (top left), N_2 flow (top right), Mach number (bottom left), and heat addition (bottom right).

In order to down-select a single condition for experimental study, an additional parameter was investigated: the N_2 concentration in the jet. Owing to the species-specific nature of the Raman scattering phenomenon, measurements can only be made where the molecule being probed is present in sufficient quantity. Therefore, it is advantageous to select jet conditions which provide a density of N_2 in the jet which approximately matches the coflow. Figure 2.10 shows the ratio of N_2 number density in the jet to that in the coflow at 1000 K for the range of jet mixtures and temperatures presented in Fig. 2.9.

Ultimately, a mixture of 68% H_2 and 32% N_2 at a stagnation temperature of 550 K was chosen as the fuel jet condition which best balanced all of the requirements.

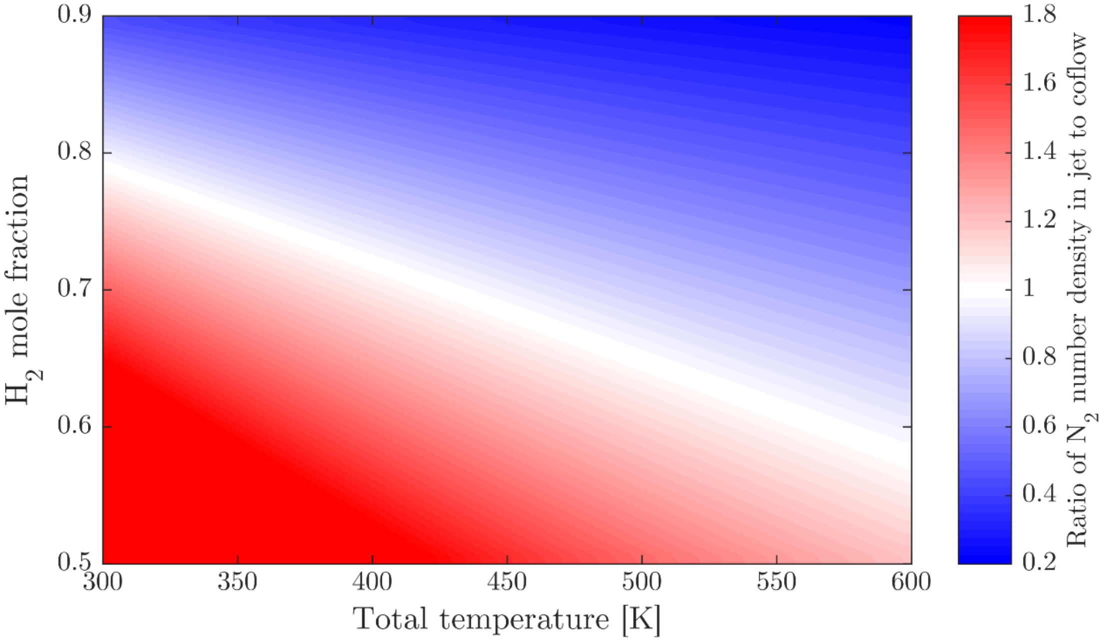

Figure 2.10: Ratio of N_2 number density in the jet to coflow for various H_2/N_2 fuel jet conditions.

The maximum coflow temperature in this study was limited to 1000 K, which was the highest temperature at which the facility could be run for long periods of time without the sealants used catching fire. This temperature ceiling limits the magnitude of vibrational non-equilibrium which can be generated by this facility. Figure 2.11 shows the fractional population in excited vibrational states over the range of coflow temperatures up to the maximum rated temperature of the heaters. At 1000 K, only 3.5% of N_2 and 10.5% of O_2 molecules are in $v > 0$ states. As mentioned in Section 2.1, other facilities use vitiation to obtain higher coflow temperatures, but the water vapor that would be introduced by the upstream combustion process renders such a design unsuitable for the current non-equilibrium study. Thus, this limitation on coflow temperature must be tolerated for the current study, and the measurement techniques used in this dissertation must be sufficiently precise in order to detect the relatively weak non-equilibrium that will be generated.

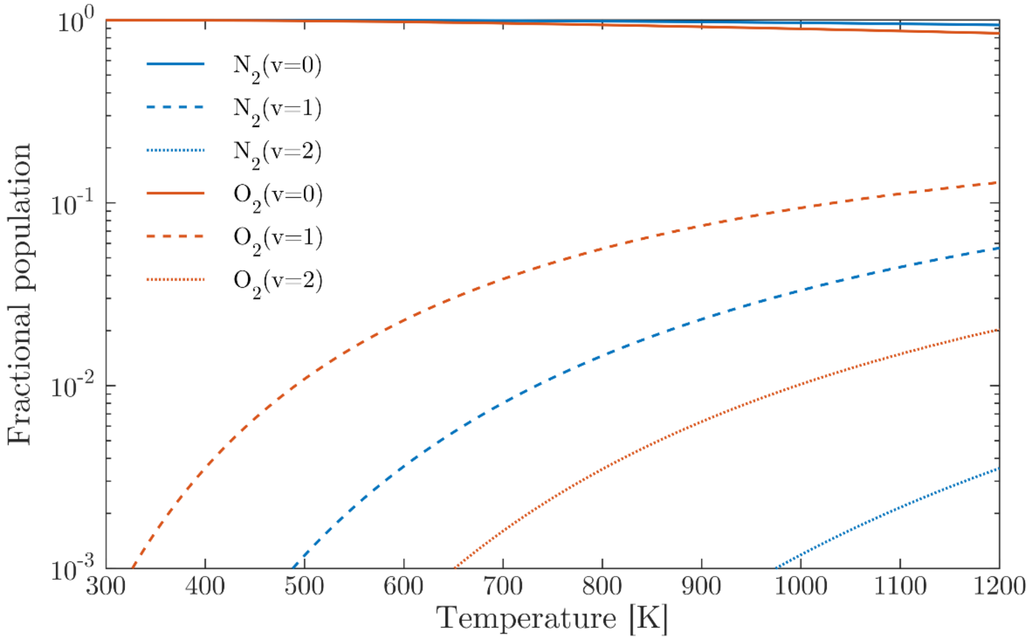

Figure 2.11: Fractional population in elevated vibrational states as a function of temperature.

No ignition source is introduced into the flow in order to initiate burning in the flames studied. Thus, the process controlling the initial flame ignition (and thus flame stabilization height) is autoignition. Numerical studies of this process in non-premixed flames have demonstrated the importance of a specific value of the global mixture fraction which represents a "most-reactive" mixture where the flame first ignites [71],[72]. Although those studies utilized detailed direct numerical simulations to study the coupled effect of mixture fraction and dissipation rate to predict autoignition, the most-reactive mixture was found to be accurately predicted by simpler laminar flow models. Specifically, the most-reactive mixture can be determined by identifying the mixture for which the ignition delay time is minimized. The most reactive mixture is determined by using detailed chemistry in a perfectly-stirred reactor model with the Cantera simulation package [73]. The UCSD combustion mechanism was used for these calculations [74]. The stoichiometric and most-reactive mixture fractions of the two fuel mixtures used in the experiments presented in this dissertation are presented in Table 2.1. The mixture of fuel and oxidizer is presented in terms of the mixture fraction, Z [75]. As in Ref. [72], the most-reactive mixtures are found to be leaner than stoichiometric. However, in the mixing layer of this study, there is also a large temperature difference between the fuel and oxidizer streams. Because the oxidizer stream is at a much higher temperature, the most-reactive mixture is shifted further to leaner mixtures. When this temperature variation with mixture is considered, the most-reactive mixture for the H_2/N_2 is shifted to $Z = 0.045$ ($\phi = 0.21$), which is very near the lean flammability limit of H_2. A similar effect is seen with the H_2/CH_4. Thus, the initial ignition of the lifted flames studied in this dissertation will occur at very lean mixtures.

Composition (by mol.)	Z_{stoich}	$Z_{most\text{-}reactive}$ (T = 1000 K)	$Z_{most\text{-}reactive}$ (T_{jet}=500 K, T_{coflow}=1000 K)
68% H_2, 32% N_2	0.181	0.097	0.045
62% H_2, 38% CH_4	0.048	0.016	0.014

Table 2.1: Mixture fraction values for fuel mixtures used in jet flame studies

Coflow temperature has been observed to exert a large effect on flame liftoff height in turbulent jet flames, while other flow parameters, such as jet temperature or coflow velocity, had a much weaker effect [76]–[78]. Wang and Pope performed a computational study of different coflow conditions which showed that the range of coflow temperatures for which the flame lift-off height is most sensitive is shifted to lower temperatures (930-970 K) for a pure air coflow than it is for vitiated coflow conditions (980-1040 K) [79]. A similar analysis was made for the flame conditions investigated in this dissertation by computing the dependence of ignition delay time on coflow temperature. The results are presented in Figs. 2.12 and 2.13 for the H_2/N_2 fuel and H_2/CH_4 fuel, respectively.

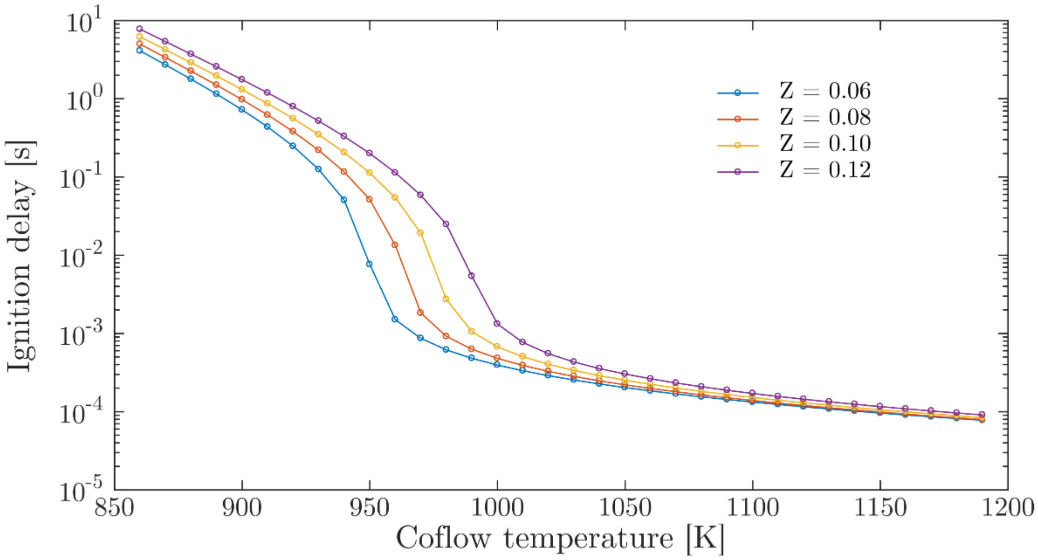

Figure 2.12: Effect of coflow temperature on the ignition delay time for the H_2/N_2 fuel at specified mixture fraction values.

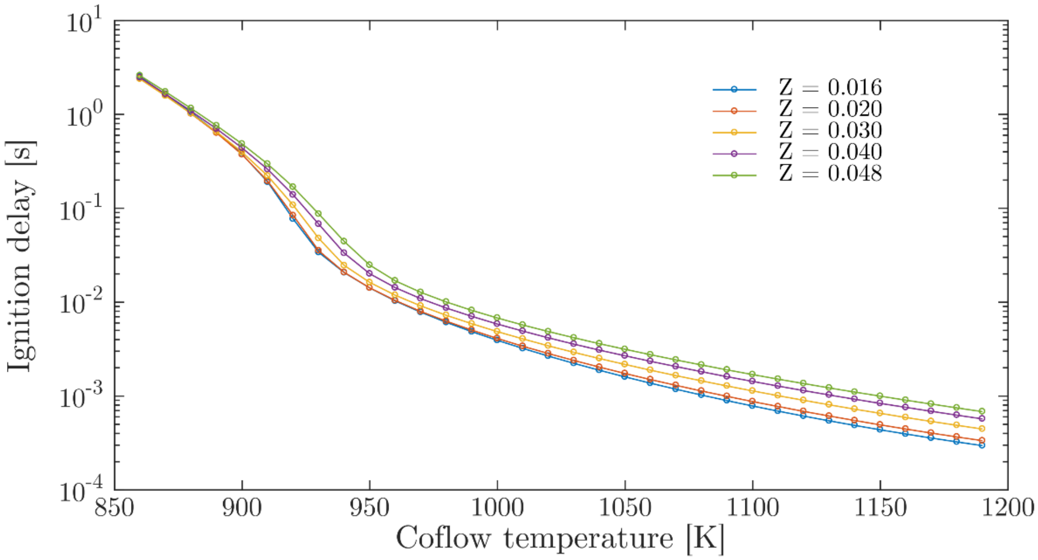

Figure 2.13: Effect of coflow temperature on the ignition delay time for the H_2/CH_4 fuel at specified mixture fraction values

As was noted in Ref. [79] with the conditions of a smililar jet-in-coflow burner, the ignition delay time shows a strong dependence on coflow temperature. The region of largest slope occurs for temperatures between 930 K and 980 K for the H_2/N_2 jet and at even colder temperatures for the H_2/CH_4 fuel for mixture fractions near the most-reactive value. Because this most-sensitive temperature range occurs below the coflow temperature used for the reacting flow experiments (1000 K), small variations in the coflow temperature are not expected to exert a large difference in the flame liftoff height. Thus, the observed lift-off height should be repeatable between runs.

In order to get maximal coflow gas temperature from the heaters, no part of the facility is water-cooled. This mode of operation leads to high material temperatures as the facility heats up to a steady-state condition. At these high temperatures, thermal expansion causes a significant shift in the nozzle and coflow shroud location during the heat-up process. Figure 2.14 illustrates this movement with a sequence of images. The nozzle exit location shifts approximately 17 mm upward and 4.5 mm laterally between room temperature and operating conditions. Several attempts were made to reduce this shift with mechanical braces, one of which can be seen in Fig. A.7. In practice, this shift in nozzle location required all optical measurements to be aligned while the coflow stream was heated to operating conditions.

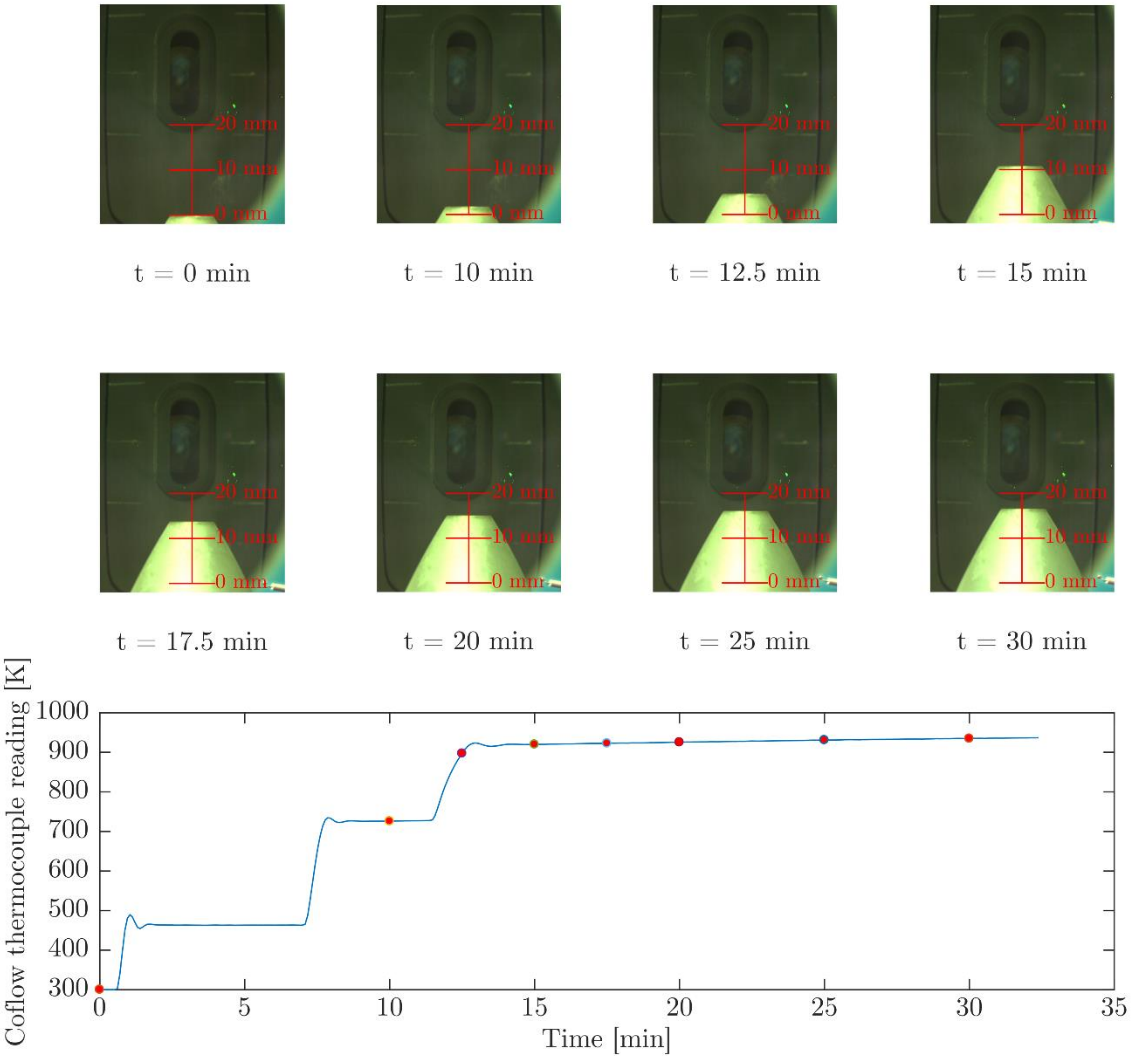
t = 0 min
t = 10 min
t = 12.5 min
t = 15 min
t = 17.5 min
t = 20 min
t = 25 min
t = 30 min

Figure 2.14: Sequence of images illustrating nozzle shift during heat-up process.

Chapter 3: Time Averaged Raman Scattering

This chapter presents measurements of vibrational non-equilibrium made with a time-averaged Raman scattering technique. We use spontaneous Raman scattering to simultaneously measure the rotational and the vibrational temperatures of N_2 and O_2 across the jet shear layer. The linear nature of the spontaneous technique greatly simplifies the theoretical model used for temperature fitting. Independent measurements of the translational temperature are also made using planar Rayleigh scattering to confirm the validity of the Raman scattering results. Section 3.1 presents results in a Mach 1.5 air jet issuing into a hot air coflow. Section 3.2 focuses on measurements made in subsonic jets of combustible fuel mixtures.

3.1 – AIR MIXING STUDIES

Initially, mixing-induced vibrational non-equilibrium of N_2 was studied in the turbulent shear layer between a supersonic cold jet and a surrounding hot air coflow. The jet fluid was either air, N_2, or Ar, and the heated coflow used was air at a maximum temperature of 850 K. The facility configuration, run conditions and measurement apparatus are described in detail in Section 3.1.1. Discussion of the measurements and their implications are presented in Section 3.1.2. The contents of this section have been published in [80].[1]

---

[1] Reising, H. H., KC, U., Clemens, N. T., and Varghese, P. L., "Measurement of mixing-induced thermal non-equilibrium in a supersonic shear layer using spontaneous Raman scattering," *Physics of Fluids*, Vol. 29, No. 7, 2017, p. 76101, DOI: 10.1063/1.4991754.
The author of this dissertation was the primary author of this manuscript and carried out the collection and analysis of the data presented within in collaboration with U. KC. N. Clemens and P. Varghese served in a supervisory role and provided critical revision of the article.

3.1.1 – Experimental Setup

3.1.1.1 – Facility Configuration

The facility for these experiments was arranged as was shown in Fig. 2.3a. The nozzle was designed for a Mach 1.5 exit condition and had an 8 mm exit diameter. The main configuration for these studies is one where air is used as both the jet and coflow fluid. Operating conditions for this air mixing case are presented Table 3.1. The jet was operated in a perfectly expanded state where the exit pressure was matched to the ambient pressure of the room. This was ensured by visually inspecting the shock/expansion structure at the nozzle lip using Schlieren imaging while adjusting the gas supply pressure. During data collection, the pressure that minimized wave formation was maintained using mass flow controllers. The convective Mach number [81], M_c, of the jet shear layer presented in the table was computed from freestream conditions. The shear layer thickness, δ, is defined by the 5% to 95% width of the mean temperature profile (determined by Rayleigh scattering) at the downstream location where Raman scattering measurements were made. The characteristic timescale of the mixing in the shear layer, which will be used to compare with the relaxation time of the vibrational energy, was defined as the eddy turnover time, $\frac{\delta}{\Delta U}$, where ΔU is the difference between the speed of the jet and the coflow.

T_{jet}	210 K
T_{coflow}	850 K
M_{jet}	1.5
$s = \frac{\rho_{coflow}}{\rho_{jet}}$	0.25
M_c	0.51
δ (z =12 mm)	2.3 mm
$\tau_{mix} = \frac{\delta}{\Delta U}$	5 μs

Table 3.1: Operating conditions and relevant flow parameters

3.1.1.2 – Spontaneous Raman Measurement Setup

Figure 3.1 shows the schematic of the set up used for Raman spectroscopy. The excitation energy for the light scattering is provided by a frequency doubled, diode pumped Nd:YAG laser with pulse energy of 4 mJ at 532 nm and operated at 10 kHz repetition rate. The pulse duration of the laser was about 160 ns, the beam height was 5 mm at the laser output window and the beam divergence was 5 mrad. The laser light was switched between the alignment mode and the experimental mode using the combination of a polarization rotator and a polarizing beam splitter. In the experimental mode, the beam splitter was removed from the set up and the polarization rotator was adjusted to maximize the Raman signal in the direction of the collection optics. The laser beam was focused using a 40 cm focal length lens. The scattered light was collected by a Nikon 105 mm f/2.8 camera lens and focused into the entrance aperture of a HoloSpec f/1.8 spectrograph manufactured by Kaiser Optical Systems, Inc. The front surface of the collection lens was placed about 22 cm from the nozzle. Camera lenses were used in the collection arm to prevent chromatic aberrations. The elastically scattered light was filtered out by a SuperNotch filter with O.D. > 4.0 and bandwidth < 350 cm^{-1}. Light was dispersed by the HDG-608 transmission grating, which had an average dispersion of ~0.03 nm per pixel. The signal was recorded using an intensified charge-coupled device (ICCD) camera with an 18 mm wide HBF Gen III intensifier (Princeton Instruments PI-MAX 3). The intensifier had a quantum efficiency of 44% at 607 nm, which is typically the near the peak of the *Q* branch of the Stokes signal from $^{14}N_2$. The CCD array had 1024 × 256 pixels each measuring 26 μm × 26 μm, of which approximately 620 × 256 were covered by the intensifier. Figure B.1 in Appendix B shows the boundary of the intensified portion of the sensor. The spectral coverage of the detector was 595 to 620 nm for these experiments. The use of a 100 μm slit width resulted in a measurement volume which measured 1.1 × 0.33 mm. The beam height at the focus sets the spatial resolution in the streamwise (vertical) direction, while the slit width and magnification set the limits the cross-stream (horizontal) resolution. The exposure time of the sensor was 20 s, i.e., each data set was obtained from 800 J of incident energy. Such a high incident energy was necessary to obtain adequate signal-to-noise ratio (SNR) in the low-intensity spectrally resolved *O* and *S* branches. As shown in Fig. 3.2, the intensity of the *O* and the *S* branches are 2-3 orders of magnitude lower than that of the *Q* branch. This large dynamic range is made possible by the relatively large vertical sensor area on which the signal was collected.

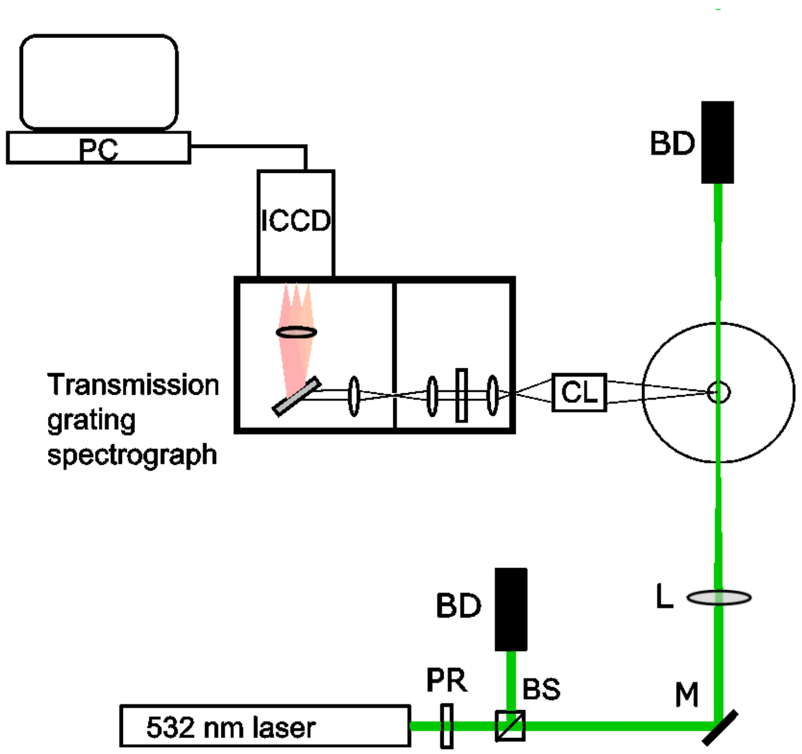

Figure 3.1: Schematic of the Raman set up: BD, beam dump; BS, beam splitter; PR, polarization rotator; M, mirror; L, lens; and CL, camera lens.

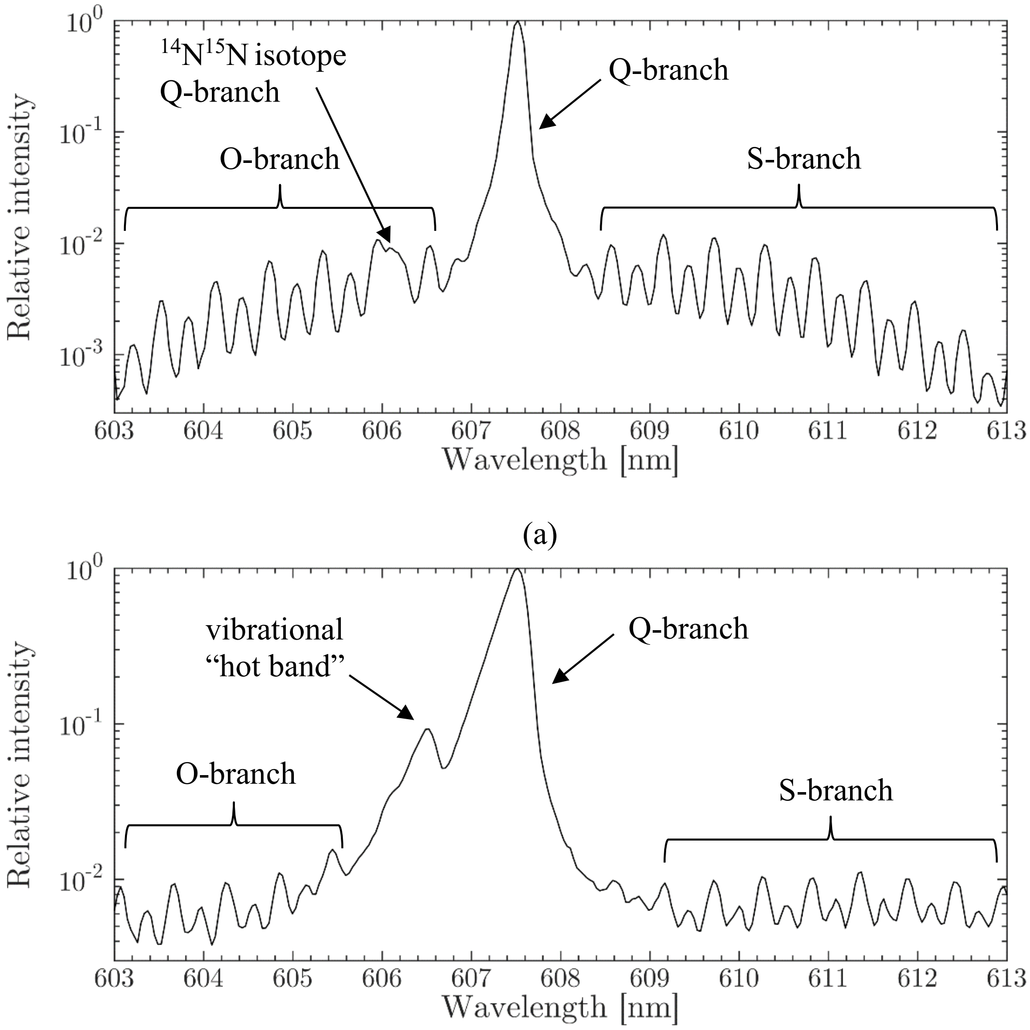

(a)

(b)

Figure 3.2: Sample Stokes Raman spectra from N_2 (a) in the jet at 210 K and (b) in the hot coflow at 1000 K.

The spectra contained in Fig. 3.2 illustrate several important features which are observed in the Raman spectra. While the O-, Q-, and S-branch lines have been discussed in Ch. 1, an additional feature which is labeled in Fig. 3.2a is the Q-branch of the diatomic species $^{14}N^{15}N$, which contains the rare isotope of nitrogen. This feature is also present in the hot coflow spectrum, although it is overwhelmed by the additional Q-branch features which become dominant in that spectra region at high temperature. The main difference between the two spectra of Fig. 3.2 is the appearance of a prominent second Q-branch line, termed the “hot band” due to its association with high temperature gas samples where higher vibrational levels become populated. The “hot band” line indicated in the figure comes from the $v'=2 \leftarrow v''=1$ fundamental band transition. Further “hot band” lines from higher vibrational levels become visible at flame temperatures, which are observed in Section 3.2 and Ch. 4.

Conversion of the raw Raman signal at the detector to spectra like Fig. 3.2 required meticulous calibration. In the raw images on the CCD array, the horizontal axis is the dispersion axis. Positions along this axis were identified in terms of the desired spectral units by comparing the pixel positions of the emission lines from a neon calibration lamp with their respective positions tabulated in the NIST database. The pixel positions of the individual neon lines were obtained to sub pixel resolution by curve fitting the instrument line shape model to the recorded spectrum. The instrument line shape function was modeled by the convolution of a trapezoid function and a Lorentzian. The free parameters of the line shape function were the half base width and the half top width of the trapezoid, and the Lorentz width. The system intensity response was also calibrated by taking the ratio of the recorded signal from a cavity blackbody (CI Systems SR-20) at 1000 K to a Planck function at the same temperature. This provided a calibration factor for the detector and collection optics accounting for any spectrally non-uniform response. Additional details on the data calibration procedure is described by Utsav and Varghese in Ref. [34], and in Appendix B.

3.1.1.3 – Rayleigh Imaging Diagnostics Setup

Planar laser Rayleigh imaging was used to provide an instantaneous measurement of the gas temperature. The light source for the 2D Rayleigh scattering is a 532 nm frequency-doubled Nd:YAG laser (Spectra-Physics GCR-150) operated at 10 Hz. The pulse width was 10 ns and the pulse energy was 300 mJ. The beam was first expanded using a pair of cylindrical lenses (with focal lengths –40 mm and 130 mm, respectively), and then focused with a 500 mm focal length positive cylindrical lens. The resulting laser sheet thickness was measured by traversing a knife edge through the beam while monitoring the power; the resulting sheet thickness was 130 μm (FWHM). The sheet height was 10 ± 1 mm.

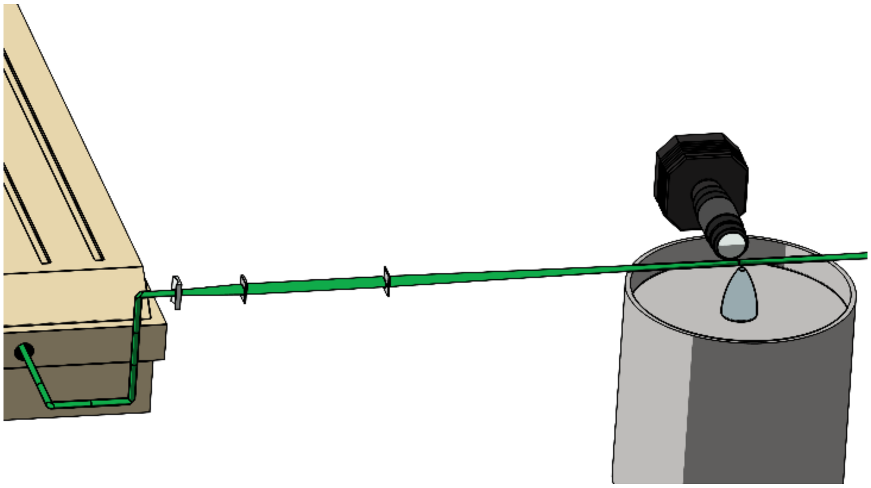

Figure 3.3: Schematic diagram of the Rayleigh scattering setup.

The Rayleigh scattering was imaged using a back-illuminated CCD camera (PixelVision SV512V1), which has an individual pixel size of 24 μm × 24 μm. A pair of Nikon 50mm f/1.4 lenses were used in unity conjugate ratio. An extension tube was not used between the lens and the camera to increase the magnification as it would also lead to barrel distortion and reduction in the amount of collected light. The imaging field of view was 12 mm × 12 mm. The short working distance of the lens configuration required that the lenses be located within the hot coflowing air. A lens protection and cooling system (not pictured in Figure 3.3) kept the temperature of the lenses at tolerable levels throughout the experiments and protected the camera from the heat load as well. Alteration of the shear layer by this intrusion was minimal due to the high velocity ratio between the jet and coflow.

Resolution of the imaging system was characterized by measuring the step response function by the scanning knife edge method outlined in Ref. [52]. A knife edge was traversed through the object plane as images are recorded from a uniform light source. By plotting the response in a single pixel as a function of knife edge position, the line spread function was obtained. Curve fitting an error function to the response showed the full width at half maximum to be 29 μm. This can be compared with the strain-limited diffusion scale, which is about 6 times larger than the Batchelor scale, $\lambda_D = 11.2\delta {Re_\delta}^{-3/4} Sc^{-1/2}$, where δ is the width of the mixing layer, Re_δ is a Reynolds number based on this width, and Sc is the Schmidt number of the gas [82]. Using gas properties at the mean temperature of the two freestreams, this value is estimated to be 13.4 μm in the shear layer at the downstream distance being studied. While this measurement does not resolve the very smallest mixing scales, it does provide a highly resolved measurement relative to the Raman scattering technique.

Rayleigh scattering as a technique to measure a two-dimensional temperature field has been used in many previous studies of subsonic jet flows [53],[65],[83]. The fraction of incident power scattered is given by [51] as

$$\frac{P_s}{P_i} = n\left(\frac{\partial\sigma}{\partial\Omega}\right)\Omega l \eta_c, \tag{3.1}$$

where P_s is the scattered power, P_i is the incident power, n is the gas number density, $\frac{\partial\sigma}{\partial\Omega}$ is the differential scattering cross-section, Ω is the collection solid angle, l is the imaging length along the beam and η_c is the optical collection efficiency. Since the last three terms are constant for a given imaging system, it is obvious that if the gas comprising the flow field being imaged has a constant scattering cross-section, then the Rayleigh scattering signal should be directly proportional to local number density, n. The pressure is assumed to be constant so that the Rayleigh signal is inversely proportional to the local temperature assuming ideal gas behavior. The raw data are calibrated against the Rayleigh signal recorded from a gas mixture at known temperature. The resultant images provide two-dimensional temperature fields in a single laser shot, which freezes the motion of the flow.

A set of sample Rayleigh scattering images is shown in Fig. 3.4 for the air mixing case specified in Table 3.1. The field of view is approximately 5 mm × 6 mm in the radial and streamwise directions, respectively, and it is centered 12 mm downstream of the nozzle exit. The denser cold jet is on the left while the hot coflow is on the right. The shear layer exhibits many small fingers of cold jet fluid reaching into the hot flow without the coherent "roller" structures. This behavior is consistent with previous studies of compressible mixing layer structure [84],[85].

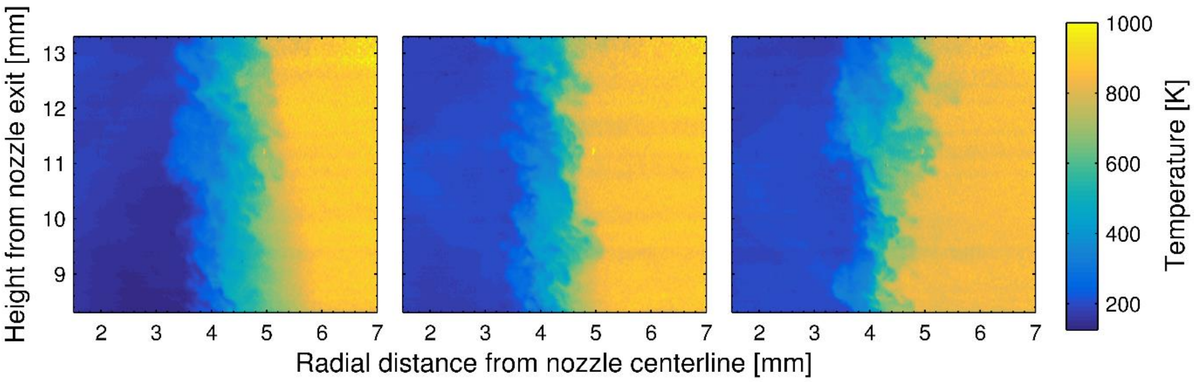

Figure 3.4: Sample Rayleigh scattering images.

3.1.2 – Results and Discussion

Figure 3.5 shows temperature profiles 12 mm downstream of the nozzle exit obtained using the previously described techniques. The cross-stream (radial) coordinate is non-dimensionalized as $\eta = \frac{r - r_{0.5}}{\delta}$, where $r_{0.5}$ is the radial location of the mean temperature of the two freestreams in a manner consistent with previous high-speed mixing studies [86],[87]. The Rayleigh scattering profile is taken from the average temperature field from the set of images for an entire run. The capture rate of the camera allowed for the collection of a set 77 images during a 3-minute run. The thermocouple measurement was obtained using 2 thermocouples with different bead diameters. The results were then extrapolated to an infinitesimally small bead size to account for the error due to bead radiation. Temperatures from the Raman scattering measurements are shown at the discrete locations that were probed. Vibrational temperatures are omitted where the flow temperature is too low (<450 K) to obtain a meaningful fit. Further explanation of this limit is provided in Appendix B. The error bars in Fig. 3.5 for the Raman temperature measurements were determined as follows. Residuals between the collected spectra and the fit results were stored in a library. These residuals were added to a simulated spectrum at known temperature and then fit for temperature. The best fit value of temperature from the spectral fit to the noisy simulated spectrum was then used to estimate the uncertainty in temperature caused by noise in the data and temperature variations in the probe volume during the collection time.

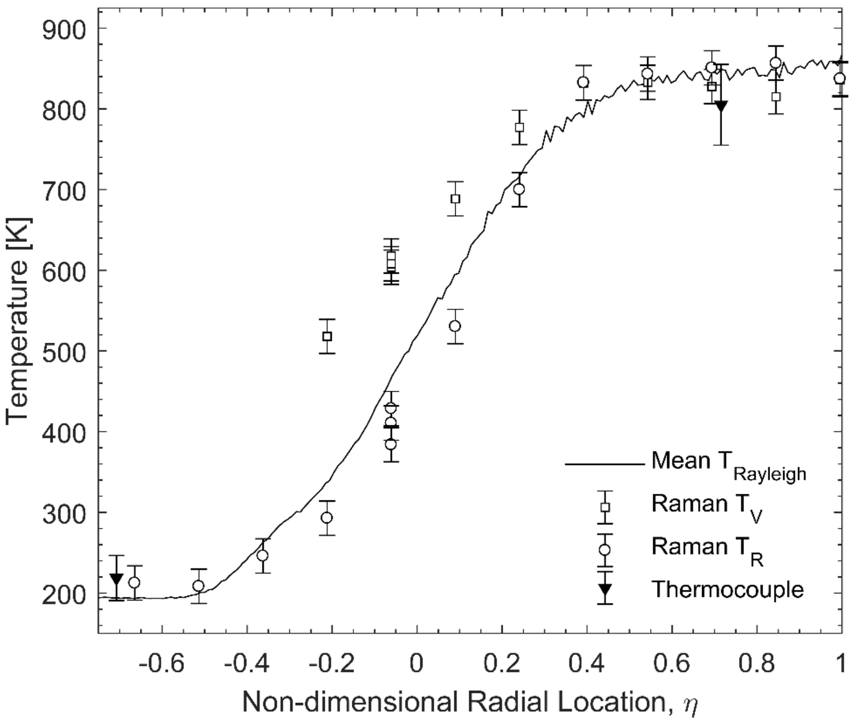

Figure 3.5: Various temperature measurements as a function of radial location at 12 mm downstream of the nozzle exit.

As shown in Fig. 3.5, there is a good agreement between the Raman, Rayleigh and thermocouple temperature measurements outside the shear layer. There is also minimal difference between T_V and T_R away from the shear layer, which is expected for flow that is in equilibrium. Within the shear layer, the effect of slow vibrational relaxation is clearly evident. The vibrational temperature remains higher than the flow temperature as the energy relaxes more slowly from the initial inflow step function profile. While the observed difference between T_V and T_R reaches a maximum of 220 K in this flow, the low population of vibrational-excited molecules means that very little energy deficit actually exists. In fact, if one assumes the total enthalpy of the flow is conserved, the excess energy in excited vibrational modes only reduces the gas temperature by 17 K from the equilibrium temperature at the location of maximum temperature difference ($\eta = -0.2$). Therefore, the effect noted by Koo et al., where mixing behavior is altered by changes in molecular viscosity, which are due to reduced gas temperature, will likely not have any measurable effect in this flow [88]. The minimal effect on viscosity is in agreement with Fuller et al. who found that energy exchange between vibrational and translational modes did not alter the viscosity for a much stronger plasma-generated non-equilibrium [89]. However, the result that high-speed mixing does indeed induce vibrational non-equilibrium is significant. This type of high-speed mixing between a jet and surrounding flow at vastly disparate temperatures is typical for the injection of hydrogen fuel in a scramjet combustor. This mixing process produces another source of vibrational non-equilibrium in a flow where both the efficiency of hydrogen combustion reactions and flame ignition are greatly affected by non-equilibrium [2],[90].

The rotational temperature from the Raman scattering measurement trends consistently with the profile from the Rayleigh scattering image set, agreeing to within 50 K at all locations. One should note that the Raman rotational temperature measurements are consistently lower than the Rayleigh scattering results in the shear layer. Because higher density fluid scatters light more effectively, the collected Raman spectra are biased toward the colder side of the local temperature probability density function (PDF). Conversely, the temperature derived from Rayleigh scattering reflects the true mean temperature profile, as there is very little spatial averaging and essentially no temporal averaging occurring within each pixel. This effect is illustrated in Fig. 3.6 for several sample PDFs. The original PDF and one weighted by gas density for different distribution widths around the same mean value. The difference between the original distribution and the density-weighted one is plotted in the lower portion of Fig. 3.6 as the "residual" value. This difference between the two techniques becomes more apparent when the temperature PDF is broadest, which manifests by a shift of the mean of the density-weighted PDF to a lower temperature. The two techniques do not show this discrepancy in the two freestreams because the fluctuations within the measurement volume are small, and thus the PDF is narrow.

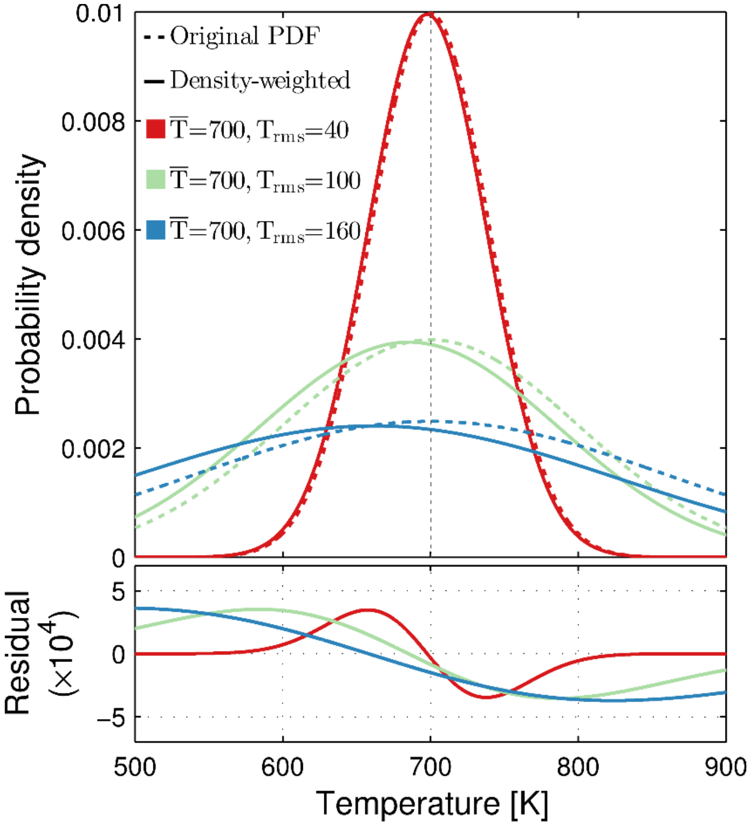

Figure 3.6: Density-weighting effects on normally-distributed temperature PDFs.

3.1.2.1 – Distinction between Compound and Non-equilibrium Spectra

We have assumed that T_R is not equal to T_V because the sample has a non-equilibrium energy distribution. However, as was shown in the previous section, in the presence of temperature fluctuations the spectra do not average in a linear sense. Since the Raman scattering intensity at a particular wavelength is a non-linear function of temperature, time-averaging in the presence of temperature fluctuations can lead to a bias error due to non-linear weighting [91]. We assess the error due to this non-linear weighting in the averaging process by computing "compound" spectra that are the average of spectra computed at different temperatures. Specifically, the compound equilibrium spectra are simulated by combining equilibrium Raman spectra on a density-weighted basis from a temperature PDF. Figure 3.7 below shows the effect of increasing width on normally-distributed temperature PDFs. It is apparent that larger local temperature fluctuations lead to an increasing difference between rotational and vibrational temperatures in the fit results. This effectively introduces a spurious non-equilibrium in the measurement results that is dependent on the local RMS temperature.

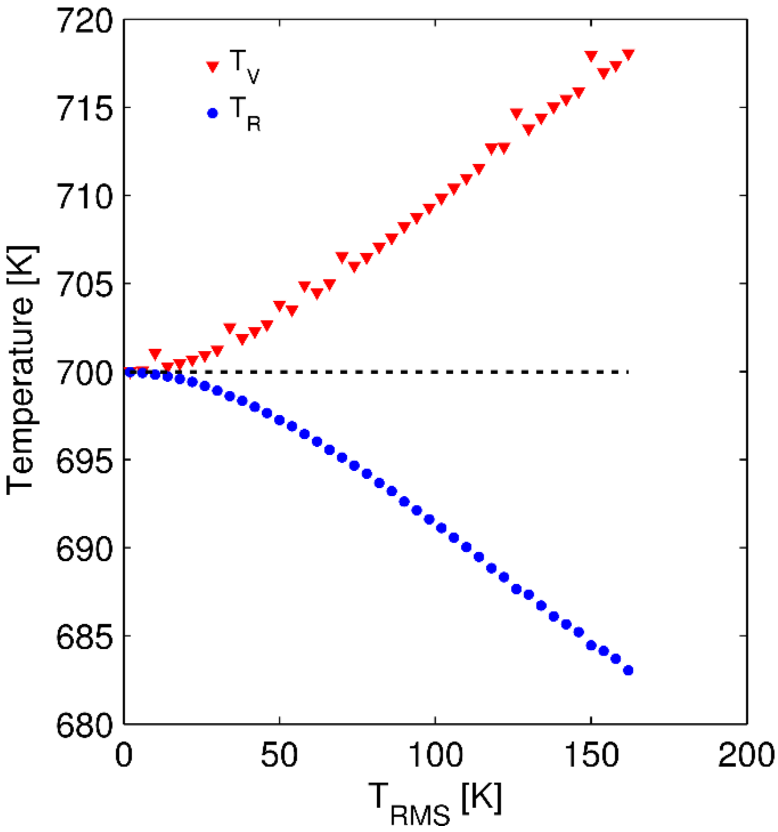

Figure 3.7: Effect of temperature distribution width on fit results for normally-distributed PDFs centered at 700 K.

In order to assess the effect of this false non-equilibrium on the apparent non-equilibrium in Fig. 3.5, the actual temperature fluctuations in the shear layer are used to compile "true" temperature PDFs for the Raman measurements. The Rayleigh temperature measurements, with higher spatial and temporal resolution, provide this information on both the spatial and temporal temperature distributions within a given Raman probe volume. As stated previously, the Rayleigh scattering measurements have a spatial resolution of 29 μm in the imaging plane and an exposure equal to one laser pulse width, 10 ns. Conversely, the Raman spectra are recorded from a 1.1 × 0.33 mm region and integrated over 20 s. Temperature distributions within a physical region of the same size as the Raman measurement volume were computed from the Rayleigh measurements. The RMS of these temperature distributions for a sliding measurement window across the shear layer is shown below in Fig. 3.8. The peak RMS temperature deviation is 92 K and is found slightly to the hot side of the location of mean temperature at $\eta = 0.12$. Comparing this with the results shown in Fig. 3.8, this level of temperature fluctuations within the Raman measurement volume would induce an artificial difference between of rotational and vibrational temperature of only about 20 K.

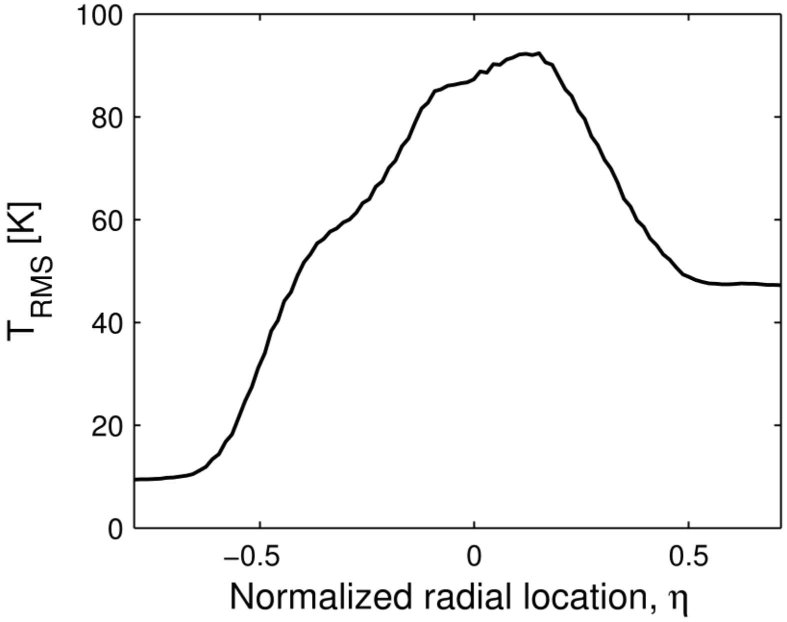

Figure 3.8: Temperature variations within the Raman measurement region at different locations across the mixing layer.

It is important to note that these PDFs are not normally-distributed in contrast to the distributions used for the calculations of Fig. 3.7. However, because we have detailed information about the true temperature distributions available to us through the Rayleigh thermometry measurements, we can perform a similar process to generate the expected Raman spectra that would be observed from a gas with these temperature distributions. Temperature PDFs for several of the Raman sampling locations are shown in Fig. 3.9.

Equilibrium Raman spectra are calculated at each of the temperatures shown in the PDF in Fig. 3.9 and are combined in a weighted average to generate a compound spectrum at each location. In order to make the simulated spectrum more similar to the experimental data, the residuals from a curve fit to the Raman data are added to the simulated compound spectrum. The non-equilibrium Raman fitting code is then used to fit the simulated noisy compound spectrum. We find that the difference between T_R and T_V in the shear layer calculated from the simulated compound spectrum is less than 50 K at all locations. This difference is significantly less than the difference between these values obtained from the experimental data shown in Fig. 3.6, which indicates clearly that the inferred levels of non-equilibrium are real, although perhaps smaller than suggested by Fig. 3.5.

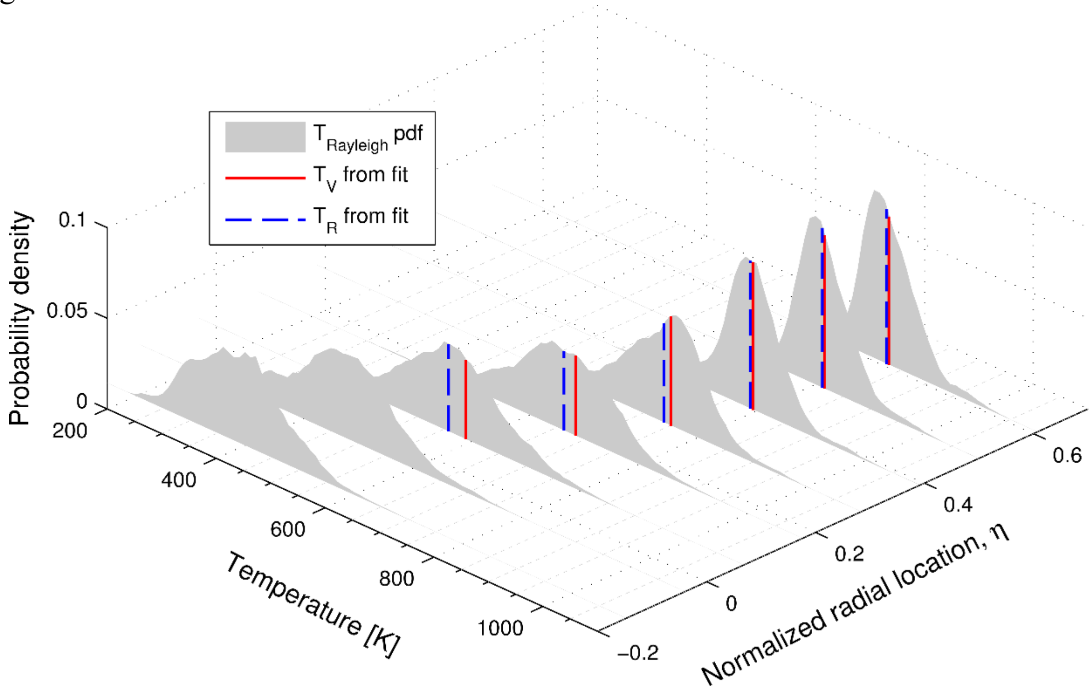

Figure 3.9: Rayleigh temperature PDFs at various Raman probe regions with the temperatures obtained from spectral fitting the average Raman spectra over the PDF.

It is worth noting that the compressible nature of the mixing layer and subsequent suppression of large-scale 2D “roller” structures may have provided sufficiently low local fluctuations within the shear layer and allowed for meaningful fitting of time-averaged samples. The narrowing of local PDFs with increasing compressibility has been found in both planar [87],[92],[93] and axisymmetric mixing layers [86]. In other flows where the fluctuations may be higher, the local PDF for each measurement may be broad enough that the difference between T_V and T_R in a compound spectrum may be of the same order as the fitting results from the actual Raman scattering data. Because of the potential for this bias error, the local temperature variations must be quantified when extending this time-average technique to other flow environments.

3.1.2.2 – Effect of CO₂ Addition

Figure 3.10 shows the result of several spectra rapidly collected at one location near the center of the shear layer. The facility was first operated at the same conditions listed in Table 3.1 and then CO_2 was introduced into the jet and coflow with a mass flow controller. The suppression of the $v'=2 \leftarrow v''=1$ hot band at 606.5 nm with increasing CO_2 concentration, signifies the reduction in the $v = 1$ population. Spectral fits showed that the difference between T_V and T_R decreased from 135 K without any addition of CO_2, to 90 K with the addition of 10% CO_2. These temperature residuals were consistent over many spectra, with a standard deviation of only 3 K without CO_2 and 12 K with 10% CO_2 by mole. This reduction in non-equilibrium reinforces the fact that true *V-T* non-equilibrium is being measured in this flow.

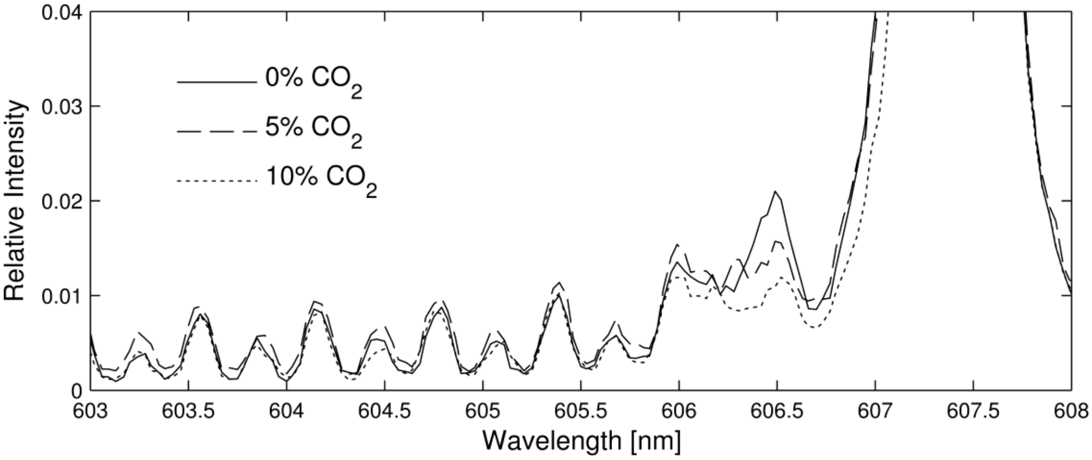

Figure 3.10: Effect of CO_2 addition on vibrational hot band population.

3.1.2.3 – Competing Excitation and De-excitation Processes

Thermal energy transfer between the two streams occurs as hot and cold packets of fluid in local vibrational-translational equilibrium are entrained from the low and high speed sides of the layer, respectively. As these two streams mix, the initially hot molecules will exhibit a vibrational temperature above the local gas temperature, while cold molecules which originated from the cold stream will show the reverse. This process is diagrammed in Fig. 3.11 below. Raman scattering measurements applied to such a packet of mixed fluid will inherently average the vibrational populations of these molecules. This can have an effect of reducing the apparent magnitude of non-equilibrium as molecules with excess vibrational energy and those with a vibrational deficit will both be present and mixed at the molecular level.

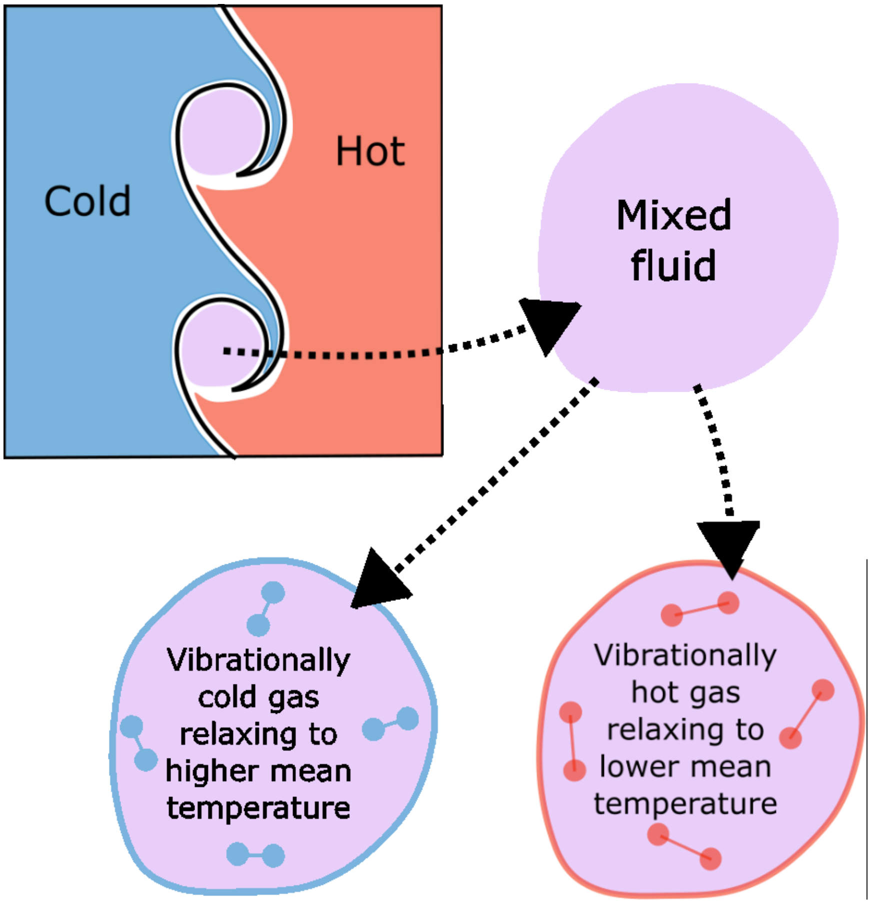

Figure 3.11: Illustration of the simultaneous hot-to-cold and cold-to-hot relaxation processes occurring in the shear layer.

To isolate this effect, dissimilar species can be used in order to track molecules from each side of the layer. Because the jet temperature is too low to probe with the current technique, it is convenient to continue to use air on the hot side of the layer and introduce the Raman inactive species, argon, in the jet. The use of argon allows the tracking of vibrationally-hot N_2 molecules as they are entrained and mixed with the cold jet. The results for an argon-air case are presented in Fig. 3.12 and compared with the air-air case shown in Fig. 3.5. The freestream conditions are also presented in Table 3.2 to illustrate the differences when the jet nozzle is run off-design to pressure match the exit with an atomic species instead of a diatomic molecule. The profile is truncated where the local concentration of nitrogen is too low for the fitting code to converge to a meaningful result.

	Air-Air	Argon-Air
T_{jet}	210 K	170 K
T_{coflow}	850 K	850 K
M_{jet}	1.50	1.55
Re_d	3.8×10^5	6.3×10^5

Table 3.2: Experimental conditions for the air-air and argon-air mixing cases.

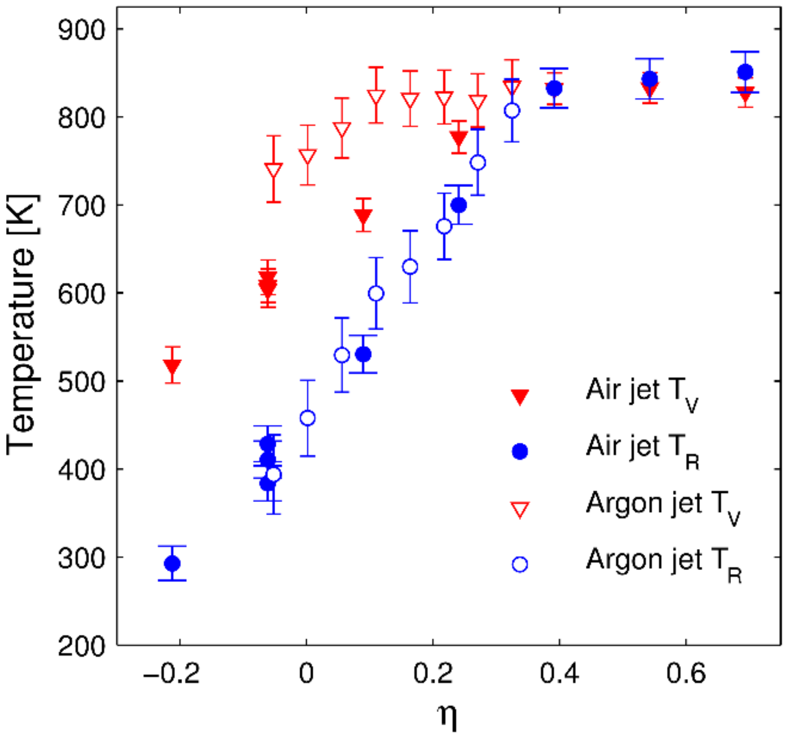

Figure 3.12: Temperature profiles for the air-air mixing and argon-air mixing cases.

The non-equilibrium can be observed deeper into the layer when vibrationally-active molecules only originate on the hot side of the layer. This observation confirms that the hot-to-cold relaxation process actually produces a stronger non-equilibrium in the shear layer than Fig. 3.5 would suggest. Therefore, a converse process of vibrationally-cold molecules relaxing to a higher temperature must also exist in the layer. Because this is an effect that is present at the molecular level, one cannot resolve this by improving the spatial resolution of the measurement. In a layer with identical species on both sides, the only way to separate the two processes would require identifying which side of the layer each molecule originated from. Because this is not possible in a real flow, this averaging effect will be present in any measurement made in a layer with vibrationally-active species in both freestreams.

The temperatures profiles of Fig. 3.12 show that the hot-to-cold process seems to be dominant for the present case. This preference the hot-to-cold process can be explained by the entrainment bias associated with shear layer mixing. If one assumes the vibrational relaxation rate to be effectively constant, the temperature profiles would be expected to evolve in a manner similar to a one-dimensional diffusion process. In this scenario, with density effects also ignored, the process would behave in a symmetrical fashion. This would be analogous to a shear layer in which the mass entrainment from both sides of the layer is balanced such that the mean temperature inside the layer would match the mean of the two freestreams. Using the relation given by Dimotakis [94], we can estimate the mass entrainment ratio, E_m, of the shear layer. Because the velocity ratio (r) in our flow is very low, the relation simplifies to

$$E_m(r \rightarrow 0) = \frac{1.68}{\sqrt{s}}, \tag{3.2}$$

where *s* is the density ratio across the shear layer. For the air-air mixing case, the entrainment ratio is approximately 3.3, which indicates a strong bias in mass flux entering the shear layer from the high-speed (cold) side. This bias will reduce the mean temperature of the shear layer so that the hot side will now be much further from the equilibrium temperature. This effect is illustrated in the cartoon profiles in Fig. 3.13. The apparent non-equilibrium appears larger in magnitude for the cooling process for entrainment ratios greater than one, which agrees with the temperature profiles presented above in Figs. 3.5 and 3.12.

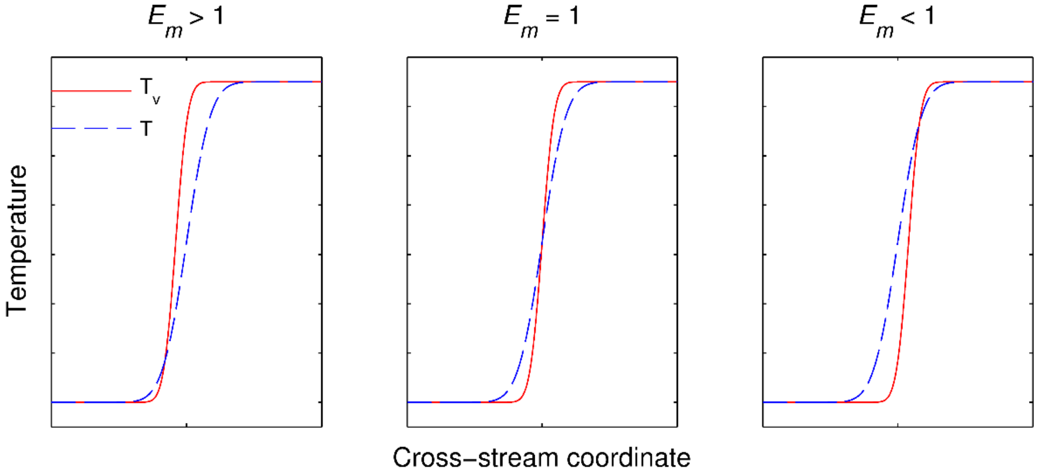

Figure 3.13: Theoretical depiction of effect non-unity entrainment ratio has on temperature profiles.

3.2 – HIGH-SPEED FLAME STUDIES

Vibrational non-equilibrium in jets containing combustible mixtures is investigated in this section. The facility configuration, run conditions and measurement apparatus are described in detail in Section 3.2.1. A key addition to the measurement capability for these experiments was the ability to quantify non-equilibrium in O_2 with the use of a different grating and alterations to the Raman fitting code. Discussion of the measurements and their implications are presented in Section 3.2.2. The results contained in this section were also used to inform a parametric study of interspecies vibrational energy transfer efficiency in large-eddy simulations [95].

3.2.1 – Experimental Setup

3.2.1.1 – Facility Configuration

In the following study, the same techniques were applied to high-speed jets of combustible gas mixing with hot air coflow. The facility was configured differently for flame studies than in Section 3.1. For these experiments, the facility was configured as pictured in Fig. 2.3b with the coflow shroud and converging nozzle installed. To avoid excessive flame liftoff heights, all the jet-exit velocities for these reacting cases were subsonic.

Several flame conditions were run, which are summarized in Table 3.3 below. For each run, the coflow temperature was kept at 1000 K. The mean jet velocity values in Table 3.3 are calculated based on input mass flow rates and thermocouple-based temperature measurements. The flow conditions in this study were chosen such that the flame stabilized at approximately the same liftoff height from the nozzle exit. Each condition provided a flame that auto-ignited immediately at the onset of fuel flow. The first two fuel mixtures listed consist of H_2 with diluents N_2 and Ar to simplify the non-equilibrium relaxation mechanism to a system of diatomic and atomic species, minimizing the computational expense of modeling these cases in companion CFD simulations. The H_2/N_2 and H_2/Ar cases also provide a comparison pair with and without the presence of vibrationally-cold N_2 from the jet. The H_2/CH_4 fuel mixture is the same as in [53] and provides a Rayleigh cross section which is identical to that of air. This cross section matching allows for the application of Rayleigh thermometry to quantify the effect of temporal averaging in the Raman measurements in a similar fashion to the air-

air mixing study. Figure 3.14 shows the average lifted flame location for the H_2/N_2 flame case as marked by a long exposure image of chemiluminescence from the hydroxyl radical (OH*). The flame lifts approximately 5 diameters from the nozzle exit in this case and is highly turbulent. For all cases the stoichiometric mixture fraction, Z_{stoich}, is relatively small and so the flame resides mainly on the low-speed side of the shear layer.

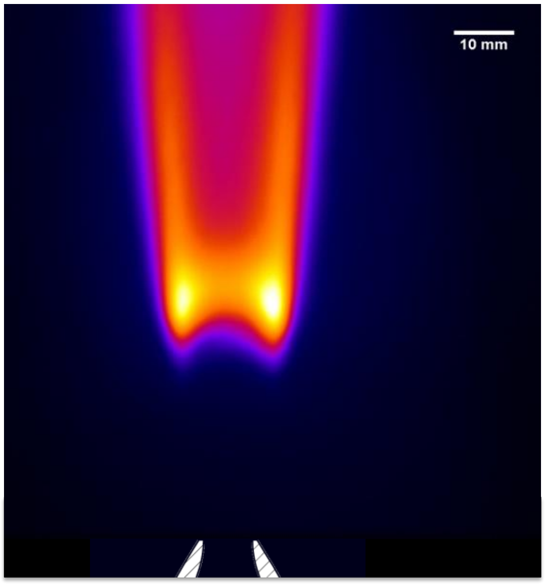

Figure 3.14: Image of OH* chemi-luminescence for the H_2/N_2 flame.

Case	Jet (by mol.)	Coflow	U_{jet} [m/s]	Re_d	$T_{o,jet}$ [K]	Z_{st}
H_2/N_2	68% H_2, 32% N_2	Air	540	75,100	560	0.181
H_2/Ar	75% H_2, 25% Ar	Air	505	77,000	570	0.183
H_2/CH_4	62% H_2, 38% CH_4	Air	300	27,400	550	0.048

Table 3.3: Summary of flame run conditions

3.2.1.2 – Optical Arrangement

For this study, several changes were made to the Raman and Rayleigh scattering measurements. The laser used was a frequency doubled diode-pumped Nd:YLF laser (Coherent Evolution 90) operated at 5 kHz repetition rate and an average power of 60W. The 105mm f/2.8 camera lens was no longer used for the collection optics. Instead, a pair of f/2.2 150 mm diameter achromatic lenses (Special Optics 54-120-260) operated at infinite conjugate ratio was used. The smaller f-number enabled reduced integration times to achieve the same signal levels as with the previous collection optics. The new optical system had a measured magnification of 1.4 at the sensor. The higher magnification of the collection system with these new lenses had the added benefit of reducing the spatial extent of the Raman measurement volume to 0.5 × 0.5 × 0.14 mm. The lenses also had a custom anti-reflection coating applied, which is specified to provide less than 0.5% reflectivity from 550 – 700 nm, which covers the entire range of Stokes Raman lines that was studied. For this study, we also used a grating that allowed for the measurement of O_2 Stokes Raman scattering by giving spectral coverage of 562 to 583 nm. Spectra collected from the coflow and shear layer are shown in Fig. 3.14 to illustrate typical equilibrium and non-equilibrium results, respectively. The spectra are integrated on the sensor for 8 or 12 s per measurement for N_2 and O_2, respectively, to obtain adequate signal-to-noise ratio in the weak rotational lines. The collected spectra contain sufficient detailed information in the rotational lines to provide independent measures of vibrational and rotational temperature. Raman shifts for the O_2 spectra are small enough that interference from H_2 rotational S-branch lines is present in the shear layer. These lines are masked off, as seen in Fig. 4d, before applying the spectral fitting code used to infer temperatures.

Owing to the heat generated by the flame, the paired lens setup was not used for the Rayleigh scattering measurements obtained in this study. Instead a forward-facing Nikon 50mm f/1.2 lens was used with 20 mm of extension to obtain sufficient magnification while maintaining a large enough working distance to protect the lens and camera from thermal damage. The incident light for the Rayleigh scattering was provided by frequency-doubled Nd:YAG laser delivering 1 J per pulse at a 10 Hz repetition rate. The scattered light was imaged by a CCD camera (PCO 1400) with 2×2 pixel binning to increase the signal-to-noise ratio. The field of view for this setup was approximately 17 mm and 10 mm in the radial and axial directions, respectively.

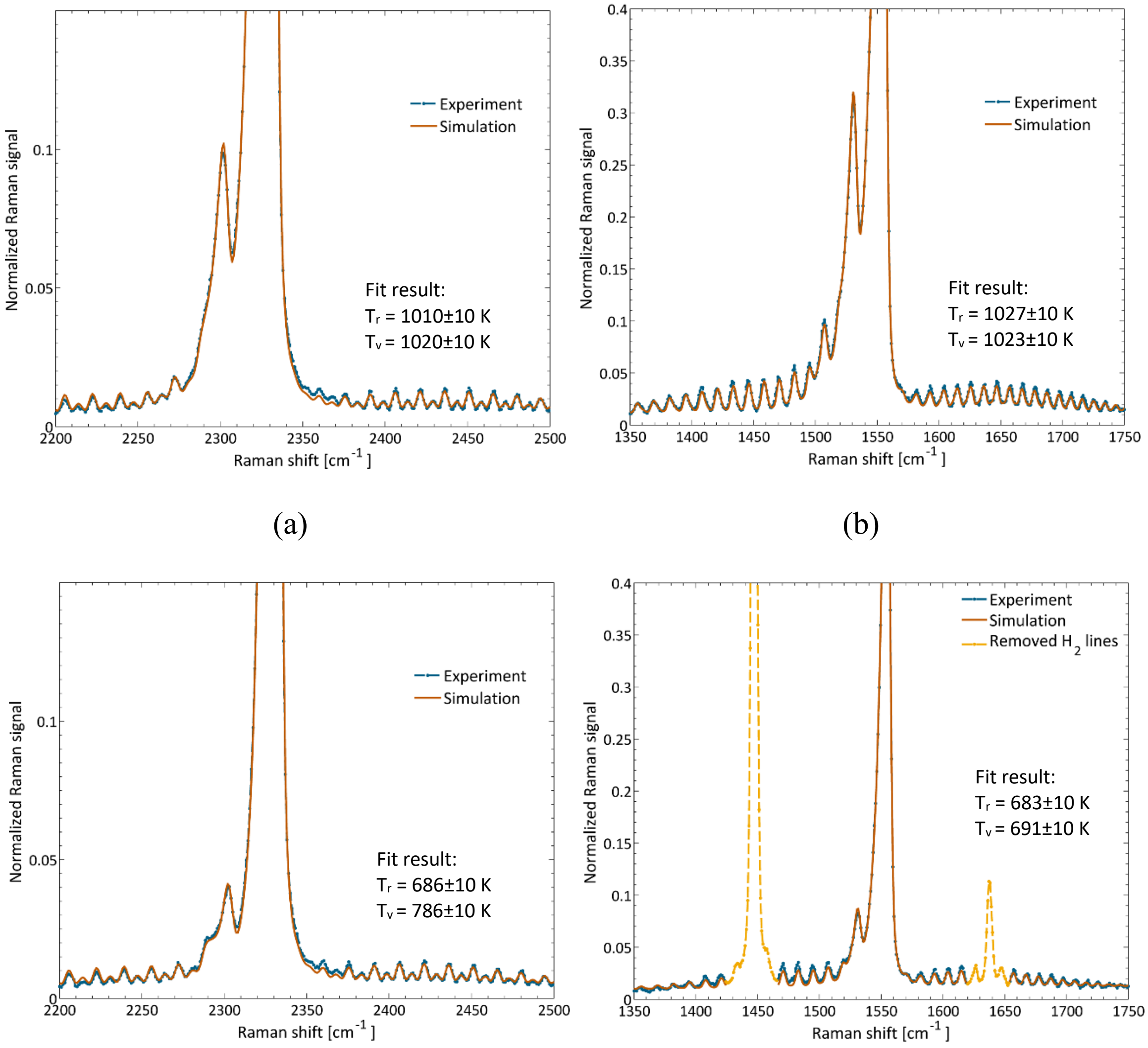

(a)

(b)

(c)

(d)

Figure 3.15: Sample Raman scattering spectra and simulations at their fitted temperatures in coflow (a,c) and shear layer (b,d). Measurements were all taken at an axial distance of 2 jet diameters downstream of the nozzle in the pre-flame region.

3.2.2.1 – Presence of Non-Equilibrium in Measured Spectra

In the non-reacting results of Section 3.1, Raman measurements were confirmed by the use of Rayleigh thermometry with a single gas composition in both the jet and coflow. The same analysis can be applied to the current H_2/CH_4 Rayleigh thermometry results to confirm that temperature variation within the measurement volume does not contribute significant error to the fit result. Temperature values for regions of the flowfield of the same physical dimension as the Raman measurement were extracted from a set of 1000 Rayleigh images. The probability density functions (pdfs) of gas temperature for discrete points across the shear layer are shown in Fig. 3.16.

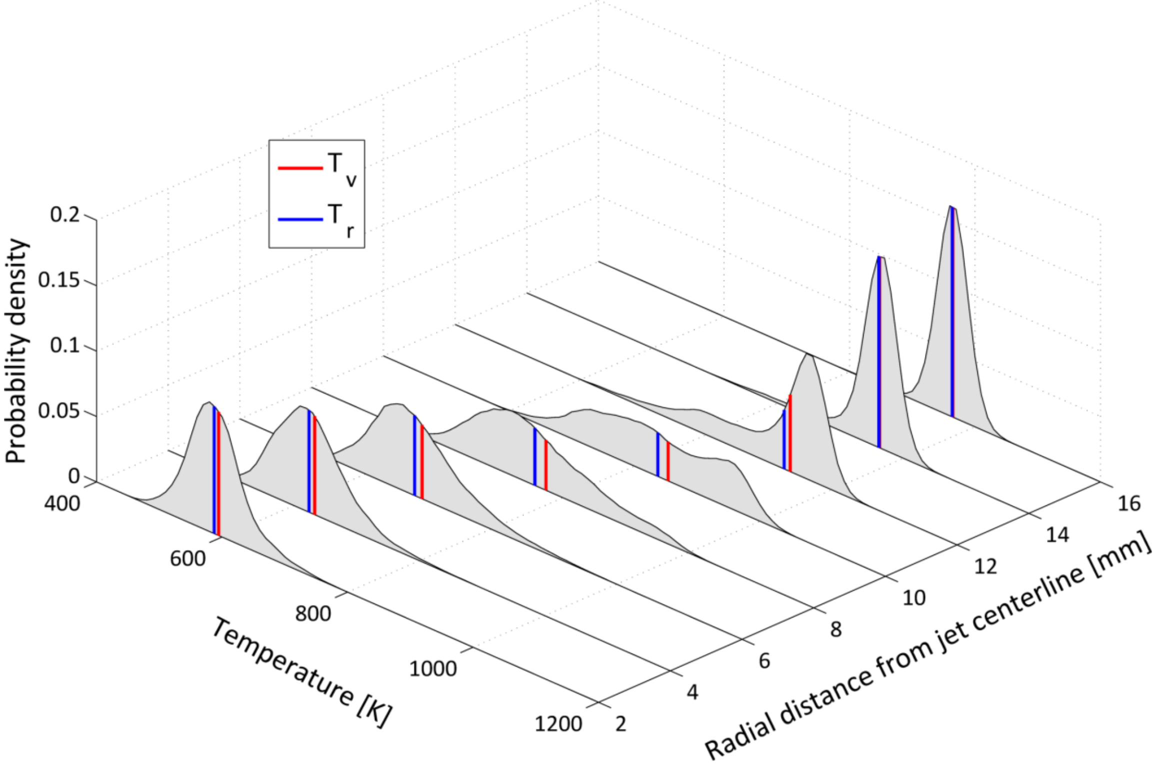

Figure 3.16: Temperature probability density functions extracted from Rayleigh thermometry images along with resultant temperatures from applying the fitting code to similarly distributed equilibrium spectra.

Equilibrium Raman spectra were calculated and summed to simulate the spatial and temporal averaging that occurred during a Raman measurement. The resultant composite spectra were then fitted for vibrational and rotational temperatures, which are also presented for each location in Fig. 3.16. As in the previous work, the temperature distributions are not broad enough to significantly affect the fit results. The maximum discrepancy between T_V and T_R is at most 15 K, which is significantly less than the magnitude of non-equilibrium seen in the collected spectra; however, this is not expected to be the case in a region in which the flame is present intermittently. Figure 3.17 shows sample Rayleigh thermometry images from the H_2/CH_4 flame, which illustrate the highly intermittent nature of the flame. The flame liftoff height fluctuates over a distance that is larger than the imaging field of view. A time-averaged Raman measurement made in this region would be integrating over gas temperature changes of over 1000 K and could not be used to detect vibrational non-equilibrium reliably.

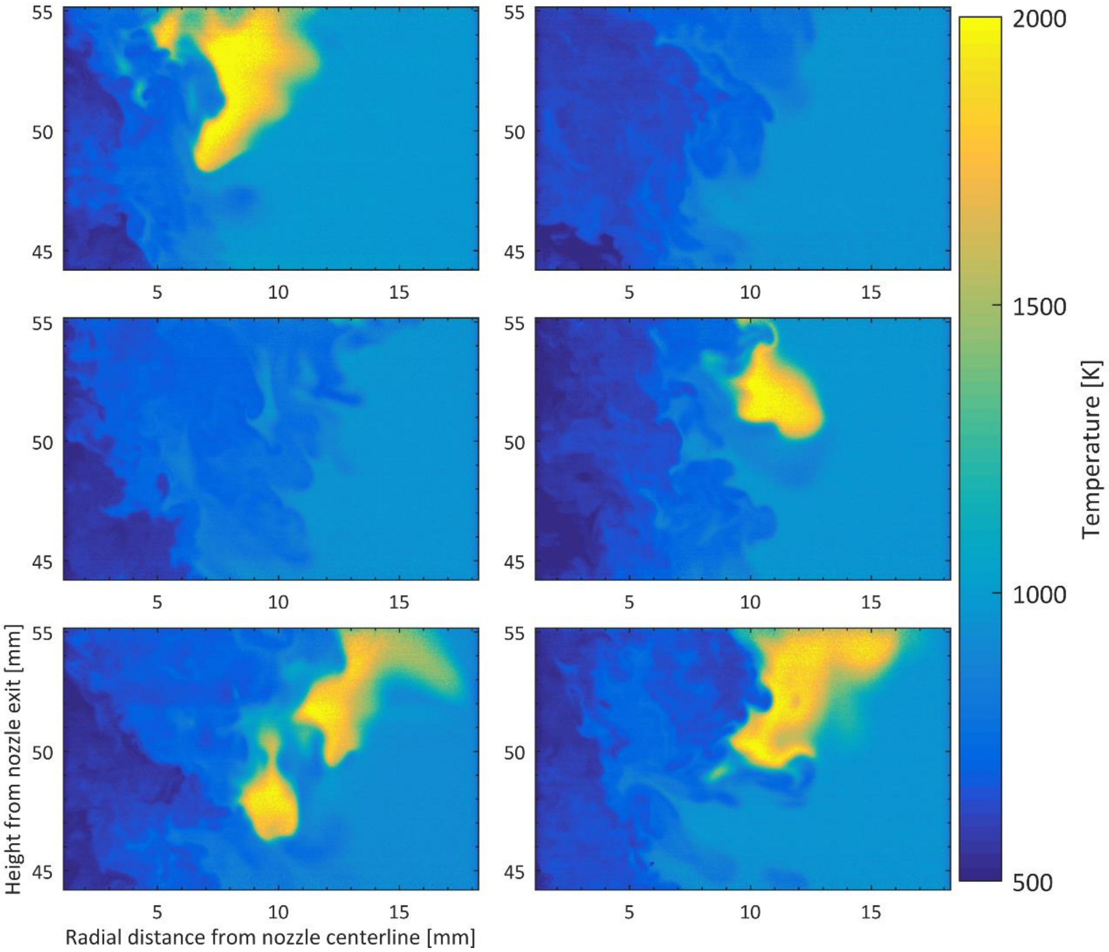

Figure 3.17: Subset of Rayleigh thermometry images for H_2/CH_4 flame. Further images are presented and discussed in Appendix D.

3.2.2.2 – Measurements in Hydrogen Flames

Using hydrogen as fuel simplifies the combustion chemistry and allows for simpler models to be used for CFD validation. The lack of carbon-containing polyatomic species also significantly simplifies the modeling of V-V and V-T energy transfer. Radial profiles across the shear layer were taken at various downstream locations to characterize the non-equilibrium in the shear layer upstream of the flame. The measurement locations are shown schematically in Figure. 3.18, where the lines indicate the downstream location and radial extent of the measurements.

Figure 3.19a shows vibrational and rotational temperature measurements at a location upstream of the lowest extent of the unsteady flame base. The rotational temperatures of N_2 and O_2 agree very well, because R-T equilibration is very fast. This consistency between measurements, which were performed with separate runs, and using a different spectral region, provides verification of the measurement accuracy. From the vibrational temperature measurements in Fig. 3.19a it is apparent that the N_2 is out of thermal equilibrium, as seen in our previous measurements [96], but interestingly the O_2 seems to be in complete equilibrium throughout the mixing layer. This would suggest that the V-V intermolecular transfer between these two species is very inefficient, which would lead to each species relaxing at its own V-T rate. This agrees with the study of Cutler et al. [97], who found that $T_{v,\mathrm{N_2}}$ and $T_{v,\mathrm{O_2}}$ were quite different in the non-equilibrium flow exiting a Mach 2 heated wind tunnel nozzle. In comparison with large-eddy simulations in Ref. [95], it was determined that conventional models for the interspecies vibrational energy transfer over-predict the coupling between O_2 and N_2 vibrational modes at these temperatures.

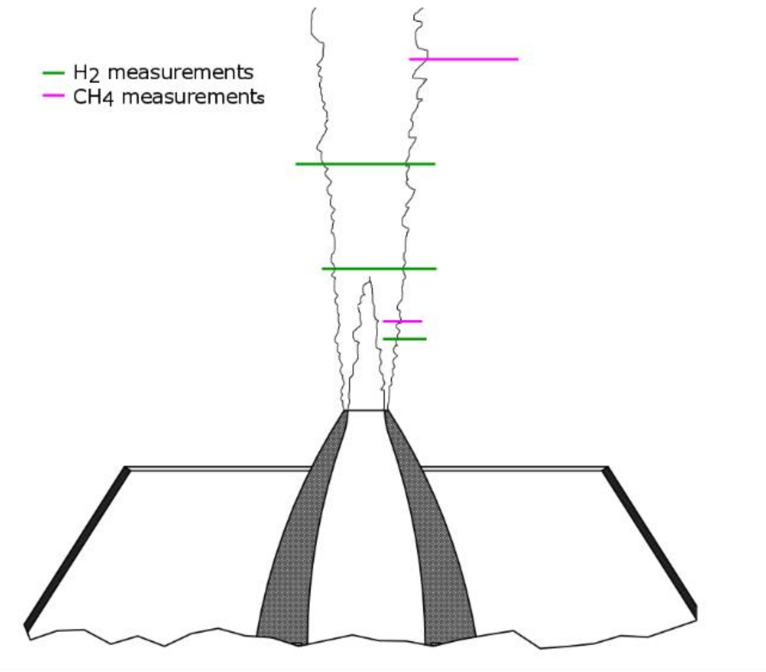

Figure 3.18: Schematic of Raman measurement locations (to scale)

The error bars in Fig. 3.19 indicate the precision uncertainty (95% confidence), and were determined using repeated measurements. Measurements are presented for radial locations where the signal-to-noise ratios are high enough that accurate fits could be made. In the near field, where there is still a potential core, there is no O_2 in the jet fluid, and so the O_2 Raman signals diminish faster than the N_2 signals as the probe volume is translated toward the jet axis.

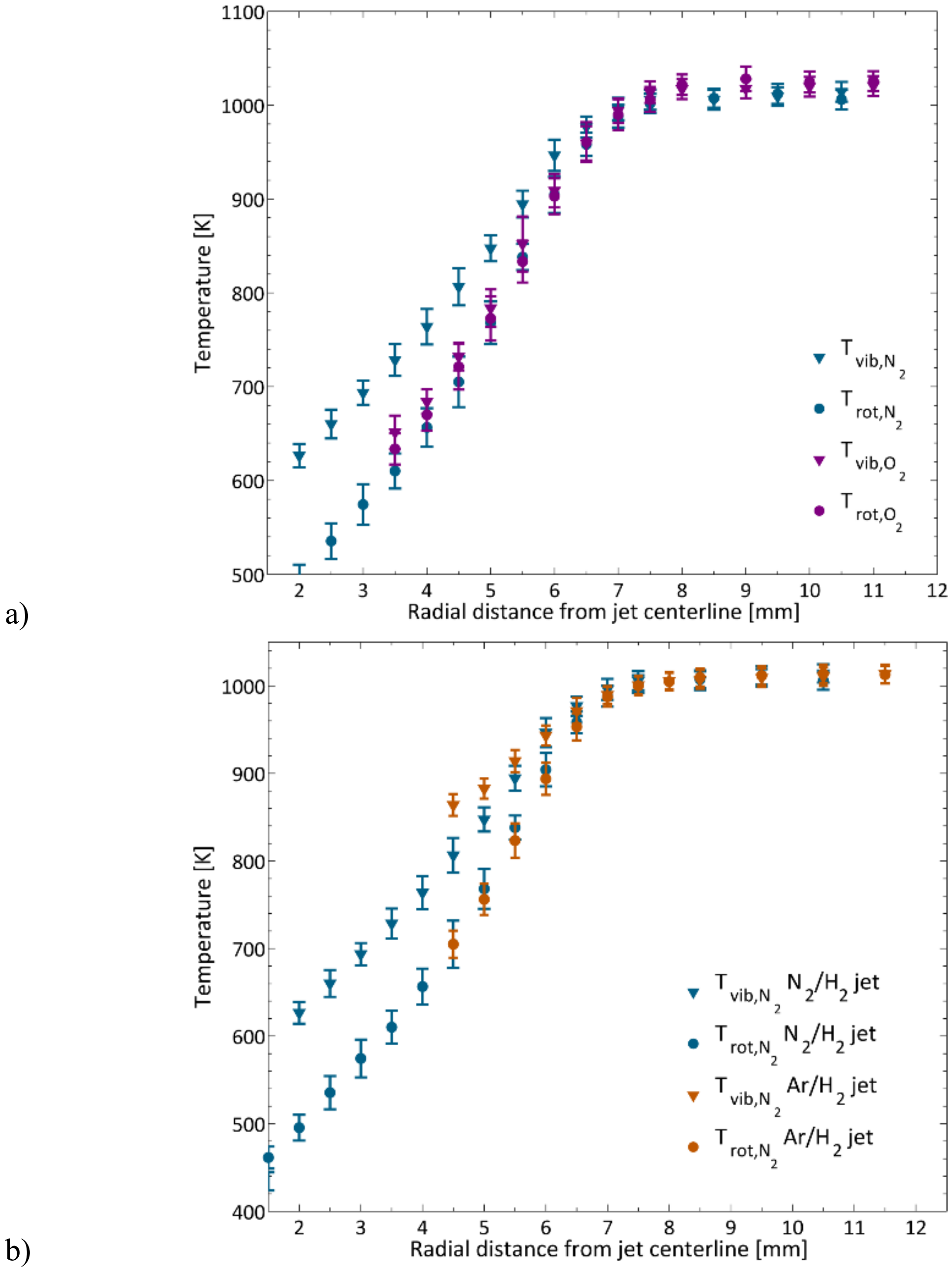

Figure 3.19: a) Radial profiles of N_2 and O_2 temperatures 2 diameters downstream of nozzle exit with H_2/N_2 fuel and b) radial profiles of N_2 temperatures with H_2/N_2 and H_2/Ar fuel.

As with the air-air mixing study, the apparent non-equilibrium magnitude in the H_2/N_2 case is reduced by the unavoidable averaging of the hot-to-cold and cold-to-hot processes. As done with the non-reacting case, the N_2 in the jet was replaced with argon to isolate the hot-to-cold relaxation process as vibrationally-cold N_2 is no longer being provided on the high speed side. This effect is illustrated above in Fig. 3.18b. While the rotational temperatures for the two different jet compositions match well, the measured non-equilibrium is much stronger when there is no longer N_2 present in the jet. Measurements with the H_2/Ar jet are particularly difficult due to the lack of N_2 from the high-speed side of the shear layer to provide scattered signal, which is why the profile for these runs does not extend as far into the jet.

Using Eq. 3.1, shear layer mass entrainment ratios can be computed for each reacting jet case. Values for freestream density and mass entrainment ratios are presented below in Table 3.4. If more mass from the cold jet is entrained ($E_m > 1$), the mixing layer temperature profile will be depressed such that the hot side will be further from the mean temperature. The hot-to-cold process dominates entrainment in all cases, which agrees with the behavior seen in the experimental shear layer profiles as well as the CFD results [95]. However, the cold-to-hot process is still present and should influence the mean vibrational temperature profiles by reducing the apparent non-equilibrium measured, as seen in Fig. 3.19b.

Case	s	E_m
H_2/N_2	1.43	1.67
H_2/Ar	1.31	1.75
H_2/CH_4	2.14	1.37

Table 3.4: Shear layer density ratios and mass entrainment ratios for the cases tested.

The temperature profile at a location farther downstream is presented in Fig. 3.20. This location corresponds to the farthest downstream location where the flame is never present. At this location, the jet potential core is just collapsing as there is no flat section in the temperature profile corresponding to a region of pure jet fluid; therefore, the entire jet width can be probed since the N_2-rich outer flow has penetrated to the center of the jet. The shear layer profiles on each side of the jet show similar behavior to the upstream profiles presented above, which is expected since this location is just beyond the shear layer region of the jet. It is important to note that non-equilibrium will not immediately disappear downstream of this point. The driving force behind non-equilibrium generation is the temperature gradient in the flow, which is still present beyond the potential core. The non-equilibrium will simply decay in magnitude as the jet centerline temperature rises to the outer flow temperature due to downstream turbulent mixing. This behavior is also observed in the simulation results presented in Fig. 12 of Ref. [95]. It is shown there that non-equilibrium at the centerline begins near the collapse of the potential core and continues until far downstream where combustion products have been entrained to the jet centerline.

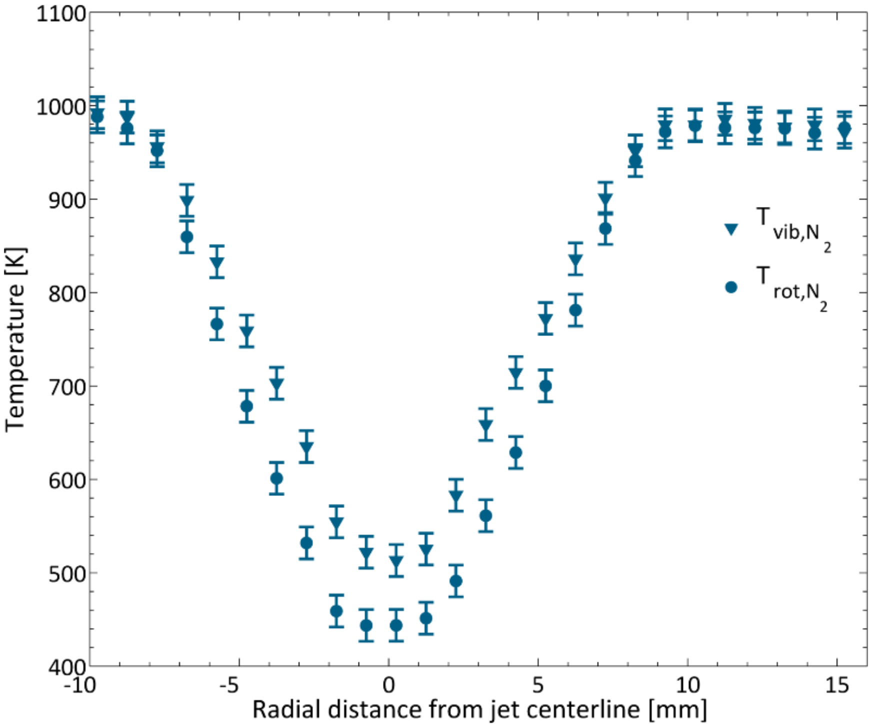

Figure 3.20: Radial mean profiles of N_2 rotational and vibrational temperature approximately 4 diameters downstream of nozzle exit.

As mentioned previously, the current time-averaged measurement technique does not allow for meaningful measurements to be made in the region where the flame base is present intermittently. However, measurements can be taken downstream of this region in the post-flame gases since the temperature fluctuations are not as large. Results at such a downstream station are plotted in Fig. 3.21 below. The spectra for this axial location required a 15 s integration time in order to collect enough signal in the low-density flame region and in the N_2-poor jet. The figure shows a mean profile through both sides of the flame, which is seen to be symmetric, as expected. It is also clear that the non-equilibrium, which is seen in the non-reacting regions upstream, is completely gone at the location of peak temperature in the radial profile. The absence of non-equilibrium is expected as the presence of flame products such as H_2O should relax the non-equilibrium quickly. Non-equilibrium is detected at the jet centerline just as it is in the upstream profile of Fig. 3.20. The simulation results in Fig. 12 of Ref. [95] show a similar non-equilibrium zone at the centerline around the height of the flame base. The peak measured temperature of 1835 K is 240 K less than the adiabatic flame temperature predicted for this fuel, which is reasonable considering the strained nature of the flame. The measured deviation from adiabatic flame temperature corresponds to a strain rate of 12,300 s^{-1} in a counterflow flame [73].

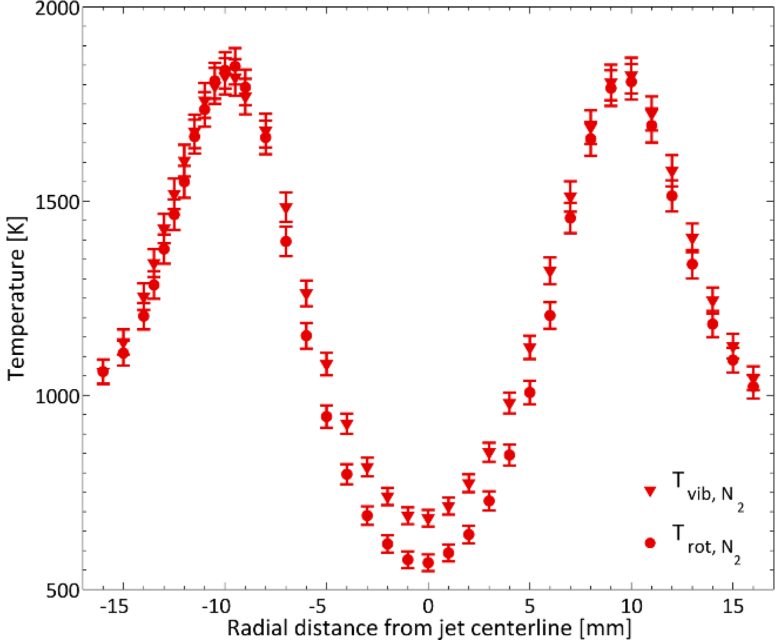

Figure 3.21: Radial trace of N_2 temperatures 7 diameters downstream of nozzle exit (downstream of flame base)

3.2.2.3 – Measurements in Methane-containing Flames

Figure 3.22a shows temperature profiles for the H_2/CH_4 jet at a location near to the nozzle exit. The non-equilibrium is clearly much weaker in this flow than in the hydrogen-containing cases. The lower level of non-equilibrium is most likely due to the much lower jet velocity that is required to prevent flame blowoff, although the inclusion of methane could also have had some effect on the relaxation process. Instead of reducing the jet velocity, the jet temperature could be increased to promote autoignition, but that would reduce the temperature difference between jet and coflow as a side-effect, and would reduce non-equilibrium magnitude. Like the H_2/Ar jet case, this fuel mixture does not contain N_2, which limits the depth into the jet that measurements can be made.

Results in the post-flame region are shown in Fig. 3.22b. Rotational temperatures could not be obtained for radial positions closer to the centerline than 19 mm. The combined effect of an N_2-free jet and the lower total number density in the high temperature region made rotational temperature fitting impossible even for spectra collected for as long as 42 seconds. Vibrational temperatures can be taken further into the jet, but do not reach far enough into the jet to show the peak flame temperature. This illustrates the need for the presence of the Raman species being probed in both fuel and oxidizer streams for full profiles of flame temperature.

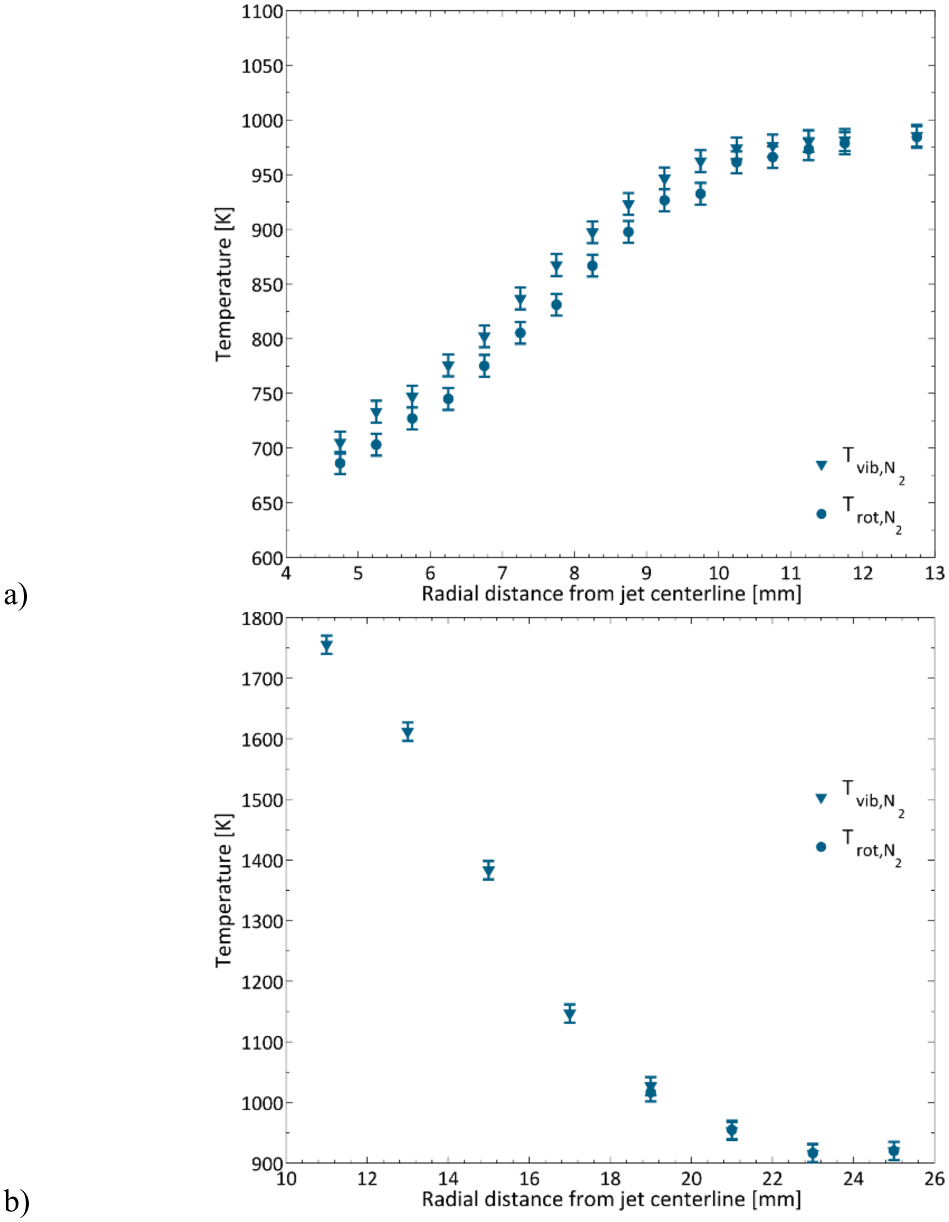

Figure 3.22: Radial trace of N_2 temperatures a) 2.5 diameters downstream in the mixing layer and b) 10 diameters downstream.

3.3 – CONCLUSIONS

In the air jet experiments, the presence of non-equilibrium between vibrational and rotational modes of N_2 was detected with the use time averaged spontaneous Raman scattering. Instantaneous planar Rayleigh scattering provided a second thermometric measurement to investigate the effect that the time averaging has on the Raman scattering results. The spectral fitting Raman code was determined to be reliable to detect the non-equilibrium at any location when the vibrational temperature is above 450 K. In the experiments reported here, it was only possible to measure the non-equilibrium between the vibrational and the rotational energy. It was not possible to measure the non-equilibrium population distribution among the vibrational states because only the fundamental and the first hot bands had sufficient intensity. The introduction of CO_2, a quenching species, suppressed the hot band further indicating the presence of non-equilibrium in the shear layer between the central jet and surrounding hot air.

This study provides the first experimental observation of mixing producing vibrational non-equilibrium in a high-speed jet shear layer. Because this flow configuration is similar to that used for fuel injection in a scramjet combustor, the production of non-equilibrium in this flow implies the same is true for the more extreme conditions in a scramjet. This could have a significant impact on engine efficiency and flame-holding.

The overall shape of the vibrational and rotational temperature profiles across the shear layer was shown to be a result of two competing non-equilibrium processes. The aggregate of these two processes manifests itself as a reduced observable non-equilibrium magnitude due to inherent averaging of the vibrational populations of both vibrationally-cold and vibrationally-hot molecules during the measurement. This averaging effect, which occurs on a molecular level, will be present in any shear layer induced non-equilibrium that has the same vibrationally-participating species on both sides of the layer, regardless of the measurement resolution.

The work described in Section 3.2 extended the use of time-averaged Raman scattering measurements at the base of lifted flames. Mixing-induced thermal non-equilibrium was detected in the shear layer upstream of the turbulent hydrogen flame in N_2 but not O_2. Rotational temperatures of the two species agree to within the measurement uncertainty. As expected, the non-equilibrium is relaxed immediately beyond the average flame-base location due to the presence of combustion products. The presence of non-equilibrium is confirmed using Rayleigh thermometry images to quantify the effect of translational temperature variation in the Raman measurement volume. These results were compared to large-eddy simulations with vibrational relaxation effects to study the effect of interspecies vibrational energy transfer models. Good agreement was found between the measurements and average simulated temperature fields when the interspecies vibrational coupling is very weak [95]. The time-averaged results from this technique do not allow for meaningful measurements to be made in the region where the flame base is present intermittently. Single-shot measurements are required in this region to freeze the flow; this would also allow for statistics to be collected for the temperature fluctuations.

Chapter 4: Single-Shot Raman Scattering

A single-shot Raman thermometry technique was developed to enable the study of instantaneous measurements of vibrational non-equilibrium in high-speed mixing and reacting flows. Although the time-averaged measurements described in Chapter 3 provided very high precision measurements, they suffer from system weighted-averaging errors in flows with high temperature fluctuations. Single-shot Raman scattering, on the other hand, enables us to make instantaneous measurements, but with much lower precision. It was not clear at the beginning of this study if sufficiently precise temperature measurements could be made to discern the presence of non-equilibrium. This chapter describes the development of a single-shot capability and the application to the same flows previously studied with time-averaged methods in order to assess the single-shot measurement validity in this flow.

4.1 – EXPERIMENTAL SETUP

The use of high energy pulsed lasers for Raman scattering point measurements is often limited by the optical breakdown of the gas in the probe volume. Optical breakdown was avoided in time-average measurements by using low pulse energy but high repetition rate lasers. In this case, the average power can be quite high (up to 100 W), providing high signal-to-noise data in several seconds of integration time. In order to freeze flow motion and isolate temporal averaging effects, a measurement from a single laser pulse is desirable.

As mentioned in Ch. 3, the time-averaged measurements were limited to regions of the flow where the temperature does not fluctuate too strongly. This is especially important near the base of the turbulent flame where it intermittently moves rapidly and chaotically up- and down-stream. This region will exhibit a bimodal temperature distribution with two peaks: one at the temperature of the unreacted upstream gas and another at much higher temperatures for partially to full-reacted samples. Applying the time-averaged technique in this region is futile, as averaging the spectra of gas samples at these disparate temperatures will yield a bias error in the fitted temperature values. Single-shot measurements, however, can not only investigate this region without issue, but also allow for the investigation of the statistics of the flame intermittency.

To perform single-shot measurements, the same Stokes Raman scattering phenomena were studied using a different laser system. This system was optimized to obtain adequate signal for temperature measurements from a single laser pulse from a 1J per pulse 6 ns Nd:YAG laser. Higher laser fluence in the probe volume was obtained through the use of a multiple-pass cell that sent the beam repeatedly through the same volume. The effect of the multiple-pass beam geometry on the collected Raman spectra is discussed in Appendix C. Additionally, an increase in signal was gained from widening the slit width in the spectrograph. Proof-of-concept studies investigating the minimum laser energy required and effects of slit width are presented in Appendix D.

The laser used for excitation is a flashlamp-pumped Nd:YAG laser (Continuum Powerlite DLS 9010), which produces 1 J per pulse at 532 nm at a repetition rate of 10 Hz. As a comparison to the previously used lasers, this laser would provide no advantage if used for time-average measurements, as it only produces 10 W of average power, as opposed to the 50 W provided by our diode-pumped laser. The flashlamp-pumped laser produces laser pulse durations of approximately 6 ns FWHM. If this pulse is focused in ambient air, the high peak power breaks down the air near the focal spot and produces a plasma spark. This gas breakdown changes the composition of the gas in the probe volume and the light emitted overwhelms any weak scattering signals collected in the detector, making Raman scattering measurements impossible. The breakdown threshold of atmospheric air for a 532 nm beam is estimated to be approximately 3×10^{12} W/cm^2 and is similar for H_2 and CH_4 [98].

To maintain the overall pulse energy while reducing the peak power, the pulse can be stretched temporally using a "pulse stretcher." For example, Nguyen et al. [99] used a pulse-stretcher apparatus to prevent optical breakdown for gas-phase Raman scattering measurements. Their pulse stretcher used partial beamsplitters and 2 time delay cavities to stretch a 10 ns, 700 mJ pulse adequately to prevent breakdown at the 750 μm beam waist. A detailed study of the design and optimal configuration of such a system was described in [100]. Through a numerical model of the pulse profile, it was determined that the ideal arrangement should have the final delay cavity with a round trip propagation time equal to the FWHM temporal pulse width of the original beam (τ_{laser}) and the cavity lengths should double in geometric progression. Thus, for a 3-cavity system, the delays should be $4\tau_{laser}$, $2\tau_{laser}$, and τ_{laser}. In addition, a beam splitter reflectivity of around 40% was found to give the best peak power reduction. By constructing a 3-cavity system, they were able to reduce the peak power of a pulse to 10% of the original while maintaining 82% of the pulse energy.

4.1.1 – Measurement Apparatus

The following section provides an overview of the final configuration used for the single-shot Raman scattering measurements. The considerations involved in designing the pulse stretcher and multiple pass cell are discussed in detail in Appendix D. Additionally, several photographs of the measurement system components in use are provided in Appendix A.

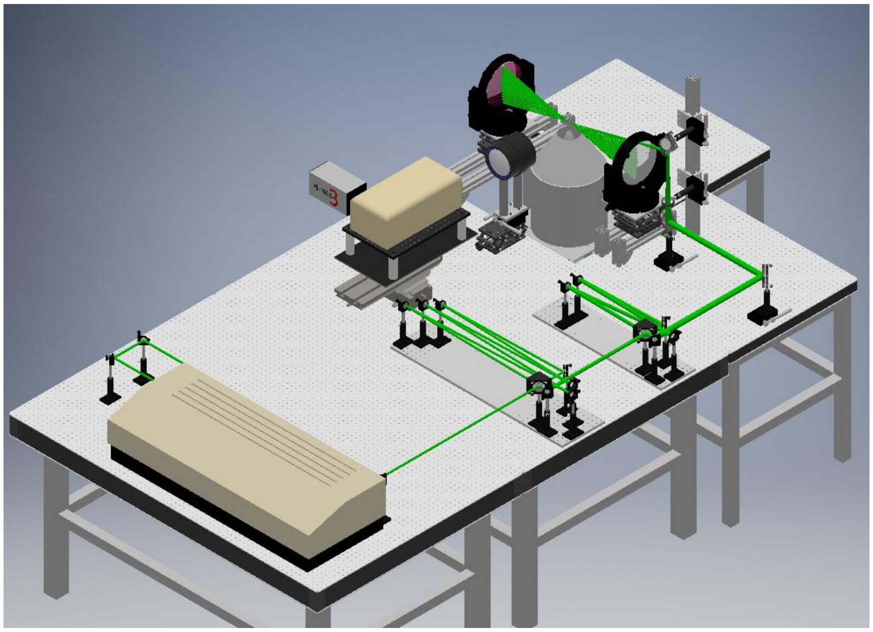

Figure 4.1: Overall view of single-shot Raman scattering measurement system.

4.1.1.1 – Temporal Pulse-Stretcher

The pulse-stretching system for this study utilized 2 cavities to limit the number of optics and therefore provide higher throughput and reduce cost. The beam entered each cavity through a partial reflector with 40% reflectivity and then was sent through a ring cavity with a specific length for a time-of-flight delay. The details of the pulse-stretcher design is presented in further detail in Appendix D. Figure 4.2 shows a dimensioned drawing of the pulse-stretching apparatus. A photograph of the pulse-stretching system is also provided in Fig. A.12. The optics for each cavity were mounted to plates to allow for each cavity to be moved as a single unit for easy use in other experiments without re-aligning each individual cavity optical component.

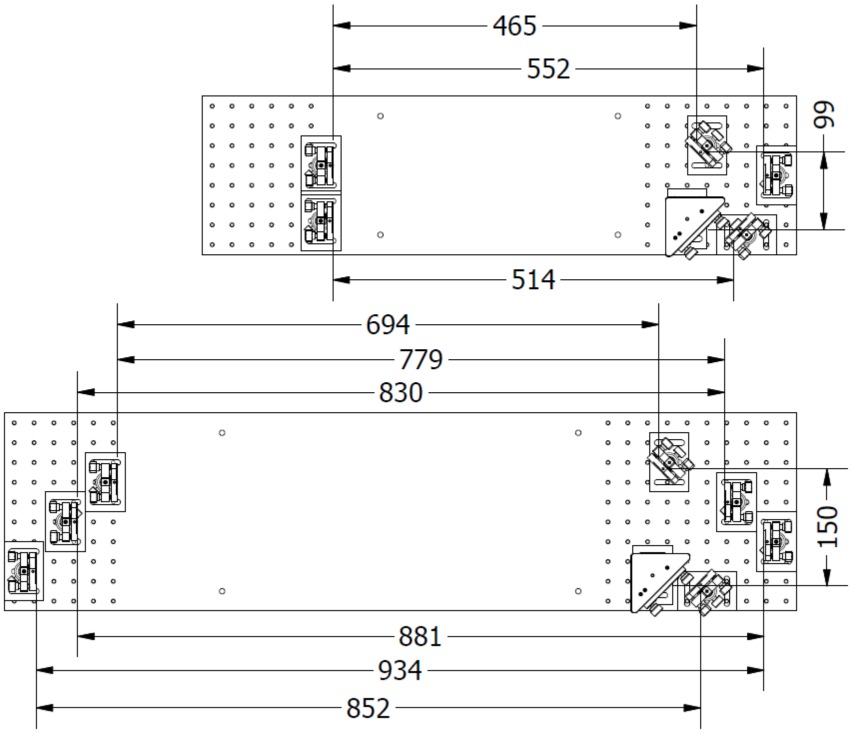

Figure 4.2: CAD drawing of pulse-stretcher. Units for the distance dimensions are millimeters.

The top plot in Fig. 4.3 shows the mean of 50 pulse profiles for the final stretcher design with the extremes denoted by the grey region. The profile shows a similar smooth shape to that in Ref. 3, due to the cavities having delays similar to the 2:1 ratio used in that study. However, the cavity lengths used in this work are slightly longer than suggested in [100] to provide a greater degree of pulse stretching. Further details on the selection of cavity lengths are given in Appendix D. The lower plot in Fig. 4.3 shows a computed pulse profile based on a 6 ns temporally-Gaussian pulse traveling through the same cavity geometry. The computed profile is similar to the measured pulse in overall pulse duration, although the computed profile does show more pronounced individual peaks from each cavity. Thus, while the top plot does not provide an absolute measure of peak laser power, it can be approximated to be less than 30 MW when compared with the peak power in the computed profile. The pulse stretcher had an energy throughput efficiency of approximately 80%. Thus, the area under the curve of the stretched pulse should be 80% of that of the original output of the laser. Using this information, the reduction in peak power due to temporal stretching was 83%.

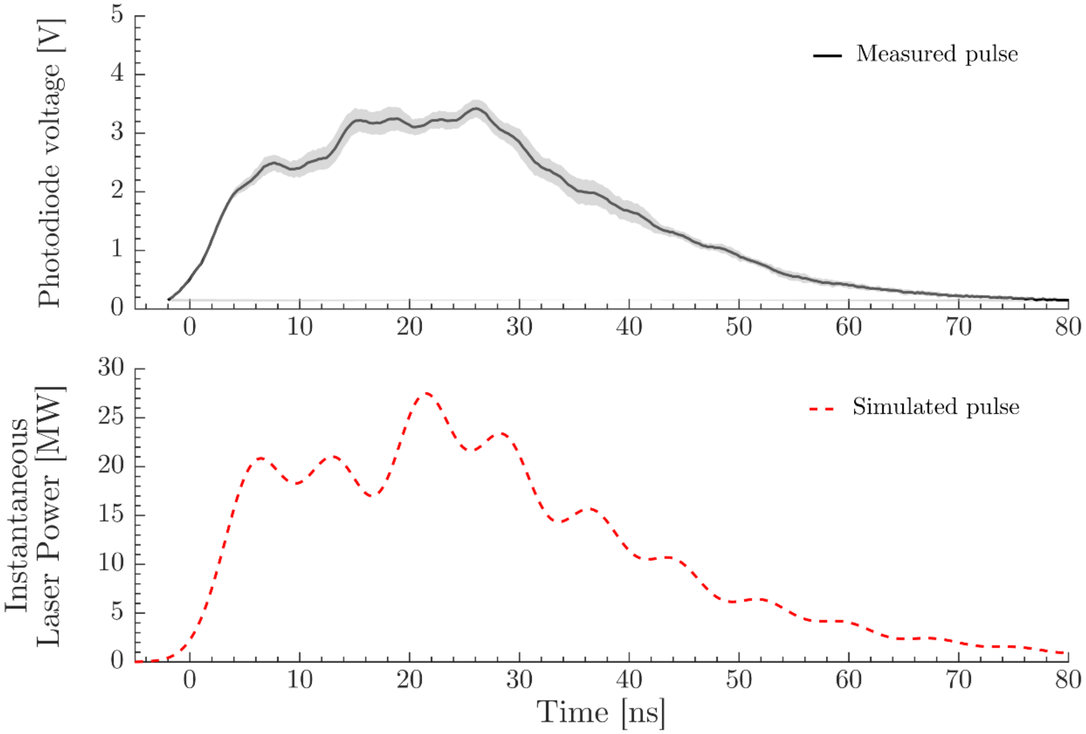

Figure 4.3: Temporal beam profile for the stretched laser pulse showing the envelope of pulse-to-pulse fluctuations in comparison with a calculated pulse profile.

4.1.1.2 – Multiple-Pass Cell

The multiple-pass cell was constructed from a pair of identical 400 mm diameter spherical mirrors with a 400 mm radius of curvature. By placing these mirrors slightly further than 4 focal lengths apart and carefully aligning the input beam, the laser passes through a pair of focal spots repeatedly. The location of incidence on the mirror surfaces traverses the mirrors vertically in a line until the beam reaches the opposite edge of the mirror and exits the cell. The cell mirrors were coated with a high reflectivity coating (Spectrum Thin Films) which was designed to provide not only a high efficiency at the laser wavelength but also a high laser-induced damage threshold in order to handle the high laser fluence without sustaining damage. One mirror had a radial slot machined into it to allow the laser beam to enter the cell. A CAD rendering of the multiple-pass cell is presented in Fig. 4.4. A detailed description of the design of the multiple-pass cell is given in Appendix D.

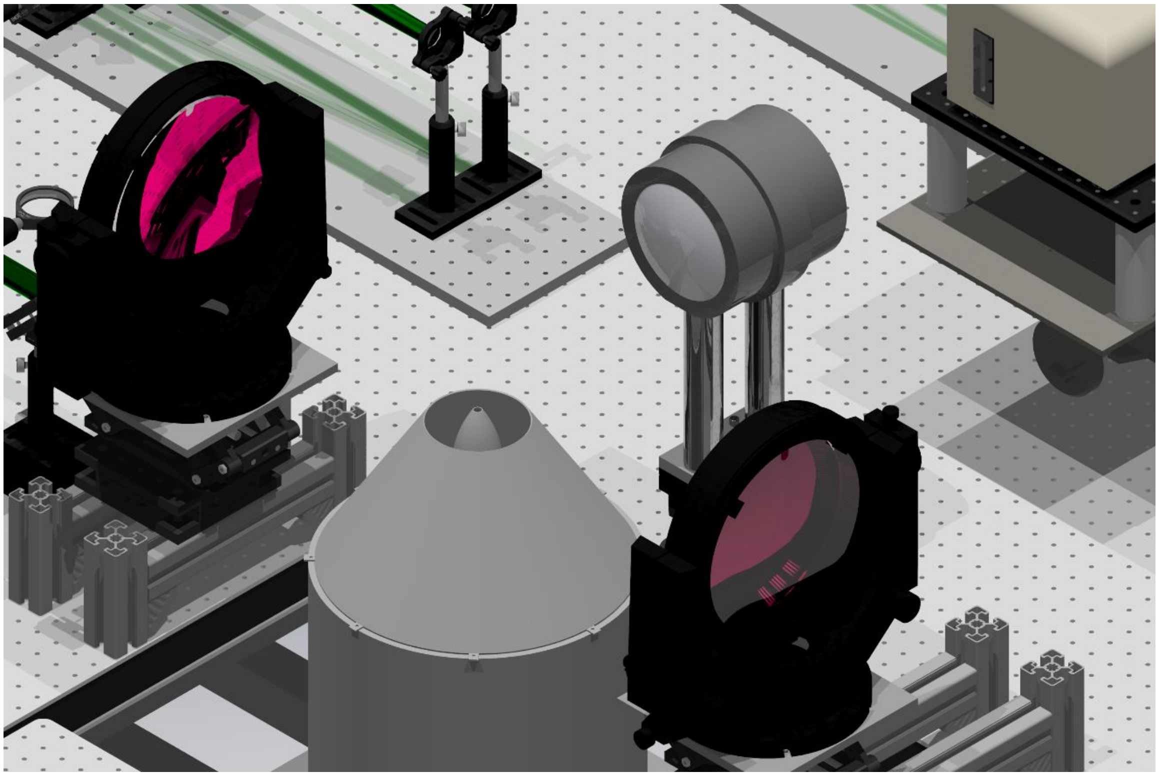

Figure 4.4: CAD image of cell geometry with jet apparatus and collection optics in place. The cell mirrors are the items with the pink color.

In practice, laser-induced breakdown was observed intermittently at much lower laser pulse energy than was predicted by the preliminary calculations for laser-induced air breakdown. Figure 4.5 shows a set images of the Rayleigh scattering from the multiple-pass cell focal spots. The bright spots shown in Fig. 4.5 show weak sparks being induced in the fan of beams within the multiple-pass cell. These sparks tended to occur away from the focal regions of the multiple-pass cell where the beams overlap. In the calm coflow, approximately 17 laser passes through the cell can be counted in the images.

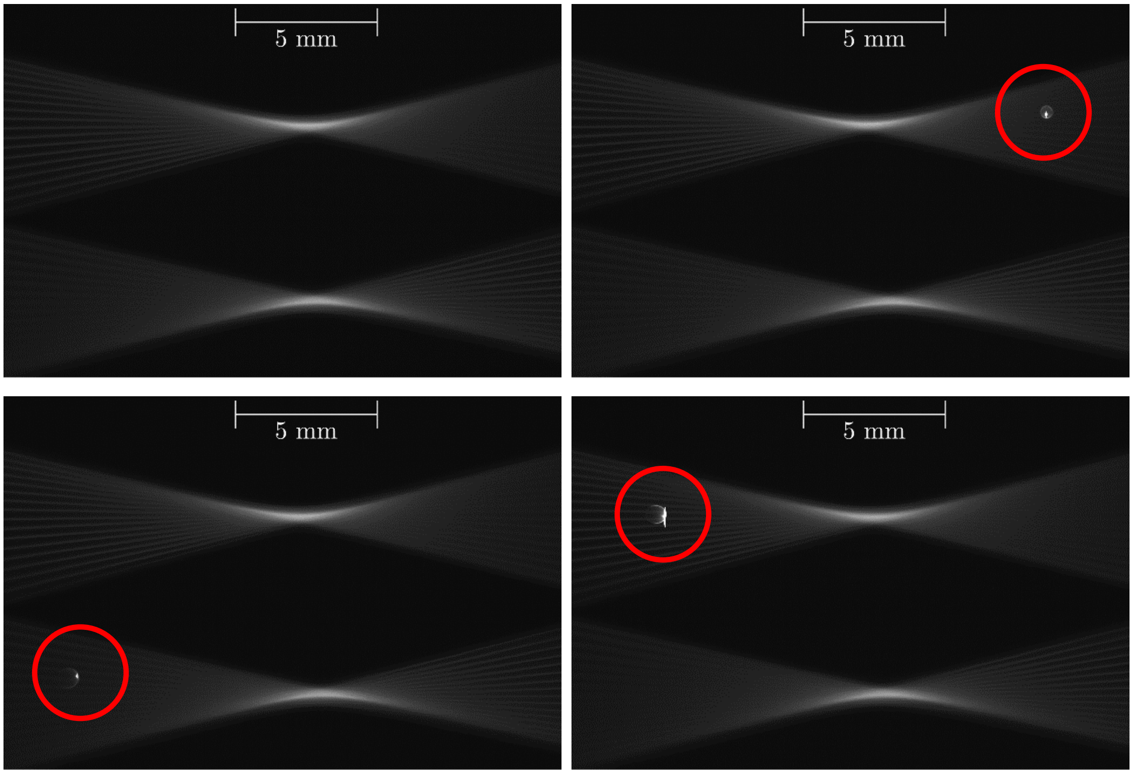

Figure 4.5: Images of laser spark events in room temperature coflow with spark events circled in red.

As the input energy is increased, the intermittently-present weak sparks of Fig. 4.5 become intense sparks, which are present for a much higher percentage of laser shots. Figure 4.6 shows images of the same physical region when the laser energy is increased to approximately 300 mJ and a spark occurs on every laser pulse. A neutral density filter was placed in front of the camera to prevent oversaturating the sensor and causing damage, and thus the Rayleigh scattering from the multiple-pass cell beams is no longer visible. Sparks appear to occur just upstream of both of the cell focal spots and never in the region where the beams overlap most. What makes these spark events different from the spark events at lower energy is that the spots tend to occur at the same location every time, whereas the low energy spots occur at random locations.

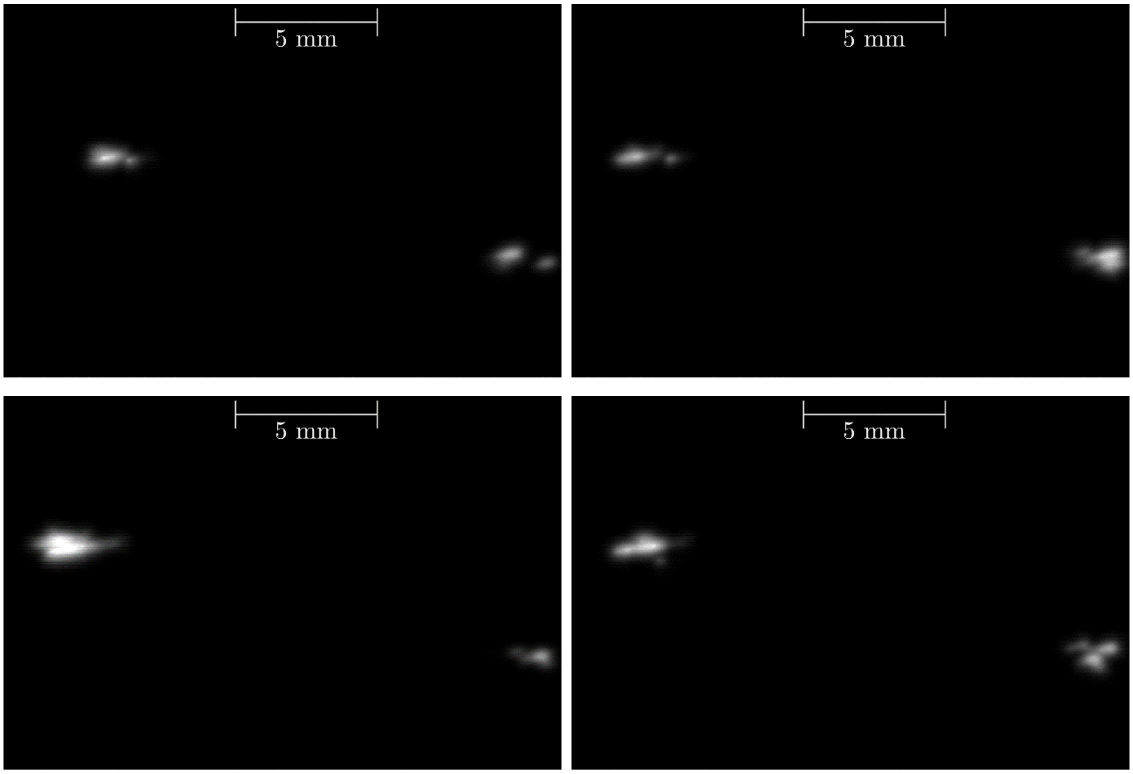

Figure 4.6: Images of laser spark events at higher input energy.

Dust is most likely the main culprit for these sparks, as the bright spots in Figs. 4.5 and 4.6 occur away from the cell focal regions where the beams overlap. However, the fact that at high enough input energy the beam induced a spark for every laser shot is evidence that air breakdown is occurring at higher pulse energy. Leaving the coflow blower operating at all times to maintain a flow through in the chamber and prevent dust from settling in the coflow chamber did noticeably increase the laser pulse energy at which breakdown occurred. Also, the frequency of breakdown events decreased dramatically as coflow temperature was increased. Increasing temperature would not be expected to have much effect on the presence of dust, as that is mostly determined by how well the upstream HEPA filter does its job. However, the reduction in gas density was expected to increase the air breakdown threshold significantly [98]. It is likely that both processes are responsible for the observed laser-induced sparks, with only dust being a factor at low energy and air breakdown causing the sparks at higher pulse energy. Therefore, the energy that was used to make measurements in the jet flame was chosen such that it was low enough that a consistent spark (from air breakdown) did not occur and only rare intermittent sparks from small dust particles occurred.

Typically, the laser pulse energy entering the multiple-pass cell was between 270 and 300 mJ for all single-shot measurements. In the rare events where a spark did occur during a measurement due to dust, the spectra were thrown out as the broadband luminescence from the spark interfered significantly with the Raman signal. Additionally, the turbulent fluctuations and large density gradients present in the jet shear layer required the cell spots to be moved slightly farther apart to keep the spots at a stable position. This reduced the number of passes to about 13 to 15, and so the cumulative energy in the probe volume was about 4 J.

The focal spots were typically separated by 4-6 mm for all of the single-shot measurements. As discussed in Appendix D, this distance between spots was the result of a tradeoff between maximizing the number of passes in the cell and maintaining cell stability. The cell mirrors were mounted on precision translation elements that allowed for fine adjustment in 5 degrees of freedom (3 axes of translation and rotation about 2 axes). The specifics of the mirror locating components are described in Appendix D. In practice, cell had to be realigned each day after the facility had reached and maintained a stable operating temperature for at least 30 minutes. This was needed to ensure precise location of the beam above the nozzle and a stable cell. Beam location relative to the facility was measured by an additional camera.

4.1.1.3 – Collection and Detector

In order to maximize collection efficiency, the 150 mm diameter f/2.2 achromat lens pair was used as in the time-average reacting flow studies. These lenses have a high f-number to collect from a large scattering solid angle. Their large size is required to maintain a large working distance (230 mm) to keep the optics a safe distance from the hot coflow. The only change in the collection system from the arrangement in Section 3.2 was that the camera no longer needed to be shifted on the spectrograph because the laser now matches the 532 nm design wavelength of the grating.

4.1.2 – Experimental Facility

No changes were made to the jet facility between the time-average and single-shot measurements in order to allow a direct comparison between results. The coflow heaters were set to provide 1000 K air, as in Section 3.2. The two jet mixtures were the H_2/N_2 and H_2/CH_4 mixtures described in Table 3.3.

4.2 – RESULTS AND DISCUSSION

This section details the results of applying the single-shot Stokes Raman scattering technique to the jet in coflow facility. Results from this new technique are compared with the time-averaged results presented in Ch. 3. Agreement between single-shot measurements and the previous time-average results will assuage any remaining doubt about the validity of using the time-averaged technique in this turbulent flow. Additionally, due to the detailed information that is available in the high signal-to-noise time-averaged measurements, temperature results are considered to have high precision.

The single-shot data, on the other hand, provide measurements that do not have the same level of signal fidelity, but do not require a secondary temperature measurement in order to quantify the bias error induced by temporal averaging. Taken together, agreement between these measurements demonstrates the self-consistency of the two Raman scattering techniques.

Figures 4.7 through 4.9 show a sampling of the spectra obtained with the single-shot Raman scattering technique in various regimes of the jet flame. These spectra show traits similar to those from the time-average measurements, albeit with a reduction in signal-to-noise ratio. The coflow and jet spectra (Figs. 4.7 and 4.8, respectively) show fairly clean Q-branch lines that are captured well by the fitting routine. The reduction in gas density for the flame spectrum (Fig. 4.9) is evident in the reduced signal-to-noise ratio in the hot band. In all 3 spectra, the O- and S-branches are practically indistinguishable from the noise. However, both rotational and vibrational temperatures inferred from fits to this spectrum are reasonable. This result, which may seem surprising, will be discussed further in Sections 4.2.3 and 4.2.4. In comparison with the time-averaged spectra, the fundamental band was broadened by the use of a wider slit in the spectrograph.

When post-processing the results, spectra were removed for laser shots where breakdown occurred and interfered with the Raman signal. The criterion for removal of spectra was whether the background signal in the image rose above 4% of the Raman signal. This threshold was selected by comparing the set of eliminated spectra for different threshold values with the set of manually-identified spark events on a set of equilibrium hot spectra. The threshold needed to be low enough to remove spectra with the weakest level of breakdown that altered the fit results while not throwing out valid spectra.

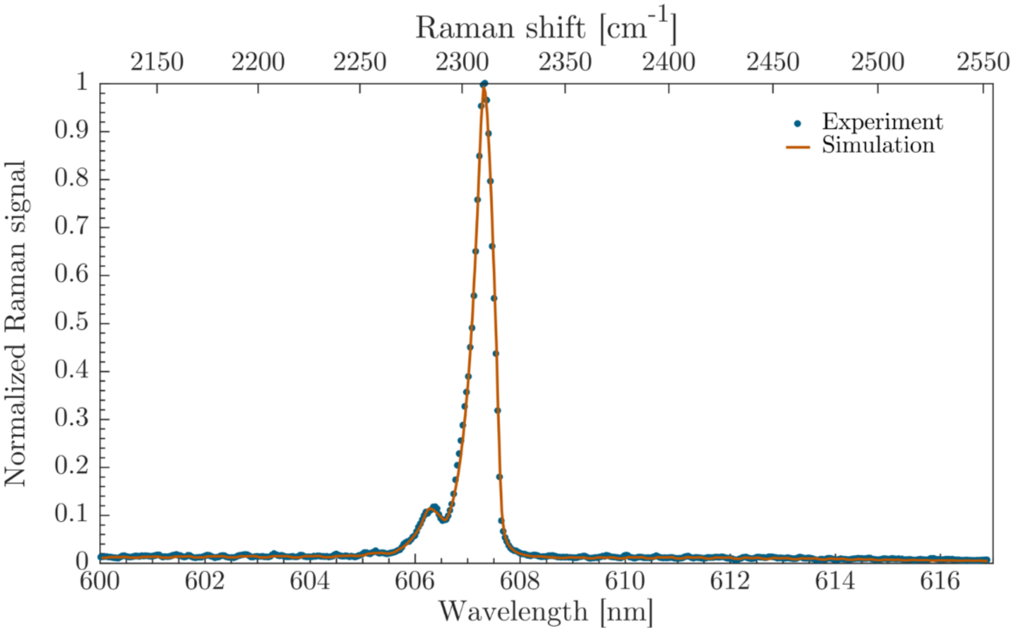

Figure 4.7: Sample single-shot spectrum in the hot coflow. Fitting this spectrum gave a vibrational temperature of 1046 K and a rotational temperature of 1044 K.

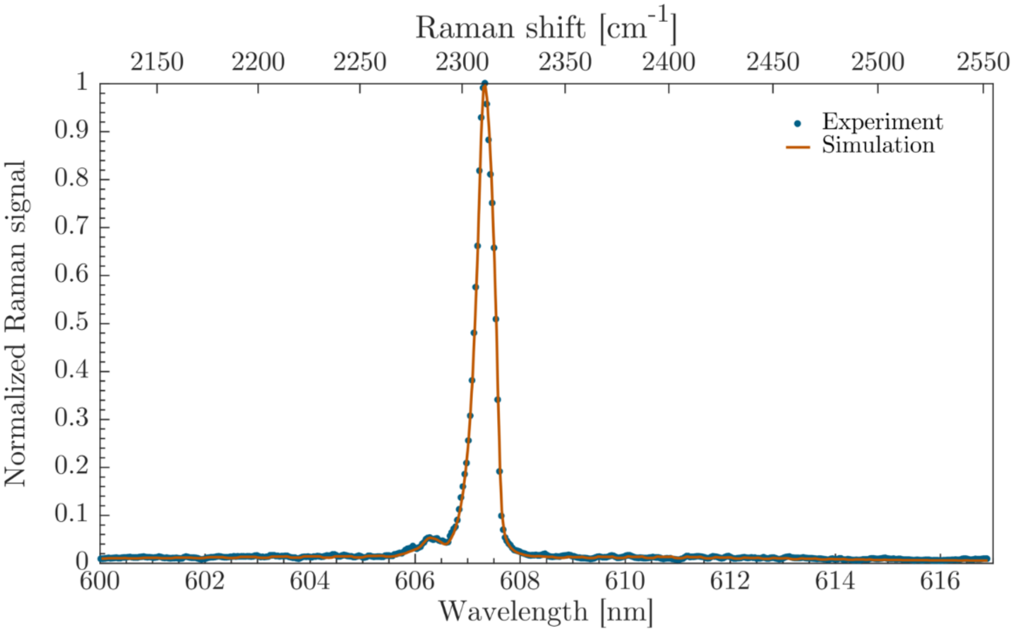

Figure 4.8: Sample single-shot spectrum in the jet shear layer. Fitting this spectrum gave a vibrational temperature of 826 K and a rotational temperature of 706 K.

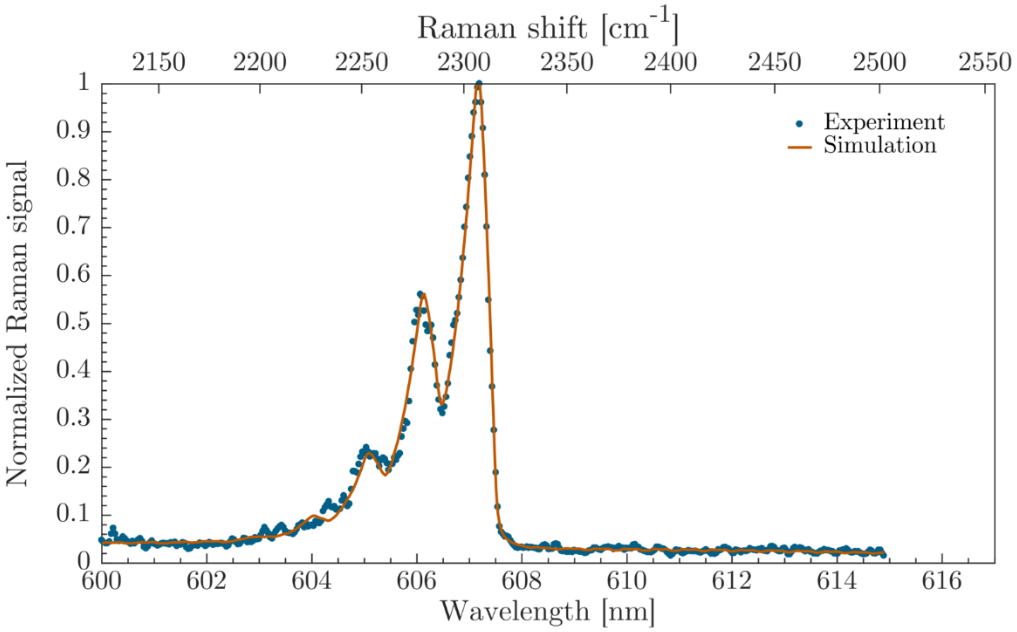

Figure 4.9: Sample single-shot spectrum in the H_2/N_2 jet flame. Fitting this spectrum gave a vibrational temperature of 2085 K and a rotational temperature of 2038 K.

Temperature measurements derived from single-shot spectra are compared with time-average results in the mixing region upstream of the flame base in Section 4.2.1. Scatter plots of temperature in the intermittent flame region were also investigated in Section 4.2.2. Section 4.2.3 discusses where the important rotational information is located spectrally and also explores the implications of cropping out regions of the spectra. Finally, the spatial resolution and measurement precision of the single-shot measurements are analyzed in Section 4.2.4.

4.2.1 - Comparisons with Time Averaged Results

To confirm the overall accuracy of the single-shot technique, radial temperature profiles were measured at the same downstream distances as time-averaged measurements presented in Ch. 3. These comparisons not only indicate the accuracy of the single-shot measurements, but also corroborate the results of Ch. 3. Because this new technique makes an effectively instantaneous temperature measurement, it also lends credence to the conclusion of Ch. 3 that the non-equilibrium observed with time-averaged Raman measurements is not an artifact of the time-averaging.

Fig. 4.10 below shows a comparison of temperatures derived from single-shot and time-averaged N_2 Stokes Raman scattering 16 mm downstream of the jet exit. Both rotational and vibrational temperature values agree well overall between the two techniques despite the fact that the single-shot measurements were made many months later. The bars on the time-average measurements represent a 95% confidence interval based on the statistical scatter from a few measurements, while on the single-shot measurements they are comprised of approximately 50 spectra per location.

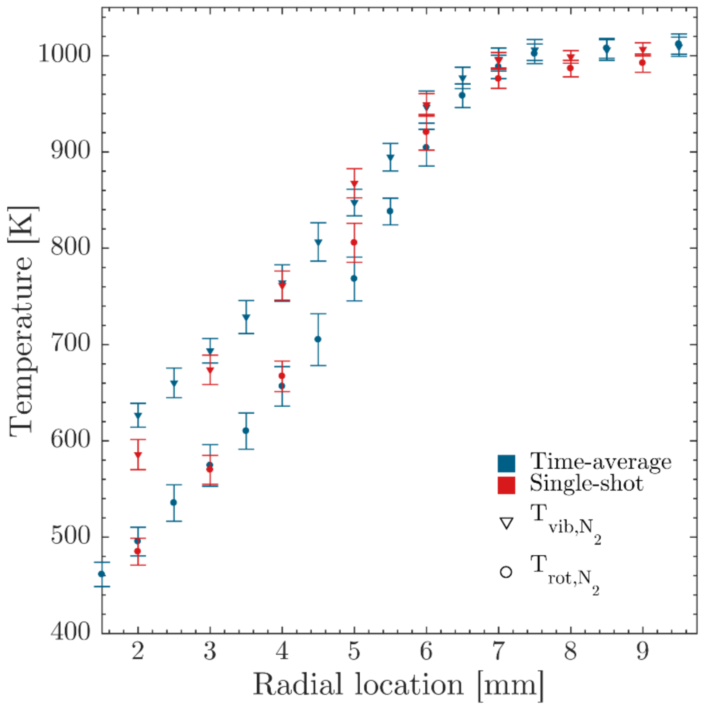

Figure 4.10: Comparison of single-shot radial profile with time-averaged measurements 2 jet exit diameters downstream for H_2/N_2 case. Color of data points indicate measurement technique. Symbol designates vibrational or rotational or rotational temperature.

Similarly, results for the single-shot and time-average techniques 32 mm downstream of the nozzle exit are presented in Fig. 4.11. The time-averaged data shown in this plot is the same as in Fig. 3.19. Again the single-shot measurements agree quite well with the time-averaged results. It does appear that the total jet width differs slightly between the two techniques, but this is most likely due to the measurements not being made a precisely the same downstream distance.

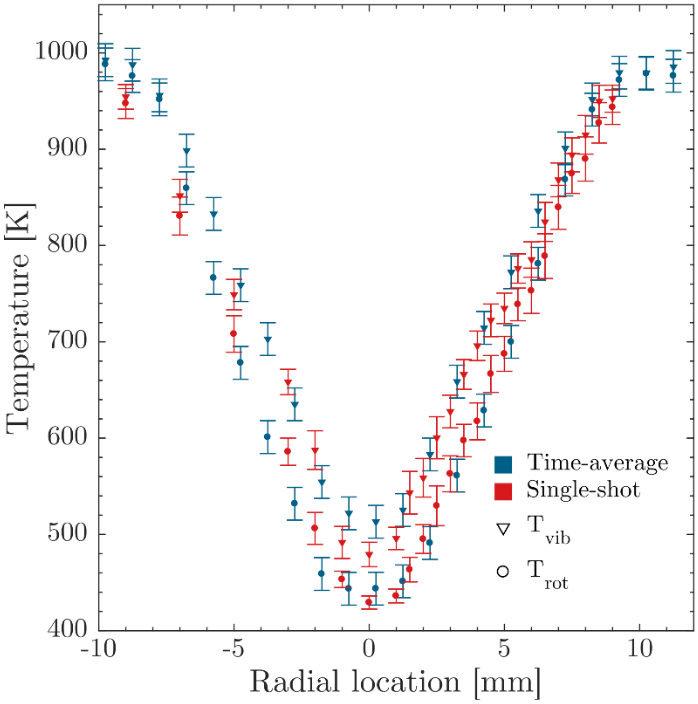

Figure 4.11: Comparison of radial profiles from single-shot and time-averaged measurements 4 jet exit diameters downstream for H_2/N_2 case.

Unfortunately, the jet core temperature at this condition is too low for reliable fitting of a vibrational temperature. In time-averaged measurements, it was determined that the lower limit for accurate fitting of vibrational temperature was around 450 K. In a similar fashion, spectra from equilibrium air were collected over a range of temperatures as the facility cooled down. Fits to the spectra should show identical rotational and vibrational temperatures down to a temperature at which vibrational temperature fitting is no longer accurate.

Figure 4.12 illustrates the lower limit on vibrational temperature fitting. Fifty spectra were collected for each data point and the scatter defining a 95% confidence interval in fitted rotational and vibrational temperatures is shown as error bars in both directions. Because the multiple-pass cell is aligned for the facility at operating temperature, these spectra must be collected quickly as the facility cools down. There is an approximately 2 minute window after the time coflow heaters are turned off before the facility shifts enough to move the multiple-pass cell out of focus.

The precision uncertainty reduces as the temperature decreases owing to higher gas density producing more Raman scattering signal. The measurements stay close to the equilibrium line down to approximately 600 K, where the vibrational temperature begins to show an artificially high value. Thus, 600 K can be assumed to be the lower limit for accurate vibrational temperature measurements with the current technique. Below 600 K, the population in excited vibrational states is 0.36%, and thus detection of a hot band is extremely difficult for the fitting code. The reason this temperature limit higher for single-shot rather than for time-averaged measurements is most likely the loss of spectral resolution with the widened slit and the overall reduction in signal-to-noise in the spectra.

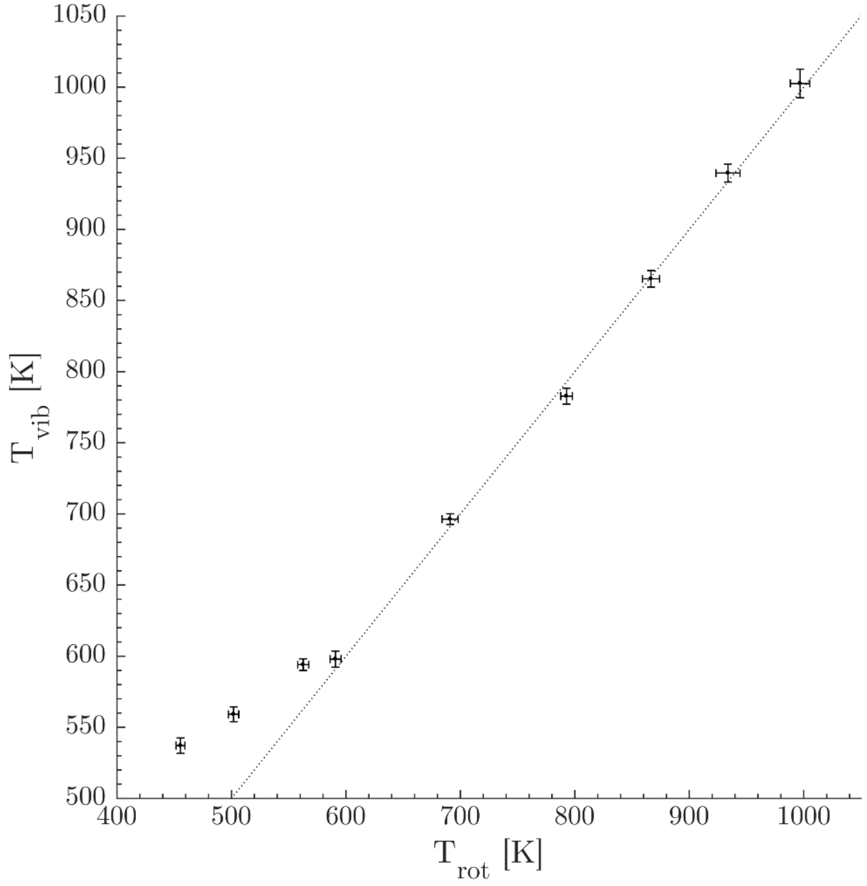

Figure 4.12: Fit results of equilibrium hot air spectra of varying temperature. Error bars illustrated the precision uncertainty from a set of 50 spectra at the same heater setting.

This limiting temperature cannot be reduced by increasing the jet temperature because a large temperature difference between jet and coflow is required in order to induce non-equilibrium. Because the maximum coflow temperature is limited to 1000 K, as described in Ch. 2, increasing the jet temperature will also reduce the temperature difference between the two streams. As the difference in temperature between the coflow and jet is reduced, the amount of induced non-equilibrium in the mixing layer will also diminish. Temperature profiles with varying jet stagnation temperatures were measured in order to illustrate this effect. Fig. 4.13 shows temperature profiles for increased jet temperatures. As expected, the observed (artificial) non-equilibrium at the jet centerline disappears as the jet temperature is increased. However, these cases also show a reduced non-equilibrium in the jet shear layer. This weak non-equilibrium brings the two temperatures to within the measurement scatter of one another. Thus, as in the time-averaged measurements, the jet was operated at the lower temperature setting and measurements of vibrational temperature at the jet centerline should be disregarded.

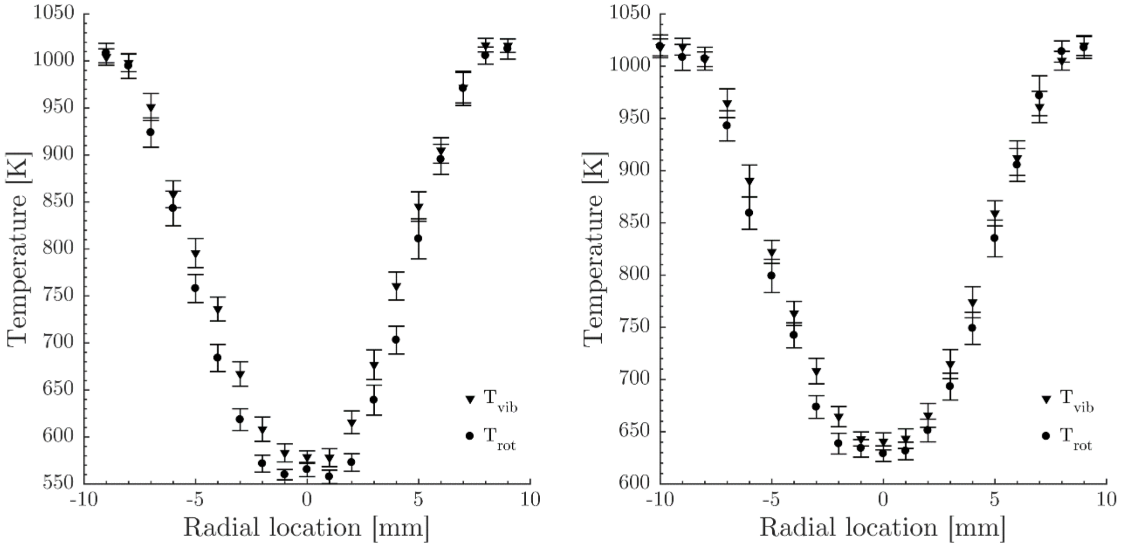

Figure 4.13: Radial temperature profiles at 2 diameters downstream of nozzle exit. Left – jet heaters set to 300 °C. Right – jet heaters set to 400 °C.

4.2.2 – Single-Shot Results at Flame Base

The single-shot technique also provides the ability to make measurements in highly fluctuating regions of the flow. These measurements freeze the flow temporally, at the cost of having poorer spatial resolution than time-averaged measurements. One region of the flow where this is especially useful is near the base of the lifted flame.

Because of the intermittency of the flame location, the plots can no longer be represented by a single point at each location with the scatter indicated by error bars. Instead, the results are presented as scatter plots of rotational and vibrational temperature.

Figure 4.14 shows a scatter plot of vibrational and rotational temperature for several radial locations at a downstream distance where the flame is seldom present. Each point represents one measurement. Error bars are omitted in these plots to avoid clutter with the large number of points being shown. An assessment of the precision uncertainty in these measurements will be presented in Section 4.2. Measurement precision clearly decreases at high temperatures as the points are clustered less tightly. This loss of precision is due to the loss in signal at higher temperatures as a result of the reduction in gas number density.

The cluster of points at the bottom-left of the plot shows the temperature behavior in the upstream unreacted jet. The scattering of high temperature points indicates instances when the flame had jumped upstream enough that post-flame gases were present at the measurement location. The outermost location shows equilibrium gas at the coflow temperature of 1000 K and no evidence of flame products. The flame was present most often in the locations 9 – 12 mm from the jet centerline. The slight reduction in temperature of the lower cluster of points at these locations indicates that this is just at the outer edge of the jet. Moving further inward, the fraction of points that exhibit elevated temperatures due to combustion rapidly declines. At these inner points, the cluster of points moves away from the equilibrium line, indicating that vibrational non-equilibrium is present in the mean.

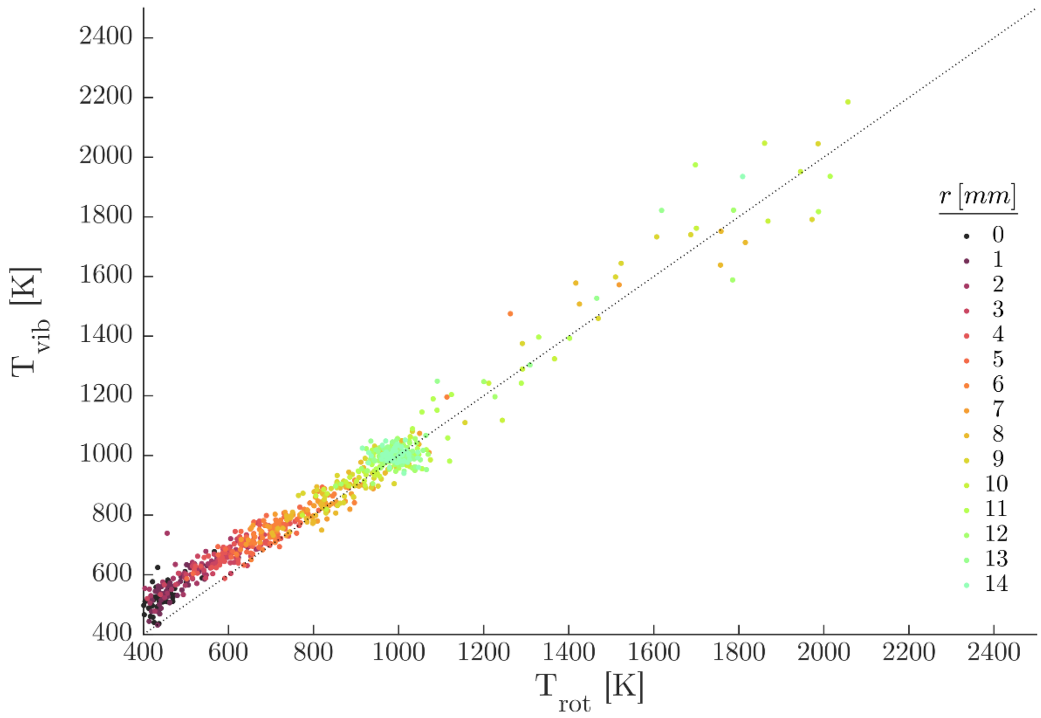

Figure 4.14: Scatter plot of temperature 45 mm downstream at different radial distances. 50 laser shots per location.

To further investigate the near-flame region, Figure. 4.15 shows individual plots of 500 laser shots for selected radial locations at a similar downstream distance as in Fig. 4.14 (slightly further downstream due to facility shifting). In these plots it is clear that the flame sits on the outermost edge of the jet, as the number of high-temperature points decreases continually from Fig. 4.15a to 4.15e. This agrees with what was observed in the Rayleigh scattering images of Ch. 3 and also with the fact that the stoichiometric mixture fraction is very low for this fuel mixture. Additionally, one can clearly see the clear trend in temperature for the unreacted data points as the cold cluster of points at the lower left of the plots shifts toward colder temperatures as the measurement location moves toward the jet centerline.

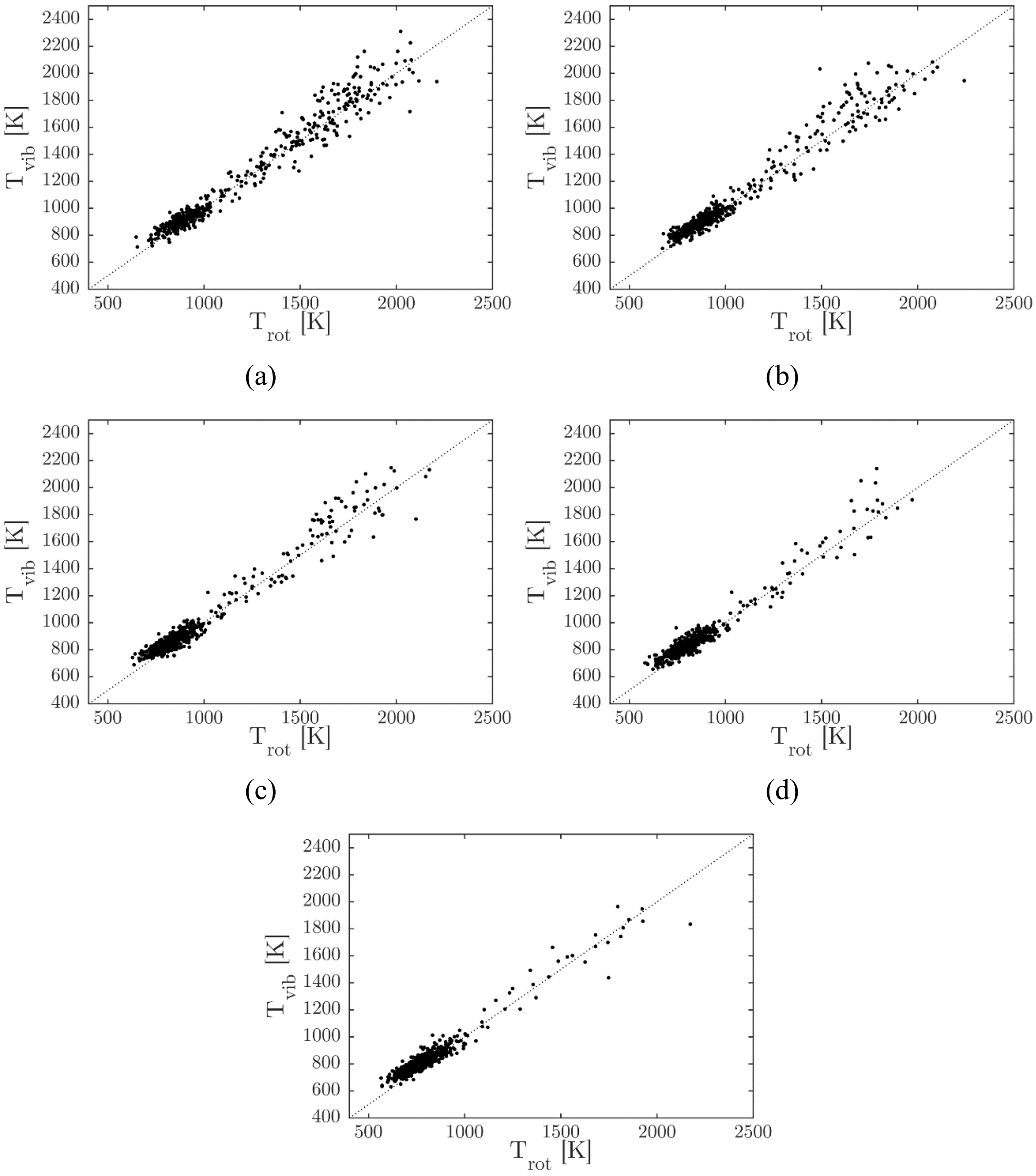

(a)

(b)

(c)

(d)

(e)

Figure 4.15: Scatter plots of temperature 46.5 mm downstream at a radial distance of (a) 9 mm, (b) 8.5 mm, (c) 8 mm, (d) 7.5 mm, and (d) 7 mm from the jet centerline. 500 laser shots per plot.

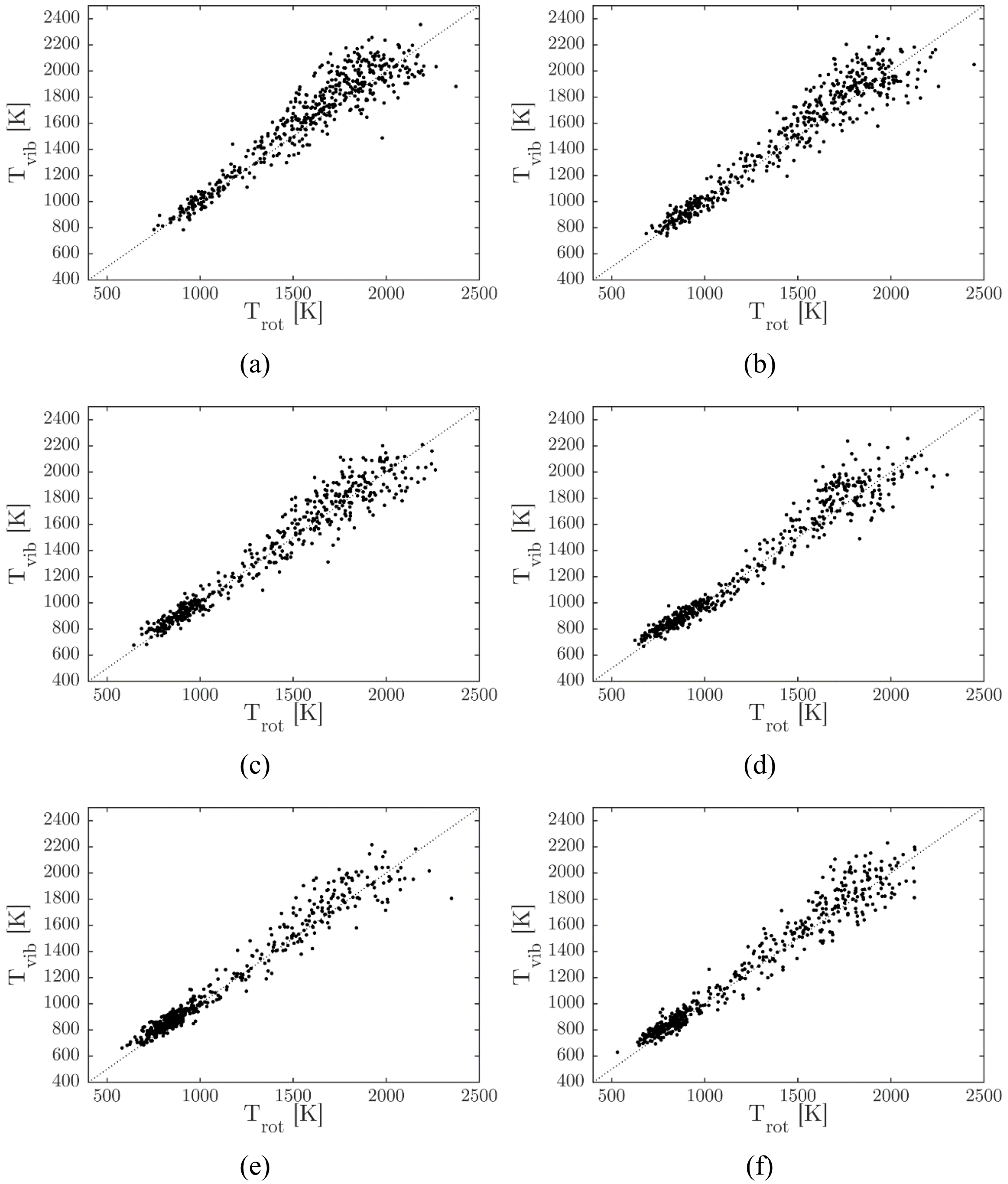

(a) (b)

(c) (d)

(e) (f)

Figure 4.16: : Scatter plots of temperature 52 mm downstream at a radial distance of (a) 10 mm, (b) 9.5 mm, (c) 9 mm, (d) 8.5 mm, (e) 8 mm, (f) 7.5 mm, and (d) 7 mm from the jet centerline. 500 laser shots per plot.

Figure 4.16 shows a farther-downstream location where the flame is present more often. Here again we can see that the flame is present most often at the outer edges of the jet profile, as the fraction of high temperature data points decreases as the measurements move radially inward. At this downstream distance flame products are present more often than unreacted at the outermost location (r = 10 mm). This figure also illustrates the overall reduction in measurement precision as the gas density decreases, as the points become more scattered at high temperature.

Both Figure 4.15 and 4.16 illustrate that the flame base is most often present at the outer edge of the jet profile where the velocity is low; however, this region is not likely associated with strong non-equilibrium since non-equilibrium is mostly produced in regions of high velocity and high shear. Therefore, the non-equilibrium in this flow may not be exerting a large effect on the flame ignition or stabilization.

It is very difficult to generate a flame in this facility that does stabilize in a region where non-equilibrium is produced. This is because adjusting the fuel mixture to have a higher stoichiometric mixture fraction necessitates a reduction in the H_2 content and, therefore, produces a flame which is much more lifted and unstable. To bring this new flame to a reasonable lift-off height, either the jet velocity must be reduced or the jet temperature increased. Each of these changes reduces the strength of the already weak non-equilibrium. An alternative method for generating vibrational non-equilibrium for study of the effects on the macroscopic combustion process is suggested in Section 4.4.

The cloud of reacted data points appears to have its centroid located on the equilibrium line, or shifted slightly to the side of elevated vibrational temperature. These points were expected to lie around the equilibrium line as fully-reacted gas is expected to be in vibrational equilibrium due to the presence of water vapor in the combustion products. The mismatch between vibrational and rotation temperature for individual points in this region likely stems from low signal-to-noise ratio or spatial averaging effects. The precision of these measurements is discussed further in Section 4.2.4.2.

Similarly, the single-shot technique was applied to the H_2/CH_4 jet flame. Figure 4.17 shows scatter plots of temperature near the flame base at different radial locations. As with the H_2/N_2 measurements, the flame is present in a larger share of laser shots as the measurement moves toward the jet. Measurements in this flame were more difficult, as keeping the cell stable required a reduction in the number of passes through the system. This is most likely due to the nature of the shear layer for this jet. Also adding to the difficulty in these measurements, as mentioned in Ch. 3, the lack of N_2 in the jet composition meant that the Raman scattering signal fell off quickly as the measurement location moved toward the jet centerline. The temperature values are gathered around the equilibrium line at all locations, indicating that this flow may not have a measureable amount of non-equilibrium at this downstream distance. Since the shear layer upstream of this location was found to have only a very weak non-equilibrium (Fig 3.21), it would seem logical that the non-equilibrium further downstream is negligible.

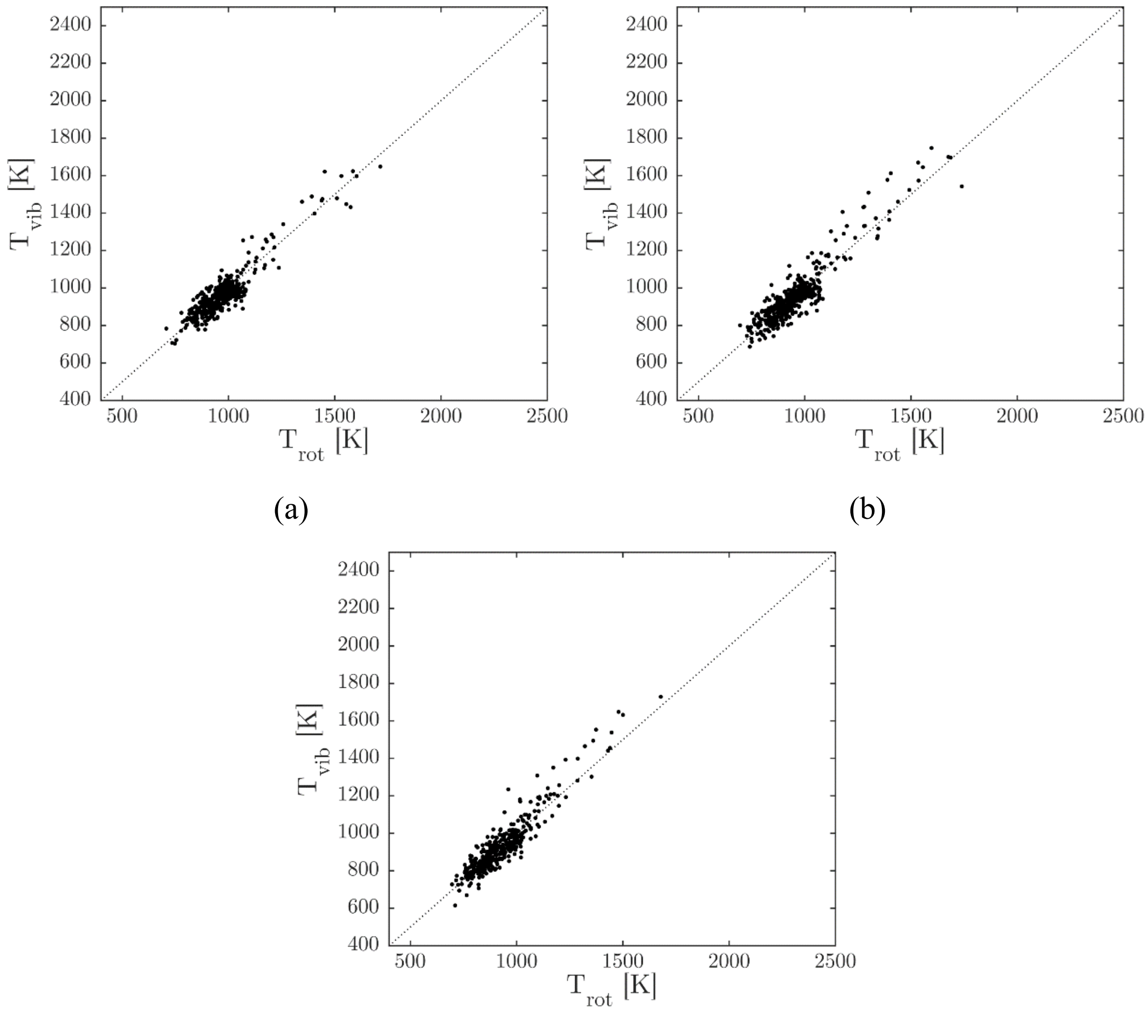

(a) (b)

(c)

Figure 4.17: Scatter plots of temperature at the base of the H_2/CH_4 flame 50 mm downstream of the nozzle exit. (a) 13 mm from jet centerline, (a) 12.5 mm from jet centerline, and (c) 12 mm from jet centerline

4.2.3 – Identifying Spectral Extent of Useful Data

The O- and S-branch regions in the sample single-shot spectra shown in Fig. 4.7 through 4.9 do not appear to have much signal that is discernable from the noise. Therefore, it is somewhat surprising that the measured rotational temperatures from the single-shot technique agree so well with time-average measurements. While the O- and

S-branches are commonly referred to as “rotational” lines, rotational information is not exclusive to these lines. The Q-branch is composed of a large number of closely spaced rotational lines as well. With the lack of detailed information in the outer regions of the O and S branches of the single-shot spectra, the most influential data may be located within the Q-branch. A quantitative analysis of the necessary spectral coverage will aid in the selection of dispersion optics and sensor size for future applications of this Raman scattering technique. Additionally, the computational cost of the fitting routine can be reduced by narrowing the spectral coverage as the cropped spectra require significantly less time to fit due to the reduced number of points that the fitting code is trying to minimize error on.

Figures 4.18 and 4.19 show the effect of cropping the shear layer spectra to different spectral ranges on the fitted vibrational and rotational temperatures. The change in fitted temperature for the cropped spectra is computed in reference to fit results for the same spectra over the entire 600 – 617 nm range. The vibrational temperature results show a stronger dependence on the cropping than the rotational temperature values, which is most likely due to the fitting code not being able to establish an accurate baseline with too few points on either side of the Q-branch. This difficulty in fitting is not as important as we know that vibrational information is contained in the Q-branch and any change in fitted vibrational temperature from cropping out the O and S branches is an artifact of the fitting routine. As discussed in Section 4.2.1, measurements of vibrational temperatures below 600 K are not reliable using this technique, which is confirmed in these plots, as the temperature values show significant scatter even for a trivial amount of spectral cropping in Fig. 4.18a.

The plots show that most rotational information is located between 604 and 610 nm as the rotational results show little change until the spectra are cropped to a smaller range than that. Thus, the measurement only requires rotational information contained within the Q-branch and in the O and S branch signal from the lowest rotational levels.

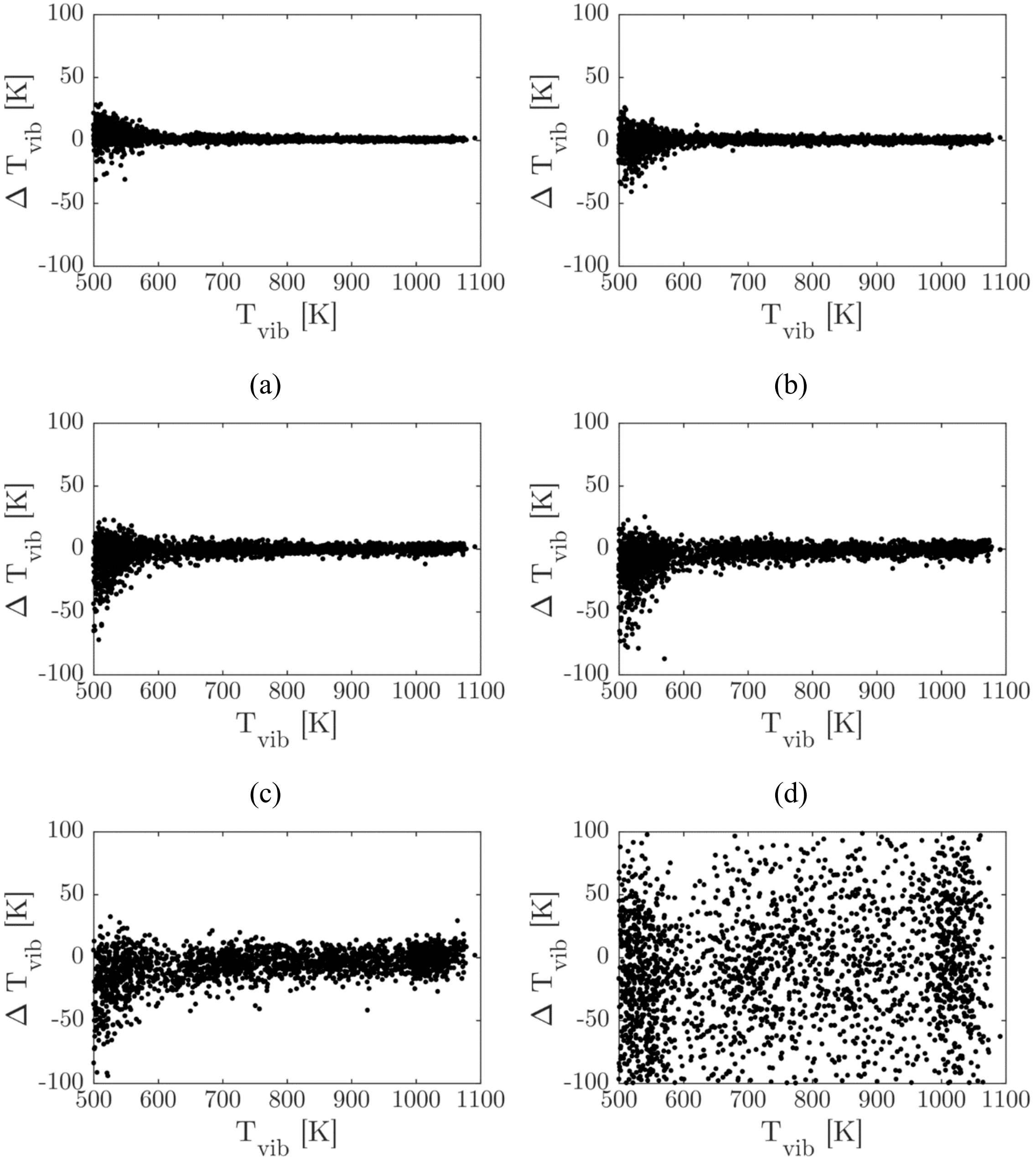

(a) (b)

(c) (d)

(e) (f)

Figure 4.18: Change in fitted vibrational temperature with different spectral cropping: (a) 601-613 nm, (b) 602-612 nm, (c) 603-611 nm, (d) 604-610 nm, (e) 605-609 nm, and (f) 606-608 nm.

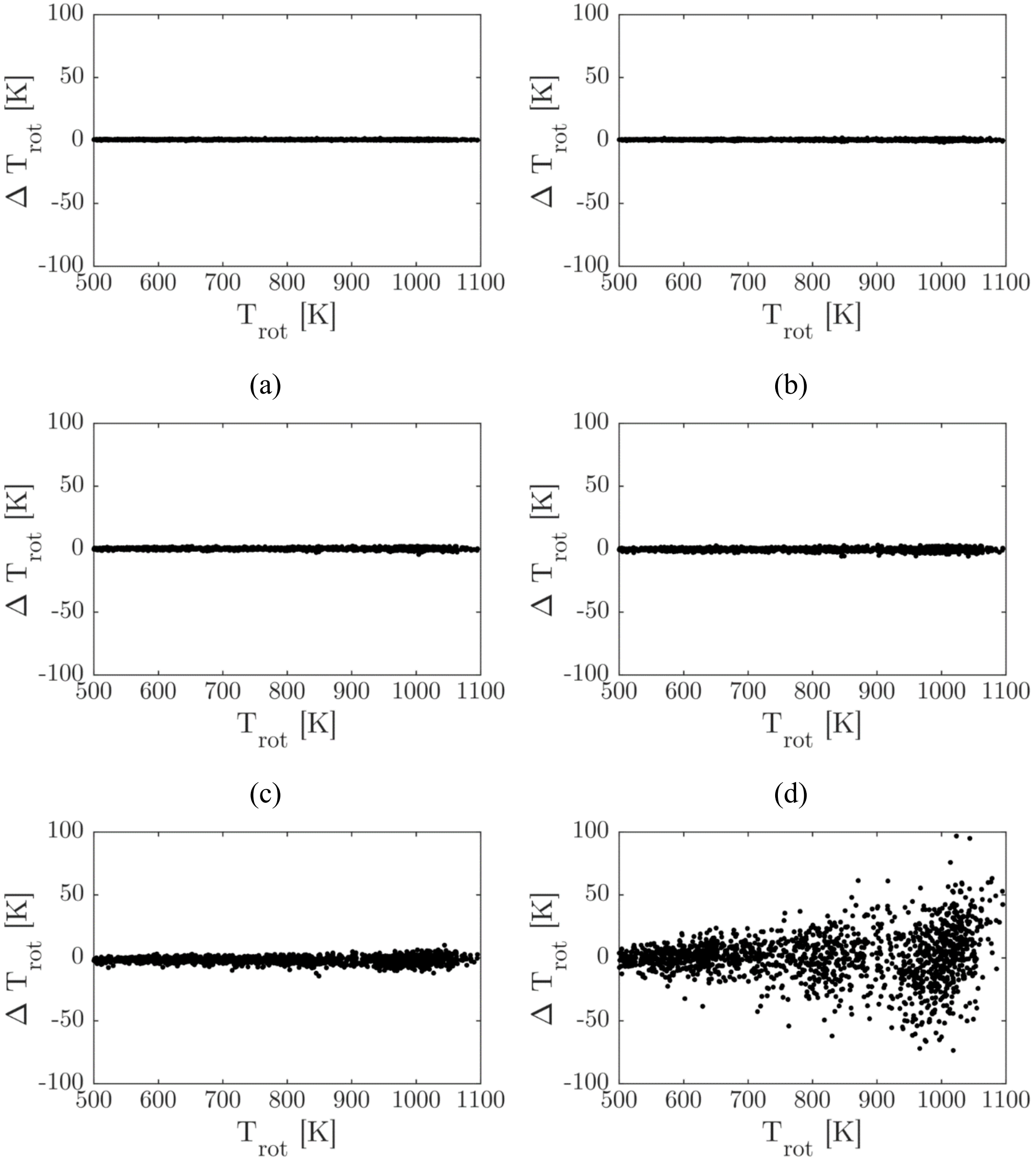

(a)

(b)

(c)

(d)

(e)

(f)

Figure 4.19: Change in fitted rotational temperature with different spectral cropping: (a) 601-613 nm, (b) 602-612 nm, (c) 603-611 nm, (d) 604-610 nm, (e) 605-609 nm, and (f) 606-608 nm.

All of these results except for the most extreme cropping case are compiled onto a single plot that shows the moving RMS of the temperature deviation in Fig. 4.20. As seen in Fig. 4.18, vibrational temperatures below 600 K are unreliable regardless of the level of spectral cropping. As discussed, the trend in vibrational temperature precision is due to the lack of a baseline for the fitting code as no vibrational information is removed by cropping to these spectral regions. In the rotational temperatures, almost no change is seen when cropping the spectra to 602 – 612 nm and the largest incremental loss in precision is from cropping the spectra to 605-609 nm, indicating that some useful rotational information is lost in the 604 – 605 and 609 – 610 nm regions.

Figure 4.21 presents the results for spectra near the flame base in the same fashion as in Fig. 4.20. Here the precision decreases dramatically in cropped spectra for temperatures higher than 1000 K. Additionally, there no longer is a significant difference between the levels of scatter in the vibrational and rotational temperatures. This is most likely due to the corresponding shift to higher energy states with the increase in temperature. For example, at 800 K the most-populated rotational state of N_2 is $J = 11$, while at 2200 K the peak population moves out to $J = 19$. The corresponding lines for these higher-lying rotational states are shifted further from the center of the peak of the Q-branch fundamental band. Thus, any amount of spectral cropping significantly affects the fit results, as necessary information is removed.

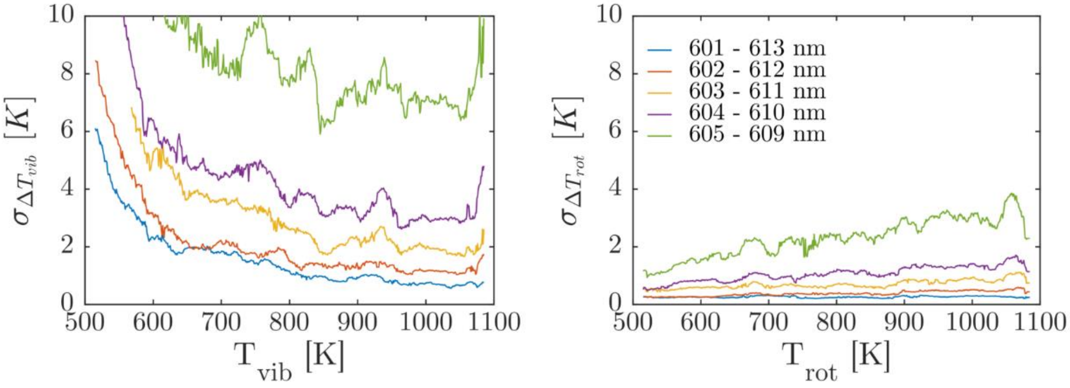

(a) (b)

Figure 4.20: Moving RMS of deviation between cropped and uncropped results for shear layer spectra for (a) vibrational and (b) rotational temperature.

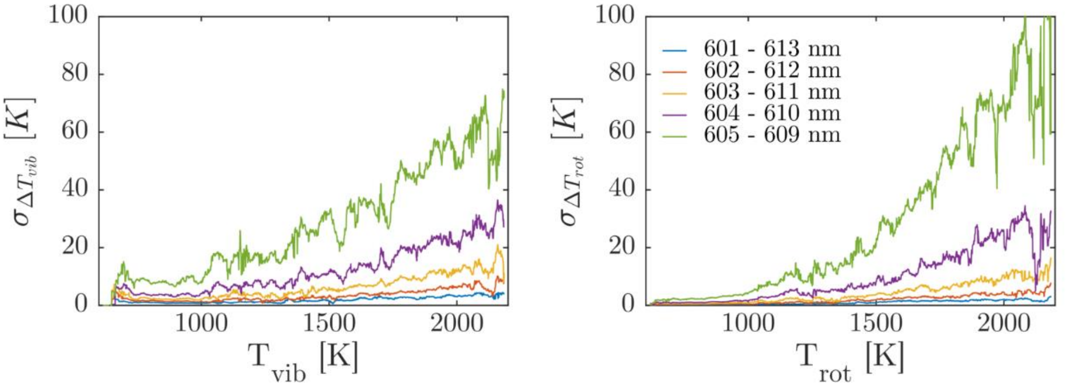

(a) (b)

Figure 4.21: Moving RMS of deviation between cropped and uncropped results for spectra at the flame base for (a) vibrational and (b) rotational temperature.

While the outer regions of the O- and S- branch do not appear to contain much useful signal above the noise, cropping the outer regions in these spectra did alter the measurement precision. Moderate amounts of cropping made only slight changes to the rotational temperature results, indicating that the most useful rotational information is contained on top of and near the fundamental band of the Q-branch. Cropping too much information led to an unexpected loss in vibrational temperature precision, although this is likely an artifact caused by the fitting code, rather than a loss of vibrational information.

4.2.4 – Single-Shot Measurement Uncertainty

4.2.4.1 – Spatial resolution

The necessary signal increase obtained with the use of the multiple-pass cell and widened slit come at a cost in spatial resolution. Figure 4.22 shows a coordinate axis system which will be used to aid the discussion of the spatial extent of the measurements, where the X axis is aligned with the centerline of the collection optics, the Y axis is oriented in the vertical direction, and Z axis aligns with the axis of the multiple-pass cell mirrors. The physical region being probed is set by the quality of beam overlap in the Y and Z directions and is set to a fixed position in the Z direction by the field of view of the spectrograph. The slit width used for these measurements was 250 μm. With the magnification of the collection optics, the resolution in this direction becomes 350 μm. The resolution in the other two directions will vary depending on how the multiple-pass cell is aligned and between individual laser shots.

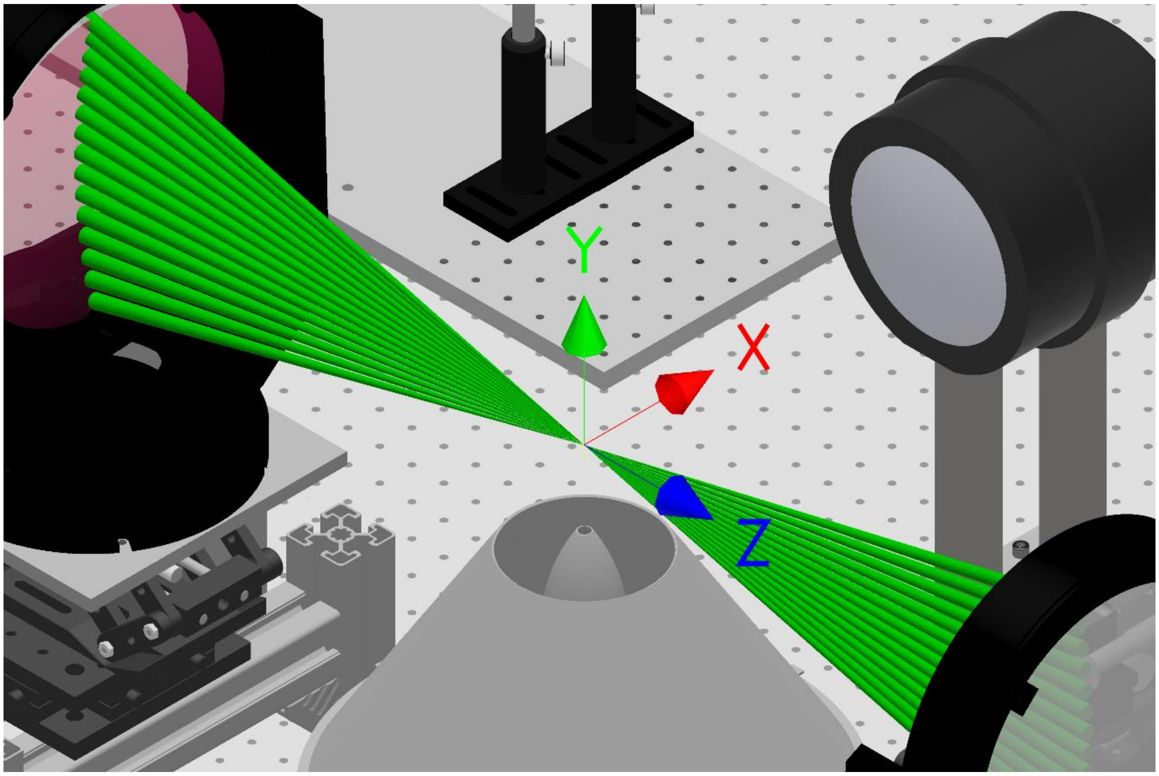

Figure 4.22: Coordinate system used to define the spatial extent of the single-shot measurements.

Images of the cell focal region were captured to observe the spot behavior during jet operation and also to make measurements of the spatial extent of the probe volume. These images were captured with a CCD camera (PCO 1400) and a 105mm f/2.8 lens with a laser line filter installed in front of the lens to protect the sensor from damage in the event of a bright spark event. Figure 4.23 shows a set of images taken with this camera. The shape in the background is the entrance to the spectrograph, which is on the opposite side of the jet facility.

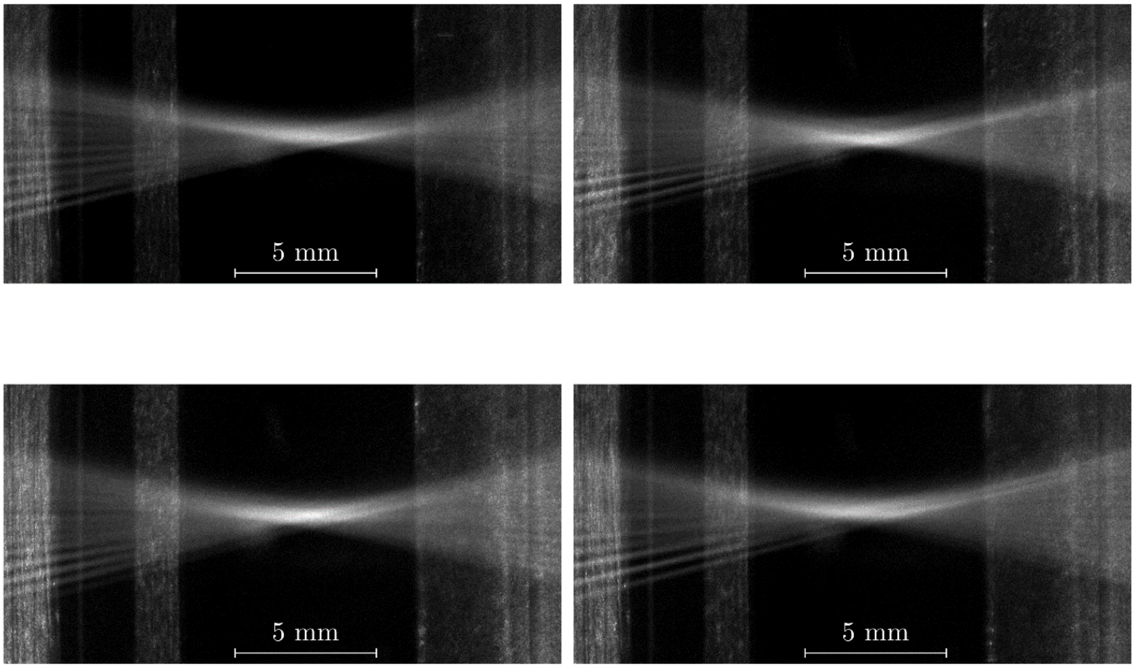

Figure 4.23: Sample images of multiple-pass cell top focal region.

From these images, the extent of the measurement volume in the vertical (downstream) direction can be assessed. Figure 4.24 shows distributions of the full width at half maximum spatial extent of the laser overlap region in the vertical direction. These are presented as cumulative distributions to illustrate the probability that the spatial extent of the measurement is smaller than a given size. As is clear in the plots, the single-shot measurements in the shear layer upstream of the flame have a similar size in the vertical direction as the time-average measurements, with 95% of realizations having a downstream extent less than 0.8 mm. This is due to the laser used in the time-averaged measurements having a poor beam quality ($M^2 \approx 25$) when compared to that of the laser used for single-shot measurements ($M^2 \approx 1$). The spatial extent of the measurements did increase for measurements in the flame, as the cumulative probability crossed the 95%

level at 1.4 mm for these locations. This increase in the focal spot is due to the stronger index of refraction gradients present in the flow downstream of the flame that induce stronger beam-steering effects.

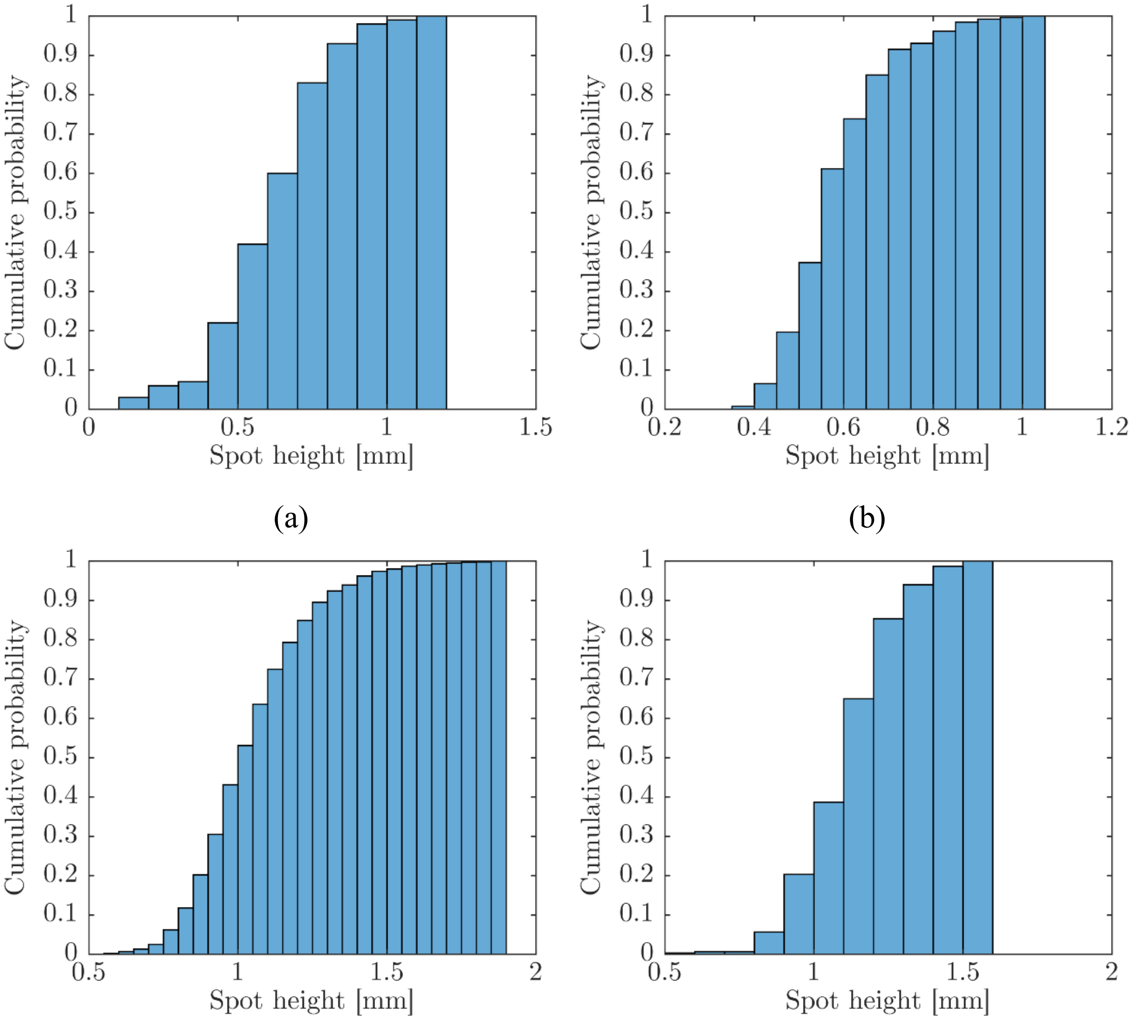

(a) (b)

(c) (d)

Figure 4.24: Cumulative distribution of multiple-pass cell spot height for measurements made (a) 2 diameters downstream in the H_2/N_2 jet shear layer (shown in Fig. 4.7), (b) 4 jet diameters downstream in the H_2/N_2 jet shear layer (shown in Fig 4.8), (c) 6 diameters downstream in the H_2/CH_4 flame (shown in Fig. 4.15), and (d) 6.5 diameters downstream in the H_2/N_2 jet flame (shown in Fig. 4.14).

In the case of the time-averaged measurements, the measurement volume was stable and the shot-to-shot variation was negligible. However, due to the use of the multiple-pass cell, the spot was able to fluctuate somewhat in downstream location in the single-shot measurements. As discussed in Appendix D, the separation of the multiple-pass cell focal spots depends on the angle and height at which the beam enters the cell. The movement of these spots relative to one another produces the movement

Figure 4.25 shows the probability distribution for the location of the spot centroid relative to the nozzle exit for four different measurement cases that were presented in Sections 4.2.1 and 4.2.2. The deviation in downstream location of the measurement region was fairly small relative to the spatial resolution, showing an RMS deviation in measurement downstream location of less than 500 μm for all locations. As each laser shot is an independent measurement, this deviation does not affect the spatial resolution as it would in a time-averaged measurement. Thus, this fluctuation is an uncertainty on the exact downstream measurement location only.

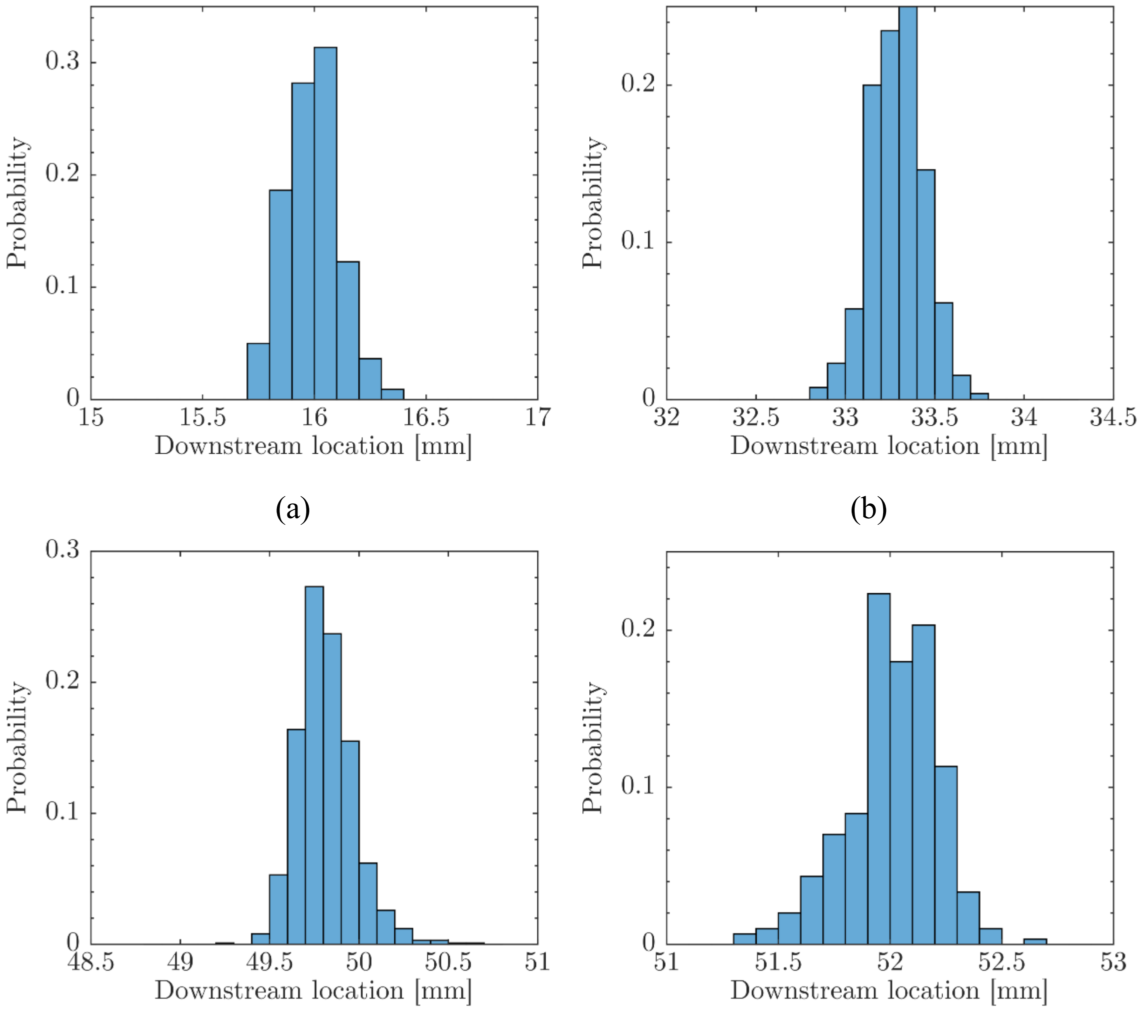

(a) (b)

(c) (d)

Figure 4.25: Probability distribution of spot center downstream location for measurements made (a) 2 diameters downstream in the H_2/N_2 jet shear layer (shown in Fig. 4.7), (b) 4 jet diameters downstream in the H_2/N_2 jet shear layer (shown in Fig 4.8), (c) 6 diameters downstream in the H_2/CH_4 flame (shown in Fig. 4.15), and (d) 6.5 diameters downstream in the H_2/N_2 jet flame (shown in Fig. 4.14).

The region probed by this measurement in the X direction is not as easily quantified. Images were captured from a high overhead view in order to look downward on the cell focal region and assess the out-of-plane extent of the beam. Unfortunately, this was not successful, as it was impossible to find a workable camera position that acquired adequate Rayleigh scattering signal from the focal spots. The camera must be placed high overhead in order to have a downward view of the focal spot that does not also include some of the beam fan in the background. In order to get this downward view and remain far enough from the coflow to avoid heat damage, the camera was placed approximately 5 feet above the nozzle exit. At this distance, the amount of Rayleigh scattering signal which reached the sensor was overwhelmed by the broadband glow of the hot coflow chamber. Additionally, the thermal gradients between the camera and multiple-pass cell focal region strongly distorted the images, making any quantitative assessment of beam size impossible.

However, we can rely on some observations about the cell in order to understand the spatial resolution in this direction. In particular, if the beam becomes offset in the X direction, the reflection spots will no longer walk vertically along the mirror surfaces, but instead to one side. This was not observed during any of the data collections. Thus, with the information at hand, the cell focal region was assumed to be limited by the quality of beam overlap, as it is in the vertical direction. The spatial resolution in the out-of-plane direction should be comparable to the distances shown in Fig. 4.24.

4.2.4.2 – Temperature measurement precision

Quantifying the measurement precision is challenging due to the lack of a secondary measurement able to quantify the vibrational and rotation temperatures as a comparison case. In these single-shot measurement, the dominant uncertainty source is the low signal-to-noise ratio, especially at higher temperatures. Because errors due to incorrect modeling are expected to be very slight [33], the residual between the measured and modeled spectra should give a good indication of the noise.

Figure 4.26 shows residuals between the observed and modeled spectra for different temperature regimes. Noise levels relative to the Q-branch fundamental band peak are higher in the high temperature spectra not only due to the overall reduction in gas density, but also due to population being shifted out of the *v*=0 state into higher vibrational states. These large sets of residuals provide a library of the typical range of noise experienced in each temperature regime.

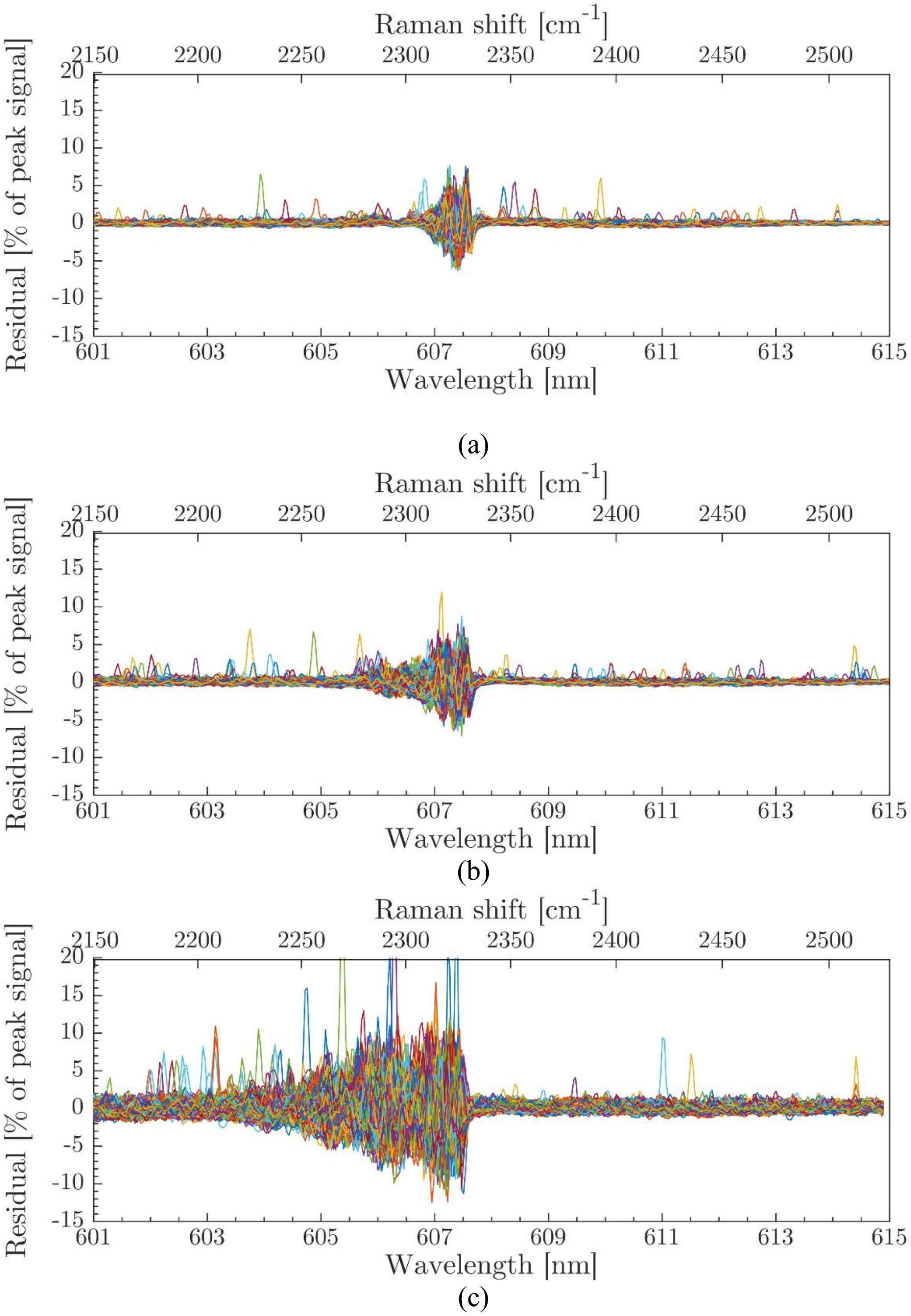

Figure 4.26: Sets of residuals for fitted temperatures between (a) 500-600 K, (b) 900-1100 K, and (c) 1800-2000 K.

Adding these residual profiles to a simulated Raman spectrum and then fitting those artificial spectra gives a measurement of the temperature uncertainty in the measurement due to noise. Fit residuals from spectra within a chosen range of temperatures are compiled into a library. These ranges were chosen to represent physically-different regimes in the flow. A single equilibrium noise-free Raman spectrum is then simulated at the mean temperature of the selected range and added to each of the residual profiles. Temperature results for re-fitting these constructed spectra are shown in Figs. 4.27 and 4.28.

Figure 4.27 shows histogram distributions of the rotational temperature values obtained from these fits. These temperature ranges represent 4 main regimes in the jet flow: jet fluid (Fig. 4.27a), mixing layer (Fig. 4.27b), coflow (Fig. 4.27c), and in the flame (Fig. 4.27d). The narrowest distribution is found in Fig. 4.27c, and most-likely results from the spectra within this range being at relatively the same temperature (around 1000 K). Samples in the 1000-1100 K are basically nonexistent in this flow as they would only be present at the very leading edge of the flame front or in a region where flame products have been heavily diluted by mixing with unreacted gas. These results are somewhat influenced by the width of temperature ranges selected. Collecting noise spectra from a larger range of temperatures does tend to show a somewhat widened distribution; however, the temperatures ranges need to be wide enough to encompass an adequate sampling of the noise profile. Thus, the ranges selected for this analysis were chosen as such to give more than 1000 residuals per plot and give a conservative estimate of the error induced by noise in the spectra.

Each of the distributions does show a slight bias error in that that mean of the resultant distribution is higher than the mean of the temperature range. In a totally unbiased result, each of these distributions should exhibit a mean value that matches the temperature of the noise-free simulated spectrum they were based on (550 K for Fig. 4.27a, 750 K for Fig. 4.27b, etc.).

Figure 4.28 similarly shows histogram distributions for vibrational temperature results. The coldest temperature range (500-600 K) exhibits a strong bias error, which is consistent with the discussion in Section 4.2.1 on vibrational temperature results in this regime. As with rotational temperature results, the narrowest distribution is observed in the coflow temperature range (Fig. 4.28c). At low temperatures, the distributions are broader than the corresponding rotational temperature distributions, and are most likely due to small amounts of noise near the hot band having a strong influence on the inferred v=0 population. As temperature increases, the vibrational results are grouped more tightly, most likely due to the emergence of the first hot band line ($v'=2 \leftarrow v''=1$) above the level of the random noise and the appearance of the second hot band line ($v'=3 \leftarrow v''=2$) at flame temperatures.

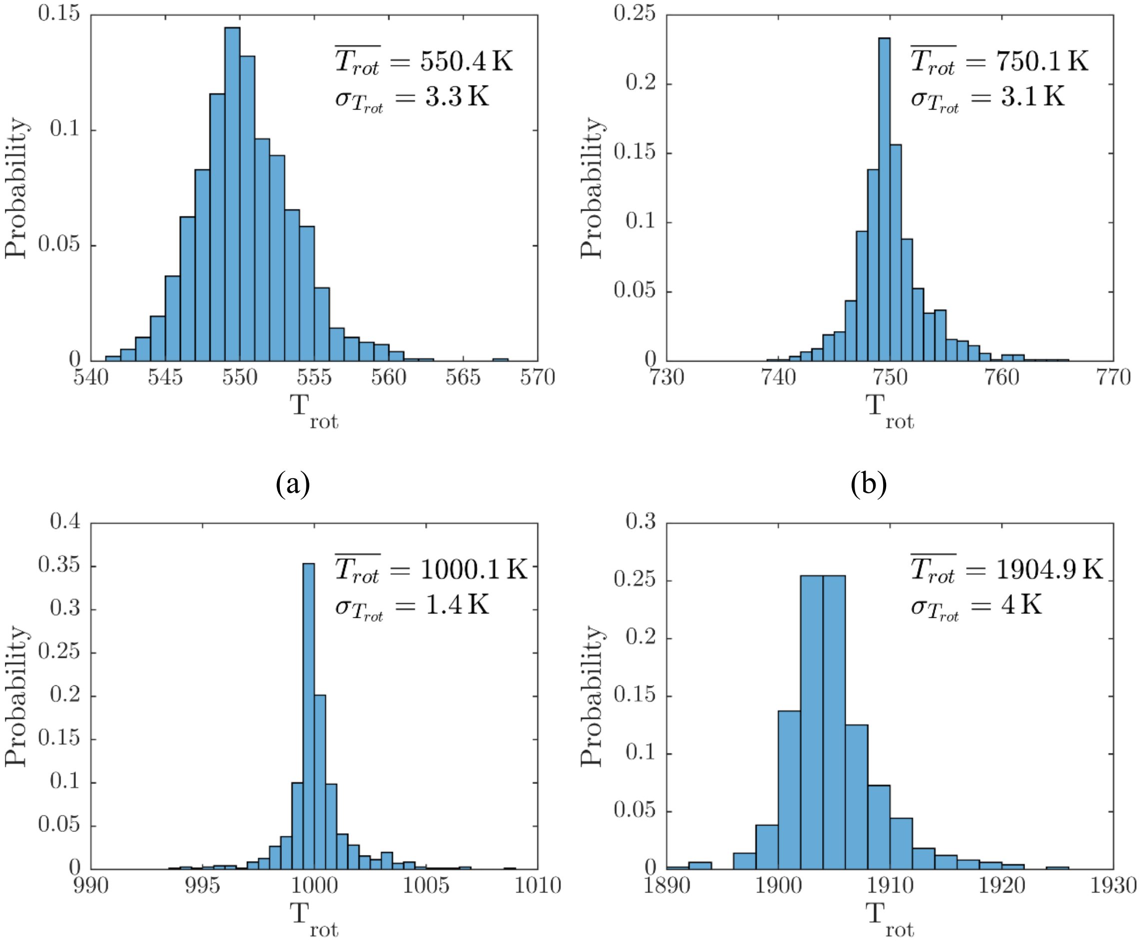

(a) (b)

(c) (d)

Figure 4.27: Histograms of fitted rotational temperatures using the noise signatures in 4 temperature ranges: (a) 500-600 K, (b) 600-900 K, (c) 900-1100 K, (d) 1800-2000 K.

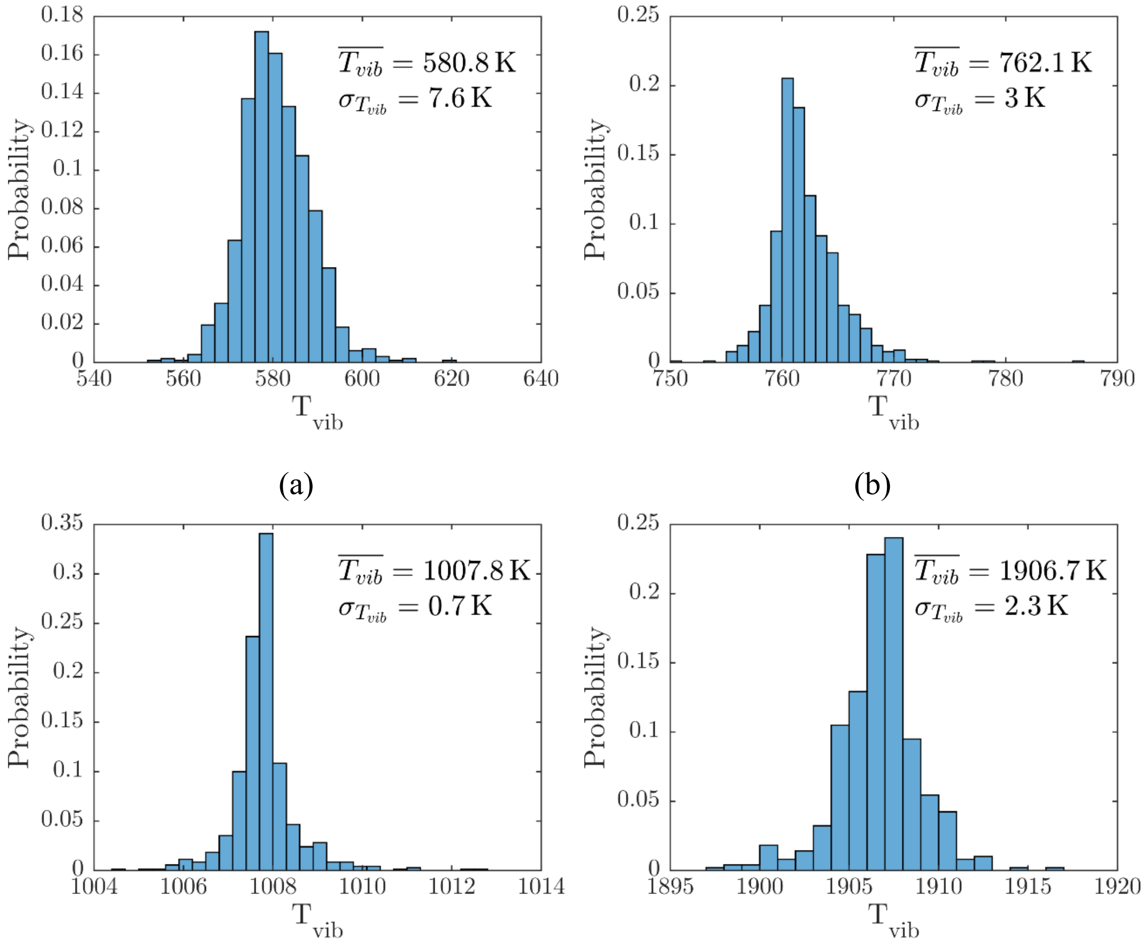

(a) (b)

(c) (d)

Figure 4.28: Histograms of fitted vibrational temperatures using the noise signatures in 4 temperature ranges: (a) 500-600 K, (b) 600-900 K, (c) 900-1100 K, (d) 1800-2000 K.

From this analysis, it would appear that the scatter seen in the results of Figs. 4.15 – 4.17 at flame temperatures is not simply due to noise in the spectra. It is unclear if this scatter arises from another source or gas in this region is truly in vibrational non-equilibrium. A possible source for this mismatch between vibrational and rotational temperatures could be an artifact of the somewhat large spatial extent of the measurement probe volume. Similar to the effect of time-averaging near the intermittent flame base, averaging over a spatial extent which contains both unreacted gas and at least some partially reacted gas. This type of sample which contains gas at various stages of reaction progress will contain a wide range of temperatures. As discussed in Section 3.1.2.1, measured temperatures for a composite equilibrium Raman spectrum from a sample with a broad distribution of temperatures shows a spurious non-equilibrium, the magnitude of which is dependent on the distribution width. However, the analysis presented in that section for normally-distributed temperature PDFs showed only a bias toward vibrational temperature values which exceed the rotational temperature, while the single-shot results showed both vibrationally-hot and vibrationally-cold data. The temperature PDFs within these flame-containing points are not likely to be normally-distributed, but instead show a bimodal behavior. Further work is needed to gather realistic temperature distributions for samples in this region in order quantify these spatial averaging effects. Other possibilities for future applications of this technique to more precisely assess the uncertainty at high temperature are presented in Section 4.4.

4.3 – CONCLUSIONS

In this chapter a two-temperature single-shot spontaneous Raman scattering measurement technique was introduced. The same Stokes scattering lines whose time-averaged measurements were reported in Ch. 3 were measured using a single laser pulse with the new apparatus. This apparatus consisted of a high-pulse energy, short-pulse width laser to provide the initial excitation energy, a set of pulse stretching cavities to reduce the peak laser power, and a multiple-pass cell to enhance the Raman signal. This improvement in temporal resolution (from 10-20 seconds to less than 200 ns) came at a cost in spatial resolution (from 0.5 × 0.5 × 0.14 mm to 0.8 × 0.8 × 0.35 mm). Results from this technique were validated by direct comparison with results from time-averaged Raman measurements.

This single-shot technique was shown to accurately quantify the vibrational non-equilibrium of N_2 in the mixing layer of the high-speed jet facility. The instantaneous nature of these measurements allowed for the technique to be applied in the region near the turbulent flame base, a region that was not amenable to time-averaged measurements. There, the intermittency of combustion intermediates and products at different radial locations was observed to peak at the outer edge of the jet profile, which agrees with the predicted behavior of this flame due to its low stoichiometric mixture fraction. Temperature measurement values near flame temperatures also showed reasonable results, albeit at a reduced precision due to the corresponding decline in signal at high temperature. This measurement was shown to have only a slight penalty in spatial resolution relative to the time-averaged measurements.

While this study focused on independent measurements of vibrational and rotational temperature, the single-shot spontaneous Raman technique could also be applied for temperature measurements of gas samples in thermal equilibrium. This technique provides species-specific temperature and number density, though number density was not the focus of this study. Additionally, this technique can be applied in any flow where the probed species is present in adequate concentration. For example, the probe gas used throughout this study, N_2, is useful in most air-fuel combustion studies as it is present in high concentration throughout the flow. There is no limitation to specific fuel mixtures, as there is with Rayleigh thermometry measurements. Additionally, the signal scales with the number density of the probed species and therefore would benefit greatly from application in a high-pressure environment. However, the reduction in spatial resolution due to beam-steering effects defocusing the cell in environments with high refractive index gradients must also be considered.

4.4 – RECOMMENDATIONS FOR FUTURE WORK

Owing to the issues with laser-induced breakdown in the multiple-pass cell and damage on the cell mirrors due to dust, it is clear that further reduction in laser peak power would be advantageous for future use of this type of measurement apparatus. The addition of a third cavity to the pulse stretcher could reduce the peak power of the current laser so that a higher laser pulse energy could be used. This would come at a cost of a few thousand dollars and may require some of the mirrors in the final delay cavity be replaced with ones of larger diameter to avoid beam clipping.

Another avenue for improving upon the single-shot technique would involve using an entirely different laser. Flashlamp-pumped dye lasers are used in the medical field to treat various skin conditions [101],[102]. The complication of the time-of-flight pulse stretcher would be removed with this type of system. For example, the Candela Vbeam Perfecta laser provides a maximum of 8 J in a pulse duration which is selectable from 0.45 – 40 ms.[2] While the longer pulse durations provided by this laser are too long to freeze the flow, the shortest pulse duration produces peak powers that are vastly lower than could be achieved with time-of-flight delay of a laser beam with nanosecond-scale pulse width. However, new dispersion optics would need to be obtained to account for the change in excitation wavelength from 532 to 585 nm.

Perhaps an even more straightforward solution would be to use a variable pulsewidth Nd:YAG laser. Such a system exists off-the-shelf in the Agilite Series from Continuum Lasers. For example, the Agilite 569 provides a maximum energy of 630 mJ

---

[2] Robles, J., Syneron Candela, Private Communication.

when a 5 μs pulsewidth is selected, while pulsewidths of up to 50 μs are possible at reduced pulse energy values.[3] These lasers provide excitation energy at the more common 532 nm wavelength.

The shift in the facility as the metal heated and cooled, made making validation measurements over a range of temperatures (as in Fig. 4.10) difficult. The ability to precisely control and vary gas temperature would allow for a more thorough analysis of the technique's limitations. One possible avenue for this type of study would be installing this single-shot measurement apparatus around a small table-top burner, like the one used previously in Ref. [103], where temperature can be controlled by the equivalence ratio of the burner. Additionally, this small burner would avoid the challenges of setting an exact height with the facility. Owing to the relatively large amounts of thermal expansion induced when the facility heats up, repeating measurements at the same location day after day is difficult. Thus, all measurements at a specific height are taken in one session and the exact height from the nozzle for that data set is found in post-processing the images taken by the side-view CCD camera. A small burner (or small heated jet) on a 3-axis motorized translation stage could provide a flow field that is much more easily traversed with the measurement.

Single-shot data provides a vastly larger amount of data per experiment than time-average methods. The fitting routine is computationally intensive, requiring approximately 74 seconds per spectrum, but is well-suited to parallel execution. Because the fitting of each spectrum is independent of the others and uses the same input constants, the problem is readily parallelizable. Current parallelization is done with MATLAB or Windows batch scripts on a single quad-core processor with 4-8 workers.

---

[3] "Agilite 560/569 Datasheet," Continuum Lasers, [Online]. Available: http://www.continuumlasers.com/images/stories/products/downloads/agilite/agilite560569_rev_E.pdf

Fig. 4.29 below show the wall-clock time required for variously sized sets of spectra. The CPU on the laptop used for most of the computation was an Intel i7-4702HQ quad-core processor. The "hyperthreading" capability of this processor allowed for each physical processor core to act as 2 virtual cores. This allowed for up to 8 fits to be computed simultaneously on this machine. The downside of this is the decrease in system stability and usability when running the processor at maximum capacity, and thus very few computations were executed with 8 parallel processes. The desktop machine used for some computations utilized an Intel i5-3330 quad-core CPU which did not have hyperthreading capability.

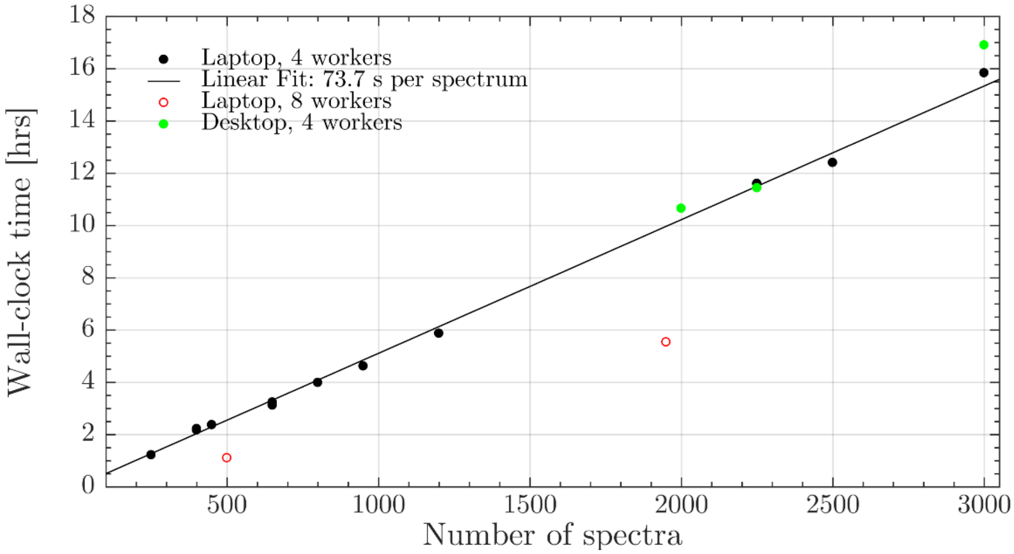

Figure 4.29: Computation time required for fitting large sets of Raman spectra.

The use of MATLAB or Windows batch commands is not ideal for massive parallel computation. MATLAB does not incur much of a speed penalty relative to the long computation time of each fit routine, but rather, it limits the scalability to computation on multiple machines or a cluster due to the requirement of installing the MATLAB environment on each PC. Similarly, the use of parallel Windows commands does not scale well to a cluster. Future effort could be made into parallelizing the file handling and fitting within a Unix shell or with compiled language code. This would allow not only increase portability for fitting simultaneously on several machines, but would allow for the computation to be scaled onto a cluster or HPC machine to significantly reduce the wall-clock time required to receive results. For example, the use of only a pair of nodes on Lonestar 5 at the Texas Advanced Computing Center provides 48 cores to perform 48 simultaneous fits and thus a factor of 12 reduction in compute time from the average fit time of 73.7 seconds shown in Fig. 4.29.

Performing the spectral fitting computations in a short time would also be a significant aid during data collection. The current rate at which fits can be obtained from the data is greatly exceeded by how much data can be generated in a single day of experiments. This leads to the issue that one has to wait a significant amount of time (days) until the fitting process completes in order to have results to look at. If something subtle is wrong in the Raman spectra, it may not be realized until after processing completes.

This facility had a few drawbacks in terms of the ability to quantify the effect of vibrational non-equilibrium on flame behavior. First, in order to obtain a stable autoigniting lifted flame it was necessary to heat the jet gas, which reduced the magnitude of the non-equilibrium. Additionally, the fuel mixtures used had low stoichiometric mixture fraction values and, thus, the flame base stabilized on the outermost edge of the shear layer. This region of stabilization did not contain appreciable non-equilibrium as it was not where rapid mixing occurred between the hot and cold streams.

Experimental study of the effect of vibrational non-equilibrium on flame behavior would be more easily accomplished in a facility where non-equilibrium is artificially produced rather than induced by mixing. For example, producing vibrational non-equilibrium with a method that could be switched on and off would allow for the macroscopic effects on flame behavior to be observed directly. Additionally, the ability to produce stronger non-equilibrium, or modulate the non-equilibrium strength, would accentuate these effects.

Optical pumping of vibrational excitation within a specific molecule has been achieved using stimulated Raman scattering [104]–[106]. A single frequency-doubled Nd:YAG laser source was used to pump a Raman gain cell to achieve up to 35%, 21%, and 10% conversion efficiency in generating beams whose wavelengths matched the first Stokes peaks of N_2, O_2, and H_2, respectively [106],[107]. These beams, along with residual 532 nm energy were sent into a second gas cell where their overlap region excited approximately 30% of the molecules of the selected species into vibrationally-excited states. This is much stronger than the vibrational excitation in the jet in coflow facility which has, at most, a fractional population of 3.4% and 10.5% in excited states for N_2 and O_2, respectively.

These studies, however, focused on the vibration-vibration energy transfer rates. A similar system could be conceived in order to generate non-equilibrium in the various diatomic species upstream of a simple flame. The behavior of this non-equilibrium as it passes through the flame as well as the flame response could be studied using this method. This circumvents the issue in the current facility where most of the non-equilibrium is generated in a region of the flow where the flame is seldom present. Additionally, the ability to produce vibrational excitation in a specific species allows for the effect of non-equilibrium on flame behavior to be studied in more detail than is possible with flow induced non-equilibrium from shocks, mixing, or expansion.

Appendices

APPENDIX A: PHOTOGRAPHS OF THE EXPERIMENTAL APPARATUS

This section provides a set of photographs which are intended to provide a better understanding of the jet-in-coflow facility and the apparatus involved in the laser measurement techniques. Section A.1 illustrates the construction involved around installing the jet-in-coflow facility in the laboratory and some of the relevant hardware required to operate it safely. Section A.2 provides photographs which correspond to the measurements presented in Ch. 3. Finally, Section A.3 is meant to supplement Ch. 4 by showing photographs of the single-shot measurement apparatus.

A.1 – Jet Facility Construction

Figure A.1: Laser barrier walls being construction around facility

(a)

(b)

(c)

Figure A.2: Images of the overhead exhaust system. (a) Hood and interior exhaust ducting. (b) Interior ducting viewed from above laser barrier walls. (c) Exterior ducting, blower and exhaust.

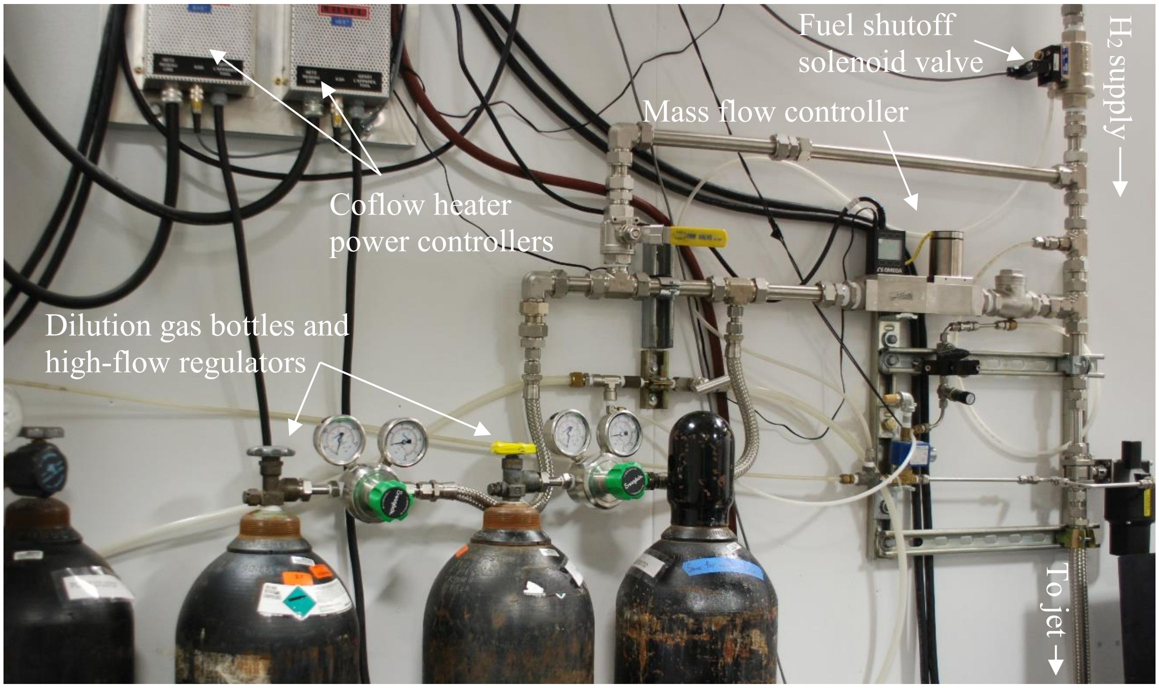

Figure A.3: Gas supply piping mounted on laser barrier wall

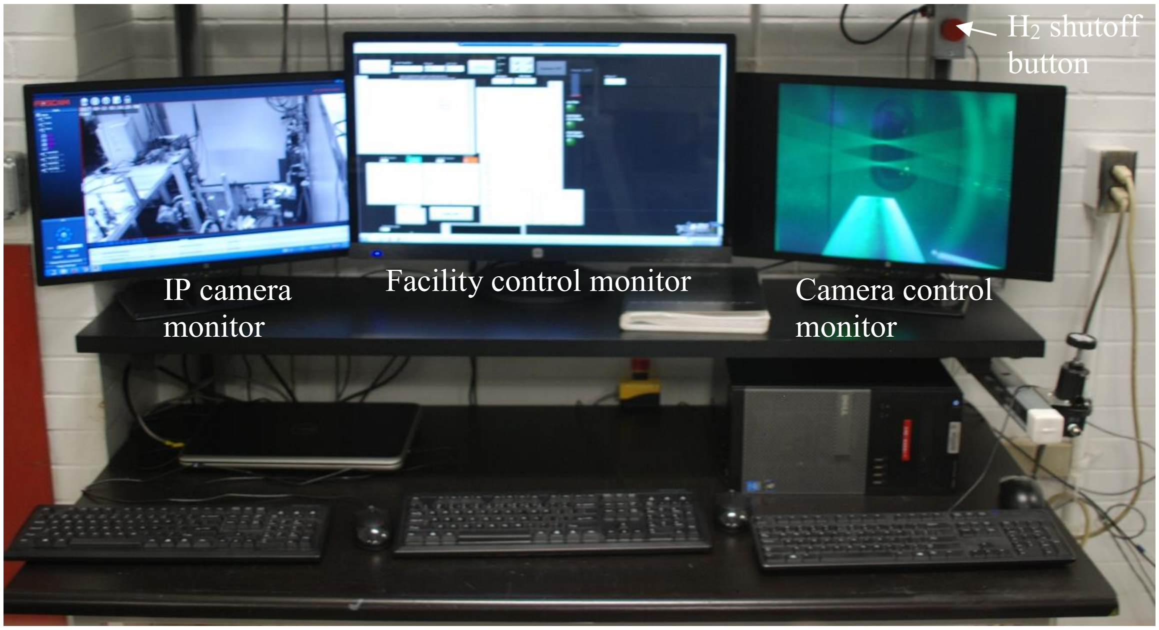

Figure A.4: Remote control station

A.2 – Time-Average Measurements

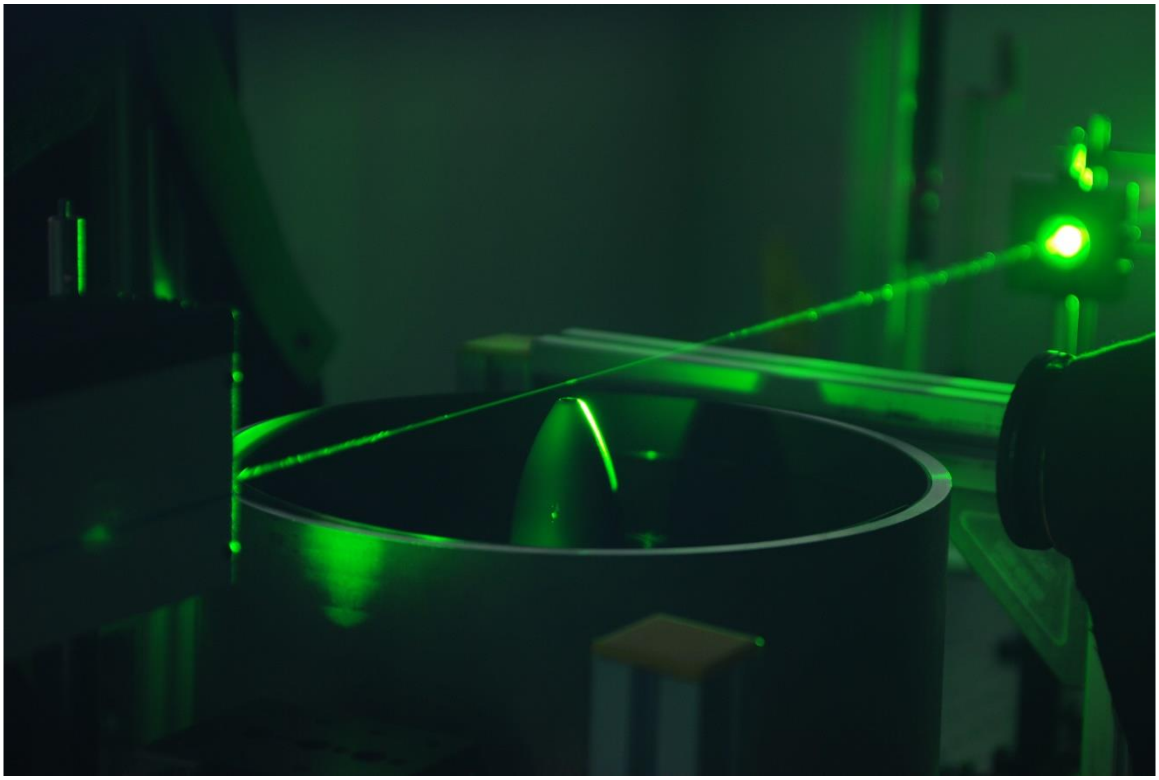

Figure A.5: Raman measurement being made near nozzle exit without coflow shroud. Scattering is visibly stronger from the colder jet flow. Pervasiveness of dust in the room air outside the coflow is also apparent.

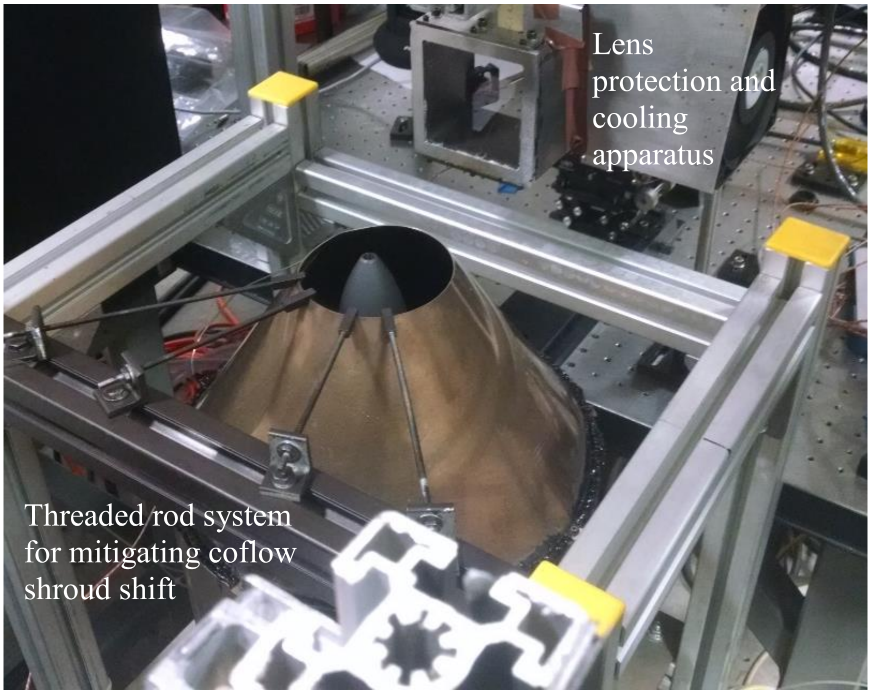

Figure A.6: Lens protection for Rayleigh scattering measurements and threaded rod system for reducing the thermal expansion shift of the coflow shroud.

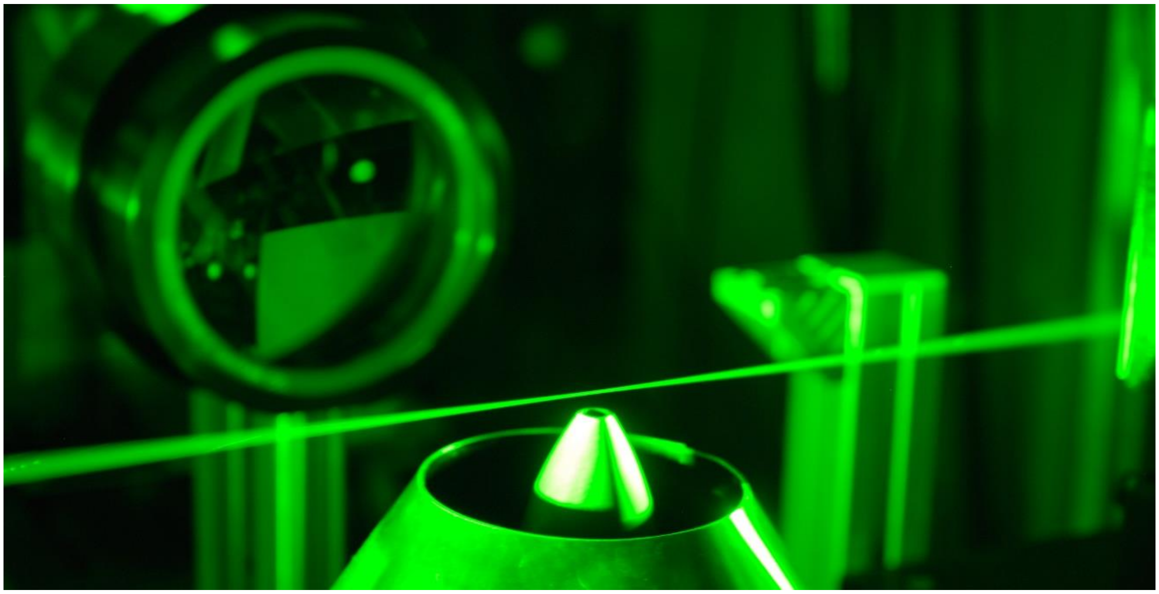

Figure A.7: Raman scattering measurement being made with larger collection optics and coflow shroud installed.

A.3 – Single-Shot Measurements

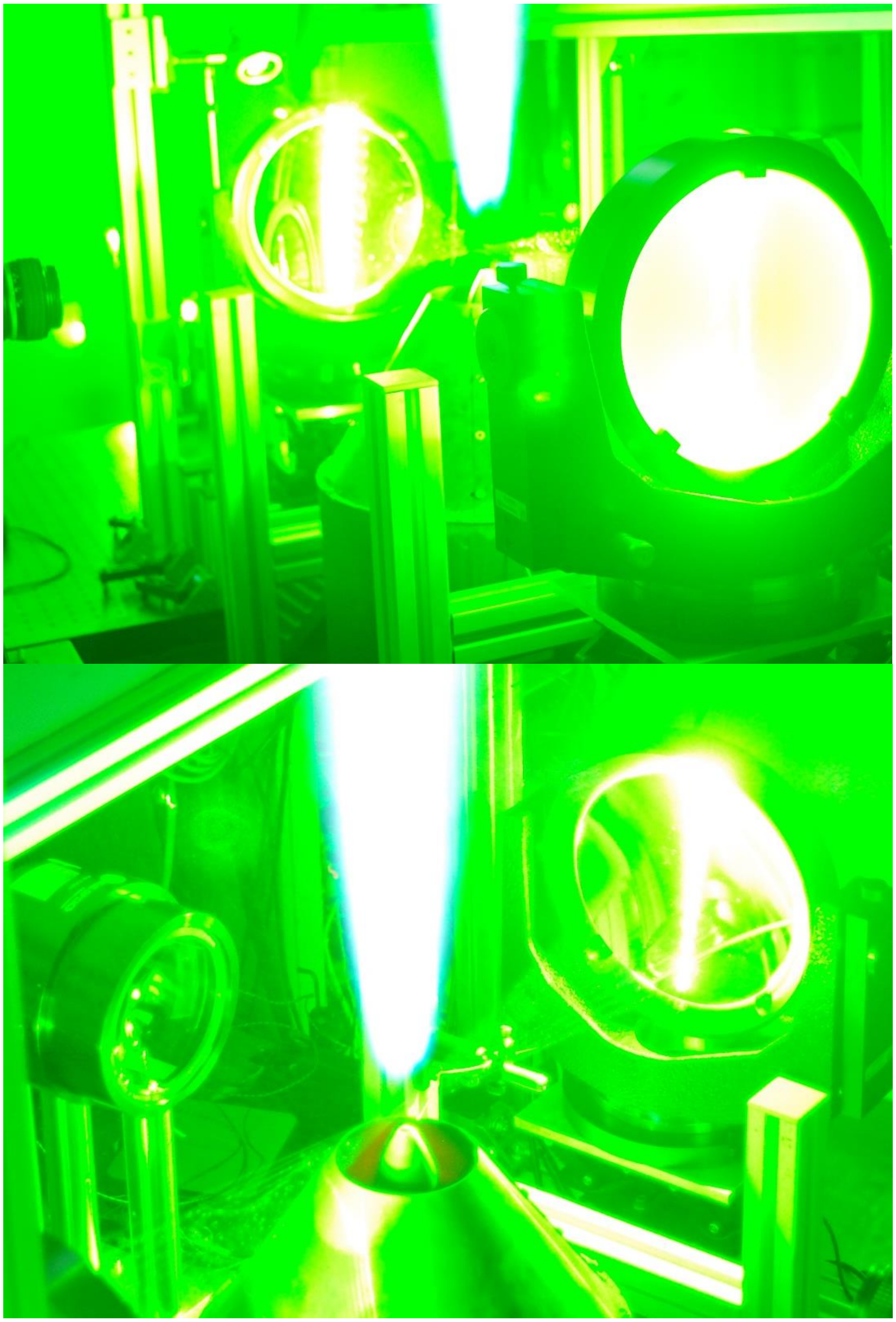

Figure A.8: Long exposure images of the H_2/CH_4 flame and single-shot Raman measurement apparatus.

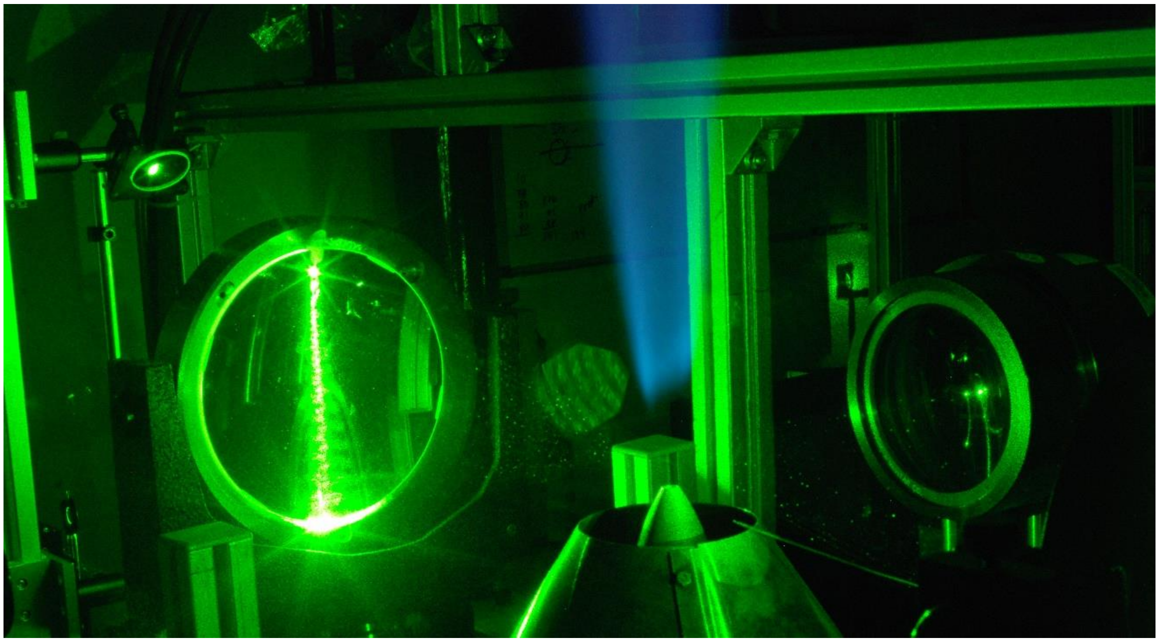

Figure A.9: Shorter exposure image of the multipass cell and H_2/CH_4 flame showing the beam spots on the multipass cell mirror.

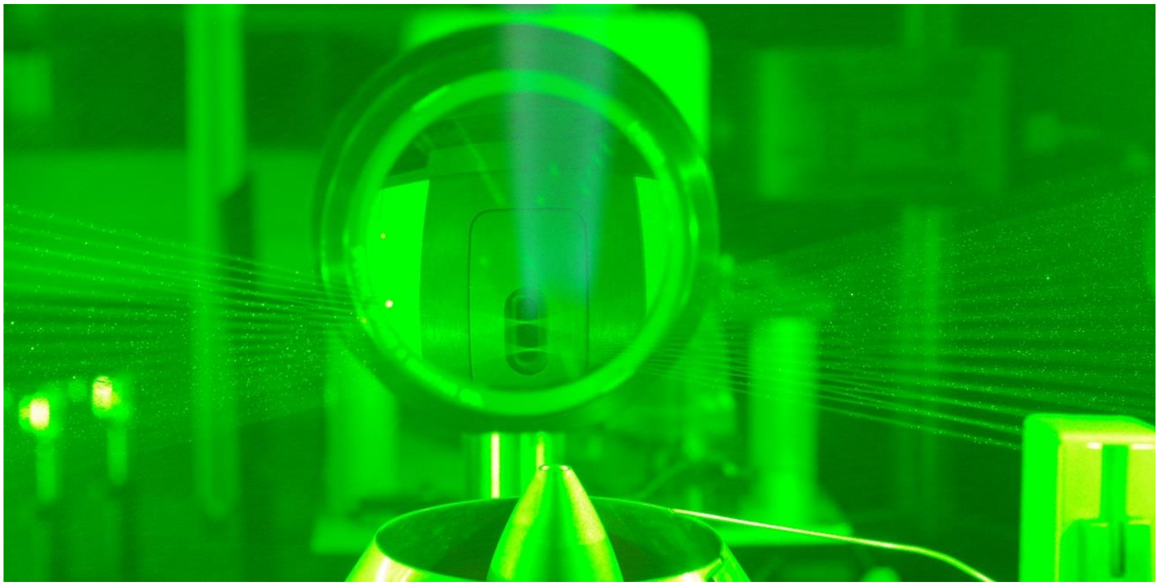

Figure A.10: Image of the H_2/N_2 flame and single-shot Raman measurement apparatus. The flame chemiluminescence is much less intense than with the CH_4-containing flame.

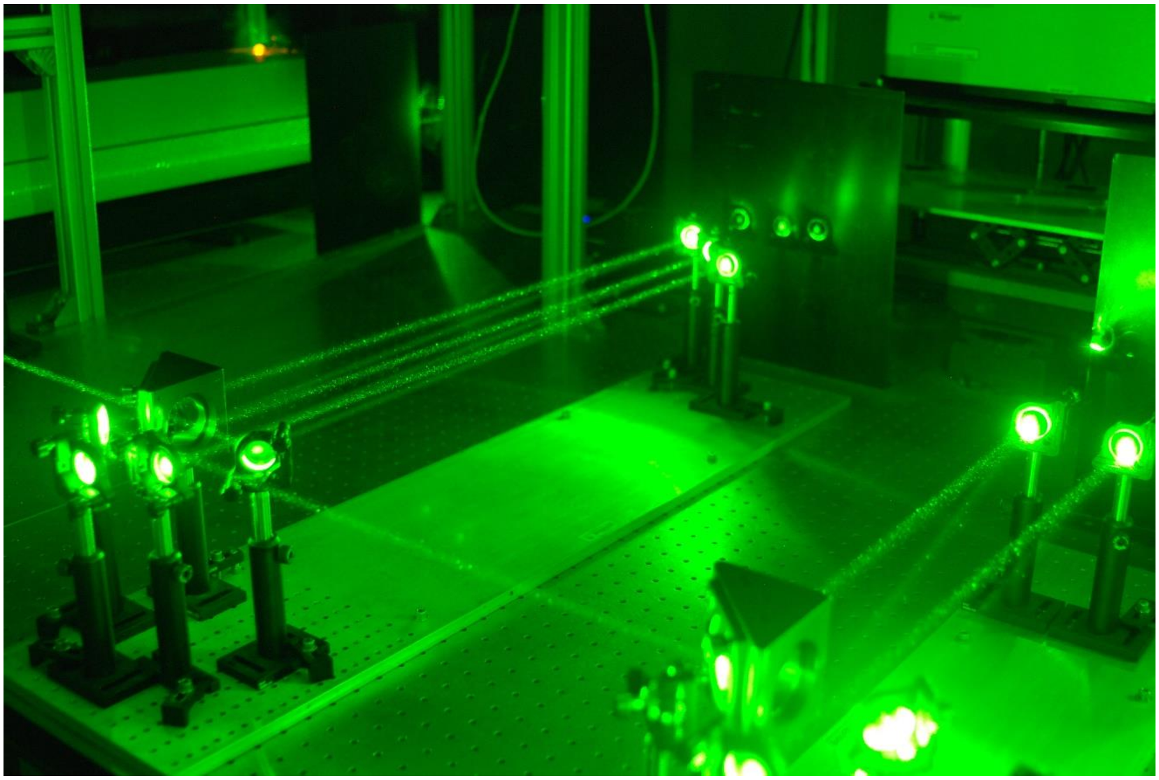

Figure A.11: Pulse-stretching apparatus in operation

APPENDIX B: RAMAN MEASUREMENT CALIBRATION

Spectra captured by the Raman measurement system typically appear on the ICCD sensor looking approximately like the image presented in Fig. B.1. The horizontal direction in the image represents the dispersion axis. To obtain useful spectra from these images, the following operations are applied to the images:

1) Background signal is subtracted from the image.
2) The rows containing Raman signal are identified and the image is vertically binned over these rows.
3) A spectral calibration function is applied to correlate between pixel column and wavelength
4) An intensity calibration is applied to accommodate for any spectral or spatial dependence in the system transmission.

The following section details this process and the characteristics of the Raman measurement system.

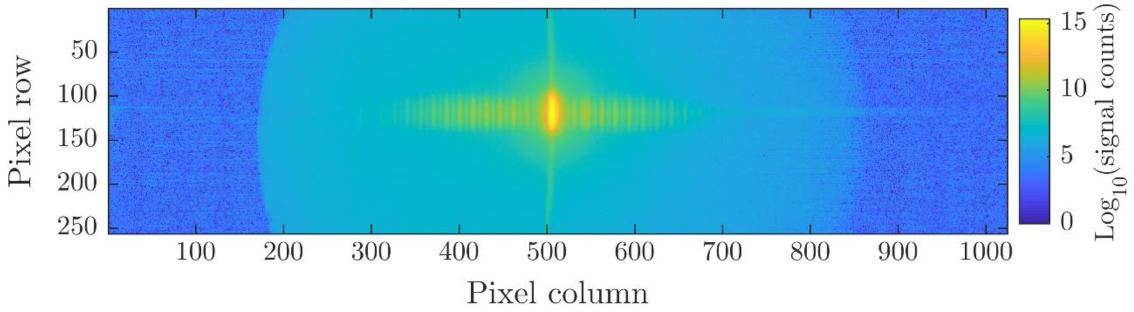

Figure B.1: Raw Stokes N_2 Raman Q-branch signal as it appears on ICCD sensor from room temperature air for the setup used in Section 3.2. Background signal has been subtracted.

The intensified camera used for all measurements was a Princeton Instruments PI-MAX3 with a 1024×256 CCD sensor with 26×26 μm pixels. The 18mm diameter intensifier is circular and therefore the width of useful sensor area depends on which rows are used. Typically, the camera height was adjusted so that the Raman signal was centered on the middle rows to maximize spectral coverage. This intensified region is clearly visible in Fig. B.1 as the large outer circle of uniform intensity surrounding the Raman signal. This "halo" showing the intensified region is only visible due to this image being captured over a much longer collection time than a typical measurement. The signal in this region is not much higher than the non-intensified region in the collection time used for a typical time-averaged measurement after background subtraction.

While the procedure behind background subtraction and vertical binning are fairly self-explanatory, the spectral calibration process is more complicated. The emission lines from a neon lamp (Electro-technic Products model SP200) are used as a calibration reference. In Figs. B.2 and B.4, typical Neon emission line spectra are shown for the HDG-607 and HDG-573 spectra, respectively. Figs. B.3 and B.5 show the corresponding calibration curves which are obtained from these spectra. The fitted spectral calibration function is a third-order polynomial fit of the horizontal pixel locations of the observed line peaks to their known spectral locations [108].

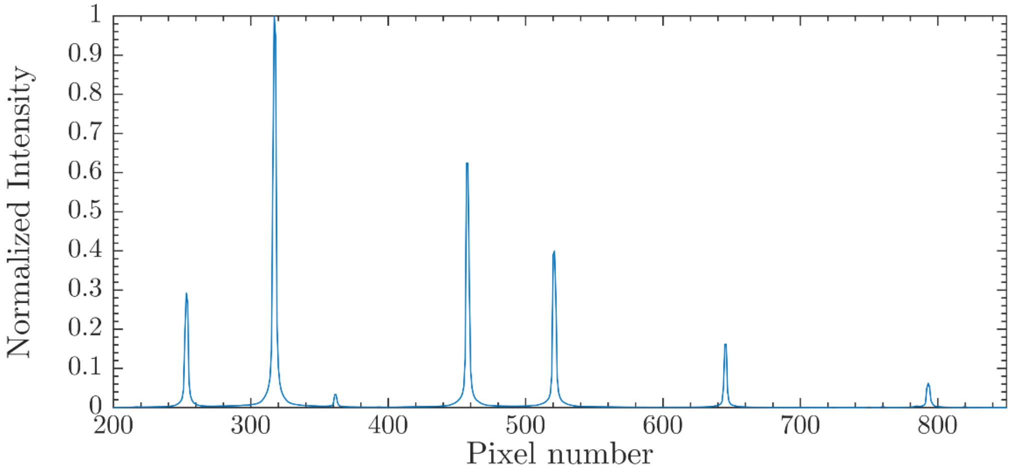

Figure B.2: Background-subtracted neon lamp spectrum for HDG-607 grating

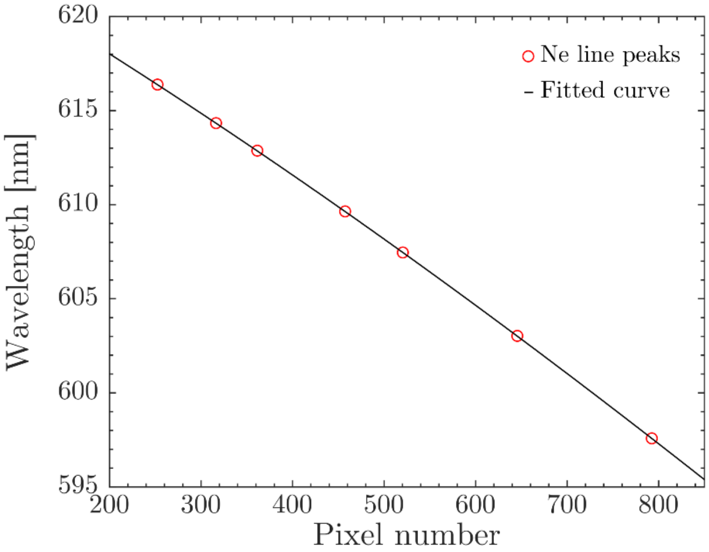

Figure B.3: Line peak locations and fitted third-order polynomial for HDG-607 grating with 532 nm excitation: $\lambda = 623.9 - (2.816 \cdot 10^{-2})x - (7.186 \cdot 10^{-6})x^2 + (9.573 \cdot 10^{-10})x^3$

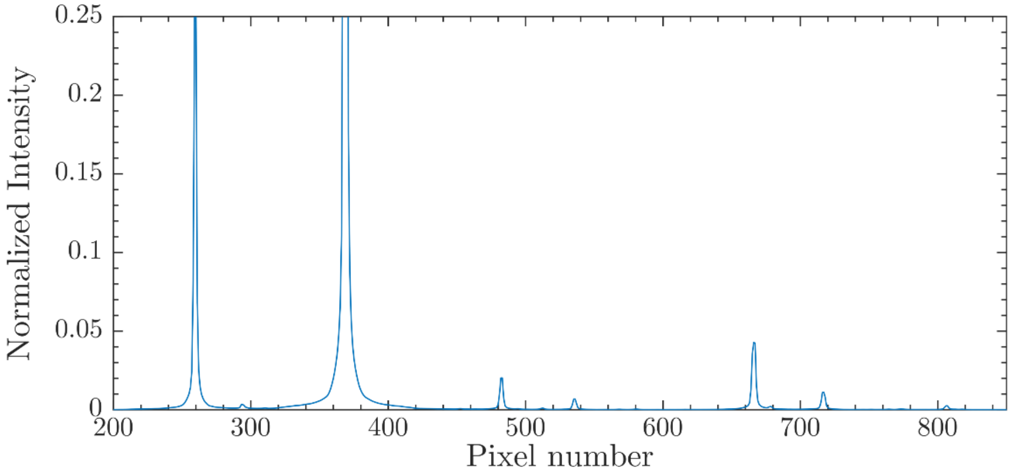

Figure B.4: Background-subtracted neon lamp spectrum for HDG-573 grating

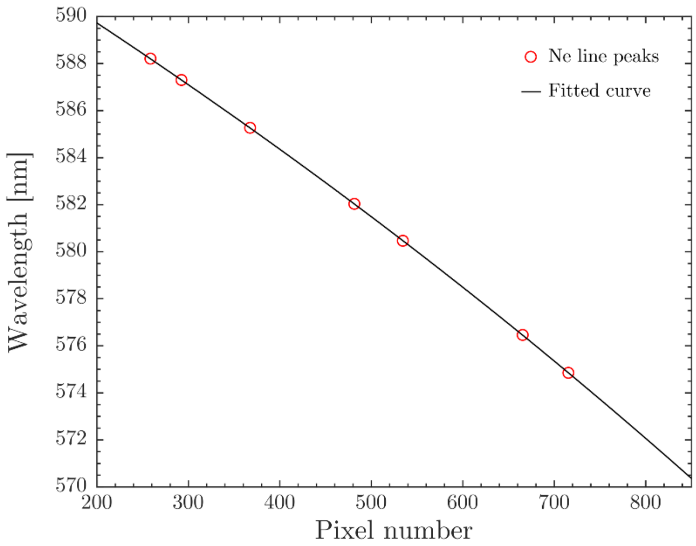

Figure B.5: Line peak locations and fitted third-order polynomial for HDG-573 grating with 532 nm excitation: $\lambda = 594.7 - (2.380 \cdot 10^{-2})x - (4.441 \cdot 10^{-6})x^2 - (1.430 \cdot 10^{-9})x^3$

While these calibration curves should provide a re-useable calibration function, it was found that a slight shift could occur whenever the grating or camera was disturbed. Thus, any time the camera or grating was removed from the spectrograph a new calibration spectrum was obtained. Table B.1 summarizes the spectral calibration constants and useful wavelength range for different grating and laser combinations. The shift of the spectral range of the grating with the Nd:YLF laser was due to the camera being shifted on the spectrograph in order to capture the Raman signal in the center of the intensified region of the sensor. The necessity of this shift is described in the following paragraphs.

Laser	Grating	A_0	$A_1 \cdot 10^{-2}$	$A_2 \cdot 10^{-6}$	$A_3 \cdot 10^{-10}$	λ_{min} [nm]	λ_{max} [nm]
Nd:YAG	HDG-607	624	-2.82	-7.19	9.57	597	619
Nd:YAG	HDG-573	595	-2.38	-4.44	-14.3	572	590
Nd:YLF	HDG-607	617	-3.11	-6.18	14.7	588	612
Nd:YLF	HDG-573	587	-1.83	-22.3	11.0	565	583

Table B.1: Summary of typical calibration constants and effective spectral coverage for all combinations of grating and excitation wavelength used. Spectral calibration constants A_0-A_3 define the function $\lambda = \sum_{i=0}^{i=3} A_i x^i$, where x is the horizontal pixel number on the sensor. λ_{min} and λ_{max} define the approximate useful spectral range on the sensor.

Several lasers were used to provide the incident excitation energy. These lasers used two specific lasing media, Nd:YAG and Nd:YLF, which provide output light at 532 and 526.5 nm, respectively after frequency-doubling. The Raman gratings used were designed to center the Stokes Q-branch lines of N_2 and O_2 on the sensor for Nd:YAG excitation. When the Nd:YLF laser was used, this spectral shift in excitation wavelength caused a subsequent shift in the location of the Raman lines on the sensor. This shift was significant enough that the Q-branch appeared near the edge of the intensified region of the sensor and much of the S-branch rotational information was lost if the system as used as-is. To remedy this, the camera sensor needed to be shifted horizontally on the spectrograph.

To accomplish this shift, a custom camera mounting system was manufactured with slots that allowed the camera to be moved horizontally on the spectrograph. The new mount required a smaller outer diameter for the mounting flange to make allowance for the flange to move without contacting the bolts. Other dimensions which are important to focusing, such as the sensor-to-grating distance matched the original mounting plate. The new and old mounting plates are depicted below in Fig. B.6. A standard dash number 154 O-ring was designed into the mounting plate to make the seal between the camera plate and the spectrograph. This new mounting system allowed the N_2 and O_2 Stokes Raman Q-branch lines to be centered on the sensor and brought into focus using the built-in internal adjustment knobs.

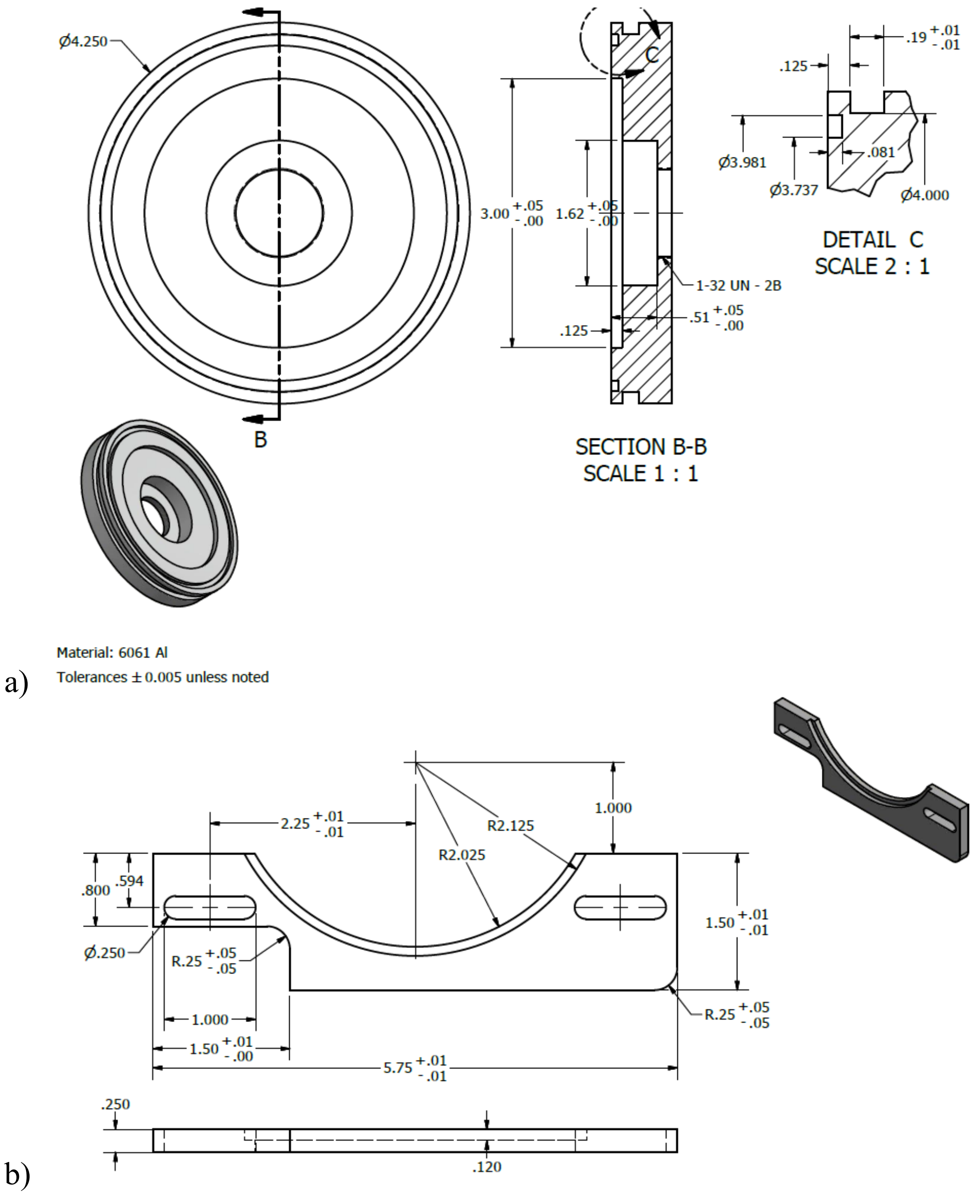

Figure B.6: CAD drawings of custom camera mounting system. (a) Camera flange. (b) Mounting bracket with slots which allow the camera flange to be shifted horizontally.

To attenuate the Rayleigh scattering signal within the spectrograph, a holographic notch filter was installed which has a high optical density at the laser wavelength. These filters also have a very narrow spectral bandwidth in order to pass the rotational Raman lines which occur very close to the incident laser frequency. For our system, this notch filter (Kaiser SuperNotch HSPF-532.0AR-2.0) was designed for Nd:YAG excitation and is specified to have a spectral bandwidth of less than 350 cm$^{=1}$ between the O.D. 0.3 points. The transmission spectrum for this filter is shown below in Fig. B.7. This narrow bandwidth meant that the Rayleigh scattering would not be attenuated by the notch filter when the Nd:YLF laser was used. Rather than purchase an expensive (over $5,000) custom notch filter designed specifically for this excitation wavelength, the existing notch filter was tilted slightly about the vertical axis such that it attenuated the 527 nm light. This was accomplished by removing the spectrograph top cover and grating and observing the throughput of incident wavelength light scattered through the spectrograph from a small metal pin placed at the measurement location. This method only works because the holographic filter shifts to the blue as it is tilted away from 90° incidence and the Nd:YLF laser operates at a shorter wavelength than the Nd:YAG lasers for which the filter was designed. We observed no ill-effects from the small shift (approximately 7°) which was required to accomplish this.

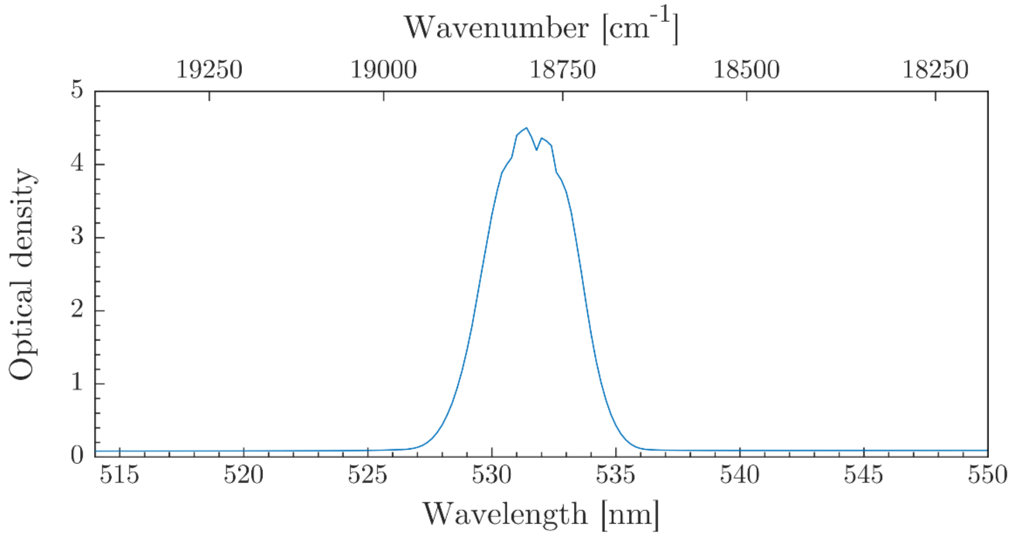

Figure B.7: Notch filter spectral performance at 0° incidence.

To account for spectral dependence of the optical system and pixel-to-pixel variation on the sensor, an intensity calibration was performed. The emission from a black body radiator (CI Systems SR-20) was used as a standard source. This signal was collected with the measurement system in the exact configuration as it is used for Raman measurements to ensure that the true system response is obtained. This collection is made over a long integration time (several minutes) in order to collect a high signal-to-noise image. This image was processed in an identical fashion to Raman scattering spectra in order to obtain a spectrum for the black body source. This spectrum is then divided by the expected black body signal as predicted by Planck's Law:

$$I(T,\lambda) = \frac{2hc^2}{\lambda^5}\frac{1}{e^{\frac{hc}{\lambda kT}} - 1}. \tag{B.1}$$

Thus, an intensity correction factor as a function of wavelength can be obtained by dividing the actual signal collected from the black body source by the expected emission at the set temperature. Figure B.8 shows typical values for this calibration factor. For both gratings, the system tends to attenuate some of the signal for shorter wavelengths, and thus the calibration factor increases to correct for this. The calibration factor becomes large near the edges of the intensifier as the signal no longer has uniform gain. For each calibration case, the black body was set to 200 °C.

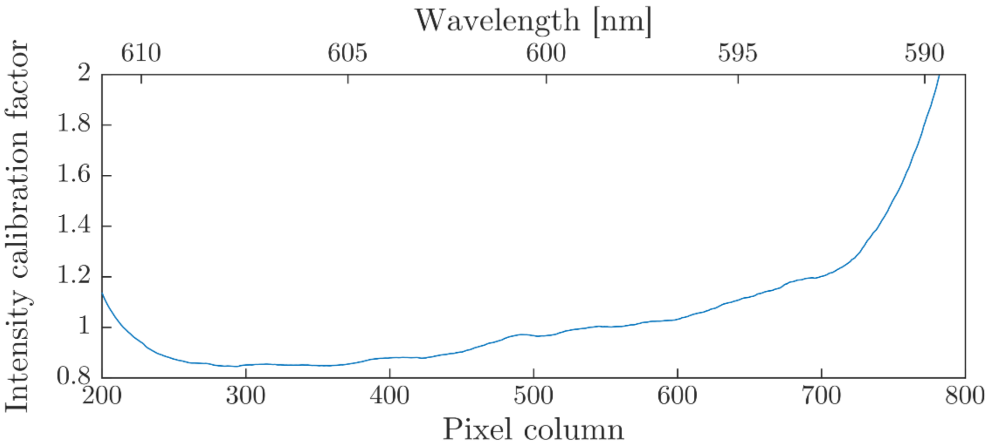

a)

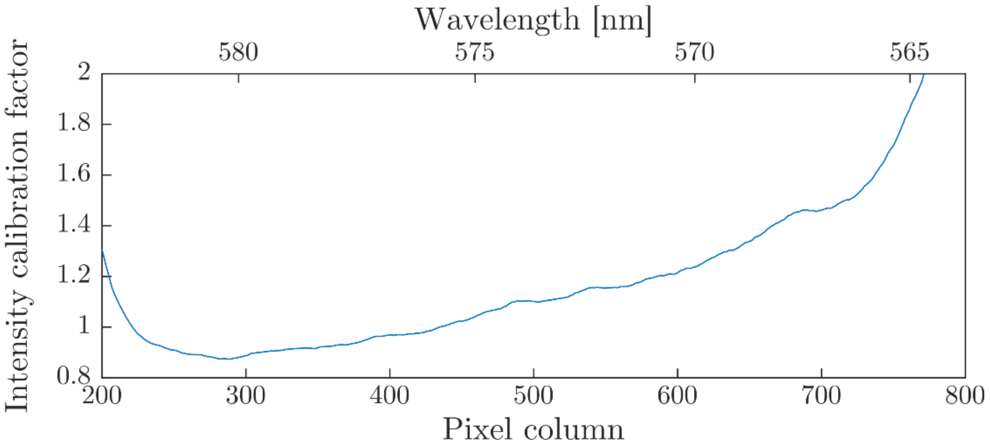

b)

Figure B.8: Intensity calibration factor for camera in position for Nd:YLF laser excitation for the (a) HDG-607 grating and (b) HDG-573 grating.

The Raman spectral simulation code must not only compute line strengths and spectral locations, but also simulate the broadening which will be present in real-world measurements. This broadening comes from two main sources: local thermodynamic conditions (Doppler and collisional broadening) and instrument resolution. In order to account for the resultant broadening from all contributions, a single "lineshape function" is applied to broaden each of the Raman lines. The lineshape function used was the convolution of a trapezoid with a Lorentzian function, which was determined to best represent the instrument function of this spectrograph in Ref. [33]. The parameters used to define these two functions were the width of the Lorentzian and the half-width of the trapezoidal function at the top and base. There parameters were used to define a shape of an individual line as

$$\begin{aligned} I(x,a,b,t) = \frac{1}{2\pi(b^2-t^2)}\Bigg\{&(x-b)\tan^{-1}\left(\frac{x-b}{a}\right) \\ &+(x+b)\tan^{-1}\left(\frac{x+b}{a}\right)-(x-t)\tan^{-1}\left(\frac{x-t}{a}\right) \\ &-(x+t)\tan^{-1}\left(\frac{x+t}{a}\right) \\ &+\frac{a}{2}ln\left[\frac{a^4+2a^2(x^2+t^2)+(x+t)^2(x-t)^2}{a^4+2a^2(x^2+b^2)+(x+b)^2(x-b)^2}\right]\Bigg\} \end{aligned} \tag{B.2}$$

where *x* is the distance from the line center in wavelength units, *a* is the Lorentzian width, *b* is the half-width of the trapezoid base, and *t* is the half-width of the trapezoid top [33].

These parameters were determined by fitting spectra of air at a known temperature (usually room temperature) and using a modified fitting routine where the lineshape parameters were the free variables. As with the spectral calibration, these parameters were highly sensitive to the exact position of the camera and grating. Thus, each time the gratings were swapped or the camera was adjusted, a new set of lineshape parameters was obtained to eliminate any errors induced by inaccurate lineshape function. A listing of typical values for these lineshape parameters with an approximate range of variation is given in Table B.2 and Figure B.9 below.

Grating	Slit width [μm]	Lorentzian width (a)	Trapezoid base (b)	Trapezoid top (t)
HDG-607	100	0.030±0.002	0.114±0.001	0.015±0.005
HDG-573	100	0.030±0.003	0.100±0.010	0.016±0.004
HDG-607	250	0.032±0.001	0.185±0.003	0.152±0.001
HDG-573	250	0.033±0.001	0.161±0.001	0.150±0.002

Table B.2: Summary of lineshape parameter values

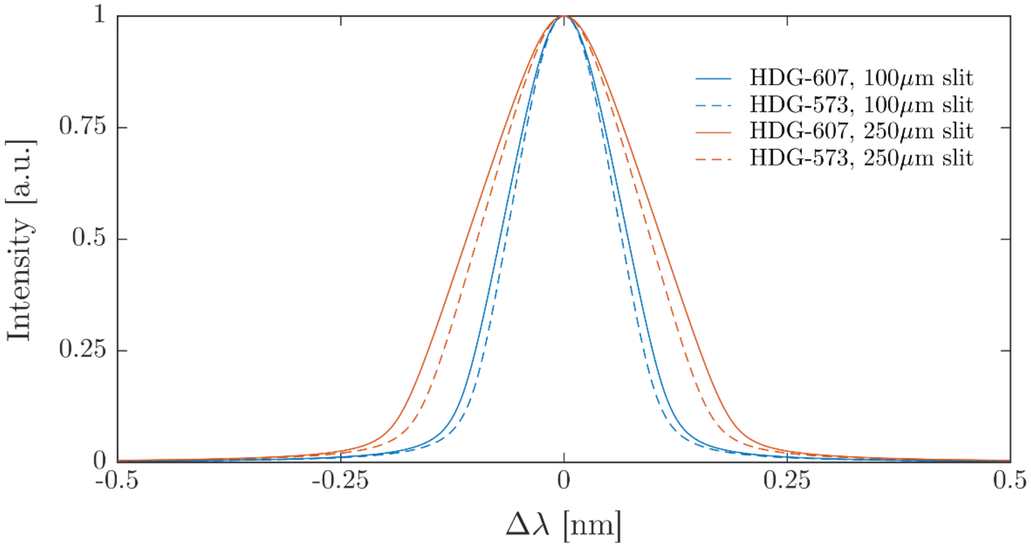

Figure B.9: Typical lineshape functions for different grating and slit combinations.

The values above for each grating can be considered appropriate for excitation by either Nd:YAG or Nd:YLF laser, as the slight shift of the camera did not change the lineshape notably. These lineshape parameters did, however, change significantly for the single-shot measurements, where larger slit sizes were used to increase signal at the expense of spectral resolution. The choice of slit width for this setup is discussed in Appendix E. The width of the Lorentzian function changes only slightly with an increased slit width, indicating that the trapezoidal function is much more sensitive to changes in instrument broadening. Because the trapezoidal function is much broader than the Lorentzian for all cases, the line broadening for this setup can be considered to be instrument dominated, and increasingly so with larger slit widths. This gives a robustness to this measurement technique, as the contribution to the lineshape from collisional and Doppler broadening are overwhelmed by the instrument broadening. Thus, this measurement apparatus could be applied as-is to large range of gas conditions at different pressures or densities.

The range of temperatures over which the code is reliable is determined in the following way. First, a noise free equilibrium spectrum is simulated and then the experimental noise profile is added to it in order to generate artificial noisy spectra. Noisy synthetic data is computed in this way because it is more representative of the real data than the one that could be obtained by adding random noise. The noise profiles that were added to the simulated noise free spectrum are shown in Fig. B.10. They are the residuals expressed in percentage units from spectral fitting the real data recorded from the jet, the shear layer and the coflow. Each curve shows residual values that are only a couple percent and peak near the Q-branch, where slight errors in line shape are dominant.

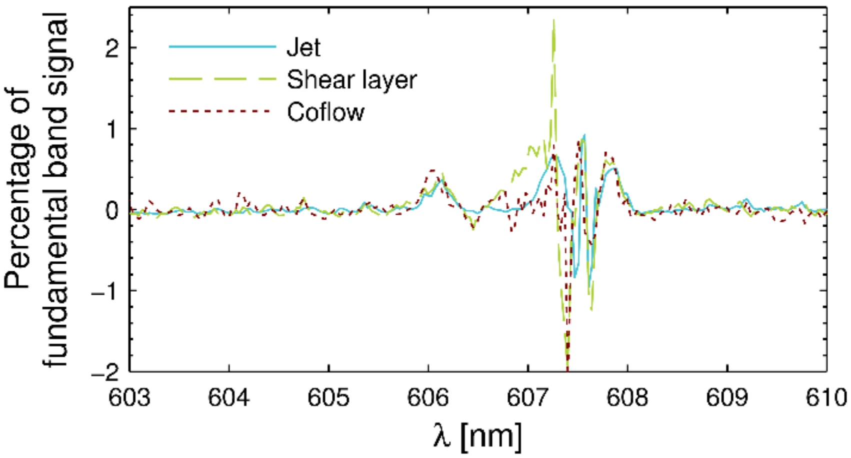

Figure B.10: Typical fit residuals as a function of wavelength in various regions of the flow.

The values of the rotational and the vibrational temperatures obtained from fitting to the synthetic noisy data are listed in Table 3. T_R and T_V are the rotational and the vibrational temperatures. The superscripts indicate the noise spectrum which was added to the synthetic equilibrium spectrum calculated at T_{Eq}. The typical noise in the jet, shear layer, and coflow are represented by *Jt*, *Sh* and *Co*, respectively.

T_{Eq}	${}^{Jt}T_R$	${}^{Jt}T_V$	${}^{Sh}T_R$	${}^{Sh}T_V$	${}^{Co}T_R$	${}^{Co}T_V$
200	306	∞	303	∞	302	∞
300	302	357	286	∞	292	∞
350	354	389	338	∞	341	∞
400	406	427	391	∞	393	123
450	457	469	443	432	444	367
500	508	514	496	496	494	472
550	559	560	549	550	545	535
600	609	608	601	602	596	592
650	660	656	654	653	646	645
700	710	705	706	703	697	697
800	810	804	810	802	798	799
900	910	903	913	901	899	900
1000	1010	1002	1016	1000	1000	1001

Table B.3: Temperatures (in K) calculated by spectrally fitting various synthetic noisy Raman spectra

In Table B.3, the non-physical negative values of temperatures are listed as ∞. The code fails to calculate the correct vibrational temperature when $T_{Eq} \leq 450$ K. This is because the vibrational temperature is effectively inferred from the ratio of the intensities of the hot band and the fundamental band, and the hot band intensity is non-negligible only at relatively high temperatures. The rotational temperature is effectively determined from the width of the bands, and the *O*- and the *S*-branches of the fundamental band. The *O*- and the *S*-branches are well resolved even at lower temperatures and so the code is able to interpret lower rotational temperatures correctly.

APPENDIX C: CHANGES TO RAMAN SIMULATION CODE

The $\Phi(\Delta v, \Delta J)$ factor presented Eq. 1.15 was given without explanation of the details of the factors it incorporates. This factor was originally computed using the relations derived in Appendix B of Ref. [33]:

$$\Phi_{v\to v+1,J\to J'} = \left[a'^2\delta_{J'J} + \frac{7}{45}\gamma'^2 b_{J',J}\right]4\varphi\cos\theta + \left[a'^2\delta_{J'J} + \frac{1}{45}\gamma'^2 b_{J',J}\frac{1}{12}(9\cos\theta - \cos 3\theta)(\sin 2\varphi - 2\varphi)\right], \tag{C.1}$$

where $b_{J',J}$ represents the Plackzek-Teller coefficients, which were defined in Ch. 1. The angular dependence of the Raman scattering is incorporated in the factors involving φ and θ. These two variables are angles defined by the collection f-number as $\varphi = \tan^{-1}\frac{1}{2f_\#}$ and $\theta = \frac{\pi}{2} - \varphi$. The polarizability terms, a' and γ', are the component of polarizability matrix elements which come from the molecular polarizability derivatives as

$$a'^2 = M(v, \alpha, \alpha', \alpha'', \alpha''') \cdot F(v, J, \alpha, \alpha', \alpha'', \alpha''') \tag{C.2}$$

$$\gamma'^2 = M(v, \gamma, \gamma', \gamma'', \gamma''') \cdot F(v, J, \gamma, \gamma', \gamma'', \gamma''') \tag{C.3}$$

In these expressions, M is the vibrational portion of the polarizability matrix element,

$$M(v, p, p', p'', p''') = \langle v|p|v+1\rangle^2 = \frac{(v+1)B_e}{\omega_e}\left\{p + \frac{2(v+1)B_e}{\omega_e}\left[\left(\frac{11}{16}a_1{}^2 - \frac{3}{4}a_2\right)p' - \frac{5}{4}a_1 p'' + \frac{1}{4}p'''\right]\right\}^2, \tag{C.4}$$

where p represents either the isotropic (α, α', etc.) or anisotropic (γ, γ', etc.) elements and a_1 and a_2 are constants of the Dunham anharmonic potential [36]. The parameter, F, is the Herman-Wallis factor, which can be expressed as

$$F(v, J, p, p', p'', p''') = \left(1 + \frac{R^p_{v,v+1}}{\langle v|p|v+1\rangle}\right)^2, \tag{C.5}$$

where $R^{p}_{v,v+1}$ is defined in Ref. [36] as a distinct function for each of the O-, Q-, and S-branches.

Previously, the Raman code accounted for the sensitivity of the collection optics to the polarization of scattered light by introducing a constant factor by which the isotropic polarizability derivatives ($\alpha, \alpha', \alpha''$, etc.) are multiplied [33]. This factor is intended to represent a ratio of polarized to de-polarized signal. However, mathematically, this does not represent a true polarization-dependence correction, which will be discussed further below. This method also makes *a priori* calculation of the effect of a multiple-pass cell on the collected signal impossible as the two polarization components are not truly isolated. Because Eq. C.1 was derived by integrating expressions that incorporated contributions from both polarization directions, new expressions needed to be computed from the first principles. Thus, expressions for the components of the $\Phi(\Delta v, \Delta J)$ factor in the overall scattered Raman signal polarized normal and parallel to the scattering plane were derived as

$$\begin{aligned}\Phi^{\perp}_{v\to v+1,J\to J'} &= a'^2\delta_{J',J}\left[2\sin\chi_m\left(\chi_m+\frac{\sin 2\chi_m}{2}\right)\right]\\ &\quad+\gamma'^2 b_{J',J}\left[2\sin\chi_m\left(\frac{7}{45}\chi_m+\frac{\sin 2\chi_m}{90}\right)\right]\end{aligned} \tag{C.6}$$

$$\begin{aligned}\Phi^{||}_{v\to v+1,J\to J'} &= a'^2\delta_{J',J}\left[\frac{2}{3}\sin^3\chi_m\left(\chi_m-\frac{\sin 2\chi_m}{2}\right)\right]\\ &\quad+\gamma'^2 b_{J',J}\left[\frac{4}{15}\chi_m\sin^3\chi_m+\frac{2}{135}\chi_m\sin^3\chi_m\right.\\ &\quad\left.-\frac{1}{135}\sin 2\chi_m\sin^3\chi_m\right]\end{aligned} \tag{C.7}$$

from the expression given in Eqs. 1.13 and 1.14. Here, χ_m is the maximum angle between the incident light and the centerline of the collection optics. The code was altered to calculate these 2 components separately so that they could each be printed to file for analysis.

The contribution to the new $\Phi(\Delta v, \Delta J)$ from each term was investigated to check the validity of the previous method for polarization sensitivity correction. The dependence on rotational state for each branch of the $v = 0$ band is shown in Fig. C.1. These calculations were carried out for a collection f-number of 2.2, which matches the achromat-lens pair used for most of the measurements.

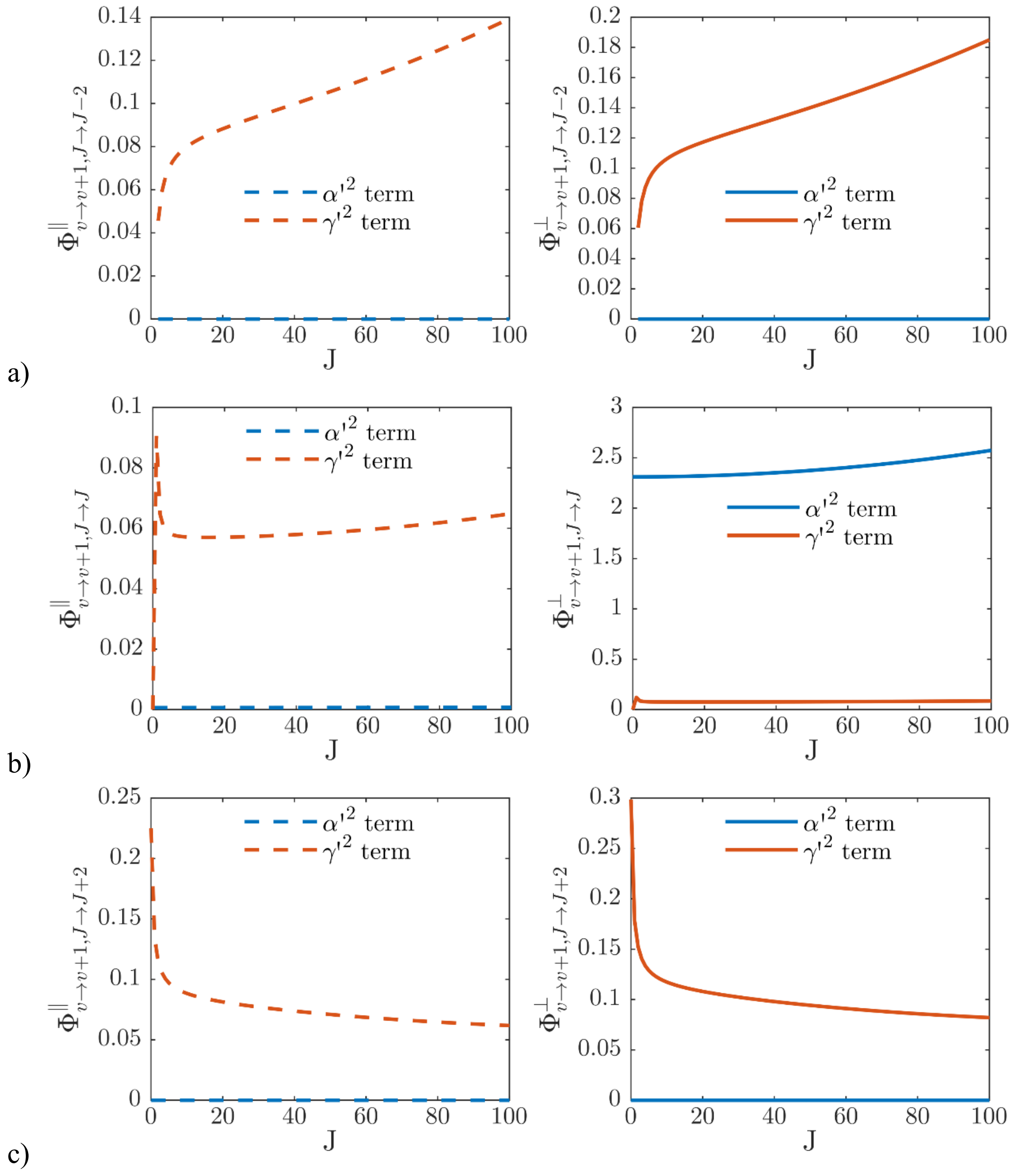

Figure C.1: Contributing components from isotropic and anisotropic polarizability derivatives for (a) O-branch, (b) Q-branch, and (c) S-branch of the Stokes $v = 0 \rightarrow 1$ transitions of $^{14}N_2$.

The Q branch is dominated by signal polarized perpendicular to the scattering plane, which comes *almost* completely from α'^2 terms. This is why the previous method of accounting for polarization sensitivity was a good approximation. However, the presence of a contribution from the γ'^2 term in $\Phi^{\perp}_{v\to v+1,J\to J}$ means that the polarization sensitivity factor is not truly a ratio of the sensitivity of the optics to the different polarization directions. Additionally, the O and S branches see no contribution from a'^2 and are thus not modified by the previous method for polarization sensitivity correction. This should not be the case in a true polarization sensitivity correction. These lines are typically considered to be strongly depolarized, having comparable contributions from both polarization components. Therefore, a multiplicative factor which accounts for enhancement of one polarization direction over the other should also modify the signal in these branches.

Combining the a'^2 and γ'^2 terms, the relative contribution of horizontally and vertically polarized signal can be compared. This comparison is presented in Fig. C.2. The O- and S-branches are strongly depolarized, while the Q-branch signal is strongly polarized, as is discussed in Ref. [31] for vanishingly small collection solid angle. At the current collection f-number of 2.2, the depolarization ratios are 0.024 and 0.753 for the Q and O/S branches, respectively.

While this study used only 2 specific collection f-numbers, the trends in these transition matrix elements was investigated for general application. Figure C.3 below illustrates the trends of Φ values and depolarization ratios for the O-, Q-, and S-branches with collection solid angle. The plot shows the transition matrix elements for Stokes $v = 0 \to 1$ transitions from the $J = 10$ rotational level. This is meant to show the relative strength of lines between the different branches. The trends with f-number for different rotational and vibrational levels show the same trend. From the upper plot, it is clear that Φ falls off for slower collection optics in a similar fashion for all 3 branches. Thus, the ratio of Q- to O/S-branch signal is expected to remain constant even for very large collection solid angles.

The bottom plot shows a more interesting trend. Fast collection optics shift all 3 branches toward being more depolarized. The depolarization ratio for all 3 branches trend toward constant values for large collection f-numbers. The depolarization ratios reach these limiting values at different f-numbers for the different branches. The Q branch converges at f-numbers greater than 2, but the O and S branch require an f-number greater than 4 to approach the large f-number limit. The current optical setup ($f_{\#} = 2.2$) lies in the region where the depolarization ratios are just transitioning from this small collection angle limit. In the future, if faster optics are to be utilized, the sharp change in depolarization ratio will mean that the collected spectra will appear drastically different. However, with the new polarization sensitivity correction, this should be accounted for in the model if the correct collection f-number is provided to the code.

In Ref. [33], the polarization sensitivity factor was determined by a trial and error method where fits to high quality spectra were performed on the Q- and O/S-branches separately. In that study, multiplying the isotropic polarizability derivatives ($\alpha, \alpha', \alpha''$, etc.) by a factor of 1.17 optimally matched the real spectra. With the new matrix element calculation, the polarization sensitivity factor is implemented differently. Now, the two polarization components are computed separately and the scattering polarized perpendicular to the scattering plane is multiplied by a polarization sensitivity factor. The value of this factor for the new code was determined by least-squares comparison with the matrix elements computed from the old method. Resulting Φ values for the optimal sensitivity factor are compared with previous values in Fig. C.4. As is clear from the figure, the values are identical down to the accuracy at which they are written to file.

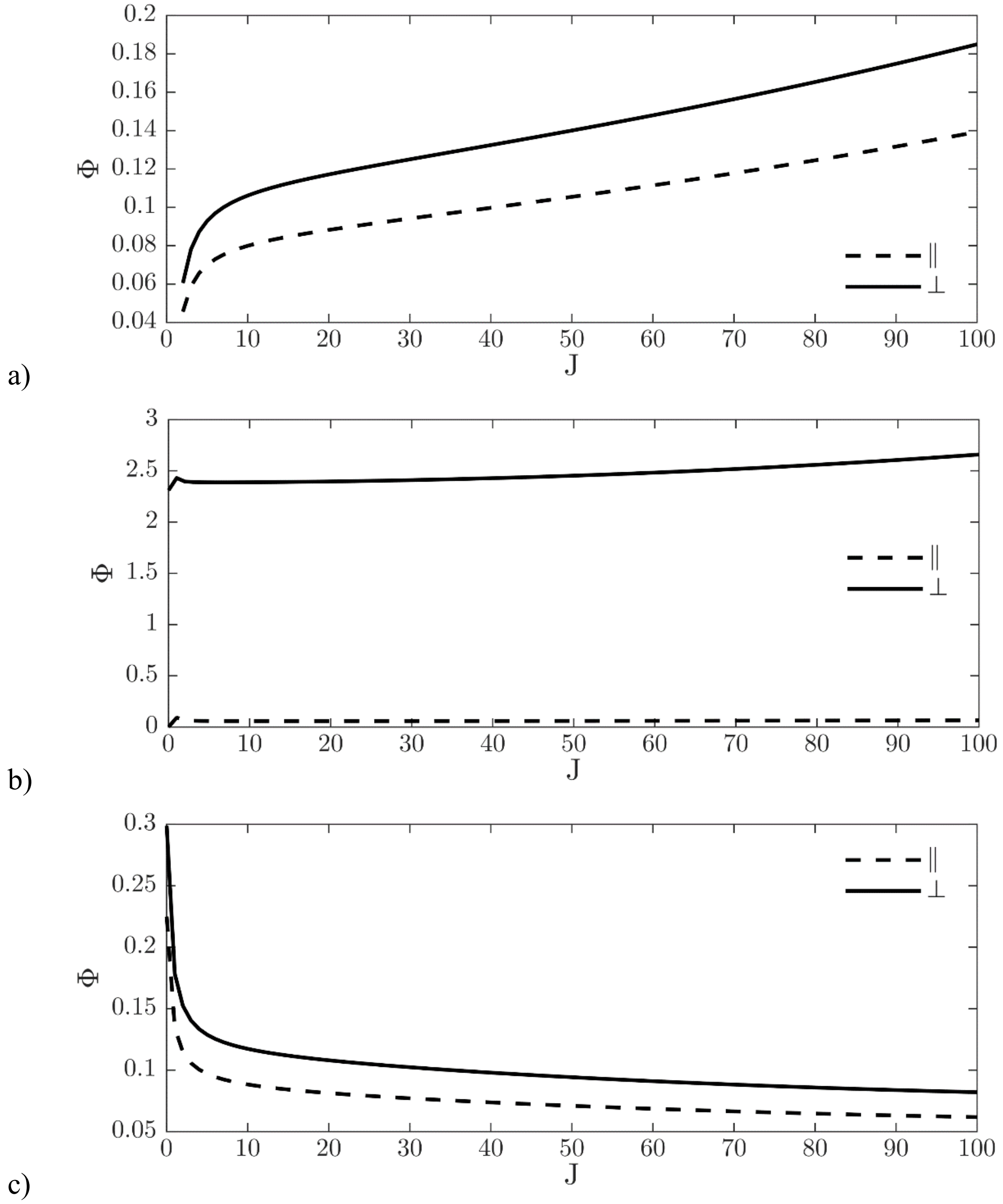

Figure C.2: Comparison of components of the Φ matrix elements polarized parallel and perpendicular to the scattering plane for (a) O-branch, (b) Q-branch, and (c) S-branch of the Stokes $v = 0 \rightarrow 1$ transitions.

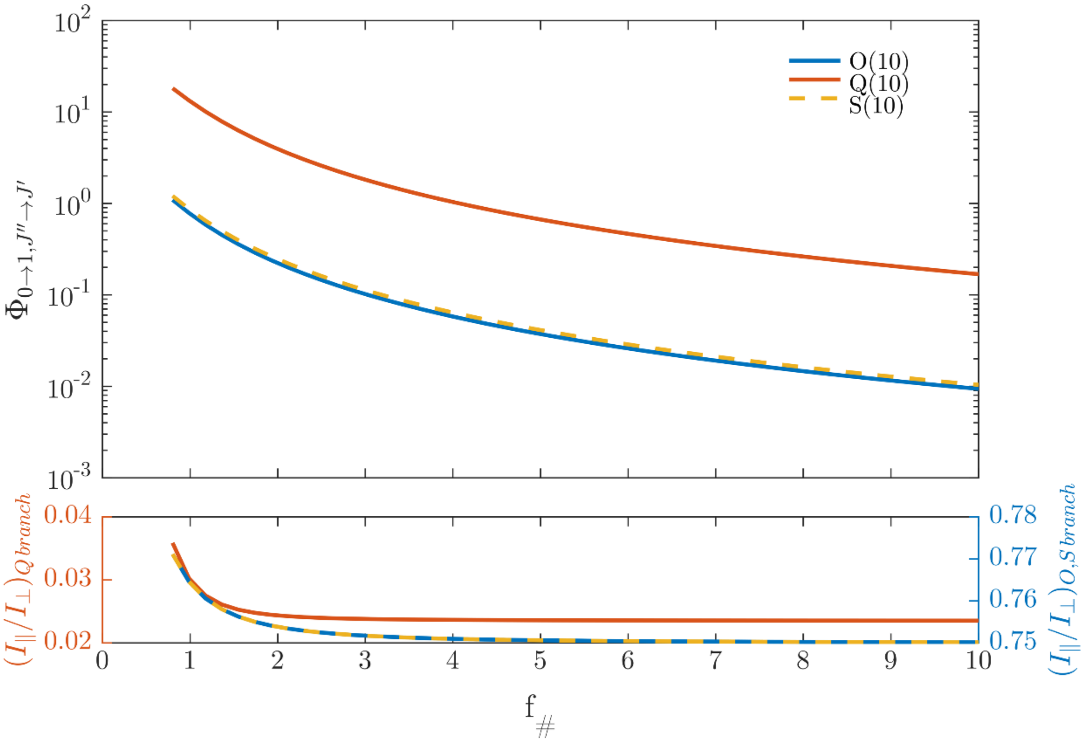

Figure C.3: Dependence of Φ transition matrix elements and depolarization ratio on collection f-number.

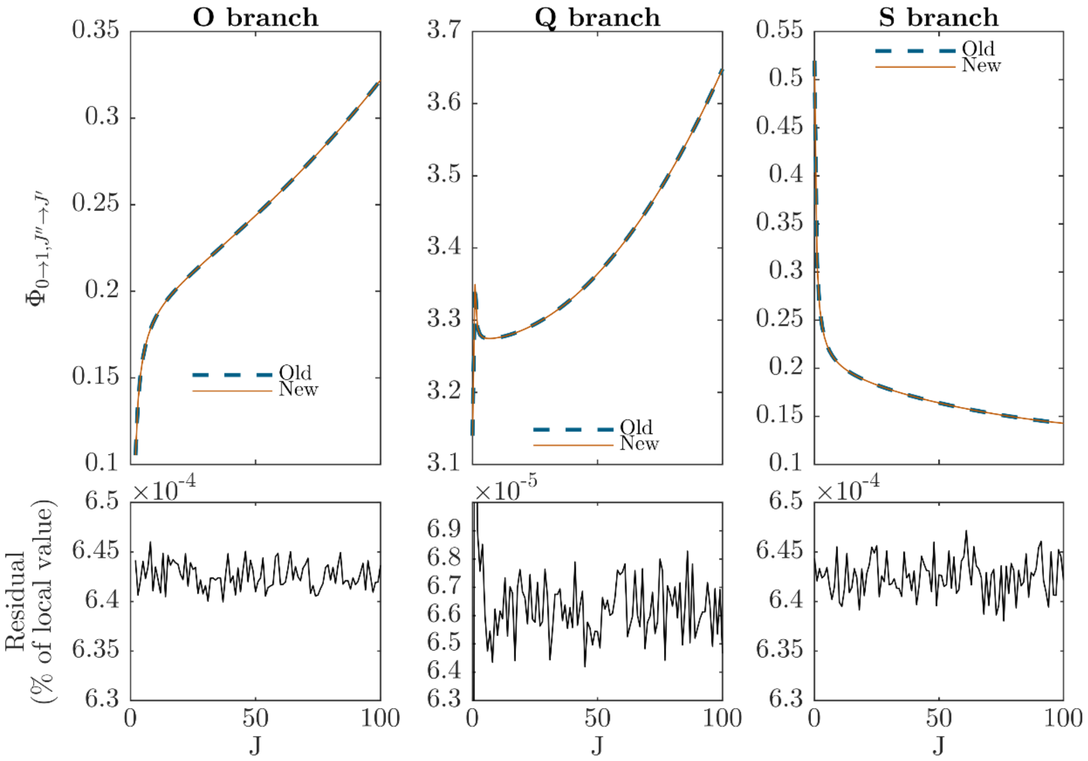

Figure C.4: Comparison between Φ matrix elements from old code using a polarization factor of 1.17 and new code with optimal polarization factor of 1.64.

An additional benefit of the new code is the ability to isolate the different polarizations within the scattered signal. This allows for the effect of the multiple-pass cell on the collected Raman signal to be analyzed. Owing to the tilting of the beam relative to the collection axis as it passes through the cavity, the effect is not straightforward. Because the polarization components are computed relative to the scattering plane, this tilt of the scattering plane relative to the collection optics must be accounted for. Fig. C.5 shows this problem schematically for the overall multiple-pass cell. The components of the scattered signal from each beam can be broken down by their polarization relative to the collection optics as

$$I_{vert} = I_{||} \sin^2 \beta + I_{\perp} \cos^2 \beta \tag{C.8}$$

$$I_{hori} = I_{||} \cos^2 \beta + I_{\perp} \sin^2 \beta \tag{C.9}$$

where β is the angle of each individual beam relative to the collection optics.

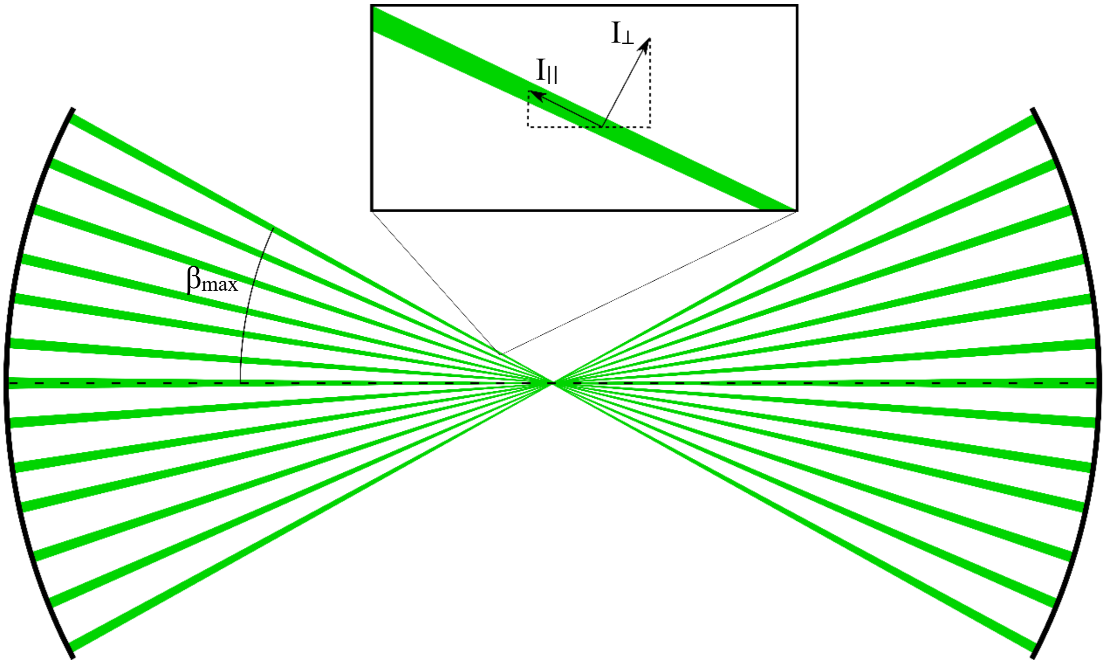

Figure C.5: Diagram of multiple-pass cell beam geometry.

The overall effect of multiple passes can be evaluating by summing the contributions from Eqs. C.8 and C.9 over all of the beams in the cell. The general effect is a reduction in the Q branch signal relative to the O and S branches due to the Q branch being primarily polarized perpendicular to the scattering plane, while the O and S branches are relatively depolarized. Figure C.6 below shows this effect for the optical arrangement of Ch. 4: a multipass cell with a maximum angle of 14° and a collection f-number of 2.2. The signal in the O and S branches is enhanced relative to the signal peak in the Q branch. Increasing the number of passes creates a more even distribution of beams between β_{max} and $-\beta_{max}$, reducing the overall effect. The effect appears to converge to a fixed pattern as the number of passes increases beyond 10. Overall, the effect on the overall spectra is very weak for this configuration, at most enhancing the O/S-branch signal by 0.008% of the Q-branch signal, or approximately 0.8% of the typical O/S-branch signal.

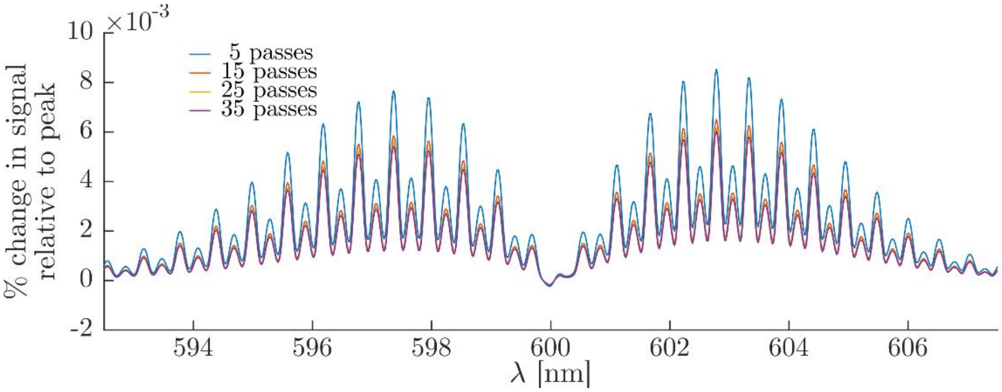

Figure C.6: Effect of number of passes on collected N_2 Raman signal at 500 K for a multiple-pass cell maximum angle of 14°.

The effect of cell maximum angle (β_{max} in Fig. C.5) on Raman signal at various collection f-numbers is presented below in Fig. C.7. As expected, the Q-branch signal reduces more drastically with increasing cell angle because it is highly polarized. As the maximum cell angle is increased, the more extreme tilt in the scattering plane relative to the collection optics reduces the component of $I_\perp$ in the vertical direction. Because the collection system has been determined to more efficiently transmit vertically polarized scattering, this reduces the Q branch signal overall. This effect is much weaker in the O and S branches as they are very weakly polarized. For the multiple-pass cell and collection used in Ch. 4, the expected gain from 25 passes is reduced only slightly: 24.67 and 24.94 for the Q- and O/S-branches, respectively.

Figure C.7 also includes curves from a range of collection f-numbers. Overall, the change in this trend with different collection f-numbers is slight, as the curves only begin to deviate noticeably at the highest values of β_{max}. The variation of Q-branch is 0.14% for the extreme change in f-number from f/1 to f/22. The O- and S-branches show a slightly larger effect than in the Q-branch, although the discrepancy is still negligible relative to the change with cell f-number.

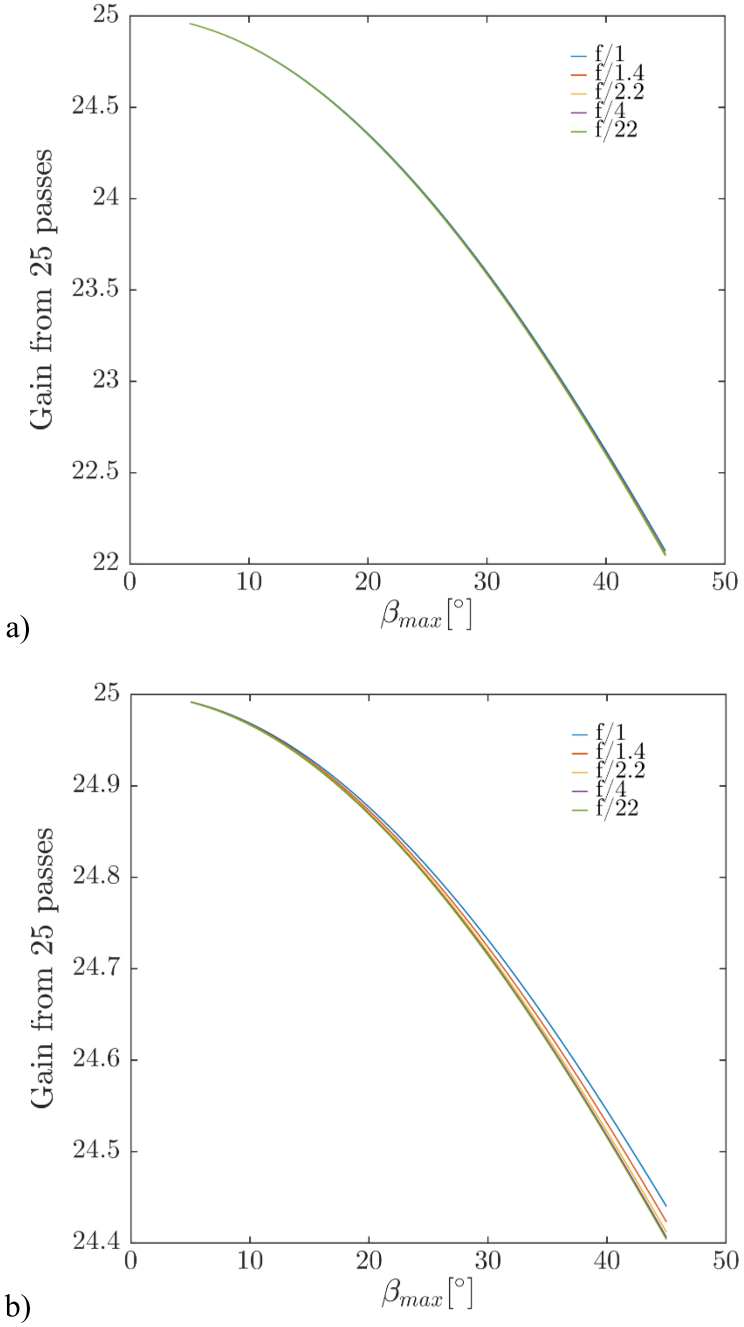

Figure C.7: Effect of maximum multiple-pass cell beam angle (β_{max}) on gain from 25 laser passes for (a) Q-branch and (b) O/S-branch transitions.

APPENDIX D: DESIGN OF SINGLE-SHOT MEASUREMENT APPARATUS

D.1 – Ring Cavity Temporal Pulse-Stretcher

A schematic of an ideal 2-cavity pulse stretcher following the 1:2:4 rule of Ref. [100] is illustrated below in Figure D.1 for a 6 ns FWHM temporally-Gaussian input beam. The expected temporal pulse profiles through each stage of the stretcher are also shown in Figure D.2. Using mirrors of 99.5% and 99% reflectivity for 0° and 45° degree incidence, this layout is expected to produce a reduction in peak power of 78% and a maximum throughput of 90%.

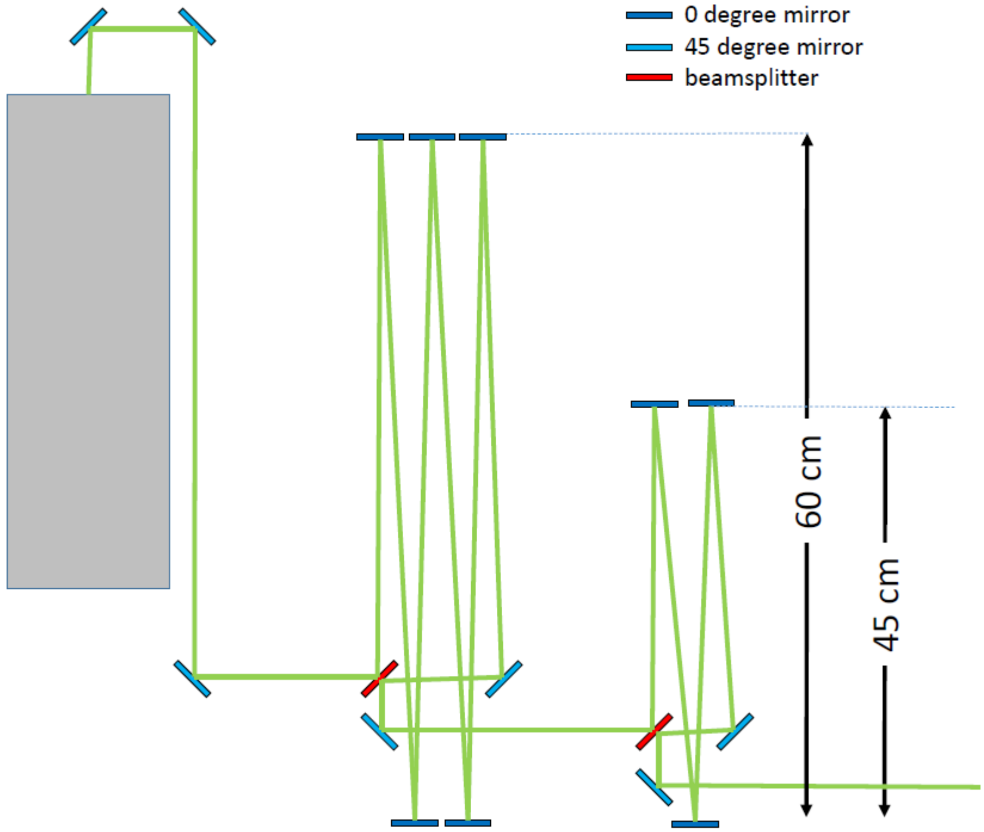

Figure D.1: Schematic of a pulse stretcher system using 2 cavities with ideal cavity lengths for a 6 ns input laser pulse.

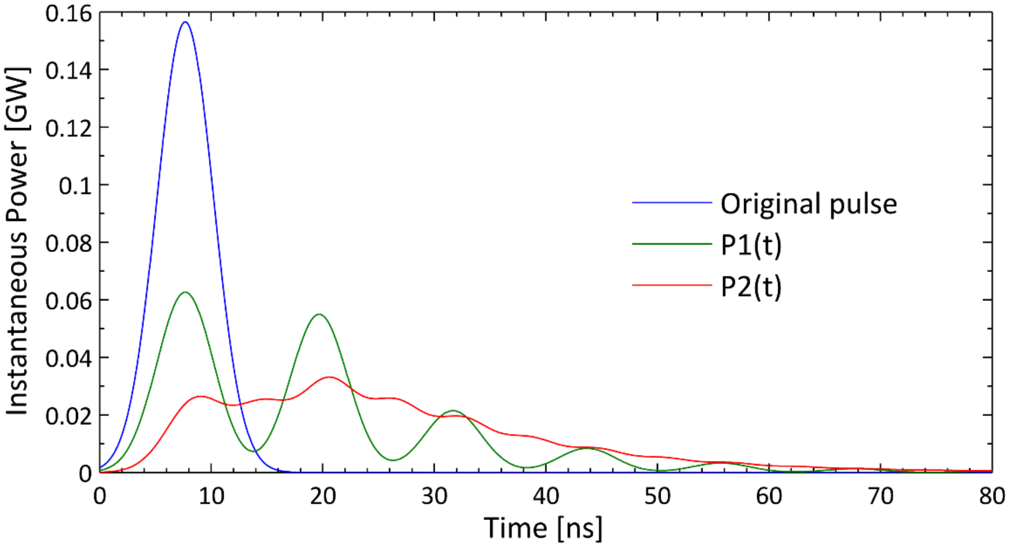

Figure D.2: Theoretical temporal pulse profile for an ideal 2-cavity pulse-stretcher with cavity delays of $2\tau_{laser}$, and τ_{laser}. P1(t) represents the pulse profile after the first cavity and P2(t) is the pulse profile after the second cavity (passing through cavities 1 and 2).

The chosen design used only 2 time-of-flight delay cavities. The cost per cavity grows drastically as the number of cavities is increased due to the geometric progression (1:2:4) of optimal delay times ratio of cavity delay. In practice, each pass within a cavity is limited in length and thus a longer cavity requires significantly more mirrors. The cost of adding a third cavity was investigated and it was determined that the additional cavity would cost more than the first 2 cavities combined. Additionally, the overall optical path length of using only 2 cavities allowed for the use of 1” diameter mirrors throughout. A third cavity would require larger mirrors as the laser beam divergence would cause the beam to clip on the edge of smaller mirrors.

With the large number of mirror reflections required in the pulse-stretcher, the chief requirement of the cavity mirrors is a high reflectivity. The mirrors used were specified to have a minimum reflectivity of 99.5% and 99.9% for the 0° and 45° angle-of-incidence mirrors in S-polarized reflections, respectively. The vertical polarization of the source laser dictated that all reflections in the pulse stretcher were S-polarized. The 45° angle-of-incidence mirrors used in the periscope to direct the stretched pulse into the multiple-pass cell (as pictured in Figs. D.12 and D.13) were P-polarized reflections, which is rated by the manufacturer at >99% reflectivity. The beam splitters used were rated at 40% reflectivity at 45° S-polarized incidence.

Alignment of the pulse stretcher apparatus is tedious as the slightest adjustment in one of the mirrors necessitates a corresponding correction in all of the downstream optics. The cavity mirrors must be adjusted with an extremely high degree of precision in order to ensure that the beam from each subsequent pass through the cavity exits the cavity superimposed with the last pass. Thus, adjustment of cavity lengths was kept to a minimum due to the laborious nature of keeping each mirror aligned to this level of precision. The final cavity lengths of were measured to be 2.17 and 5.12 m. While these lengths do not perfectly match the "ideal" values suggested in Ref. [100], they actually provide a slightly better reduction in peak instantaneous laser power. This is due to having cavity delays longer than the 180 and 360 cm ideal lengths for a 6 ns pulse. The 1:2:4 cavity length rule was suggested based on a balance between peak power reduction and pulse profile smoothness. The current arrangement gives up a small penalty in smoothness for a further reduction in peak power relative to the recommended 1:2:4 cavity length progression. Precise measurement of the cavity delays is also possible by observing the temporal profile of each delay stage. The profiles for laser pulses processed by each cavity is presented below in Fig. D.3. By measuring the delay between peaks, cavity delay times of 16.6 and 7.2 ns are obtained for the first and second cavity, respectively, which agree very well with the measured cavity lengths. The final system dimensions and measured temporal beam profile are presented in Figs. 4.3 and 4.4, respectively. As pictured in Figure 4.3, the optics for each cavity were mounted to plates to allow for each cavity to be moved easily as a single unit for use in other experiments without re-aligning each individual cavity optical component.

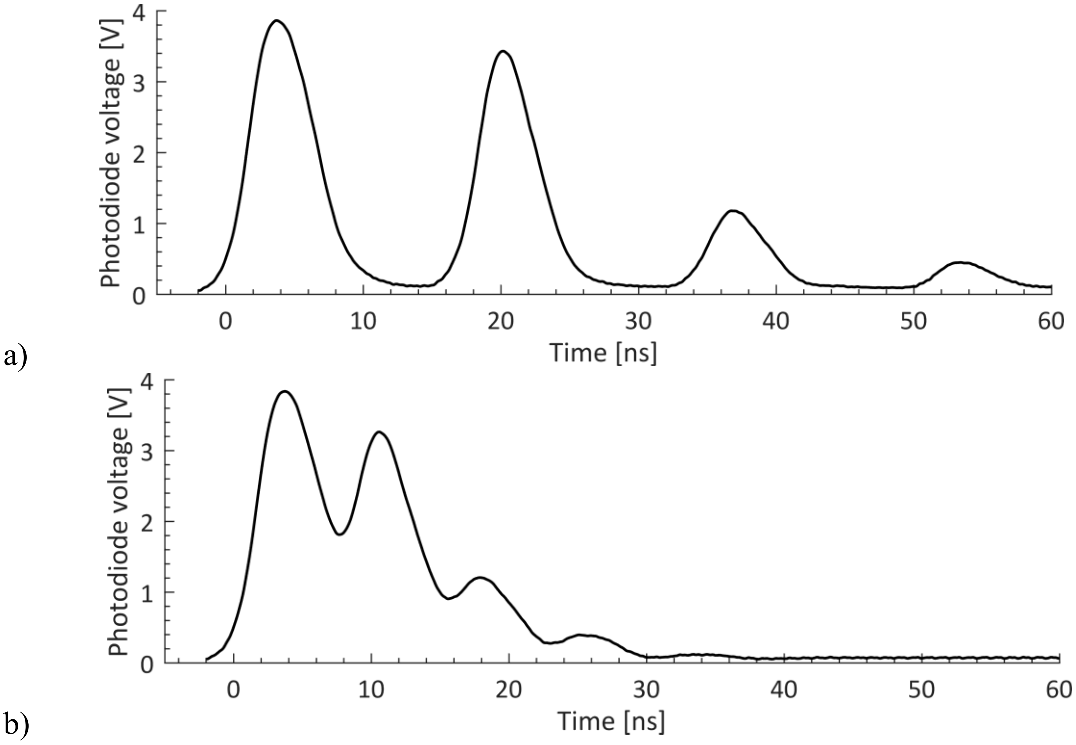

Figure D.3: Temporal pulse profiles generated by (a) the long cavity and (b) the short cavity of the pulse stretcher.

The source laser was equipped with an injection seed laser, which provides a narrower spectral bandwidth (0.003 cm^{-1} instead of 1 cm^{-1}), reduced timing jitter, and smoother temporal pulse profile. While the second two effects of injection seeding are desirable for the current experiment, the narrowed spectral bandwidth (linewidth) causes an increase in the coherence length of the pulse. Because the beam will be introduced into a multiple-pass cell where it is passed over itself, the coherence length needs to be considered to ensure that the coincident pulses at the cell foci do not add in phase, thus negating any reduction in laser power obtained by stretching the pulse. The coherence length is the propagation distance over which the laser pulse's coherence function drops to $1/e$. It can be defined mathematically as

$$L_{coh} = \frac{c}{\pi \Delta \nu} \tag{D.1}$$

where c is the speed of light and $\Delta \nu$ is the FWHM linewidth of the laser [109]. This coherence length value is 1.06 m for the injection seeded case and only 3 mm for the unseeded linewidth. These distances are much shorter than the round-trip distance of 1.6 m for the multiple-pass cell used in these experiments (described in Section D.2). Thus, the pulses are not expected to add coherently at the measurement location.

Figure D.4 shows a comparison of stretched laser pulses with and without the injection seeder active. Using the injection seeding made pulse profiles much more smooth and consistent. This meant that the input energy could be brought closer to the limit at which laser-induced sparks occurred in the cell due to spurious spikes in laser power not being present. At a fixed input pulse energy, spark events were observed to occur less frequently with the seed laser in use. Thus, the laser was operated with the injection seeder active for the measurements made in Ch. 4.

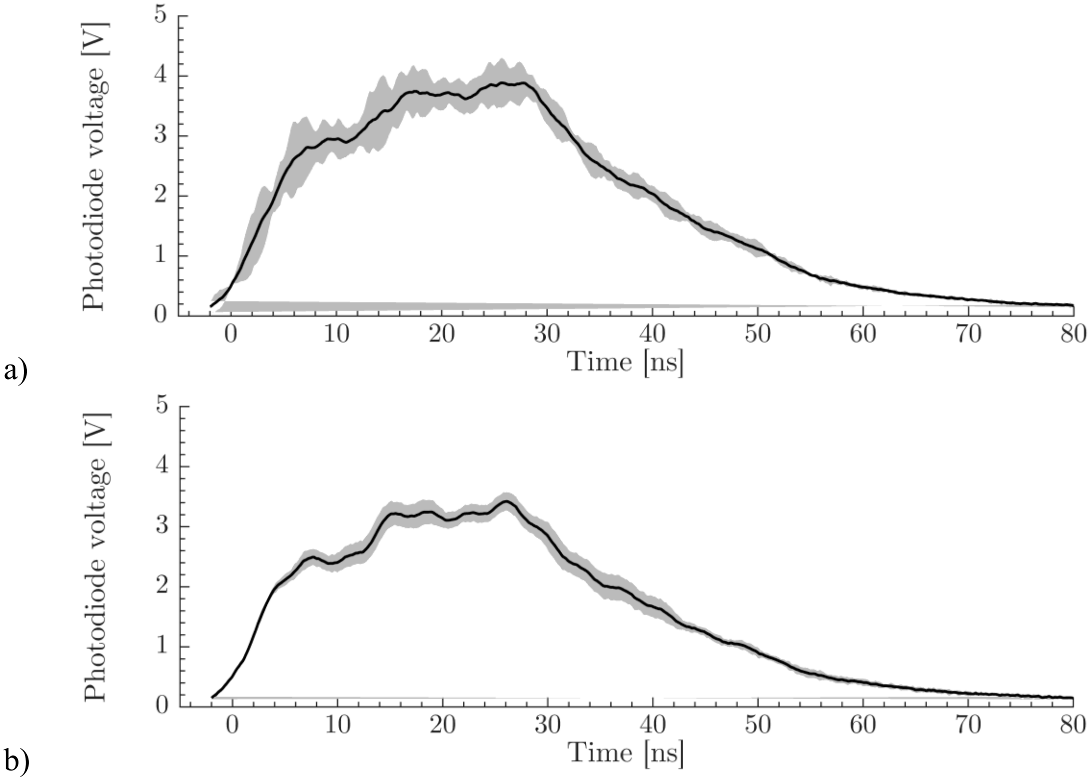

Figure D.4: Temporal laser pulse profiles downstream of the pulse stretcher for (a) with injection seeder inactive and (b) with injection seeding active. The lines indicates the mean profile, while the gray shaded region indicates the envelope of extreme values for

D.2 – Multiple-Pass Cell

In addition to preventing breakdown, sufficient excitation energy must be provided in a single pulse to achieve adequate signal. The time-average results above utilized approximately 500-700 J of incident laser energy per measurement. Generally, this integration time could be reduced without significant loss in quality of the spectra, but the energies required are still 2 orders of magnitude larger than what is provided in a single pulse of a high energy Nd:YAG laser. One way of increasing collected signal is to increase the slit size of the spectrograph. The time-average measurements used a 100 μm slit for high spectral resolution. This is not necessary for the single-shot measurements, as the rotational structure of the O- and S-branches will not be discernable from the noise.

First, a preliminary study was performed to observe the effect of excitation energy and slit size on the resultant spectra. Fits to these spectra were performed to investigate the effect on the derived temperature values. Excitation for this study was provided by the same 11 mJ pulse energy Nd:YLF laser which was used in the time-average measurements. Spectra were collected from different numbers of laser pulses to simulate the effect of different incident pulse energy. Results of the study are summarized below in Figs. D.5 and D.6. The error bars in the plot show 2 standard deviations of the temperature results from the 100 spectra collected for each case. As expected, a larger slit size increases signal, as seen in Fig. D.5. In addition, fit results obtained from only 5.5 J of incident energy with a 250 μm slit size compare well with the results for much higher energy, where the magnitude of temperature variations are approaching the actual fluctuations in the air flow temperature.

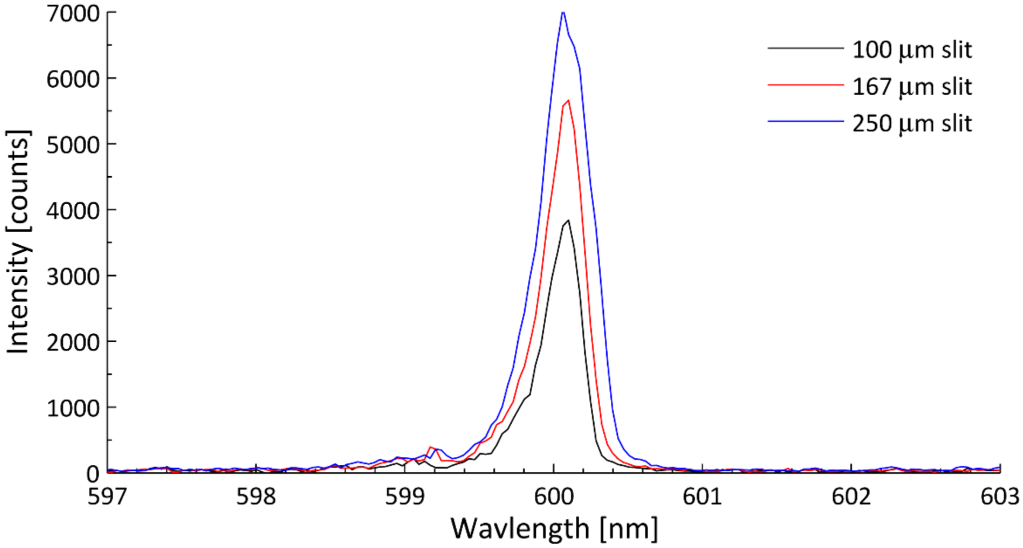

Figure D.5: N_2 spectra of 750 K air for different slit sizes for 500 laser pulses (5.5 J)

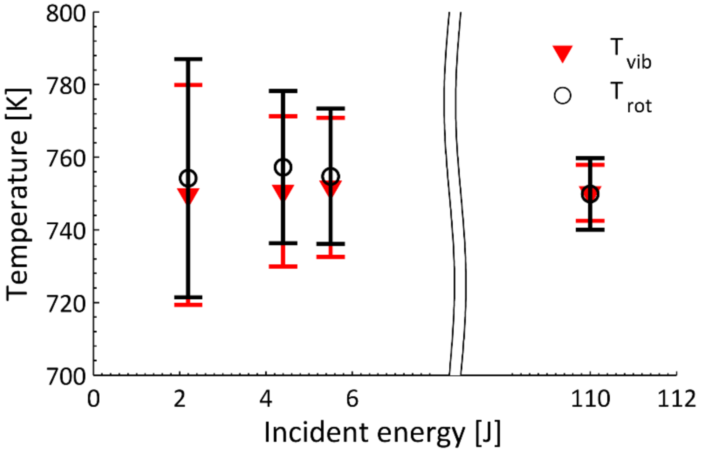

Figure D.6: Effect of incident laser energy on fit results from N2 spectra of 750 K air using a 250 μm slit

In order to obtain multiple joules of incident laser energy from the available laser, multiple laser passes through the measurement volume is required. Multiple-pass ("multipass") cells have been used in many applications to enhance Raman scattering signal as discussed above [34],[46],[110]–[112]. The current system utilizes a pair of concave mirrors that will be separated by slightly more than 2 times their common radius of curvature. This configuration provides two distinct focal regions in the cavity while the beam walks in a line across each mirror surface. A system of this type has been demonstrated previously with a signal gain of 20 [34]. The multiple-pass cell for this study consisted of a pair of matched 101.6 mm diameter, 100 mm focal length mirrors with 99.7% reflectivity at 532 nm. This system used in this study was obtained and installed in the current facility to evaluate the focusing characteristics in the turbulent jet. The cell was found to maintain a stable focus (with only slight movements from turbulent fluctuations) during jet operation. An image of the focal regions of this configuration is shown below in Fig. D.7. The mirrors from this system do not have long enough focal length to provide adequate distance from the hot coflow for them to be used with the heaters running for actual Raman measurements. Thus a new pair of mirrors needed to be selected to create a cell with a larger mirror separation distance. Additionally, the new cell mirrors will require a much higher laser damage threshold, as the laser used in Ref. [34] had a pulse energy of only 6 mJ.

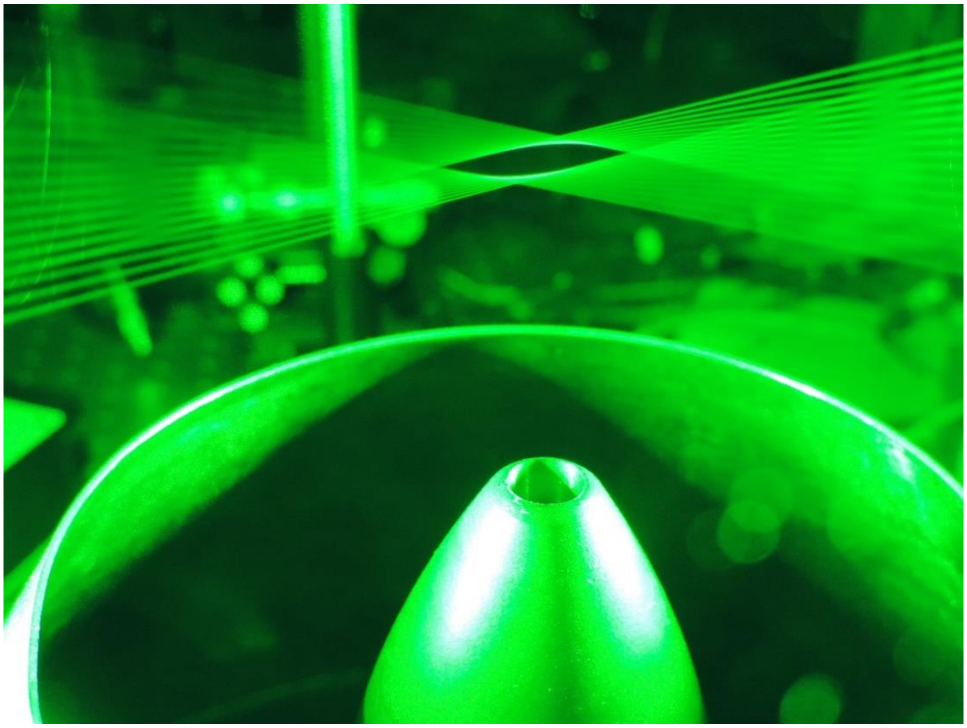

Figure D.7: Focal region of small multipass cell installed above current facility for proof-of-concept study

The design of the multipass cell requires a balance between the speed of the focusing optic and the size of the laser spot on the multipass mirror surfaces. A slower (longer focal length) focusing optic will produce a larger focal spot and therefore avoid air breakdown. This slow focusing will also lead to a smaller spot size of the laser beam on the mirrors, which may damage the mirror surface. The parameter space of focusing optic configurations is illustrated below in Figure D.8 for a multipass mirrors of 8 inch focal length and the temporal pulse profile of Fig. D.2. For this preliminary study, a conservative mirror damage threshold of 20 J/cm^2 was used. The shaded region shows the region of valid configurations where air breakdown and mirror damage are both avoided. In practice, this will require testing to determine the fastest possible lens that does not cause air breakdown for the temporally stretched pulse before the laser is introduced to the multipass cell.

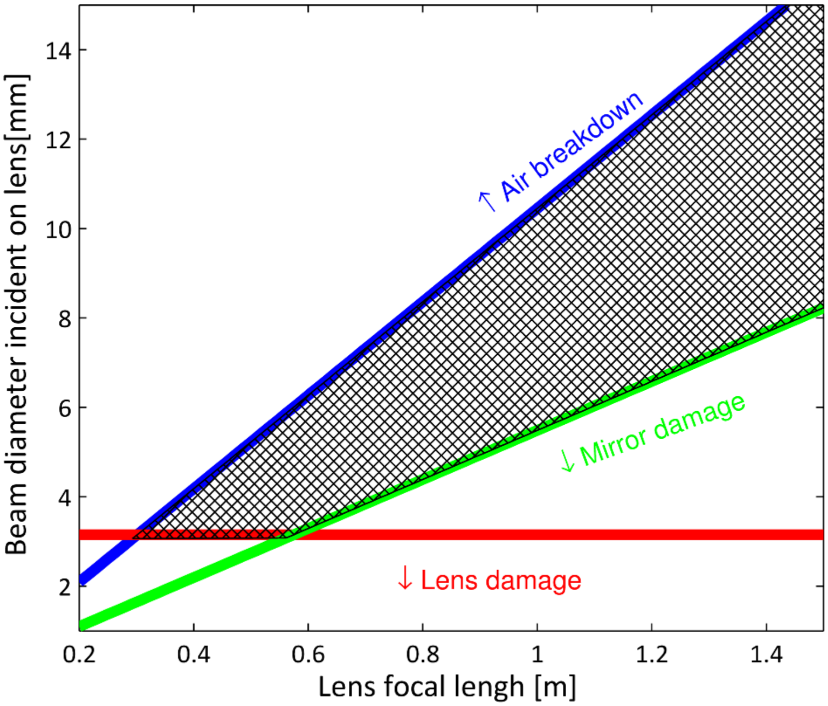

Figure D.8: Possible input beam configurations to prevent air breakdown and mirror damage

In order to choose an exact configuration for the multiple-pass cell mirrors, the ZEMAX ray tracing software package was used. The ray tracing software allowed for us to vary an array of different system parameters and study the effect on the overall system performance (number of laser passes, peak fluence on the mirror surfaces, etc.). Due to the vast number of configurations possible, being able to tweak the angle and separation of each optic individually is invaluable in diagnosing issues in the actual system.

The typical arrangement for the multipass system modeled in the ZEMAX non-sequential environment is show in Fig. D.9. The beam is shown to change color with each reflection in order to identify individual passes through the cell. The system consisted of a pair of identical spherical mirrors and a plano-convex lens to focus the beam into the cell. The circulating power in the cell was monitored by placing a transparent plane at the center of the cell and the distribution of laser fluence on each mirror surface was also examined.

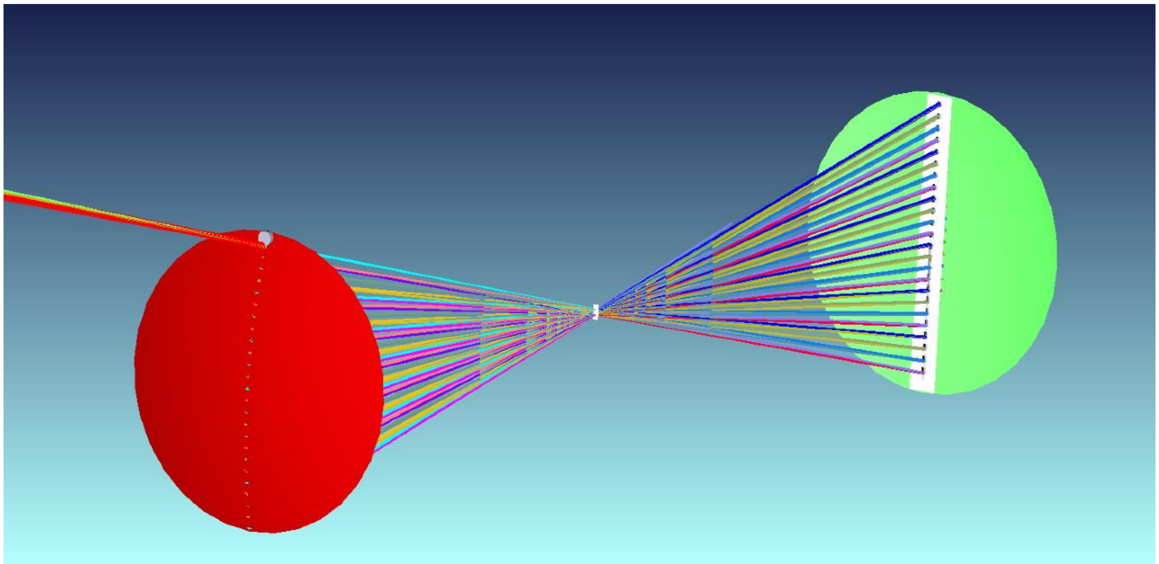

Figure D.9: Configuration of the multiple-pass cell in ZEMAX model.

Without going into details of the ZEMAX modeling, several key insights into the operation of a multiple-pass system were obtained by adjusting the relative position of the optics and noting the change in the spot pattern on the mirrors and total circulating energy in the cell. A sample pair of laser fluence distributions on the cell mirror surfaces for off-design cases are presented in Fig. D.10. First, the mirrors need to be separated by slightly more than 2 radii in order to have a stable two-focus system. If the mirrors are too close together, the system becomes unstable and the beam is never retro-reflected back through the same point. Too large of a separation between mirrors causes the beam spots on the mirror surface to have a repeating pattern of large and small spots, which risks damaging the mirror coating (shown in Fig. D.10a).

If the lens which initially focuses the beam into the cell is placed too close to the cell focus, the beam spot pattern shows a first reduction in size and then growth as the beam traverses the cell. A far more favorable error to make is placing at too long of a distance from the cell, which causes the spots to gradually grow as they traverse the cell (shown in Fig. D.10b).

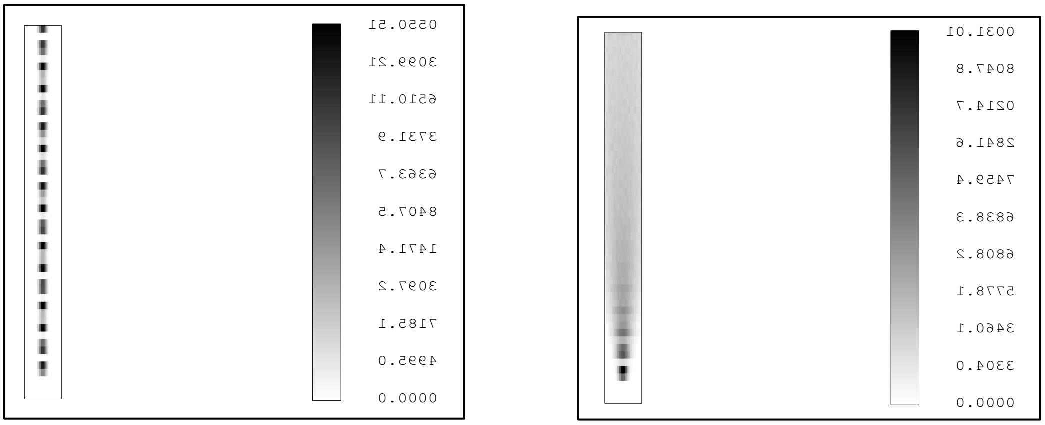

(a) (b)

Figure D.10: Laser fluence distributions on mirror surfaces generated in ZEMAX for (a) cell mirrors separated by too large of a distance and (b) the input lens located too far from the cell center. Units are in J/cm^2.

Neither of these scenarios affected the overall number of passes circulating in the cell. That was dictated almost completely by the angle and height at which the beam enters the cell. The highest number of passes through the cell is made possible with a beam that enters the cell as near to the mirror periphery as possible. However, the beam cannot simply be directed into the cell past the edge of the mirror, as the subsequent reflection will not occur within the clear aperture of the mirror, which is the region of the surface which adheres to the reflectivity and curvature specifications. Typically the edges of optical components are beveled to make them more robust and coatings such as the high reflectivity coating on these mirrors cannot be applied all the way to the edge. Thus, a relief must be cut into the mirror to allow the beam to enter the cell. This slot should be just large enough so that first pass falls within clear aperture specification of the mirror, intruding any further into the mirror reduces the maximum number of laser passes possible. The beam should then be aimed into the cell so that it is at the very bottom of the slot and the next reflection on the slotted mirror falls fully on the mirror surface.

The separation of the two focal spots of the cell gives a good indication of being near the peak number of passes in the cell. As one brings the two spots together, the spots on the mirrors move close together as well, and the beam traverses the cell more times before exiting. At a very small separation between spots, a significant portion of the beam overlaps with the previous spot and leaks back out of the cell through the slot after one round trip. Getting as close as possible to this condition without going too far provides the maximum number or passes and therefore maximum energy at the focal spot. For example, the configuration in Fig. D.9 shows the beam entering the cell 92 mm from the centerline at an angle of 13°, which results in a spot separation of 4 mm and 22 J at the foci. Figure D.11 below shows the resulting beam fan for a slight change in input angle to 13.25°, which increases the total energy to 136 J and moves the focal spots to within 750 μm of each other. The spacing of the reflections of the mirror is greatly reduced in this configuration. This configuration represents an ideal alignment, as bringing the cell foci any closer leads to a reduction in total energy due to the portion of the beam leaving the cell through the cell becoming significant.

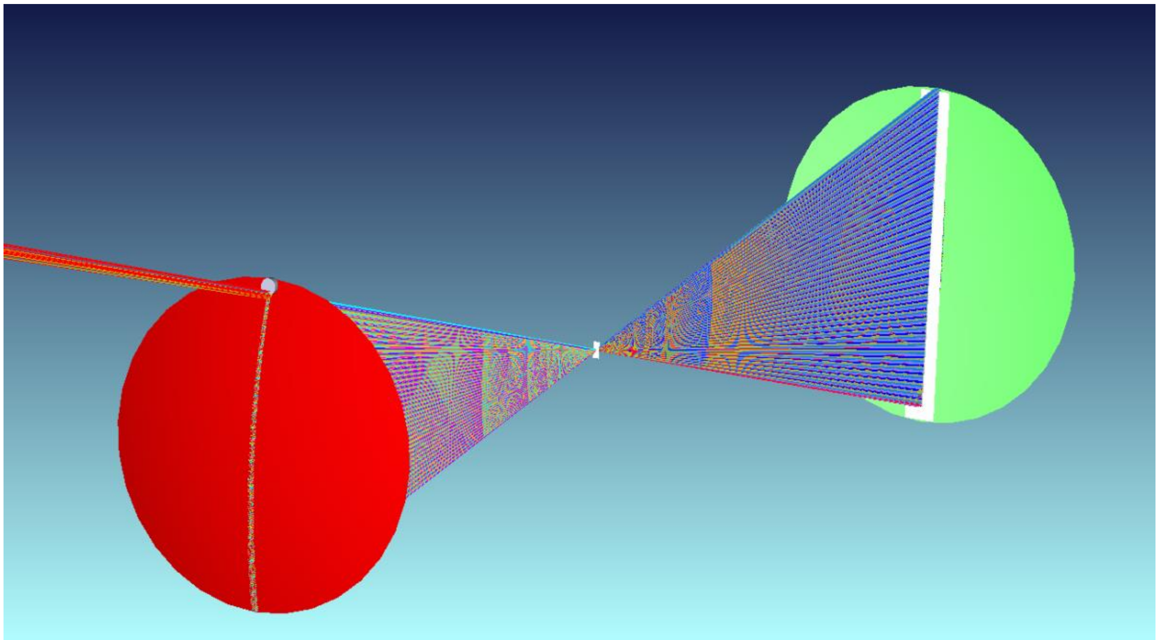

Figure D.11: ZEMAX model of the multiple-pass cell beam pattern for very small separation between cell foci.

While the ZEMAX model predicts the possibility of a very high number of passes (> 100) in an ideal alignment, in practice the number of passes will be limited by the precision at which the cell can be adjusted. Another effect, which was not observed in ZEMAX but became apparent in practice, was that bringing the two foci close together (and thus getting more passes) made the cell much more unstable. This is due to the fact even the smallest perturbation from this state (due to vibration in a mirror or refraction of the beam) causes initial beam to be retro-reflected back out of the cell through the input slot. Thus, in the experiments presented in this dissertation, the strong turbulence near the measurement location and large thermal gradients in the flow limited the number of passes. The final alignment was a balance of achieving a maximum number of passes in the cell which would remain stable throughout the experiment.

The final mirror design was selected to be a pair of spherical mirrors with a 200 mm focal length. The most important parameter in selecting the manufacturer for the mirrors was the performance of the high reflectivity coating. The coating on the purchased mirrors was specified to have a reflectivity of > 99.9% at 532 nm. The coating was specified have a clear aperture out to 2 mm from the edge of the mirror, ensuring a maximal number of passes will be possible in the cell. A radial slot cut was cut into one of the mirrors in order to allow for the ingress of the laser beam into the cell. The dimensions of the slotted mirror and a photo are shown in Fig. D.12 below. The other mirror is identical except that it did not have a slot. The high reflectivity coating applied to both mirrors was tested by the manufacturer to not show damage when up to 45 J/cm^2 of peak fluence for a 1064 nm pulse with a 20 ns FWHM pulsewidth. This specification of damage threshold based on peak energy density can be adjusted to give a rough outline of the coating's limitation for the laser beam used in this study. Scaling to the current laser wavelength of 532 nm using the guideline that laser damage threshold scales as the inverse square root of laser wavelength in the visible range, this damage threshold becomes 31.8 J/cm^2 [113]. Accounting for the reduction in peak power due to the temporal stretching of the pulse, the maximum acceptable energy density is raised to 107.7 J/cm^2 [114]. Thus, the relation between laser pulse energy and the acceptable minimum beam spot size on the mirror to not exceed this energy density at the beam center can be expressed as

$$d_{min} > \sqrt{\frac{2E}{1.077\pi}} = 0.769\sqrt{E} \tag{D.2}$$

where d_{min} is the minimum $1/e^2$ spot diameter in mm and E is the laser pulse energy in J. This, however, does not come with any factor of safety or account for "hot spots" in the beam spatial distribution. In practice, the mirror spots were always larger than 5 mm, keeping the peak fluence far from the laser-induced damage threshold. Some damage did occur on the mirror surfaces in a few cases, but were likely due to dust in the room settling on the mirror during an experiment. These events tented to occur when the laser had been operating for a long period without any adjustment being made to the optics, so a change in spot geometry on the mirror surface is highly unlikely. Continued damage was avoided by rotating the damaged regions away from the vertical line where the laser contacts the mirror, if possible.

As shown in Fig. D.10b, the high reflectivity coating is missing from the mirror surface in 4 small strips around the periphery. These regions are 5 mm wide and are caused by the clamps used to secure the mirror during the coating process. It is important that the laser does not impinge upon these regions as the lack of a high reflectivity coating will lead to laser-induced damage occurring rapidly. Because the locations of beam incidence on the mirror form a vertical line, it is imperative that these uncoated regions are located away from the 12 o'clock and 6 o'clock positions on the mirrors. For the unslotted mirror, this merely requires rotation in its mount. In the case of the slotted mirror, the requirements given to the manufacturer required that these clamps would be kept away from the slot and 180° from the slot and thus the uncoated regions ended up located in the positions shown in Fig. D.12.

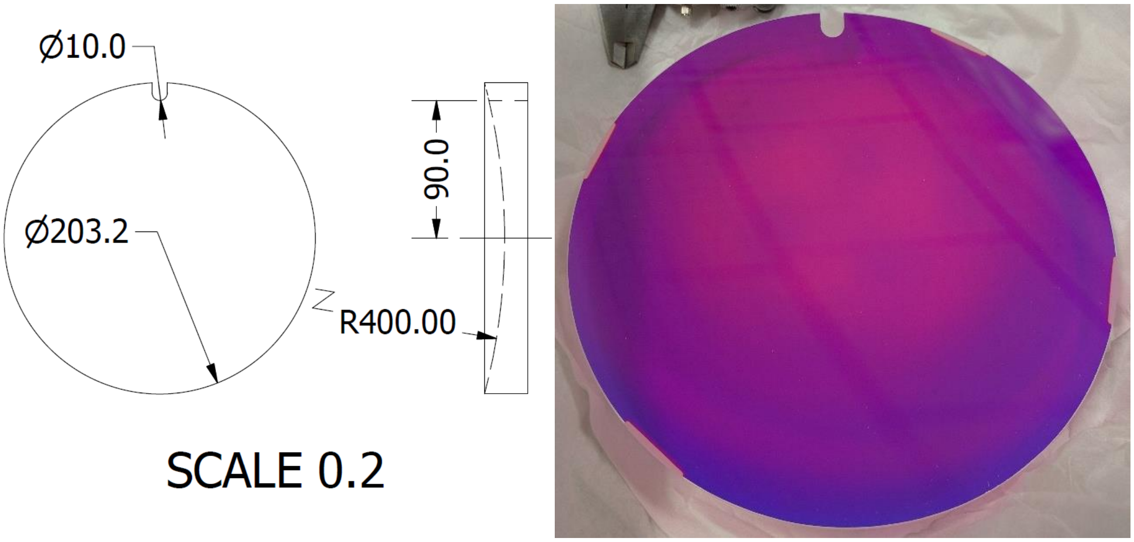

(a) (b)

Figure D.12: Slotted multiple-pass cell mirror in (a) dimensioned CAD drawing and (b) photograph. Dimensions in the drawing are in millimeters.

In addition to the slot cut into the mirror, the mirror mount also needed to be modified in order to allow for the beam to pass into the cell. A radial slot was machined into the mount to allow for the high angle at which the beam enters the cell. Additionally, the set screw located at the top of the mount which secures the mirror in the mount had to be relocated away from the slot. A set of dimensioned drawings of the modification made to the mirror mounts is shown in Fig. D.13 below.

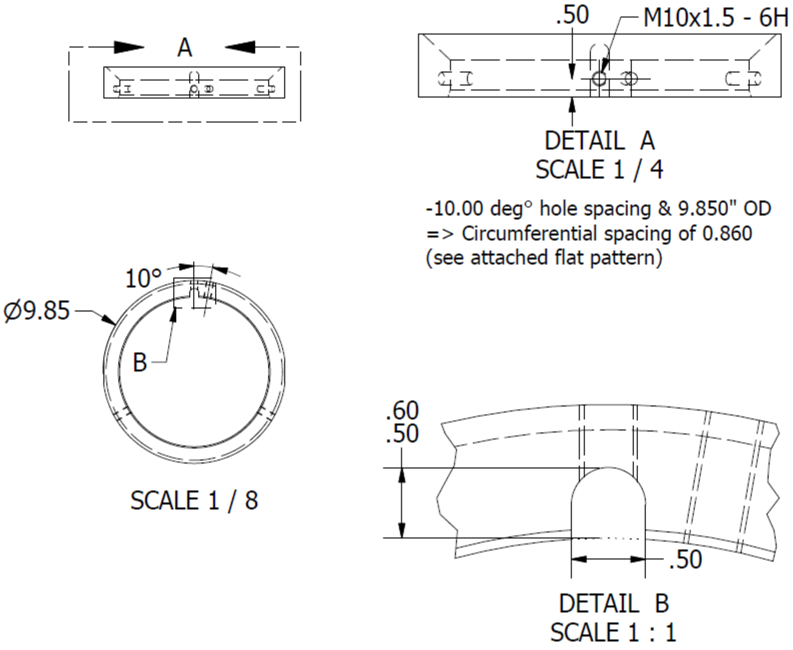

Figure D.13: Modification made to multiple-pass cell mirror mount to allow for beam ingress. Dimensions are in inches.

In order to direct the beam into multiple-pass cell, the beam was raised from the table and directed downward by a periscope consisting of a pair of 50.8 mm diameter mirrors. The larger mirrors were used to allow for the beam to be shifted with translation stages in order to align it perfectly with the cell mirrors. The lens used to focus the laser beam into the multiple-pass cell was a 1.5 m focal length plano-convex lens. The lens had an anti-reflection coating for < 0.2 % reflectance at 532 nm. CAD renderings of the lens and periscope, as well as the rest of the multipass system are presented in Figs. D.14 and D.15 below.

Due to the high risk of laser-induced damage from a focused laser spot, the cell mirrors must be placed at approximately correct positions before the beam can be introduced into the cell and fine adjustments can be made. Additionally, if the cell mirrors are set in the correct position for a few degrees of freedom, the amount of time required for aligning the cell is greatly reduced; i.e. the user has many fewer free parameters to play with while trying to achieve optimal alignment. To aid in the alignment process, circular targets with the exact diameter of the mirrors and a small center hole were fabricated using a laser cutter. First, the laser beam was set at the desired height above the mid-plane of the nozzle exit. The beam was confirmed to be aligned with the facility by observing that the beam location relative to the nozzle was unchanged over the full range of movement of the facility's translation stage. Next, the two mirror mounts were located so that the beam passed through the center hole with all of the adjustment controls at the center of their travel. The second (non-slotted) mirror was then installed in its mount and its angle was adjusted so that the laser beam is retro-reflected back through the center hole in the other target. At this point, the mirror centerlines were aligned with one other and with the desired measurement location. The slotted mirror was then installed and made parallel with the other mirror with careful measurements of the distance between the edges of the 2 mirror mounts around their circumference. Thus, the free variables for aligning the cell were reduced to the height and angle of the input beam, which were adjusted at the final 50.8 mm flat mirror. At this point the other cell mirror was installed and the beam was brought into the cell using the lens and periscope system previously described and precise alignment was achieved by observing the cell focal region.

The long beam propagation distance within the multiple-pass cell provided an incidental benefit for optimizing the pulse-stretcher alignment. For example, 20 round-trip passes through the multiple-pass cell add up to over 30 m of beam flight distance. Over such a large propagation distance, very small spatial deviations of successive passes through the pulse-stretcher cavities (the peaks in Fig. D.3) can be observed. By alternately blocking and unblocking each cavity and observing the spot pattern on a multipass cell mirror, precise superposition of these individual pulses can be achieved to a degree which is unattainable without the cell.

With 4 passes through each cavity, the beam propagates a distance of approximately 35 m from the first partial reflector to the focal spot. Thus, a shift at the focal spot of 100 μm occurs with only a 3 μrad shift in the first partial reflector. This corresponds to a 0.15° rotation in the 100 thread per inch angular adjustment knob on the mirror mount. In this setup, these tiny adjustments were made by hand, as there is not much benefit to perfect cell alignment due to the defocusing that occurs due to the turbulent fluctuations and high thermal gradients. Future applications of this type of pulse stretcher to a calmer flow could benefit from the use of piezo actuators for higher precision mirror adjustment, especially on the partial reflectors. For example, piezo-actuated mirror mount models such as Thorlabs' PIAK10 and model number 8809 from Newport provide angular resolution of 0.5 and 0.7 μrad, respectively.

Alignment of the multiple-pass cell mirrors also required precise control of the mirror position and angle. A combination of manually-driven positioning components was assembled to allow the cell mirror to be precisely controlled in 5 degrees of freedom (translation in all directions and rotation about the vertical and scattering axes). The stack of kinematic elements for the cell mirrors can be seen in Fig. D.15 below. The mirrors were held in gimbal mounts which rotated the mirrors about their center to a precision of 8 μrad (for 1° of rotation of the adjustment knobs). Horizontal location of the mirrors was controlled with Vernier micrometer-driven translation stages, while vertical position was achieved with large screw-driven jacks. While the translation stages provided single micron precision, the jacks were not as exact. Their movement was non-linear, providing, on average, approximately 4 μm of movement for 1° of rotation of the adjustment knob.

These large jacks were used because they could handle the weight of the mirrors and gimbal mounts.

Future applications of this type of multiple-pass system could improve upon the current setup with a few specific upgrades. The two most important parameters when aligning the multiple-pass cell were the distance between mirrors and the mirror angle about the scattering direction. While the micrometer-driven stages gave adequately precise control of the mirror separation, getting the absolute maximum number of passes through the cell was difficult with the precision of the angular adjustment knobs on the gimbal mounts. Upgrading the mirror adjustment mechanism to dual-thread differential micrometers (replacing the current Newport part number BM17.04 with BD17.04) will improve the angular precision to 0.8 μrad. The coarse control over the vertical position of the mirrors also restricted how well the multiple-pass cell could be aligned a maximal number of passes. At the expense of overall travel (which was not needed for this application), inclined ball bearing stages, such as model number MVN120 from Newport, could replace the current jacks to provide vertical translation of heavy loads at up to 0.5 μm precision. As with the actuators suggested for the pulse-stretcher cavity mirrors, these improvements would only have aided slightly in the current work, but could prove to be significantly more useful for measurements made in a flow without such strong thermal gradients and turbulence.

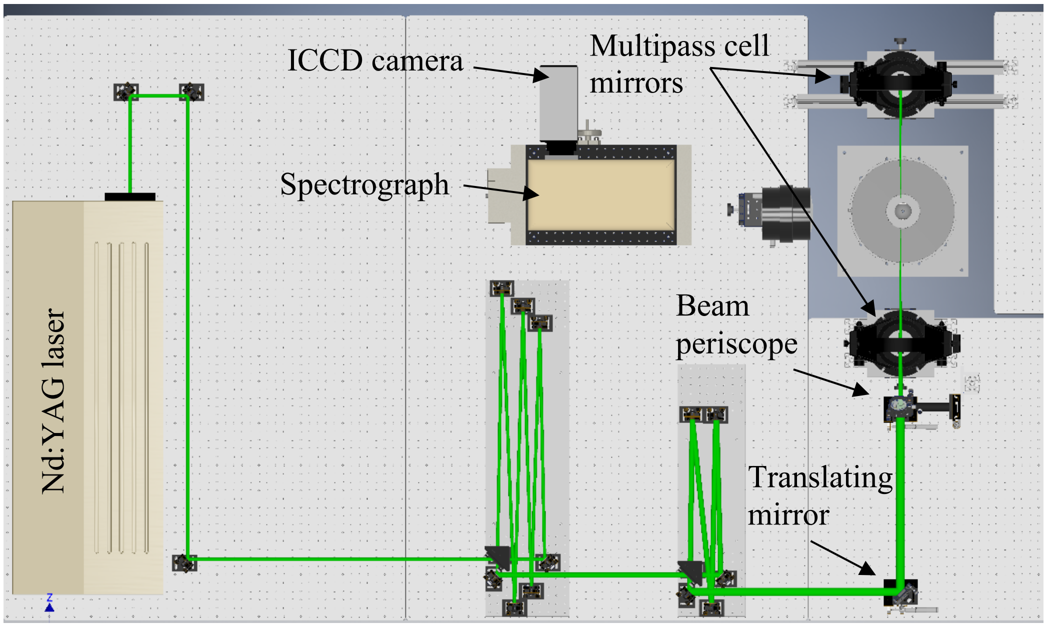

Figure D.13: Top view of actual pulse stretcher and multiple-pass cell layout.

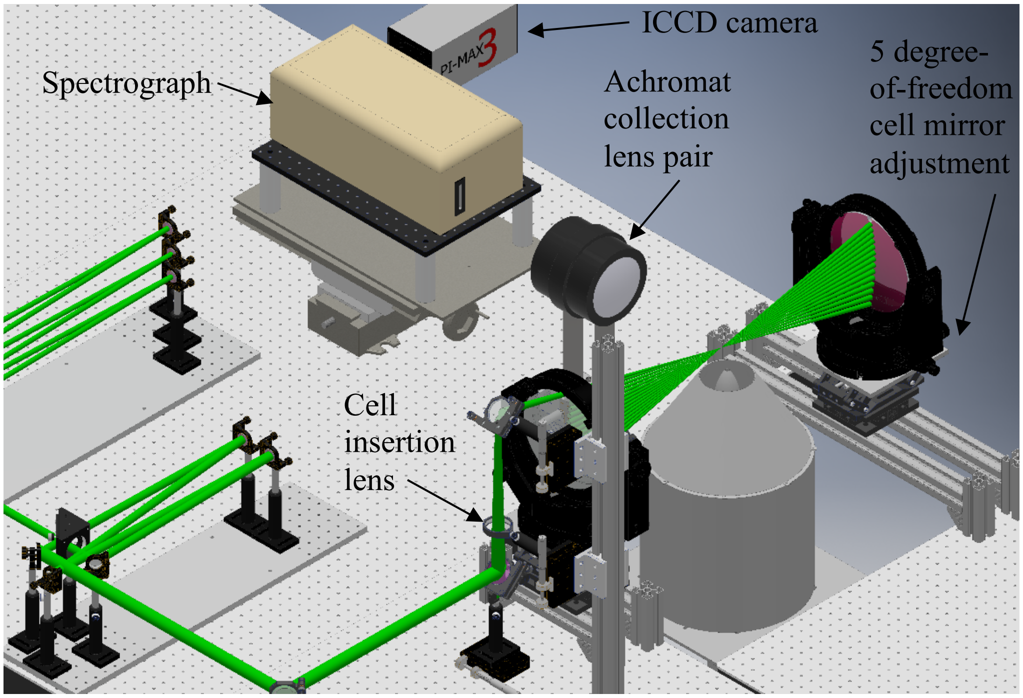

Figure D.14: Isometric view of multiple-pass cell mounting system.

References

[1] Vincenti, W. G., and Kruger, C. H., "*Introduction to Physical Gas Dynamics,*" John Wiley, New York, 1965.

[2] Fiévet, R., Voelkel, S., Koo, H., Raman, V., and Varghese, P. L., "Effect of thermal nonequilibrium on ignition in scramjet combustors," *Proceedings of the Combustion Institute*, Vol. 36, No. 2, 2017, pp. 2901–2910, DOI: 10.1016/j.proci.2016.08.066.

[3] Clarke, J. F., and McChesney, M., "*The Dynamics of Real Gases,*" Butterworth, Washington, D.C., 1964.

[4] Cohen-Tannoudji, C., Diu, B., and Laloë, F., "*Quantum Mechanics,*" Wiley-VCH, Paris, 1977.

[5] Montroll, E. W., and Shuler, K. E., "Studies in Nonequilibrium Rate Processes. I. The Relaxation of a System of Harmonic Oscillators," *The Journal of Chemical Physics*, Vol. 26, No. 3, 1957, pp. 454–464, DOI: 10.1063/1.1743326.

[6] Bazley, N. W., Montroll, E. W., Rubin, R. J., and Shuler, K. E., "Studies in Nonequilibrium Rate Processes. III. The Vibrational Relaxation of a System of Anharmonic Oscillators," *The Journal of Chemical Physics*, Vol. 28, No. 4, 1958, p. 700, DOI: 10.1063/1.1744217.

[7] Bazley, N. W., Montroll, E. W., Rubin, R. J., and Shuler, K. E., "Errata: Studies in Nonequilibrium Rate Processes. III. The Vibrational Relaxation of a System of Anharmonic Oscillators," *The Journal of Chemical Physics*, Vol. 29, No. 5, 1958, p. 1185, DOI: 10.1063/1.1744680.

[8] Herzfeld, K. F., and Litovitz, T. A., "*Absorption and Dispersion of Ultrasonic Waves,*" Academic Press, New York, 1959.

[9] Schwartz, R. N., Slawsky, Z. I., and Herzfeld, K. F., "Calculation of Vibrational Relaxation Times in Gases," *The Journal of Chemical Physics*, Vol. 20, No. 10, 1952, p. 1591, DOI: 10.1063/1.1700221.

[10] Schwartz, R. N., and Herzfeld, K. F., "Vibrational Relaxation Times in Gases (Three-Dimensional Treatment)," *The Journal of Chemical Physics*, Vol. 22, No. 5, 1954, p. 767, DOI: 10.1063/1.1740190.

[11] Adamovich, I. V., "Three Dimensional Analytic Model of Vibrational Energy Transfer in Molecule-Molecule Collisions," *AIAA Journal*, Vol. 39, No. 10, 2001, pp. 1916–1925.

[12] Secrest, D., "Exact Quantum-Mechanical Calculation of a Collinear Collision of a Particle with a Harmonic Oscillator," *The Journal of Chemical Physics*, Vol. 45, No. 12, 1966, p. 4556, DOI: 10.1063/1.1727537.

[13] Chapuisat, X., and Bergeron, G., "Anharmonicity Effects in the Collinear Collision

of Two Diatmoic Molecules," *Chemical Physics*, Vol. 36, 1979, pp. 397–405.

[14] Hernández, R., Toumi, R., and Clary, D., "State-selected vibrational relaxation rates for highly vibrationally excited oxygen molecules," *The Journal of Chemical Physics*, Vol. 102, No. June, 1995, pp. 9544–9556, DOI: 10.1063/1.468770.

[15] Billing, G. D., "Vibration-Vibration and Vibration-Translation Energy Transfer, Including Multiquantum Transitions in Atom-Diatom and Diatom-Diatom Collisions," *Nonequilbirium Vibrational Kinetics*, Vol. 39, 1986, pp. 85–112, DOI: 10.1007/978-3-642-48615-9_4.

[16] Billing, G. D., and Fisher, E. R., "VV and VT Rate Coefficients in N_2 by a Quantum-Classical Model," *Chemical Physics*, Vol. 43, 1979, pp. 395–401.

[17] Billing, G. D., and Kolesnick, R. E., "Vibrational relaxation of oxygen. State to state rate constants," *Chemical Physics Letters*, Vol. 200, No. 4, 1992, pp. 382–386, DOI: 10.1016/0009-2614(92)87008-D.

[18] Billing, G. D., "VV and VT rates in N_2-O_2 collisions," *Chemical Physics*, Vol. 179, No. 3, 1994, pp. 463–467, DOI: 10.1016/0301-0104(94)87022-5.

[19] Eden, D., Lindsay, R. B., and Zsnk, H., "Acoustic Attenuation and Relaxation Phenomena in Steam at High Temperature and Pressure," *Journal of Engineering for Power*, Vol. 83, 1961, pp. 137–144.

[20] Taylor, R. L., Camac, M., and Feinberg, R. M., "Measurements of Vibration-Vibration Coupling in Gas Mixtures," *Symposium (International) on Combustion*, Vol. 11, No. 1, 1967, pp. 49–65.

[21] Lukasik, S. J., and Young, J. E., "Vibrational Relaxation Times in Nitrogen," *The Journal of Chemical Physics*, Vol. 27, No. 5, 1957, p. 1149, DOI: 10.1063/1.1743947.

[22] Millikan, R. C., and White, D. R., "Systematics of Vibrational Relaxation," *The Journal of Chemical Physics*, Vol. 39, No. 12, 1963, p. 3209, DOI: 10.1063/1.1734182.

[23] White, D. R., and Millikan, R. C., "Vibrational Relaxation of Oxygen," *The Journal of Chemical Physics*, Vol. 39, No. 7, 1963, p. 1803, DOI: 10.1063/1.1734532.

[24] White, D. R., and Millikan, R. C., "Vibrational Relaxation in Air," *AIAA Journal*, Vol. 2, No. 10, 1964, pp. 1844–1846.

[25] Center, R. E., and Newton, J. F., "Vibrational relaxation of N_2 by H_2O," *The Journal of Chemical Physics*, Vol. 68, No. 8, 1978, p. 3327, DOI: 10.1063/1.436237.

[26] Whitson, M. E., and McNeal, R. J., "Temperature dependence of the quenching of vibrationally excited N2 by NO and H2O," *The Journal of Chemical Physics*, Vol.

66, No. 6, 1977, p. 2696, DOI: 10.1063/1.434217.

[27] Henderson, M. C., Clark, A. V., and Lintz, P. R., "Thermal Relaxation in Oxygen with H_2O, HDO, and D_2O as Impurities," *The Journal of the Acoustical Society of America*, Vol. 37, No. 3, 1965, pp. 457–463.

[28] Taylor, R., and Bitterman, S., "Survey of Vibrational Relaxation Data for Processes Important in the CO_2-N_2 Laser System," *Reviews of Modern Physics*, Vol. 41, 1969, pp. 26–47, DOI: 10.1103/RevModPhys.41.26.

[29] Joly, V., and Roblin, A., "Vibrational relaxation of CO_2 (m, n^l, p) in a CO_2-N_2 mixture . Part 1 : Survey of available data," *Aerospace Science and Technology*, Vol. 3, No. 4, 1999, pp. 229–238.

[30] Rothman, L. S., "Infrared energy levels and intensities of carbon dioxide. Part 3," *Applied Optics*, Vol. 25, No. 11, 1986, pp. 1795–1816.

[31] Long, D. A., "*The Raman Effect: A Unified Treatment of the Theory of Raman Scattering by Molecules,*" West Sussex, England: John Wiley & Sons Ltd, John Wiley & Sons, New York, 2002, DOI: 10.1002/0470845767.

[32] Rychlewski, J., "A variation-perturbation calculation of the dynamic polarizability of the H2 molecule," *Chemical Physics Letters*, Vol. 73, No. 1, 1980, pp. 135–138.

[33] KC, U., "Development of a Multiple-Pass Raman Spectrometer For Flame Diagnostics," The University of Texas at Austin, 2013.

[34] Utsav, K. C., and Varghese, P. L., "Accurate temperature measurements in flames with high spatial resolution using Stokes Raman scattering from nitrogen in a multiple-pass cell.," *Applied Optics*, Vol. 52, No. 20, 2013, pp. 5007–21, DOI: 10.1364/AO.52.005007.

[35] Buldakov, M. A., Ippolitov, I. I., Korolev, B. V., Matrosov, I. I., Cheglokov, A. E., Cherepanov, V. N., Makushkin, Y. S., and Ulenikov, O. N., "Vibration rotation Raman spectroscopy of gas media," *Spectrochimica Acta - Part A: Molecular and Biomolecular Spectroscopy*, Vol. 52, No. 8, 1996, pp. 995–1007, DOI: 10.1016/0584-8539(95)01631-7.

[36] Buldakov, M. A., Cherepanov, V. N., Korolev, B. V, and Matrosov, I. I., "The role of intramolecular interactions in Raman spectra," *Journal of Molecular Spectroscopy*, Vol. 217, 2003.

[37] Laher, R. R., and Gilmore, F. R., "Improved Fits for the Vibrational and Rotational Constants of Many States of Nitrogen and Oxygen," *Journal of Physical and Chemical Reference Data*, Vol. 20, No. 4, 1991, pp. 685–712, DOI: 10.1063/1.555892.

[38] Huber, K. P., and Herzberg, G., "Constants of Diatomic Molecules," *NIST Chemistry WebBook, NIST Standard Reference Database Number 69*, DOI: 10.18434/T4D303.

[39] Bérard, M., Lallemand, P., Cebe, J. P., Giraud, M., Berard, M., and Laliemand, P., "Experimental and theoretical analysis of the temperature dependence of rotational Raman linewidths of oxygen Experimental and theoretical analysis of the temperature dependence of rotational Raman linewidths of oxygen," *Journal of Chemical Physics*, Vol. 78, No. 1983, 1983, p. 672, DOI: 10.1063/1.444811.

[40] Fanjoux, G., Millet, G., and Chaux, R., "Coherent anti-Stokes Raman spectroscopy in the O_2-H_2O Q branch study of collisional broadening," *The Journal of Chemical Physics*, Vol. 101, No. July, 1994, pp. 1061–1071, DOI: 10.1063/1.467803.

[41] Millot, G., Saint-Loup, R., Santos, J., Chaux, R., Berger, H., and Bonamy, J., "Collisional effects in the stimulated Raman Q branch of O_2 and O_2-N_2," *The Journal of Chemical Physics*, Vol. 96, No. 2, 1992, pp. 961–971, DOI: 10.1063/1.462116.

[42] Drake, M. C., and Rosenblatt, G. M., "Flame Temperatures from Raman Scattering," *Chemical Physics Letters*, Vol. 44, No. 2, 1976, pp. 313–316.

[43] Alessandretti, G., "Some Results on the Measurement of Temperature and Density in a Flame by Raman Spectroscopy," *Optica Acta: International Journal of Optics*, Vol. 27, No. 8, 1980, pp. 1095–1103, DOI: 10.1080/713820364.

[44] Fernández, J. M., Punge, A., Tejeda, G., and Montero, S., "Quantitative diagnostics of a methane/air mini-flame by Raman spectroscopy," *Journal of Raman Spectroscopy*, Vol. 37, No. 1–3, 2006, pp. 175–182, DOI: 10.1002/jrs.1462.

[45] Karpetis, A. N., and Gomez, A., "Temperature measurements in spray flames by spontaneous Raman scattering.," *Optics letters*, Vol. 21, No. 10, 1996, pp. 704–6.

[46] Utsav, K. C., Silver, J. a, Hovde, D. C., and Varghese, P. L., "Improved multiple-pass Raman spectrometer.," *Applied optics*, Vol. 50, No. 24, 2011, pp. 4805–16.

[47] Kojima, J. J., and Nguyen, Q.-V., "Single-shot rotational Raman thermometry for turbulent flames using a low-resolution bandwidth technique," *Measurement Science and Technology*, Vol. 19, No. 1, 2008, p. 15406, DOI: 10.1088/0957-0233/19/1/015406.

[48] Fuest, F., Barlow, R. S., Chen, J. Y., and Dreizler, A., "Raman/Rayleigh scattering and CO-LIF measurements in laminar and turbulent jet flames of dimethyl ether," *Combustion and Flame*, Vol. 159, No. 8, 2012, pp. 2533–2562, DOI: 10.1016/j.combustflame.2011.11.001.

[49] Sepman, A. V, Toro, V. V, Mokhov, A. V, and Levinsky, H. B., "Determination of temperature and concentrations of main components in flames by fitting measured Raman spectra," *Applied Physics B*, Vol. 112, No. 1, 2013, pp. 35–47, DOI: 10.1007/s00340-013-5389-2.

[50] Samson, J. A. R., "On the measurement of Rayleigh scattering," *Journal of*

Quantitative Spectroscopy and Radiative Transfer, Vol. 9, No. 6, 1969, pp. 875–879, DOI: http://dx.doi.org/10.1016/0022-4073(69)90081-8.

[51] Eckbreth, A. C., "*Laser diagnostics for combustion temperature and species,*" CRC Press, 1996.

[52] Clemens, N. T., "Flow Imaging," *Encyclopedia of Imaging Science and Technology*, 2002, pp. 390–419.

[53] Dibble, R. W., and Hollenbach, R. E., "Laser Rayleigh thermometry in turbulent flames," *18th Symposium (International) on Combustion*, Vol. 18, No. 1, 1981, pp. 1489–1499, DOI: 10.1016/S0082-0784(81)80151-8.

[54] Barlow, R. S., and Karpetis, A. N., "Measurements of scalar variance, scalar dissipation, and length scales in turbulent piloted methane/air jet flames," *Flow, Turbulence and Combustion*, Vol. 72, No. 2–4 SPEC. ISS., 2004, pp. 427–448, DOI: 10.1023/B:APPL.0000044405.96071.e1.

[55] Cabra, R., Chen, J., Dibble, R. W., Karpetis, A. N., and Barlow, R. S., "Lifted methane–air jet flames in a vitiated coflow," *Combustion and Flame*, Vol. 143, No. 4, 2005, pp. 491–506, DOI: 10.1016/j.combustflame.2005.08.019.

[56] Wang, G.-H., Clemens, N. T., Barlow, R. S., and Varghese, P. L., "A system model for assessing scalar dissipation measurement accuracy in turbulent flows," *Measurement Science and Technology*, Vol. 18, No. 5, 2007, pp. 1287–1303, DOI: 10.1088/0957-0233/18/5/015.

[57] Barlow, R. S., Wang, G.-H., Anselmo-Filho, P., Sweeney, M. S., and Hochgreb, S., "Application of Raman/Rayleigh/LIF diagnostics in turbulent stratified flames," *Proceedings of the Combustion Institute*, Vol. 32 I, No. 1, 2009, pp. 945–953, DOI: 10.1016/j.proci.2008.06.070.

[58] Bergmann, V., Meier, W., Wolff, D., and Stricker, W., "Application of spontaneous Raman and Rayleigh scattering and 2D LIF for the characterization of a turbulent $CH_4/H_2/N_2$ jet diffusion flame," *Applied Physics B: Lasers and Optics*, Vol. 66, No. 4, 1998, pp. 489–502, DOI: 10.1007/s003400050424.

[59] Fourguette, D. C., Zurn, R. M., and Long, M. B., "Two- Dimensional Rayleigh Thermometry in a Turbulent Nonpremixed Methane-Hydrogen Flame," *Combustion Science and Technology*, Vol. 44, No. l, 1986, pp. 307–317.

[60] Fielding, J., Schaffer, A. M., and Long, M. B., "Three-Scalar Imaging in Turbulent Non-Premixed Flames of Methane," *Symposium (International) on Combustion*, 1007–1014, 1998.

[61] Frank, J. H., Kaiser, S. A., and Long, M. B., "Reaction-rate, mixture-fraction, and temperature imaging in turbulent methane/air jet flames," *Proceedings of the Combustion Institute*, 2687–2694, 2002, DOI: 10.1016/S1540-7489(02)80327-3.

[62] Frank, J. H., Kaiser, S. A., and Long, M. B., "Multiscalar imaging in partially

premixed jet flames with argon dilution," *Combustion and Flame*, Vol. 143, No. 4, 2005, pp. 507–523, DOI: 10.1016/j.combustflame.2005.08.027.

[63] Kelman, J. B., Eltobaji, A. J., and Masri, A. R., "Laser Imaging in the Stabilisation Region of Turbulent Lifted Flames," *Combustion Science and Technology*, Vol. 135, No. 1–6, 1998, pp. 117–134, DOI: 10.1080/00102209808924153.

[64] Everest, D. A., Driscoll, J. F., Dahm, W. J. A., and Feikema, D. a., "Images of the Two-Dimensional Field and Temperature Gradients to Quantify Mixing Rates within a Non-Premixed Turbulent Jet Flame," *Combustion and Flame*, Vol. 101, 1995, pp. 58–68.

[65] Frank, J. H., and Kaiser, S. A., "High-resolution imaging of dissipative structures in a turbulent jet flame with laser Rayleigh scattering," *Experiments in Fluids*, Vol. 44, 2008, pp. 221–233, DOI: 10.1007/s00348-007-0396-x.

[66] Wang, G.-H., Clemens, N. T., and Varghese, P. L., "High-repetition rate measurements of temperature and thermal dissipation in a non-premixed turbulent jet flame," *Proceedings of the Combustion Institute*, 691–698, 2005, DOI: 10.1016/j.proci.2004.08.269.

[67] Wang, G.-H., Clemens, N. T., Varghese, P. L., and Barlow, R. S., "Turbulent time scales in a nonpremixed turbulent jet flame by using high-repetition rate thermometry," *Combustion and Flame*, Vol. 152, No. 3, 2008, pp. 317–335, DOI: 10.1016/j.combustflame.2007.08.010.

[68] Papageorge, M. J., McManus, T. a., Fuest, F., and Sutton, J. a., "Recent advances in high-speed planar Rayleigh scattering in turbulent jets and flames: increased record lengths, acquisition rates, and image quality," *Applied Physics B*, Vol. 115, No. 2, 2013, pp. 197–213, DOI: 10.1007/s00340-013-5591-2.

[69] Barlow, R. S., Fourguette, D. C., Mungal, M. G., and Dibble, R. W., "Experiments on the structure of an annular compressible reacting shear layer," *AIAA journal*, Vol. 30, No. 9, 1992.

[70] Cabra, R., Myhrvold, T., Chen, J. Y., Dibble, R. W., Karpetis, A. N., and Barlow, R. S., "Simultaneous laser raman-rayleigh-lif measurements and numerical modeling results of a lifted turbulent H_2/N_2 jet flame in a vitiated coflow," *Proceedings of the Combustion Institute*, Vol. 29, No. 2, 2002, pp. 1881–1888, DOI: 10.1016/S1540-7489(02)80228-0.

[71] Mastorakos, E., Baritaud, T. A., and Poinsot, T. J., "Numerical simulations of autoignition in turbulent mixing flows," *Combustion and Flame*, Vol. 109, No. 1–2, 1997, pp. 198–223, DOI: 10.1016/S0010-2180(96)00149-6.

[72] Hilbert, R., and Thévenin, D., "Autoignition of turbulent non-premixed flames investigated using direct numerical simulations," *Combustion and Flame*, Vol. 128, No. 1–2, 2002, pp. 22–37, DOI: 10.1016/S0010-2180(01)00330-3.

[73] Goodwin, D. G., Moffat, H. K., and Speath, R. L., "Cantera: An object-oriented software toolkit for chemical kinetics, thermodynamics, and transport processes," 2015.

[74] "Chemical-Kinetic Mechanisms for Combustion Applications," *San Diego Mechanism web page, Mechanical and Aerospace Engineering (Combustion Research), University of California at San Diego (http://combustion.ucsd.edu)*.

[75] Bilger, R. W., Starner, S. H., and Kee, R. J., "On reduced mechanisms for methane-air combustion in nonpremixed flames," *Combustion and Flame*, Vol. 80, No. 2, 1990, pp. 135–149.

[76] Wu, Z., Starner, S. H., and Bilger, R. W., "Lift-off heights of turbulent H_2/N_2 jet flames in a vitiated co-flow," *Proceedings of the 2003 Australian Symposium on Combustion and the 8th Australian Flame Days*, 2003.

[77] Gordon, R. L., Stårner, S. H., Masri, A. R., and Bilger, R. W., "Further Characterisation of Lifted Hydrogen and Methane Flames Issuing into a Vitiated Coflow," *Fifth Asia-Pacific Conference on Combustion*, No. July 2005, 2005, pp. 333–336.

[78] Cao, R. R., Pope, S. B., and Masri, A. R., "Turbulent lifted flames in a vitiated coflow investigated using joint PDF calculations," *Combustion and Flame*, Vol. 142, No. 4, 2005, pp. 438–453, DOI: 10.1016/j.combustflame.2005.04.005.

[79] Wang, H., and Pope, S. B., "Auto-ignition test of flame condition of Cabra H_2/N_2 lifted flame," *Ninth International Workshop on Measurement and Computation of Turbulent Nonpremixed Flames*, 224–225, 2008.

[80] Reising, H. H., KC, U., Clemens, N. T., and Varghese, P. L., "Measurement of mixing-induced thermal non-equilibrium in a supersonic shear layer using spontaneous Raman scattering," *Physics of Fluids*, Vol. 29, No. 7, 2017, p. 76101, DOI: 10.1063/1.4991754.

[81] Papamoschou, D., and Roshko, A., "The compressible turbulent shear layer : an experimental study," *Journal of Fluid Mechanics*, Vol. 197, 1988, pp. 453–477, DOI: https://doi.org/10.1017/S0022112088003325.

[82] Buch, K. A., and Dahm, W. J. A., "Experimental study of the fine-scale structure of conserved scalar mixing in turbulent shear flows. Part 2. Sc≈1," *Journal of Fluid Mechanics*, Vol. 364, 1998, pp. 1–29, DOI: 10.1017/S0022112098008726.

[83] Fourguette, D. C., Zurn, R. M., and Long, M. B., "Two-Dimensional Rayleigh Thermometry in a Turbulent Nonpremixed Methane-Hydrogen Flame," *Combustion Science and Technology*, Vol. 44, 1986, pp. 307–317.

[84] Clemens, N. T., and Mungal, M. G., "Two- and Three-Dimensional Effects in the Supersonic Mixing Layer," *AIAA Journal*, Vol. 30, No. 4, 1992.

[85] Thurow, B., Samimy, M., and Lempert, W. R., "Compressibility effects on

turbulence structures of axisymmetric mixing layers," *Physics of Fluids*, Vol. 15, No. 6, 2003, p. 1755, DOI: 10.1063/1.1570829.

[86] Clemens, N. T., and Paul, P. H., "Scalar measurements in compressible axisymmetric mixing layers," *Physics of Fluids*, Vol. 7, No. 5, 1995, pp. 1071–1081, DOI: 10.1063/1.868761.

[87] Goebel, S. G., and Dutton, C., "Experimental Study of Compressible Turbulent Mixing Layers," *AIAA Journal*, Vol. 29, No. 4, 1991, pp. 538–546.

[88] Koo, H., Raman, V., and Varghese, P. L., "Direct numerical simulation of supersonic combustion with thermal nonequilibrium," *Proceedings of the Combustion Institute*, Vol. 35, No. 2, 2015, pp. 2145–2153, DOI: 10.1016/j.proci.2014.08.005.

[89] Fuller, T. J., Hsu, A., Sanchez-Gonzalez, R., Dean, J. C., North, S., and Bowersox, R. D. W., "Radiofrequency plasma stabilization of a low-Reynolds-number channel flow," *Journal of Fluid Mechanics*, Vol. 748, 2014, pp. 663–691, DOI: 10.1017/jfm.2014.189.

[90] Voelkel, S., Raman, V., and Varghese, P. L., "Effect of thermal nonequilibrium on reactions in hydrogen combustion," *Shock Waves*, Vol. 26, No. 5, 2016, pp. 539–549, DOI: 10.1007/s00193-016-0645-0.

[91] Weber, R. F., and Garscadden, A., "Errors Due to Averaging Spectral-Line Intensities in the Presence of Electron-Temperature Variations," *Journal of the Optical Society of America*, Vol. 61, No. 10, 1971, pp. 1330–1334.

[92] Elliott, G. S., and Samimy, M., "Compressibility effects in free shear layers," *Physics of Fluids A: Fluid Dynamics*, Vol. 2, No. 7, 1990, p. 1231, DOI: 10.1063/1.857816.

[93] Clemens, N. T., Paul, P. H., Mungal, M. G., and Hanson, R. K., "Scalar Mixing in the Supersonic Shear Layer," *AIAA 22nd Fluid Dynamics, Plasma Dynamics & Lasers Conference*, 1991.

[94] Dimotakis, P. E., "Two-dimensional shear-layer entrainment," *AIAA Journal*, Vol. 24, No. 11, 1986, pp. 1791–1796, DOI: 10.2514/3.9525.

[95] Reising, H. H., Haller, T., Clemens, N. T., Varghese, P. L., Fiévet, R., and Raman, V., "Spontaneous Raman Scattering Temperature Measurements and Large Eddy Simulations of Vibrational Non-equilibrium in High-Speed Jet Flames," *32nd AIAA Aerodynamic Measurement Technology and Ground Testing Conference*, 2016, DOI: 10.2514/6.2016-3550.

[96] Reising, H. H., Kc, U., Voelkel, S., Clemens, N. T., Raman, V., Varghese, P. L., and Koo, H., "Vibrational Non-equilibrium Effects in Supersonic Jet Mixing," *52nd AIAA Aerospace Sciences Meeting*, 2014, DOI: 10.2514/6.2014-0231.

[97] Cutler, A. D., Cantu, L. M. L., Gallo, E. C. A., Baurle, R., Danehy, P. M.,

Rockwell, R., Goyne, C., and McDaniel, J., “Nonequilibrium Supersonic Freestream Studied Using Coherent Anti-Stokes Raman Spectroscopy,” *AIAA Journal*, Vol. 53, No. 9, 2015, pp. 2762–2770, DOI: 10.2514/1.J053748.

[98] Phuoc, T. X., “Laser spark ignition: Experimental determination of laser-induced breakdown thresholds of combustion gases,” *Optics Communications*, Vol. 175, No. 4, 2000, pp. 419–423, DOI: 10.1016/S0030-4018(00)00488-0.

[99] Nguyen, Q.-V., Dibble, R. W., Carter, C. D., Fiechtner, G. J., and Barlow, R. S., “Raman-LIF measurements of temperature, major species, OH, and NO in a methane-air Bunsen flame,” *Combustion and Flame*, Vol. 105, No. 4, 1996, pp. 499–510, DOI: 10.1016/0010-2180(96)00226-X.

[100] Kojima, J. J., and Nguyen, Q.-V., “Laser Pulse-Stretching Using Multiple Optical Ring-Cavities,” *Applied Optics*, Vol. 41, No. 30, 2002.

[101] Bernstein, E. F., “The new-generation, high-energy, 595-nm, long pulse-duration pulsed-dye laser improves the appearance of photodamaged skin,” *Lasers in Surgery and Medicine*, Vol. 39, No. 2, 2007, pp. 157–163, DOI: 10.1002/lsm.20463.

[102] Kauvar, A. N. B., “The role of lasers in the treatment of leg veins,” *Seminars in Cutaneous Medicine and Surgery*, Vol. 19, No. 4, 2000, pp. 245–252, DOI: 10.1053/sder.2000.18364.

[103] Utsav, K. C., and Varghese, P. L., “Accurate temperature measurements in flames with high spatial resolution using Stokes Raman scattering from nitrogen in a multiple-pass cell.,” *Applied optics*, Vol. 52, No. 20, 2013, pp. 5007–21.

[104] Ahn, T., Adamovich, I. V., and Lempert, W. R., “Determination of nitrogen V-V transfer rates by stimulated Raman pumping,” *Chemical Physics*, Vol. 298, No. 1–3, 2004, pp. 233–240, DOI: 10.1016/j.chemphys.2003.11.029.

[105] Ahn, T., Adamovich, I. V., and Lempert, W. R., “Stimulated Raman scattering measurements of V-V transfer in oxygen,” *Chemical Physics*, Vol. 323, No. 2–3, 2006, pp. 532–544, DOI: 10.1016/j.chemphys.2005.10.036.

[106] Ahn, T., Adamovich, I. V., and Lempert, W. R., “Stimulated Raman scattering measurements of H_2 vibration-vibration transfer,” *Chemical Physics*, Vol. 335, No. 1, 2007, pp. 55–68, DOI: 10.1016/j.chemphys.2007.03.025.

[107] Zhang, B., Lempert, W. R., Miles, R. B., and Diskin, G., “Efficient vibrational Raman conversion in O2 and N2 cells by use of superfluorescence seeding,” *Optics Letters*, Vol. 18, No. 14, 1993, pp. 1132–1134.

[108] Saloman, E. B., and Sansonetti, C. J., “Wavelengths, energy level classifications, and energy levels for the spectrum of neutral mercury,” *Journal of Physical and Chemical Reference Data*, Vol. 33, No. 4, 2004, pp. 1113–1158, DOI: 10.1063/1.2204960.

[109] Hecht, J., "*The Laser Guidebook,*" TAB Books, Blue Ridge Summit, PA, 1992.

[110] Trutna, W. R., and Byer, R. L., "Multiple-pass Raman gain cell.," *Applied optics*, Vol. 19, No. 2, 1980, pp. 301–312, DOI: 10.1364/AO.19.000301.

[111] Pearman, W. F., Carter, J. C., Angel, S. M., and Chan, J. W.-J., "Quantitative measurements of CO_2 and CH_4 using a multipass Raman capillary cell.," *Applied optics*, Vol. 47, No. 25, 2008, pp. 4627–4632, DOI: 171384 [pii].

[112] Li, X., Xia, Y., Zhan, L., and Huang, J., "Near-confocal cavity-enhanced Raman spectroscopy for multitrace-gas detection," *Optics Letters*, Vol. 33, No. 18, 2008, pp. 2143–2145, DOI: 10.1364/OL.33.002143.

[113] Carr, C. W., Radousky, H. B., and Demos, S. G., "Wavelength Dependence of Laser-Induced Damage: Determining the Damage Initiation Mechanisms," *Physical Review Letters*, Vol. 91, No. 12, 2003, p. 127402, DOI: 10.1103/PhysRevLett.91.127402.

[114] Bennett, H. E., "Laser induced damage in optical materials, 1982: proceedings of a symposium," *Lasers, Annual Symposium on Optical Materials for High Power*, Boulder, CO, Fourteenth Symposium on Optical Materials for High, 1984.